MODULATION EXCITATION SPECTROSCOPY APPLIED ON HETEROGENEOUS LEWIS ACID CATALYSIS

by

Philipp Müller

A dissertation submitted in partial fulfillment of
the requirements for the degree of

Doctor of Philosophy

(Chemistry)

at the

UNIVERSITY OF WISCONSIN–MADISON

2017

Date of final oral examination: 05/31/17

The dissertation is approved by the following members of the Final Oral Committee:

Ive Hermans, Associate Professor, Chemistry & Chemical and Biological Engineering
Thomas C. Brunold, Professor, Chemistry
Randall H. Goldsmith, Assistant Professor, Chemistry
Clark R. Landis, Professor, Chemistry
Thatcher W. Root, Professor, Chemical and Biological Engineering

© Copyright by Philipp Müller 2017
All Rights Reserved

Dedicated to Dr. Urs Leisinger for showing me his passion for science

ACKNOWLEDGMENTS

First and foremost, I would like to thank Professor Ive Hermans for giving me the chance to join his journey across the atlantic ocean and build a new lab. Ive, I really appreciated the freedom you gave me in pursuing different research directions and am thankful for your advice whenever I needed it. I would also like to thank the members of my committee, Professors Randy Goldsmith, Thomas Brunold, Clark Landis, and Thatcher Root. The financial support of my research by the University of Wisconsin - Madison, the Army Research Office, as well as the Petroleum Research Fund of the ACS is kindly acknowledged.

During my time in the Hermans group, I was fortunate to collaborate with many great scientists, engineers and most of all friends. I would like to especially thank Patrick who made the transition to a foreign country much easier and more fun. Sabrina for always having an open ear and helping me with my research. Joe who shared an apartment with me for a year and who went skiing with me at legendary Mount Bohemia a couple of times. Sam for being a great roommate for two years and his help with XPS and EXAFS. Alyssa for helping me with NMR and sharing the best hotline bling dance with us. Also, all the other graduate students and postdocs Sarah, Will, Juan, Dongting, Lifeng, Shao-Chun, Melissa, Peter, and Casey who I was able to teach some things but from whom I also learned a lot. Alessandro, Florian and Carlos for organizing many social events outside of the lab, but also for letting me look at science from different angles. The undergraduates who worked with me, Trevor and Sherry, who did a great job in helping me with some of the projects. The staff at the Chemistry Department was always helpful and friendly.

I would like to especially thank my parents and my sister for the continuing support during all my scientific endeavours, even though they often did not understand a single word of what I was talking about when explaining my latest experiments. My friends, near and far, for letting me think about other things than science from time to time. Finally, Judith, who I was fortunate to meet at a random night out in Chicago and who was there for me ever since.

Thank You, Danke, Merci!

CONTENTS

ABSTRACT

Obtaining a molecular level understanding of reaction mechanisms is one of the great challenges in heterogeneous catalysis. Heterogeneous reactions are inherently complex, as many different reaction steps, such as adsorption, reaction, and desorption of reactants, intermediates and (by)-products occur simultaneously over few active sites. Hence, highly sensitive and selective experimental tools are required to study such reactions. Modulation Excitation Spectroscopy (MES) provides such a tool by periodically modulating the concentration of reactants or intermediates and analyzing the dynamic changes on the catalyst surface as well as in the outlet streams. In this work, we study porous heterogeneous Lewis acids, an important class of catalysts with various applications in biomass upgrading, oxidations, and transfer hydrogenations. As a first example, we investigate the cyclization of citronellal over different stannosilicates. We find vast differences in terms of activity depending on the used solvent and pore structure that we further investigate with an extensive MES-ATR-IR study (Chapter 2). Based on these findings, we perform experiments with additional solvents that suggest diffusion to be influencing the reactivity of these systems (Chapter 3). Experimentally determined diffusion coefficients agree with this hypothesis, but only for the microporous Sn-Beta catalyst. We then move from liquid to gas phase reactions and study the production of 1,3-butadiene from ethanol over Lewis acid catalysts. Therefore, a newly developed *operando* DRIFTS-MS setup is used to simultaneously study changes on the catalyst surface as well as in the gas phase. Purely Lewis acidic catalysts such as Ta-BEA require a mixture of acetaldehyde and ethanol to produce 1,3-butadiene. We find that the Meerwein-Ponndorf-Verley (MPV) mechanism occurs over Ta-BEA, indicated by a distinct surface intermediate (Chapter 4). Adding a metal functionality to a Lewis acid catalyst allows for the direct conversion of ethanol. As an example, we study a Ag-Zr-BEA catalyst and find that at high ethanol pressures the MPV mechanism takes place (Chapter 5). In both cases a subtle control of the ratios of reactants and intermediates is crucial to reach highest 1,3-butadiene yields. The fundamental insights obtained in this work might eventually lead to improved

catalysts making the production of chemicals more sustainable.

1 INTRODUCTION

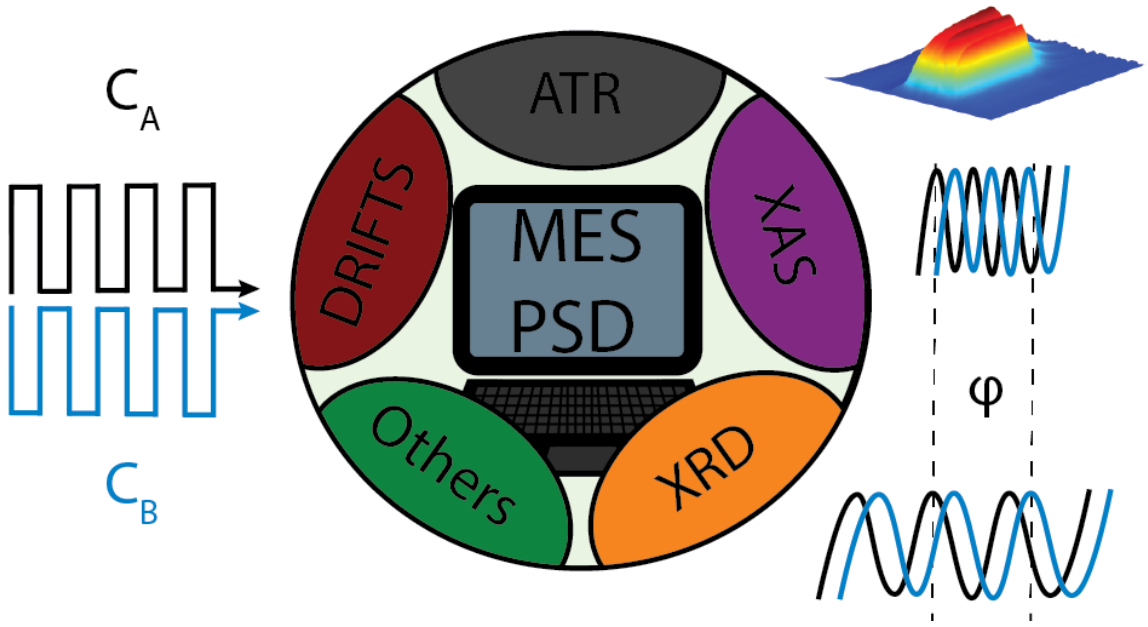

In this chapter, an introduction on modulation excitation spectroscopy and different application examples are given. Then, the materials that were studied in this thesis, namely porous Lewis acid catalysts, are discussed. Finally, the scope of the thesis is presented. Parts of this introduction were published in the form of a review article in Industrial & Engineering Chemistry Research.[1]

1.1 Introduction of Modulation Excitation Spectroscopy

One of the great challenges for the *in situ* characterization of catalysts is the fact that most often the active sites are only present in small quantities. Hence, it is important to use highly sensitive spectroscopic tools, including sophisticated data treatments, to extract the most information possible from catalyst surfaces.

Furthermore, especially in heterogeneous catalysis, many different phenomena such as adsorption, (by)-product formation and desorption are spectroscopically superimposed and occur simultaneously which makes spectra interpretation highly challenging. It was in the year 2001, when Baurecht and Fringeli[2] introduced a novel methodology called modulation excitation spectroscopy (MES) that added such a highly sensitive and selective method to the toolbox of *in situ* and *operando* spectroscopic techniques that was found to be especially valuable for the analysis of heterogeneous catalysts. As shown in Figure 1.1, since 2001, the number of articles using or discussing MES has been increasing since then. Initially, attenuated total reflection infrared spectroscopy (ATR-IR) was the spectroscopic technique of choice, but more recently other techniques such as polarization-modulation infrared reflection absorption spectroscopy (PM-IRRAS), diffuse reflectance infrared Fourier transform spectroscopy (DRIFTS), X-ray absorption spectroscopy (XAS), X-ray diffraction (XRD) and combinations of these techniques and others have been used in conjunction with MES as well. Any time-resolved spectroscopic technique can, in principle, be combined with MES.[3;4] When choosing a specific technique, there are certain limitations, in terms of time-resolution of the spectrometer and kinetics of the studied systems that must be considered. To be able to capture dynamic processes, the sampling rate of time-resolved spectra must be about one order of magnitude greater than the modulation frequency, which itself should be chosen in a similar range to the relaxation times of the studied system. For instance, FT-IR spectrometers can easily acquire several spectra per second, thanks to the use of the rapid scan mode, which means that the monitored transient processes in the studied system should not be complete within less than 10 seconds. For even faster kinetics, the step scan mode can be used in which time resolutions in the range of a few nanoseconds can be achieved.[5;6] Thus, a suitable spectroscopic technique must be chosen, depending on the studied materials and the kinetics of the studied catalytic processes.

In this article, we review the origin and the theory behind MES, we give an overview on different applications focusing on heterogeneous catalysis and, finally, we give an outlook on possible future directions.

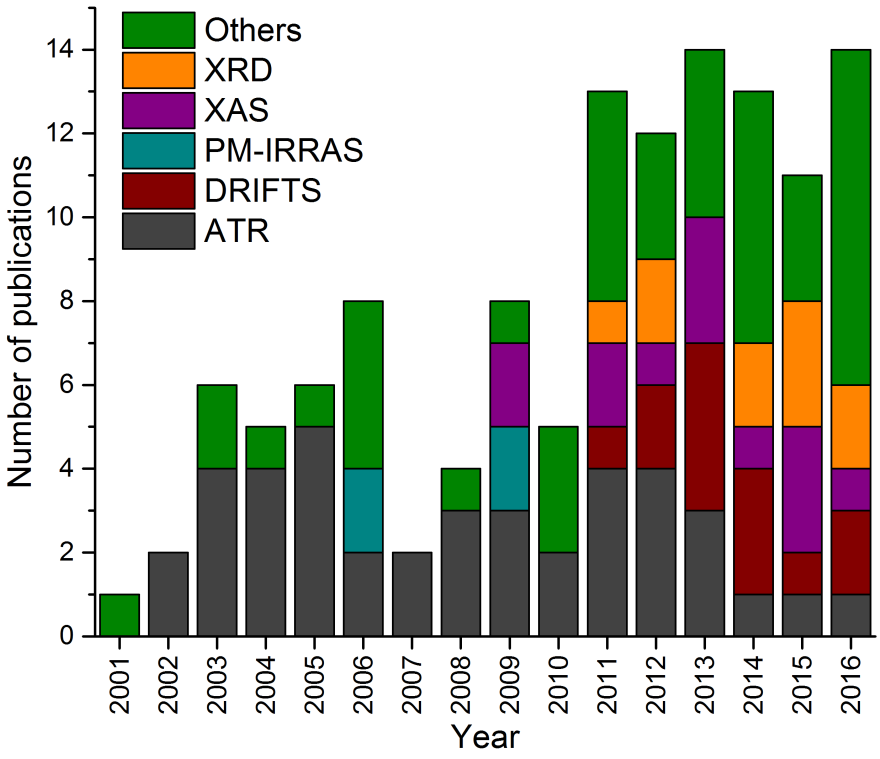

Figure 1.1: Development of the number of modulation excitation spectroscopy articles published in the last 15 years (list might be incomplete). Others include, imaging, combinations of techniques, accessories for MES, theoretical development, and reviews.

1.2 Origin of MES & Theory

While it is true that the contribution by Baurecht and Fringeli in 2001[2] was the one that sparked the use of MES for applications in heterogeneous catalysis, it was much earlier that scientists developed similar ideas for other applications. For instance, Hexter[7] suggested a procedure for MES as a technique to obtain vibrational spectra of excited electronic states by modulating UV-vis light and recording the transient behavior of IR vibrations. Others took up the idea, further developed the technique, designed new spectrometer arrangements and applied it to various systems.[8–15] In the late 1990s, first works on heterogeneously catalyzed reactions, where concentration modulation was applied to get insights into the reaction mechanisms, were published.[16–19]

However, in these early works the demodulation or phase-sensitive detection (PSD) that transforms spectra from the time- to the phase-domain and leads to some advantageous properties that will be discussed in detail below, was performed during data collection. This lead to significant challenges associated with the general applicability of the technique. For instance, step-scan spectrometers were required, phase-corrections for the fast Fourier transformation were more complicated, and additional lock-in amplifiers, data acquisition channels, electronics and special software were needed. Vector-based PSD as described by Baurecht and Fringeli[2] eliminated most of these challenges and allowed for a convenient offline demodulation after the acquisition of time-resolved spectra.

The working principle of MES is similar to a digital lock-in amplifier, where a weak signal has to be filtered out of a noisy background, as represented in Figure 1.2. The chosen type and frequency of stimulation A(t) are crucial to obtain high quality spectra. In most of the applications that are discussed in the next sections, concentration modulation, *i.e.* the periodic change of the concentration of a certain species, was used. Other possibilities are a modulation of the sample temperature, pressure, pH, light flux, electric potential, isotopic labels amongst others. A prerequisite of MES is that the studied process is reversible or quasi-reversible within the time frame of one modulation period and that the system does

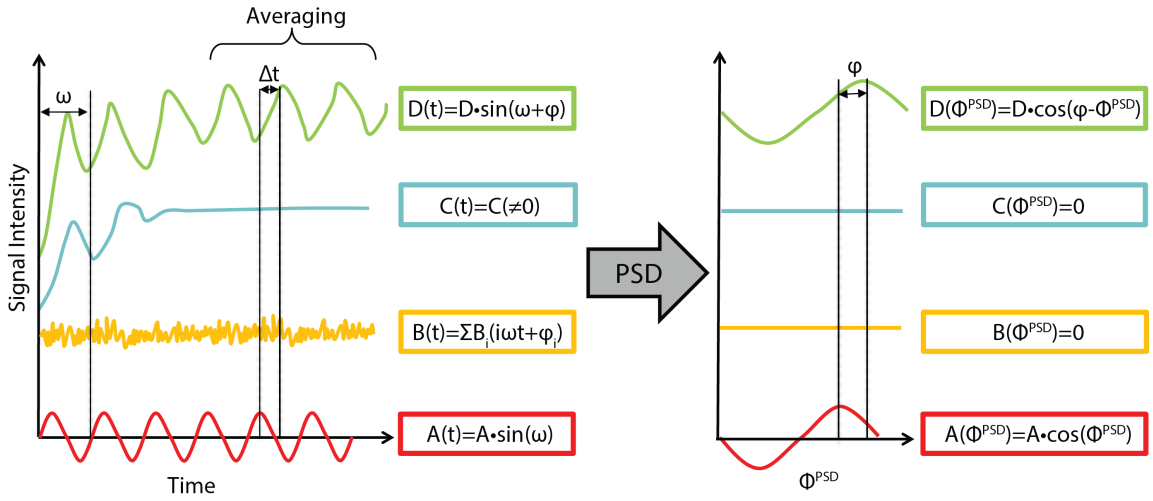

Figure 1.2: Schematic illustration of the working principle of PSD. A(t) is the stimulation function, B(t) is noise, C(t) is a response of a spectator species, and D(t) is the response of an active species. The stimulation function is, in this case, a sine wave with frequency ω. Demodulation using PSD transforms time-domain spectra to the phase-domain. Instead of being time-dependent, the spectra are now a function of the phase angle Φ_{PSD}. Instead of appearing at a certain time delay Δt, in the phase-domain, the absolute phase delay φ contains information about the dynamics and kinetics of the studied system.

not significantly deactivate throughout the experiment. During this modulation, the spectrometer is continuously acquiring spectra and hence records the response of the studied system to the chosen stimulation. Different species will respond differently to the stimulation.[20] As shown in Figure 1.2, noise B(t) is not affected by the stimulation and occurs randomly while spectator species C(t), *i.e.* species that are not directly involved in the mechanism *e.g.* from the catalyst support or species that adsorb to the surface and do not react further, might follow the stimulation initially and then reach a steady signal. Finally, the species that we are most interested in, *i.e.* active species D(t) that are perturbed by the stimulation, follow the stimulation with the same frequency but with a certain time delay Δt. Note that the time-resolved spectra that are actually measured at each spectral position i, $E_i(t)$, are a linear combination of contributions from B(t), C(t) and D(t):

$E_i(t) = b_i \cdot B_i(t) + c_i \cdot C_i(t) + d_i \cdot D_i(t)$. Once the system reaches a quasi-steady state (usually after few modulation periods), several modulation periods are averaged to further enhance the signal-to-noise ratio. The subtraction of the background spectrum, *i.e.* the first spectrum of the averaged period, further filters out unwanted signals which is especially important for solid-liquid reactions, where the solvent and liquid-phase components absorb a lot of infrared radiation and might mask active species signals. Then, the mathematical treatment (PSD) is applied on the averaged spectra to transform them from the time- to the phase-domain according to the following equation:

$$E_{i,k}(\phi_k^{PSD}) = \frac{2}{T}\int_0^T E_i(t) sin(k\omega t + \phi_k^{PSD}) dt \tag{1.1}$$

where T is the length of one period, ω is the modulation frequency, k is the demodulation index, ϕ_k^{PSD} is the phase angle for demodulation k, and $E_i(t)$ and $E_{i,k}(\phi_k^{PSD})$ are the response at spectral position i in the time- and phase-domain. Only the signals that follow the fundamental frequency ω or a multiple of it (harmonics) will show up significantly in the phase-domain, allowing for discrimination between active and spectator species. However, there are also exceptions to this general rule, if, for instance, spectator species follow similar or faster kinetics than active species, this discrimination is not possible. As an example in heterogeneous hydrogenations over supported noble metals the reactants might adsorb to the support and show similar kinetics than active species but are catalytically inactive.[21] The signal-to-noise ratio gets further enhanced, as any noise that is not affected by the stimulation gets eliminated. Another advantage of the PSD analysis is that the absolute phase delay φ *i.e.* the difference in phase between the modulation function $A(\phi_k^{PSD})$ and one specific spectral position $E_{i,k}(\phi_k^{PSD})$ is well defined, which is not always the case in transient time-resolved experiments. Furthermore, φ can be used for the microkinetic analysis of the studied processes. In the case of a two-step reaction A$\rightarrow$ B $\rightarrow$ C, for instance, the characteristic signals of the different species will have maximum amplitudes according to $\phi_A^{PSD} < \phi_B^{PSD} < \phi_C^{PSD}$. Hence, a thorough analysis allows for kinetic differentiation of pathways and lifetimes of

active species during the modulation period. This kinetic differentiation also allows for distinguishing between heavily overlapping peaks, as long as they exhibit different kinetics during the modulation. Ultimately, the phase-domain analysis could be used to yield quantitative kinetic information such as rate constants from the amplitudes and phase delays after back-transformation to the time-domain. However, so far mostly qualitative or semi-quantitative analyses have been performed. Even though the mathematical framework of MES and PSD is based on sine-wave stimulation, in practice, especially for concentration modulations, square-wave modulations are more commonly used. The reason for this is the much simpler setup, where basically only two valves need to be switched on and off repeatedly and no steady concentration change is required.[22] As a square-wave can be mathematically written as a sum of sine-waves with odd frequencies, the response to a square-wave stimulation is hence the sum of the responses to the stimulation of each of the (2n-1)ω frequency components.[23] By setting k=2n-1 it would be possible to separately extract the different (2n-1)ω frequency components with just one experiment, whereas 2n-1 sine-wave stimulation experiments would be needed to obtain the same information. A nonlinear response to the perturbation leads to significant contributions of higher order harmonics (k>1). An example in chemical kinetics would be a reaction step that does not follow first order kinetics. Most often, however, only the fundamental frequency (k=1) is analyzed.

1.3 MES Applications

Attenuated Total Reflection Infrared Spectroscopy

As mentioned above, the first applications of MES to study solid-liquid interfaces were predominantly conducted using ATR-IR spectroscopy. The main advantages of using ATR-IR compared to other infrared techniques are the close contact of the catalyst with the internal reflection element (IRE) and the several reflections along the catalyst bed that significantly increase the sensitivity.[24–28] As shown in Figure 1.3, the evanescent wave emerging at the boundary between the sample (low refractive

index) and the IRE (high refractive index) penetrates ca. 1-2 μm into the sample and hence probes the solid-liquid interface with high sensitivity. The penetration depth is wavelength-dependent and is determined by the ratio of refractive indices of the sample and the IRE. Commonly used IRE crystals are made of ZnSe, Ge, Si or diamond and they are chosen based on their optical properties as well as the chemical compatibility. Typically, the catalyst is deposited onto the IRE by letting the solvent of a slurry evaporate, leaving a thin catalyst layer on the IRE. To get a mechanically stable layer, it is important to use small catalyst particles, to sonicate the slurry before applying it and to choose an appropriate evaporation temperature. However, depending on the type of catalyst, the polarity of the solvent, and the chosen flow rate, the catalyst layer might still be washed off over time, limiting the possible operational conditions of such ATR experiments. Figure 1.3 also shows a common setup for concentration-modulation for studying solid-liquid interfaces with ATR-IR. Two tanks, one filled with a low concentration (C_{low}) and one filled with a high concentration (C_{high}), are connected *via* two electronically activated valves to the ATR cell in the IR spectrometer. An accurate synchronization between spectra acquisition and switching of the valves is ensured through a trigger box that sends an electronic signal to the valves once the measurement starts. In order to get a fast exchange of the liquids, the dead volume between the valves and within the cell must be kept as small as possible. A volume of less than 100 μL is typically required to get fast exchange and diffusion at typically used MES frequencies (1-100 mHz for ATR).[22] In addition, it is advisable to use small diameter tubing to further reduce the dead volume as well as being aware of the operational limits with regard to heat and mass transport of the used ATR accessories.[29;30] In terms of liquid pumps, two different options have been applied. Either the liquids are pushed through the ATR accessory, for instance with an HPLC or syringe pump, or, more commonly, the liquids are pulled through with a peristaltic pump. The latter has the advantages that it is relatively inexpensive and easy to implement with the electronically controlled valves shown in Figure 1.3. Most accessories can also be heated to reaction temperatures and some can be operated at elevated pressures.

In their publication from 2001[2], Baurecht and Fringeli used an example of pH-

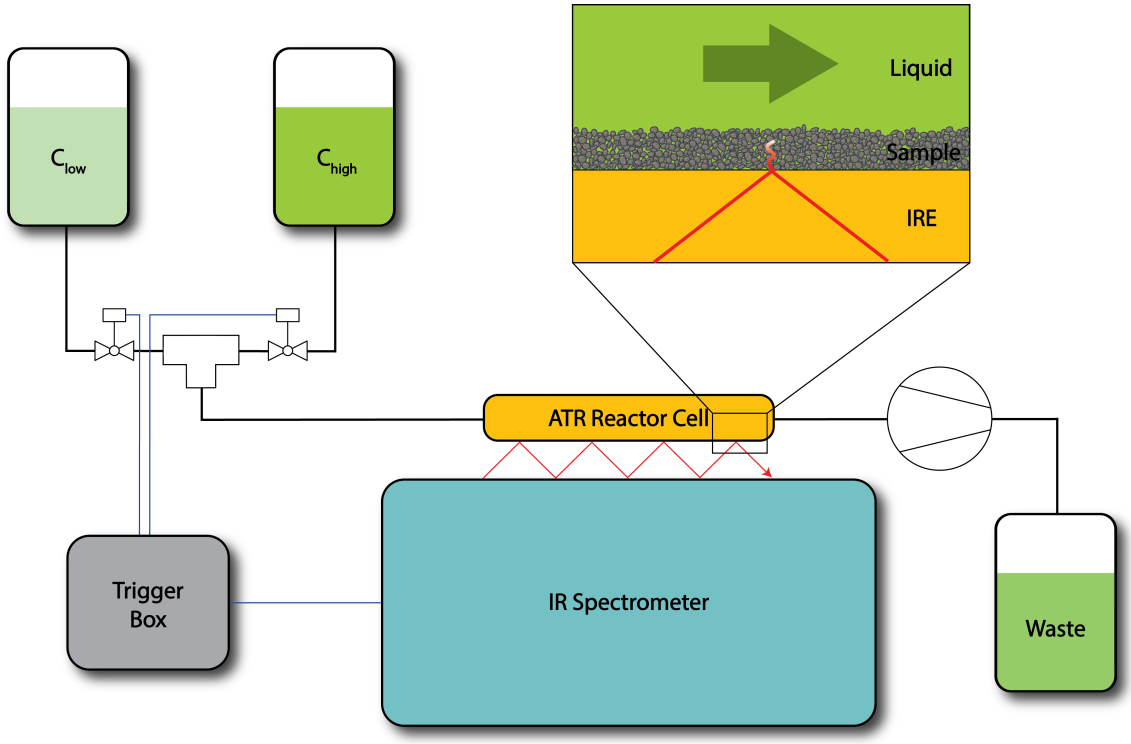

Figure 1.3: Schematic illustration of a concentration-modulation ATR-IR setup. Two tanks are connected to the ATR cell through electronically actuated valves that are triggered by the spectrometer. At the outlet, a peristaltic pump pulls the liquids over a thin catalyst layer (µm range) that is deposited on the ATR crystal.

modulation with an arachidic acid bilayer to show the benefits of MES. In a follow up study, they investigated folding and unfolding dynamics of RNase A using temperature-modulation with ATR.[31] This type of stimulation has not been applied very often since then, probably due to technical difficulties associated with fast heat exchange and temperature control in ATR accessories. The temperature amplitude was around 10 °C with a mean temperature of 63 °C which is roughly the melting point of RNase A. Although the aim of that work was to show the applicability of PSD and to obtain high quality phase-resolved spectra, details about the conformation of different functional groups and amino acids were also obtained. In the following years, additional reports studying biochemical applications were

published[32–38], but the focus of MES-ATR shifted more toward applications in heterogeneous catalysis where concentration-modulation was often applied. In particular, adsorptions, oxidations, and (asymmetric) hydrogenations have been studied. Baiker *et al.* used ATR-MES to probe chiral recognition in liquid chromatography.[39;40] To do so, they immobilized chiral selector units on porous silica particles that were deposited onto the IRE. It was shown that a specific hydrogen-bonding interaction between the immobilized selector and only one of the two enantiomers forms which ultimately leads to the desired separation. A later study used a commercially available chiral stationary phase deposited on the IRE and came to similar conclusions.[41] Bürgi and co-workers used ATR-MES to study self-assembled monolayers (SAM) of chiral amino acids and short-chain peptides on gold surfaces.[42–49] Such SAMs have the potential for sensing and specific recognition of certain organic molecules. Since the formation of an SAM can take up to two hours, this process is usually monitored using standard time-resolved techniques without MES. However, to get a fundamental understanding, for instance, of the interaction with other molecules or the influence of the pH on the SAMs, MES can be efficiently used. To perform these experiments, an IRE was coated with a thin film of gold onto which the SAM was formed. MES proved to be a valuable tool in such applications, revealing details about different adsorption modes, enantiodiscrimination, and differences between chemisorbed and physisorbed layers. Other examples of adsorption studies include the adsorption of BINAP (2,2′-bis(diphenylphosphino)-1,1′-binaphthyl) to Pd[50] or the interaction of cholate with immobilized human serum albumin.[51]

In the field of oxidations, early work was done on epoxidations over titania-silica catalysts.[52;53] The example in Figure 1.4, where the cyclohexene concentration was modulated at constant *tert*-butyl hydroperoxide concentration, demonstrates how the application of PSD increases the signal-to-noise-ratio and makes it easier to identify spectral features. In a standard transient experiment with background subtraction (b), most of the features are not discernible. Other studies looked at aerobic oxidations of cyclic alcohols, where the tanks in Figure 1.3 are saturated with the desired gases, *i.e.*, bubbling an inert gas through C_{low} and air through

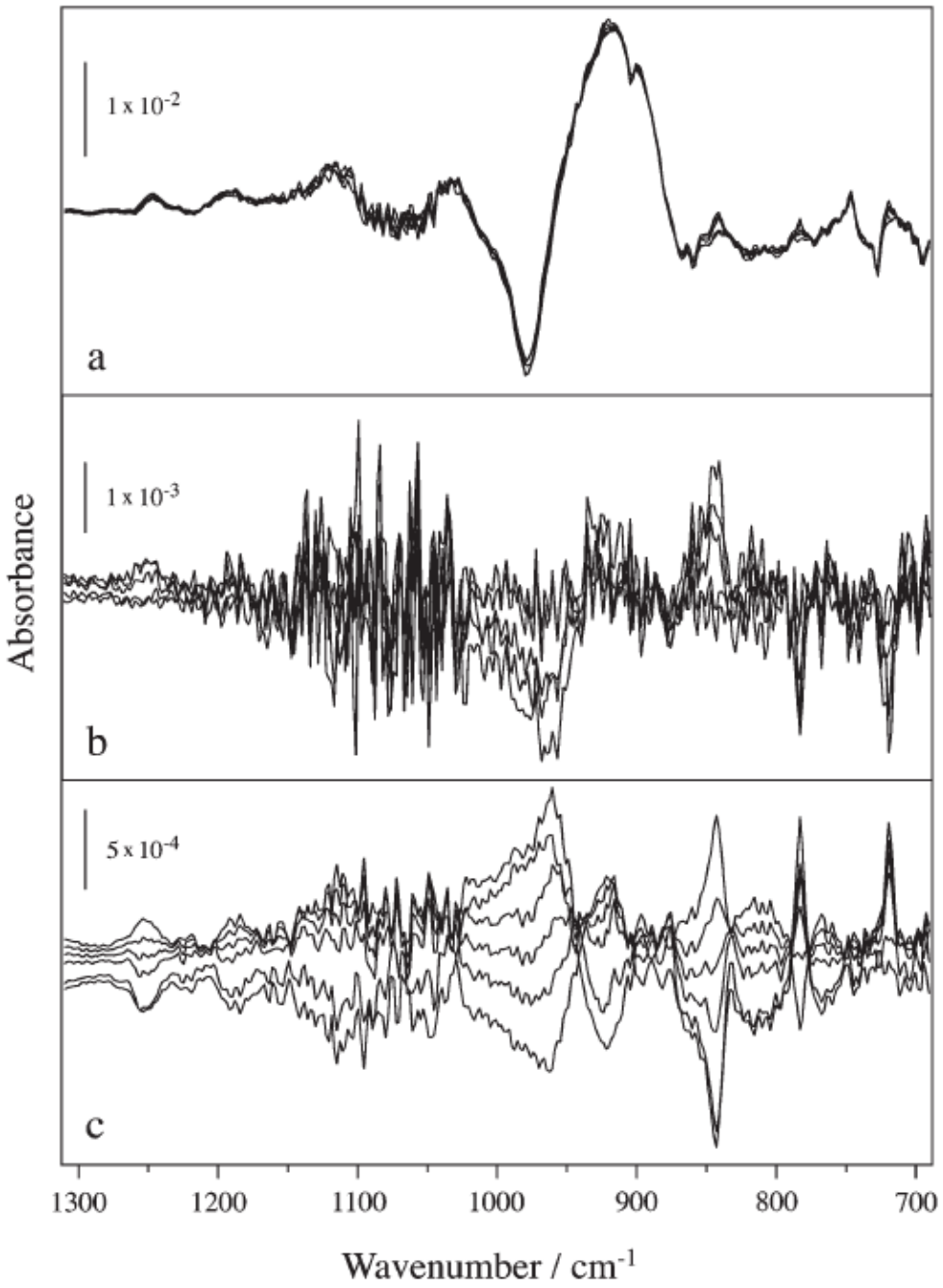

Figure 1.4: ATR spectra for epoxidation experiment recorded under forced modulation of the cyclohexene concentration. (a)time-resolved absorbance spectra, (b) difference spectra (obtained by just subtracting one arbitrary spectrum), (c) phase-domain spectra after PSD of the spectra in (a) Reproduced with permission from reference[52] Copyright 2003 Royal Society of Chemistry, London.

C_{high}.[54–56] A highly cited publication used modulation experiments with CO_2-saturated toluene to probe the basic properties of the supported gold catalyst.[57] Using MES, distinct differences compared to transient adsorption experiments were found, and it was concluded that some of the signals that were visible in the transient experiments were actually originating from spectator species. In another example, the oxidation of 2-propanol over Pd/Al_2O_3 was studied.[58] In addition to the ATR cell, a UV-vis spectrometer was added to the outlet of the cell to measure the liquid-phase online. This approach is well suited for monitoring fast changes that occur at the solid-liquid interface. In that work, the authors found evidence for a 2-propoxide intermediate and proposed an oxidative dehydrogenation mechanism.

In asymmetric hydrogenations, weak hydrogen-bonding interactions between a chiral modifier and the prochiral substrate lead to enantioselective catalysis, similar to the discussed chiral separations.[59;60] Hence, such reactions have been studied with ATR-MES as well. The example of cinchonidine (CD)-modified noble-metal surfaces is probably the system that has been studied most with MES. In the enantioselective hydrogenation of a pyrone catalyzed by CD-modified Pd/TiO_2, MES was used to disentangle crowded spectra in the phase-domain.[61] Carboxylate species were identified and appear to have a negative effect on enantioselection. In 2003, the first indications for weak N-H-O interactions between ketopantolactone and cinchonidine adsorbed on a Pt/Al_2O_3 catalyst were found using ATR-MES.[62] More recently, the proposed interactions were refined, as an additional O-H-O interaction between CD and the substrate was found.[63;64] Interactions with other substrates and additives were studied as well.[21;65–71]

ATR-MES has also been applied to study photocatalytic systems[72;73], where a UV-light source was used for stimulation. Other monitored reaction systems include amine-functionalized silicas that catalyze Knoevenagel condensations[74] and heteropoly acids that catalyze decomposition reactions[75].

Recently, we have extended the use of MES-ATR to microporous and mesoporous materials, namely porous stannosilicates.[76] The different pore structures of these materials lead to different spectroscopic features that allowed us to explain macroscopic observations and computational predictions on a molecular level. MES

also helped in analyzing diffusion within these materials. It was found, for instance, that for the microporous catalyst the reaction product did not easily diffuse out of the catalyst pore and once it had left the pore, it did not re-enter, preventing further reactions and hence leading to higher selectivities.

Polarization-Modulation Infrared Spectroscopy

In another interesting application, an attempt was made to couple MES with polarization-modulation infrared reflection absorption spectroscopy (PM-IRRAS).[77;78] PM-IRRAS is a reflection infrared technique that is highly surface sensitive and is often applied for thin films. In standard PM-IRRAS measurements, the gas-phase contribution to the acquired spectrum is filtered out by taking the difference between the p- and s-polarized reflections over metallic surfaces. For heterogeneous catalysis under relevant pressure regimes, however, the gas-phase contribution can be used to simultaneously monitor reactions.

To study dynamic processes, PM-IRRAS was used together with MES to get insights into CO oxidation over Pt. Also in this application, the signal-to-noise ratio was significantly increased and some new spectroscopic features could be observed besides the adsorbed CO.[77] The PM-IRRAS accessory that was used was especially designed for application with MES to have a small cell volume, excellent mixing properties and fast exchange of the gas-phase. PM-IRRAS can also be applied for studying solid-liquid interfaces.[79] To do so, a CaF_2 prism was used atop the reflection element to achieve a liquid film thickness of about 10μm.[80] For instance, the adsorption behavior of different acids on alumina was studied using this technique, together with MES.[81] It was found that dimer-like salicylic acid species formed through hydrogen-bonding close to the alumina surface when increasing the concentration. Even though PM-IRRAS allows forthe simultaneous monitoring of surface and bulk species for both gas- and liquid-phase reactions, there are only few examples of its use in conjunction with MES, likely due to the relatively high cost of a PM-IRRAS setup.

Diffuse Reflectance Infrared Spectroscopy

Besides PM-IRRAS, diffuse reflectance infrared spectroscopy is another technique that is well-suited for monitoring heterogeneously catalyzed gas-phase reactions. In DRIFTS, a powdered sample is placed in a sample cup where its rough surface creates diffuse reflections when infrared radiation is directed onto the sample. The main advantage of this technique is that no sample preparation is needed prior to the measurement, which, for instance, enables studying support effects of supported metals much more easily than with PM-IRRAS. Furthermore, the samples can be heated to high temperatures and subjected to elevated pressures to simulate reaction conditions for gas-phase reactions. On the other hand, the gas flow patterns and temperature distributions in DRIFTS accessories are not always optimal and the particle size/packing of the bed might influence the outcome of a measurement.[82–84] Nevertheless, DRIFTS has been increasingly used together with MES to obtain insights into gas-solid interfaces under reaction conditions. Figure 1.5 shows an example of a DRIFTS setup equipped for MES.[85] The chosen modulation in that specific example was a concentration modulation between H_2O and D_2O and was achieved by simply switching a four-way-valve (feature 3 in Figure 1.5). The DRIFTS cell itself should have a low dead volume to ensure fast exchange of the gas phase upon switching the valve.

The first MES study using DRIFTS was published in 2011.[86] A commercially available DRIFTS accessory was customized, replacing the conventional dome with a flat CaF_2 window to reduce some dead volume. In addition, a mass spectrometer was connected to the outlet to simultaneously monitor the gas-phase composition. The preferential oxidation of CO over Cu-CeO_2 catalysts was investigated using that setup. MES was very useful in this example as a strong carbonyl signal that was detected under steady-state reaction conditions was found not to participate in the oxidation reaction under transient oxygen conditions, suggesting it to be a signal from a spectator species. Additionally, weak variations in intensity of vibrations associated with carbonate and formate species below 2000 cm^{-1} could be distinguished, because of the increased signal-to-noise ratio in the phase-domain

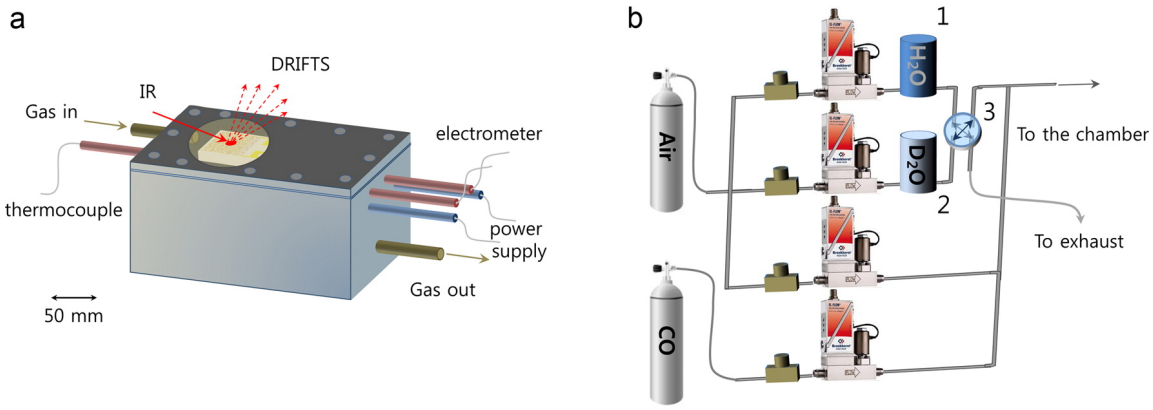

Figure 1.5: (a) Environmental chamber for operando DRIFTS and resistance measurements, and (b) gas-mixing system to perform H_2O/ D_2O exchange in the presence of CO. Reproduced with permission from reference[85] Copyright 2014, American Chemical Society, Washington DC.

as shown in Figure 1.6. By running the same experiment at 80 and 140 °C, it was found that two carbonyl vibrations responded differently to the temperature change, which helped them assign one of them (CO bound to slightly oxidized Cu) to be more readily oxidized than others.

In another study on CO hydrogenation over Pd using a similar setup, it was found that only a fraction of about 4 % of the adsorbed CO molecules were reacting with hydrogen.[87] Also in this case, under steady-state conditions, mainly the unreactive species were probed while the more important reacting species were overshadowed due to their low abundance. CO oxidation and related reactions have specifically benefitted from applying MES and PSD because of the existence of such spectator species.[88–92] In a further example, isotope-modulation was applied on the preferential oxidation of CO.[93] By switching between a flow of H_2 and D_2, as well as between ^{12}CO and ^{13}CO, further insights into the reaction mechanism were obtained. For instance, water was found to be involved in the reaction pathway but not consumed. Also, the surface CO species were found to exchange much faster than formate or bicarbonate species, indicating a rather slow reaction of adsorbed CO and OH^- species. The most interesting aspect about isotope-modulation is that

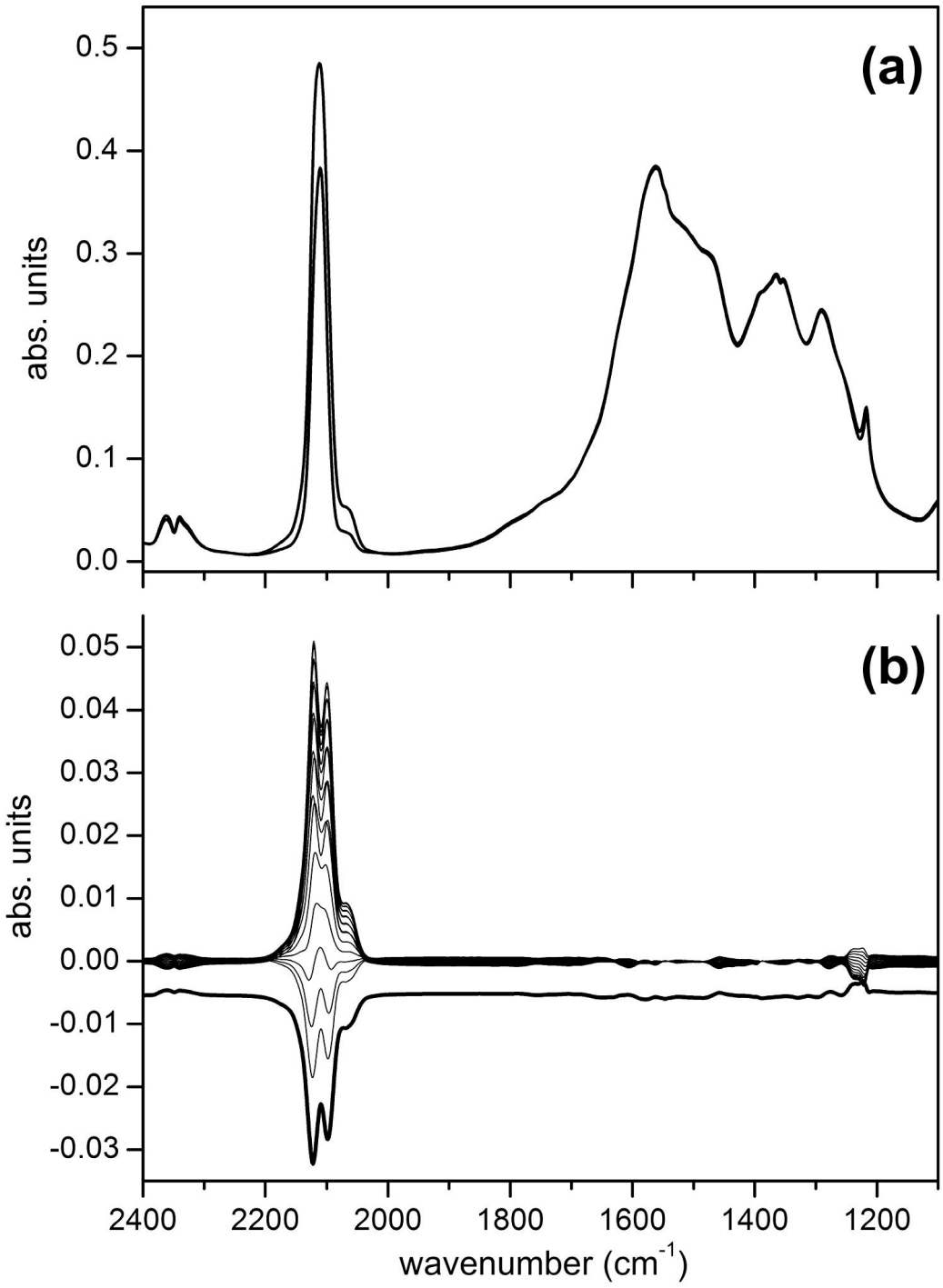

Figure 1.6: (a) Time- and (b) phase-resolved spectra during oxygen concentration modulation $CO/H_2/O_2$ vs. CO/H_2 on Cu-CeO_2. A phase-resolved spectrum is offset to show the anticorrelation of gas-phase CO_2 and carbonyl species. Reproduced with permission from reference[86] Copyright 2011, Elsevier, Amsterdam.

the reaction is chemically under steady-state, which is not the case for standard concentration-modulation where the reaction is studied under quasi-steady state.

Collins and co-workers studied the adsorption of H_2 and CO_2 on a Pd/Ga_2O_3 catalyst using DRIFTS-MES.[94] Their study nicely demonstrates the kinetic differentiation of various carbonate species after applying PSD. Figure 1.7 shows the time-domain (a) and phase-domain (b) spectra, as well as a phase delay φ analysis. For instance, the band at 1660 cm^{-1} attributed to monodentate-HCOO species shows a higher phase delay than the band at 1600/1580 cm^{-1} attributed to bidentate-/bridged-HCOO and hence is more rapidly formed and decomposed to CO than the latter. The same research group also studied the role of oxygen vacancies in the water gas shift reaction on ceria-supported platinum catalysts.[95] It was found that monodentate-HCOO species and carboxylate species located at the metal support interface could be reaction intermediates, something that likely would have been overlooked with standard steady-state investigations.

In a similar approach, the H_2O/D_2O exchange was studied over SnO_2 materials in the presence of CO.[86] It was found that only traces of Cl in the material induce dramatic changes in water adsorption kinetics and the CO sensing mechanism. Also zeolites were studied using isotope MES in the catalytic methanol amination over sodium-exchanged mordenite.[96] In that study, methanol and deuterated methanol were modulated in the presence and absence of ammonia. It was found that, besides the well-known shape-selectivity, other factors such as a hydrogen-bond network of methanol agglomerates also play an important role in this reaction.

Finally, we recently published a study using both concentration and isotope modulation in the production of 1,3-butadiene over Ta-BEA zeolites.[97] We built a new setup that consists of two independent syringe pumps that deliver liquids into a heated spiral, where evaporation takes place. By adjusting the inert gas flow and the liquid flow rates, the gas phase concentration can be conveniently controlled. In this particular example, the reaction pathway involves many reaction steps and intermediates, which makes a steady-state spectroscopic analysis challenging. Hence, switching between different combinations of reactants and intermediates in a modulated fashion can help disentangle the spectra. The gas-phase composition

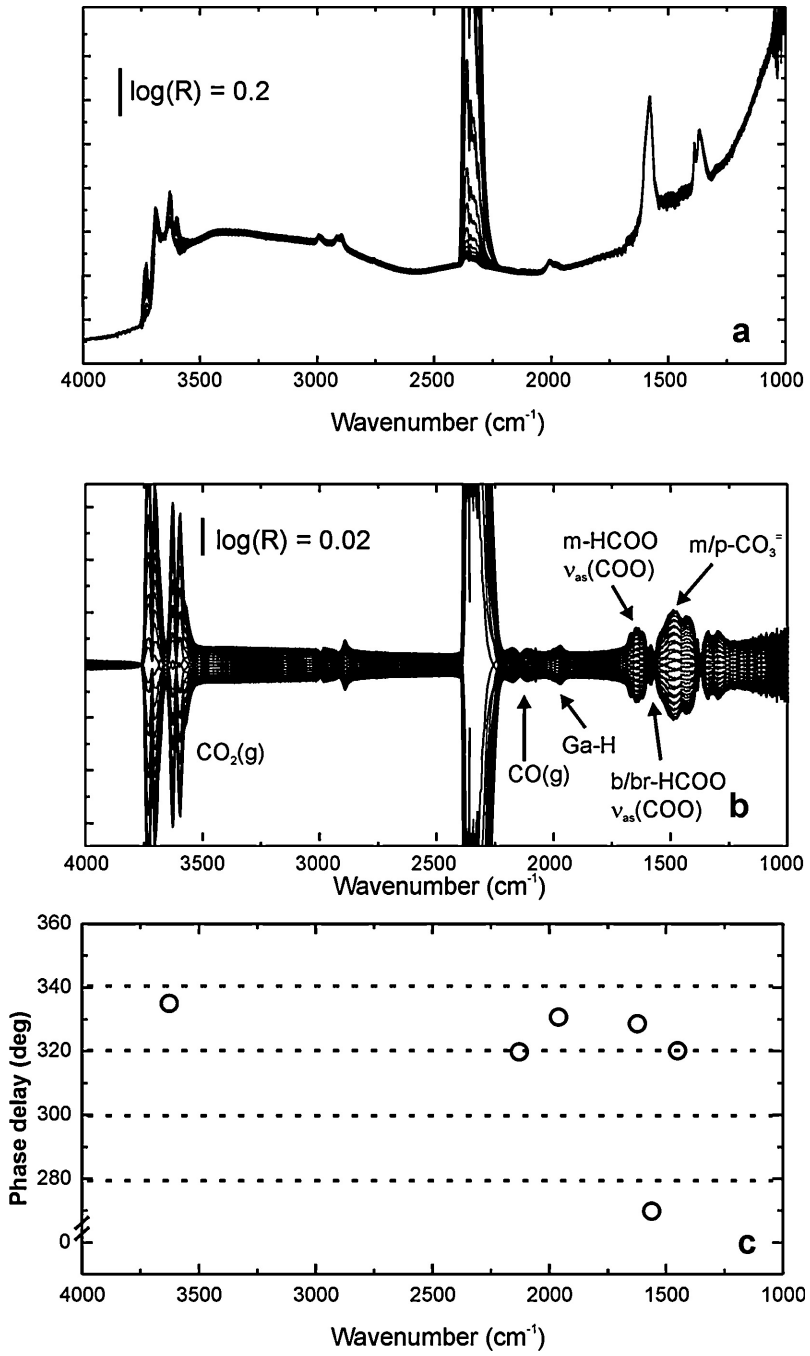

Figure 1.7: (a) Time-domain DRIFT spectra during concentration modulation with CO_2/H_2-Ar over Ga_2O_3 (b) phase-domain spectra after PSD (c) phase delays (φ)for selected bands. Abbreviations: m-HCOO monodentate; b-HCOO bidentate; p-HCOO polydentate; br-HCOO bridged carbonate. Reproduced with permission from reference[94] Copyright 2013, Elsevier, Amsterdam.

was simultaneously monitored with a mass spectrometer at the outlet of the DRIFTS cell. The information from the gas-solid interface and the gas-phase was then analyzed together to obtain a reaction mechanism of 1,3-butadiene production over Lewis acidic Ta-BEA.

X-ray Absorption Spectroscopy

X-ray absorption spectroscopy is another technique that has been frequently coupled with MES to obtain increased sensitivity. Because of the large penetration depth of X-rays, the obtained spectra are an average over many atomic structures within a specific sample. Most often, however, only a few atoms at the surface, *e.g.*, of a metal nanoparticle, are actually of interest and may only be observed with highly sensitive techniques. Hence, the first *in situ* studies were performed during periodic operation, where some of them increased the sensitivity of the spectra by simply averaging over several modulation periods.[98–100] The first step towards an analysis with PSD was reported in 2009, where the ignition behavior of noble-metal-catalyzed partial oxidation of methane was studied using quick-scanning extended X-ray absorption spectroscopy (QEXAFS).[101] QEXAFS allows for a fast data acquisition in the subsecond range under realistic *in situ* conditions. The application of MES on QEXAFS improves the signal-to-noise ratios without losing time- or energy-resolution, which makes this approach attractive for relatively fast reactions.[102–104] In that example, a principal component analysis (PCA) revealed two distinct regimes (heating up and ignition) within the full modulation period.[101] Later, Ferri and co-workers published phase-resolved spectra of noble-metal catalysts during the catalytic oxidation of CO and the reduction of NO by CO.[105–107] These studies showed the potential of MES for XAS as it drastically increased surface sensitivity and ultimately formed the basis to study working catalysts, even at low metal loading that have been previously intractable for dynamic *in situ* studies. However, the usefulness of PSD for X-ray absorption spectra has also been questioned.[108] It was found that applying a low-pass filter yields spectra with similar signal-to-noise ratios, while no artifacts are introduced, which was not always the

case with PSD. Indeed, the interpretation of EXAFS spectra in the phase-domain is much more complex than in the case of vibrational spectroscopy.[109] As the EXAFS spectrum is essentially a combination of scattering properties that are not affected by the modulation experiment and structural properties that are affected by the modulation experiment, a systematic evaluation of the effect on the structural parameters needs to be done. Chiarello and Ferri resolved most of these issues in a combined simulation and experimental work with Pd/Al_2O_3 which provides some tools and guidelines to qualitatively and quantitatively understand phase-resolved EXAFS spectra.[110] For instance, the FT-phase-resolved spectrum can only be directly fitted if a shell completely appears and disappears during one modulation period. Besides these initial works and case studies, some additional applications of XAS with MES and PSD have been reported. For Pd incorporated in a perovskite structure, it was found that applying a periodic change in the feed composition for methane oxidation actually enhances the activity, compared to steady-state.[111] PSD analysis indicates that Pd reversibly leaves the perovskite framework, which influences catalytic activity. This highly active transient species most likely would not have been detected with conventional methods, again highlighting the usefulness of MES. An increased activity or selectivity in periodic operation is an effect that has been observed for other catalytic processes as well.[112–115] For such systems, XAS with MES and PSD is an outstanding too,l because, in that case, the information is obtained truly under reaction conditions. In an interesting application of MES, Nachtegaal *et al.* used a modulation that consisted of more than two discrete states, *i.e.*, supported Ru particles were exposed to three different atmospheres: reducing (H_2 and CO), reducing and sulfiding (H_2, CO and H_2S) and oxidizing (O_2).[116] The demodulated spectra of the entire modulation experiment is, in that case, simply the sum of the individual demodulated spectra of each square-wave function. At certain phase angles, some contributions will be zero, while others will not, which was used to conveniently analyze the data. Using this approach, they found that the formation of a Ru-sulfide phase was deactivating the catalyst.

Also methane oxidation has been studied over supported Pd nanoparticles.[117] Differences in the conversion between supports was most pronounced at the

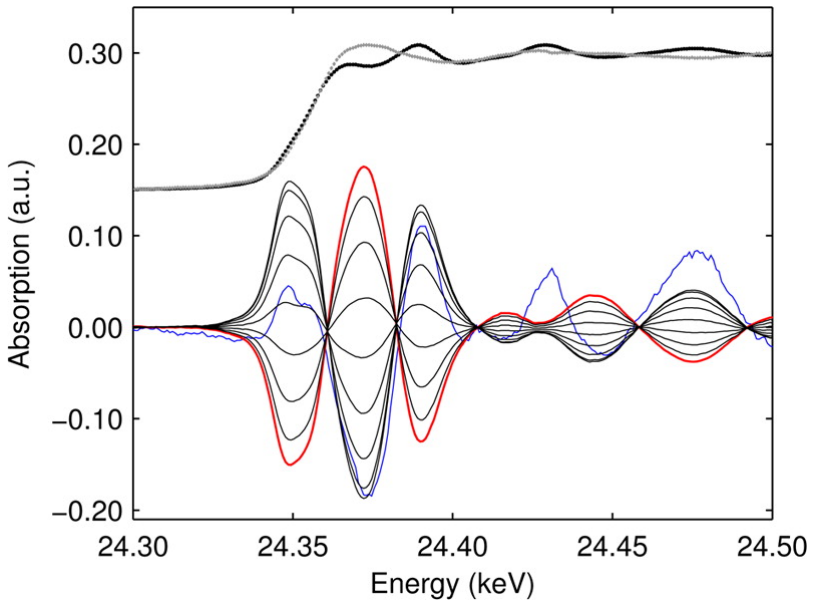

Figure 1.8: Demodulated spectra obtained from Pd/Al_2O_3 at 400 °C (ϕ_k^{PSD}=0-160°) together with scaled spectra of Pd foil (black) and PdO powder (gray). The red spectrum corresponds to ϕ_k^{PSD}=0°, and the blue spectrum is the scaled difference spectrum Pd_{foil} - PdO. Reproduced with permission from reference[117] Copyright 2015, American Chemical Society, Washington DC.

switches between oxidizing and reducing conditions. Those differences were attributed to different oxygen-storage capacities of the supports. Figure 1.8 shows the demodulated spectra of such an experiment over Pd/Al_2O_3. It is evident that the phase-domain spectra are significantly better resolved than the scaled difference spectrum (blue).

More recently, X-ray emission spectroscopy has been used with MES and PSD.[118] For instance, the redox behavior of Pt/Al_2O_3 and CO oxidation over Pt/CeO_2 were studied.[119;120] In the latter case, a short-lived active Ce^{3+} species was found. In this material, the initial rate of ceria oxidation is at least ten times higher than the rate of reduction, which is why these species cannot be observed under steady-state conditions. Interestingly, even under oxygen-rich conditions, the Ce^{3+} signal from the spectator species does not completely disappear, indicating that they are not involved in the catalytic cycle.

X-Ray Diffraction, Combinations & Others

Another evolving technique in conjunction with MES is X-ray diffraction (ME-XRD or MED).[121–123] The idea here is to periodically stimulate a crystal structure, where only a subset of atoms will change its properties.[124] The fundamental limitation of XRD is that it is based on an interference phenomenon and, therefore, the contribution of different subsets of atoms cannot be separated. This fact also does not allow for measuring the phase of the diffracted waves (the so-called phase problem of crystallography). MED can, in some cases, solve or at least greatly reduce these issues. Generally, there are two different problems that can be studied with MED. In the direct problem, structural information is recovered from MED intensities. In this case, it is assumed that a subset of atoms responds to the stimulation in a linear fashion in terms of structure amplitudes. This approach allows the separation of interferences from both silent and active atoms from the diffraction contribution of the active subset, something that is not possible with standard diffraction experiments. In the inverse problem, information about kinetics induced by the stimulation are studied. Here, it is assumed that the structural changes are known. This approach is suited for obtaining kinetic information on non-equilibrium systems *in situ*. Several examples will be discussed in this section, however, a more detailed theoretical background of MED can be found in literature.[124–127]

As a first proof of principle, ZrO_2 powder has been studied using MED and different approaches to extract interferences have been tested.[128] Also Pd supported on ceria-zirconia (Pd/CZ) has been characterized using MED and showed the detailed redox dynamics when exposed to a concentration modulation with CO and O_2.[129] Figure 1.9 shows time-resolved spectra as well as phase-resolved spectra of such an experiment. The change in oxidation state from metallic Pd(0) to Pd(II) oxide can be observed by the appearance and disappearance of the specific diffraction patterns.

This catalyst is particularly difficult to characterize with EXAFS because of the small amount and size of Pd nanoparticles and the highly absorbing and scattering ceria in the sample. Some subtle changes induced by the modulation between

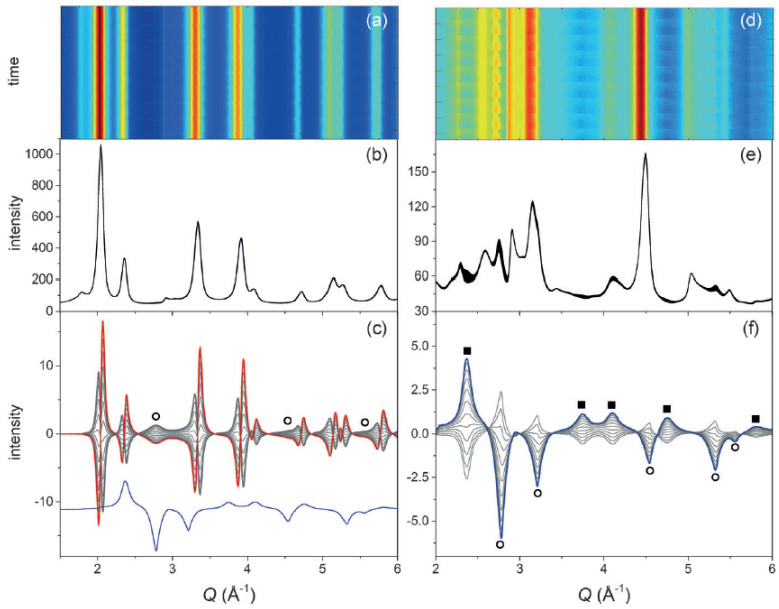

Figure 1.9: (a) Color map representation and (b) time-resolved hard XRD patterns for 2 wt% Pd/CZ during a full CO/O_2 modulation experiment at 573 K (t=50 s). (c) Corresponding set of phase-resolved data (ϕ^{PSD}=10-150°); the red profile is the in-phase pattern. The blue profile is the in-phase pattern obtained for 2 wt% Pd/Al_2O_3. (d)-(f) High-energy XRD data for an experiment with identical parameters with 2 wt% Pd/Al_2O_3 (ϕ^{PSD}=70-180°). circles : Pd; black squares : PdO. Reproduced with permission from reference[129] Copyright 2014, John Wiley and Sons, New York.

CO and O_2 were greatly enhanced when applying PSD. Thus, MED provides an additional tool to characterize changes in the oxidation state of Pd.

In a promising application, Palin *et al.* studied the thermal behavior of xenon in a MFI zeolite.[130] By periodically exciting xenon inside the zeolite pores with a laser and subsequent mathematical treatment with PSD as well as principal component analysis (PCA), they managed to selectively probe the Xe atoms and filter out the contribution from the nonresponding zeolite. This method is particularly promising, because it could also be applied to light elements and molecules provided that the electron density of the light element can be modulated by an external stimulation.

Also Raman spectroscopy can be used together with MES. In a combined MED and modulated Raman spectroscopic study, the structure of a spin crossover ma-

terial was investigated using temperature modulation.[131;132] It is technically challenging to perform temperature modulation as heating and cooling rates have to be equal in order to obtain a symmetric stimulation. Hence, the applied modulation frequencies are usually lower than, *e.g.*, in concentration modulations. However, this also enables the use of spectroscopic techniques that do not have a particularly high temporal resolution, such as Raman spectroscopy. In the aforementioned example, the used modulation frequency was 0.5 mHz, which is an order of magnitude lower than in a typical MES-ATR experiment. Nevertheless, the authors found interesting details about their system such as a hysteresis loop that was much more pronounced in the XRD patterns than in the Raman spectra. This was attributed to the different sensitivities toward short- and long-range ordering of the two techniques. Finally, they attributed the crystallographic phase change triggered by the spin inversion to have a marked one-dimensional character since it occurs through the elongation in one direction within the material. In another example, time-dependent surface-enhanced Raman spectra (SERS) of the surface plasmon resonance mediated oxidation of p-aminothiphenol on Au/TiO_2 catalysts has been studied in a manner similar to MES.[133] Only when the UV light was turned on, signals originating from the oxidation product started to appear due to charge transfer from UV-excited TiO_2 to Au. Because of the relatively low spectra acquisition time (ca. 5 seconds), this would be an example where Raman-MES could have been applied and further kinetic information and increased signal-to-noise ratio could be obtained.

Other examples of combinations of techniques are XRD-DRIFTS[134;135], XAS-DRIFTS[105;136;137] and DRIFTS-UV-vis[138].

MES can also be applied to other chemical systems. In an example by Jullien *et al.*, the response of the pH to a periodic UV illumination of 2-hydroxyazobenzenes with a relatively high frequency (210 mHz) was studied.[139] By extracting the phase-delay of the pH response, the authors were able to calculate rate constants for the *trans*-to-*cis* and the *cis*-to-*trans* isomerization. The same research group also built and refined the theoretical framework to apply MES on imaging techniques, which is especially promising for selective detection in mixtures of probes as well

as heterogeneous systems.[140–146] For instance, the brightness and the thermokinetic features of a probe are often strongly dependent on its environment. Hence, in a multiphasic medium, *e.g.*, a living cell, it is difficult to quantitatively analyze concentrations of probes of interest without prior knowledge of the probe location. Here, the out-of-phase first-order response in a modulation-excitation experiment can be used to get quantitative information on probes in a specific phase.

All of these examples show that the principle of modulation excitation can be applied to various (chemical) systems using different analysis techniques. The choice of an appropriate technique for a given chemical system in combination with the proper conditions such as modulation frequencies, time resolutions, and concentrations is crucial to obtain high-quality results. In this work, we focus on the use of infrared spectroscopy and apply it on heterogeneouos Lewis acids.

1.4 Lewis Acid Catalysis

Acid catalysis plays a pivotal role in the production of many chemicals across all sectors of chemical manufacturing.[147–149] In numerous (industrial) liquid-phase reactions inorganic (or mineral acids) such as H_2SO_4, HF, $AlCl_3$, or BF_3 are used. Often, these processes are truly catalytic, while in some cases, for instance, in acylations stoichiometric amounts of anhydrous $AlCl_3$ are required. Generally, the role of the acid is to activate an organic reactant, making it susceptible for the reaction with a nucleophilic reagent.[150] Common acid-catalyzed liquid-phase reactions are Friedel-Crafts alkylations, acylations, aromatic halogenations, nitrations, sulfonations, isomerisations and oligomerisations. The aforementioned acids are usually very active and selective toward the desired products. However, in terms of process safety and environmental impact, these acids bring along some disadvantages.[151–153] Mineral acids are highly corrosive and toxic, which makes handling and storage demanding for material and personnel and consequently more expensive. In particular for Lewis acids, quenching and separation of the catalyst from the products is required after reaction, leading to large volumes of toxic and corrosive wastes. The neutralization of these wastes consumes additional

(alkaline) resources, which finally leads to waste disposal costs exceeding the costs of the raw materials. Considering all these points, the potential of making chemical production safer, more sustainable and hence greener by developing and applying alternative (Lewis) acid catalysts is enormous.

In industrial gas-phase chemistry, the use of solid acids has quite a long tradition. Synthetic zeolites, crystalline and microporous aluminosilicates, for instance, have been used for decades in fluid catalytic cracking and hydrocracking applications, drastically improving yields.[154] Also in the liquid phase, for instance in alkylation reactions, *e.g.* forming ethylbenzene from benzene and ethene, or in the oligomerization of 1,3-butadiene, solid acid catalysts have been applied. These solid acids can be repeatedly used and the separation from liquid products is convenient, making them environmentally benign by avoiding the creation of large amounts of waste. Furthermore, solid catalysts can be used in continuous fixed bed reactors which reduces reactor sizes, process costs and hazards.

Purely Lewis acidic solid acids, on the other hand, have been developed much later. In 1983, researchers from Eni S.p.A. discovered titanium silicalite-1 (TS-1), a zeolite where tetrahedral framework positions are occupied by titanium atoms.[155;156] This catalyst showed unique characteristics especially useful for the activation of peroxides. Since then, other transition metals such as Sn, Zr, Ta, Hf, and Nb have been successfully incorporated, also into other zeolite topologies.[155;157;158] Pioneered by Avelino Corma and his research group, such zeolites were synthesized in a fluoride medium at neutral pH, leading to highly crystalline, hydrophobic and hydrothermally stable catalysts that found many applications mostly in the upgrading of biomass to value-added chemicals.[155;159]

However, the syntheses of these catalysts take from several days up to weeks and in most cases require relatively large amounts of hazardous hydrofluoric acid just shifting the problems associated with safety and waste creation from the reaction to the catalyst synthesis. Hence, alternative synthesis methods that also allow for easy scale-up are highly desirable. In 2012, such a post-synthetic method was developed for the synthesis of Sn-BEA in our research group.[160] As shown in Figure 1.10, the synthesis is a two-step process, where first a commercially available zeolite

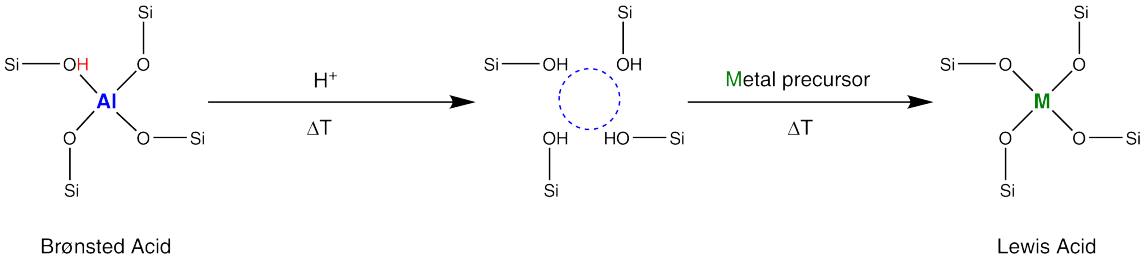

Figure 1.10: Postsynthetic procedure for the incorporation of Lewis acidic heteroatoms into a zeolite framework. In an acid treatment, the zeolite gets dealuminated. Then, a metal precursor is brought into contact with the dealuminated zeolite. A heat treatment finally incorporates the metal into the zeoilte framework. Adapted from reference[161].

is dealuminated using an acid treatment at elevated temperatures, followed by the incorporation of a metal. For the second step, different methods have been used, such as solid-state ion exchange by simply grinding the precursor and the dealuminated zeolite together, or chemical grafting by exposing the dealuminated zeolite to a solution containing the metal precursor, usually in absence of water.

Not only Sn, but also other heteroatoms, such as Ti, Zr, Hf, Ta, Nb, V and Mo have been incorporated into zeolite structures by this method.[161–166] After incorporation, these isolated metal centers possess an open coordination site that is available for reactants, giving them their Lewis acid character. Upon coordination, the reactant gets activated by donating electron density into the LUMO of the metal, forming a Lewis acid-base adduct. Initially, it was believed, that the metal incorporation leads to well-defined and dispersed single active sites. More recently, however, it was found both computationally and experimentally that these metals can not only occupy different T-sites within the framework, but also within the same positions a variety of sites are possible.[167–169] For Sn-BEA, for instance, the presence of a "closed" site, where Sn is fully incorporated and four-fold bound to the framework, and of an "open" site, where one of the bonds is hydrolyzed and forms a hydroxyl group, were proposed.[170] NMR studies further revealed that depending on the pretreatment conditions, various degrees of hydration can be found and that different synthesis protocols lead to different NMR signatures.[168;171–174]

Since only recently the use of solid Lewis acids has become more common, these materials are still relatively unexplored, which makes them interesting but also challenging materials to study. Furthermore, they have the potential to be industrially applied and hence to have an impact on making chemical manufacturing more sustainable. Obtaining a fundamental understanding of these materials, might uncover the catalyst properties needed to achieve better catalyst performance. Coupling back to catalyst synthesis, might eventually lead to more efficient catalysts and catalytic processes. Finally, Lewis acids activate organic reactants often at C-O/C=O bonds changing the dipole moment of this vibration, a process that one should be able to conveniently monitor using infrared spectroscopy due to the resulting changes in vibrational frequencies. These are some of the reasons, why we chose to study solid Lewis acid catalysts using Infrared Modulation Excitation Spectroscopy throughout this dissertation.

1.5 Scope of the thesis

This thesis is based on several publications that have been published in (or submitted to) peer-reviewed journals. Hence, most of the chapters can be read independently. Accordingly, some overlap in the chapter introductions and experimental parts occurs. In the introduction (Chapter 1), the concept of modulation excitation spectroscopy is explained and many literature examples using different spectroscopic techniques are presented. Chapter 2 uses these concepts and applies them on the isomerization of citronellal over different stannosilicates. In Chapter 3 the results from Chapter 2 are further refined by studying the effect of the solvent on this reaction and determining diffusion coefficients of citronellal through layers of the different stannosilicates. In Chapter 4 we move from liquid-phase reactions to gas-phase reactions and study the coupling of ethanol to butadiene over a Ta-BEA catalyst. A new *operando* DRIFTS-MS setup has been specifically developed to study this catalytic system. Then, this study is taken a step further by investigating a Ag-Zr-BEA catalyst that allows for the one-step reaction of ethanol to butadiene in chapter 5. Finally, an outlook over future directions of MES for heterogeneous

Lewis acids and other catalysts is given.

2 INSIGHTS INTO THE COMPLEXITY OF HETEROGENEOUS LIQUID-PHASE CATALYSIS: CASE STUDY ON THE CYCLIZATION OF CITRONELLAL

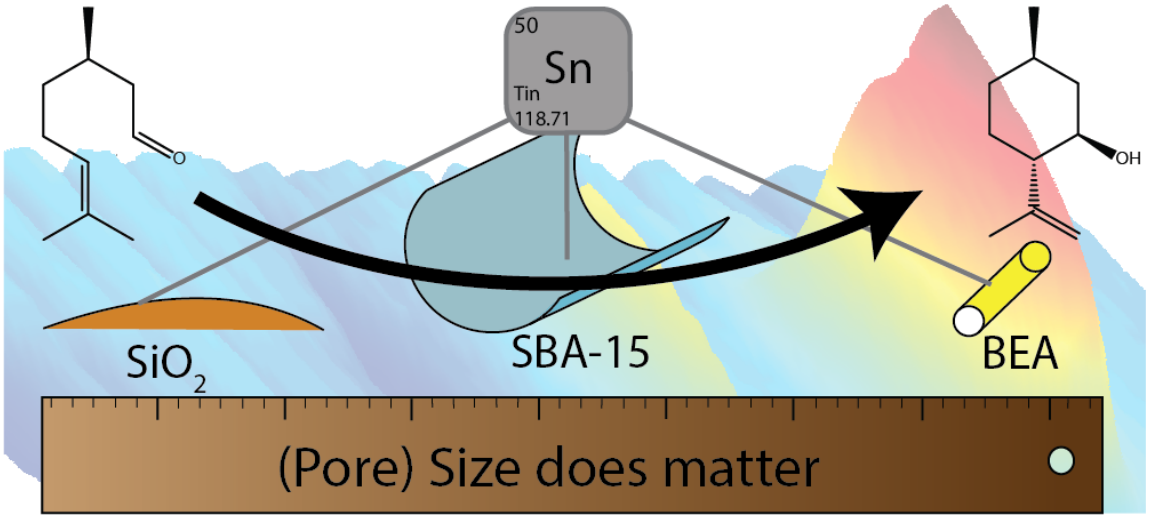

This chapter gives a first example of the application of Modulation Excitation Spectroscopy on a heterogeneously catalyzed liquid-phase reaction. We use the cyclization of citronellal over porous stannosilicates as a case study to investigate different effects influencing heterogeneous liquid-phase catalysis. This chapter was published in ACS Catalysis.[76]

2.1 Introduction

In heterogeneous catalysis it is widely accepted that the catalytic performance does not only depend on the precise atomistic coordination of the active sites, but also on the embedment of these sites in the support material. For instance, catalysts with narrow pores of molecular dimension can trigger size-exclusion reactions,[175] or induce confinement effects that influence both the activity and selectivity.[176;177] Specifically for liquid-phase reactions, also the solvent (composition) can affect

the overall performance of the catalytic system (vide infra). All these effects are often encountered in Lewis acid-catalyzed liquid-phase catalysis. Indeed, solid Lewis acids are widely used catalysts for various reactions, e.g. in biomass upgrading,[178] selective oxidations/hydrogenations[179;180] and the production of fine chemicals.[150] In particular, site-isolated Lewis acids incorporated in siliceous frameworks such as zeolites or (mesoporous) silicas have shown great potential, yet they are also notoriously complex.[158;168;181–183] Especially, Sn(IV) incorporated in the BEA framework (Sn-Beta) obtained significant attention due to its exceptional activity and stability.[157] Two different types of active sites have been proposed, a four-fold framework-incorporated Sn(IV) species (so-called closed site) and a partially hydrolyzed (so-called open) site, with tin three-fold bound to the zeolite framework.[170;184] Not only does the nature of the active site play a role, but also its local molecular environment seems to influence the reactivity of Sn(IV)-containing materials.[185] Testing Sn(IV)-incorporated in microporous (*viz.*, Sn-Beta and Sn-MFI) and mesoporous catalysts (*viz.*, Sn-MCM-41 and Sn-SBA-15), Osmundsen *et al.* observed a distinct dependency of the activity for the conversion of biomass-derived substrates on the framework structure.[186] As briefly mentioned above, a solvent can also affect the performance of a catalyst, e.g. by disturbing the substrate adsorption,[187] preferentially solubilizing certain molecules,[188] or altering the active site.[189] For instance, Boronat *et al.* studied solvent effects in the cyclization of citronellal to (-)-isopulegol, an important step in the artificial production of the flavoring agent (-)-menthol (see Figure 2.1) over Sn-Beta.[190;191]

Adding the Lewis base acetonitrile to citronellal improves both activity and selectivity towards (-)-isopulegol. The authors hypothesize that both acetonitrile and citronellal adsorb to the Sn(IV)-site, which results in enhanced stereoselectivity, due to a confined space around the catalytic center. Moreover, product desorption from the active site and diffusion inside the pores would be further facilitated by the presence of acetonitrile. Other solvents, such as longer chain nitriles and alcohols also affect the reaction. However, a general understanding of these effects is lacking, as a correlation between the catalytic performance and a single solvent characteristic, such as the dielectric constant or the molecular diameter,

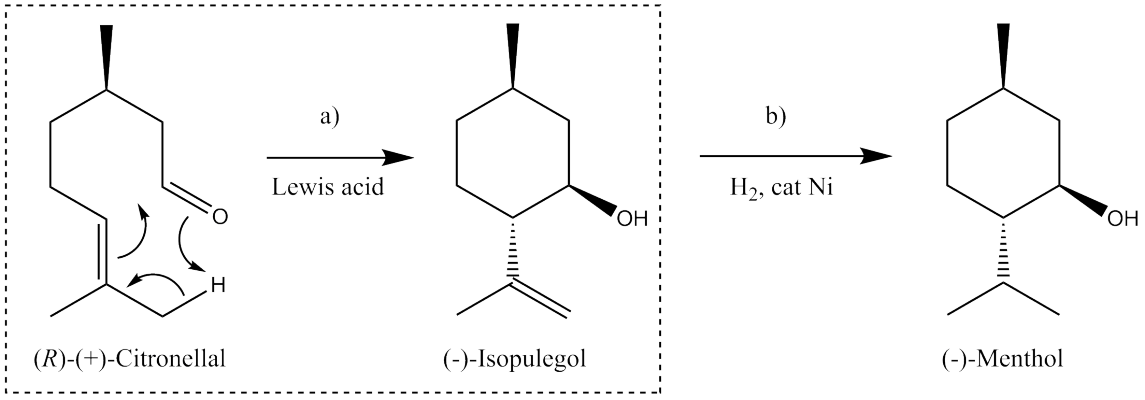

Figure 2.1: Cyclization of (*R*)-(+)-citronellal to (-)-isopulegol, followed by the hydrogenation to (-)-menthol.

is not sufficient to capture the complexity of such catalytic systems. A sensitive approach towards the understanding of heterogeneous liquid phase reactions, in particular on a molecular level, is vibrational spectroscopy.[192,28] For the cyclization of citronellal, an experimental FT-IR study has been performed, monitoring the disappearance of the characteristic vibrations of pre-adsorbed citronellal on Sn-Beta.[184] Two bands at 1729 cm^{-1} and 1715 cm^{-1} were observed and assigned to weakly and strongly adsorbed carbonyl groups, respectively. The presence of a C=C stretch vibration at 1645 cm^{-1} indicated the simultaneous formation of the isopulegol product. While valuable information can be provided by such an approach, many of the described effects are neglected, for instance due to the absence of solvent. Conclusive experimental studies under relevant conditions that address the mechanism on a molecular level are still missing. *in situ* spectroscopic studies would in principle be able to provide this information. However, a poor signal-to-noise ratio as a consequence of low concentrations of active species is a frequently encountered problem that limits the applicability and interpretation of *in situ* spectroscopic studies. One highly sensitive and selective method to study reaction mechanisms at the solid-liquid interface is the application of a modulation excitation spectroscopy (MES) approach in combination with *in situ* attenuated total reflection infrared (MES-ATR-IR) and phase sensitive detection (PSD).[26] While

the use of conditions that are close to actual reaction conditions are desirable for a spectroscopic study, they also impose significant complications. Indeed, in a solid-liquid reaction, multiple phenomena such as adsorption, (by-)product formation and desorption of various species occur simultaneously. It is hence difficult to distinguish between species that are actually involved in the surface reaction, *i.e.* active species, and those that just adsorb to the solid-liquid interface and do not react further, *i.e.* spectator species. PSD makes use of a mathematical treatment that is explained below, and transforms time-dependent spectra into phase-resolved spectra.[20] This transformation increases the signal-to-noise ratio, allows for differentiation between active and spectator species and simplifies the micro-kinetic analysis. This technique is hence ideal to shed light on the mechanisms involved in complex multi-phase reactions.[64;69] In the present work, we demonstrate the use of MES-ATR-IR in the case of the cyclization of citronellal, a model reaction of contemporary interest. Correlating macroscopic differences in the reactivity with a molecular understanding based on the information obtained from the solid-liquid interface allows us to draw conclusions on pore-size and solvent effects.

2.2 Results

Materials & Batch Reactivity

Three different Sn(IV)-containing catalysts were synthesized following known procedures: an amorphous Sn-SiO_2,[193] a mesoporous Sn-SBA-15,[194;195] and a microporous Sn-Beta.[160;161;196] In addition, the siliceous analogues Si-Beta[197] and SBA-15[198] were prepared. Characterization of all synthesized materials is provided in the appendix (Figures A.1, A.2 and Table A.1). The catalytic performance of these materials in the cyclization of citronellal was determined under batch reaction conditions with toluene and acetonitrile as solvent. Both solvents are widely used for carbonyl-ene reactions and strongly differ in polarity and size.[199] The diastereoselectivity was constant for all materials and solvents throughout the course of the reaction (see Figures A.3 and A.4). Overall higher activity was observed in

Table 2.1: Batch reactivity data for the cyclization of citronellal over different catalysts.

Catalyst [i]	Solvent	Conv. [%] [ii]	TOF [h^{-1}] [iii]	Sel. [%] [iv]	$Sel._{dia}$ [%][v]
-	Toluene	4	-	50	67
SBA-15	Toluene	27	-	67	66
Sn-SBA-15	Toluene	89	115	92	64
Sn-SiO_2	Toluene	60	42	90	65
Si-Beta	Toluene	9	-	40	70
Sn-Beta	Toluene	66	185	89	70
-	Acetonitrile	-	-	-	-
SBA-15	Acetonitrile	-	-	-	-
Sn-SBA-15	Acetonitrile	15	12	50	65
Sn-SiO_2	Acetonitrile	7	6	0	0
Si-Beta	Acetonitrile	-	-	-	-
Sn-Beta	Acetonitrile	63	127	88	77

toluene, where small amounts of products are already formed without a catalyst. In the presence of weakly Brønsted acidic SBA-15, both activity and selectivity increased. Significantly better catalytic performance was observed with the Lewis acidic stannosilicates, of which Sn-Beta yielded highest activity and diastereoselectivity, followed by Sn-SBA-15 and Sn-SiO_2. The achieved diastereoselectivity for Sn-Beta is slightly lower than reported values,[200] which could be explained by the post-synthetic preparation of the material. This leads to minor amounts of remaining silanol groups, possessing Brønsted acidity and slightly different active sites than in hydrothermal Sn-Beta.[201] An analysis of the Arrhenius plots (see Figures A.6 and A.7) indicates mass transfer to be influencing the reaction.

With acetonitrile as the solvent, the blank reaction and the reaction with the pure

[i]Reaction conditions: 50 mg of catalyst, 5 mL of 0.5 M citronellal solution in solvent at 333 K, reaction time 4 hr.

[ii]Conversion = (moles of citronellal initial - moles of citronellal after 4 hr)/moles of citronellal initial

[iii]Turnover frequency (TOF) = moles of citronellal converted/moles of Sn after 1 hr

[iv]Selectivity is defined as the moles of all produced isomers of isopulegol divided by the moles of converted citronellal

[v]Diastereoselectivity is defined as the moles of produced (-)-isopulgeol divided by the moles of all isomers of isopulegol produced.

silica materials, SBA-15 and Si-Beta, did not show any activity. Sn-Beta performed similarly in terms of selectivity compared to the reaction in toluene but was slightly less active. Conversely, Sn-SBA-15 is one order of magnitude less active when employed in acetonitrile and only reaches a selectivity of 50%, compared to 92% in toluene. One possible explanation for this is the competitive adsorption of acetonitrile and citronellal (both Lewis bases) to the Sn(IV)-site. However, it is not readily clear why the activity only drops by 30% in the case of Sn-Beta, whereas it drops significantly more (about 90%) for Sn-SBA-15. These observations prompted us to perform a detailed *in situ* spectroscopic investigation. Due to the significantly lower activity of Sn-SiO_2, this material was not considered further.

Citronellal adsorption monitored with ATR-IR-MES

A suitable method to study adsorption/desorption dynamics, as well as reaction mechanisms at solid-liquid interfaces is ATR-IR spectroscopy combined with MES.[2;20;23] The latter follows an analogous principle as a lock-in amplifier by analyzing the response of a system to a periodic external stimulation, such as a change in temperature, radiation, pH, or as applied in the present work, reagent concentration. This approach is not only able to decrease the noise level to less than 10^{-5} absorbance units,[2] but also allows for the discrimination between active and spectator species. The application of PSD [eq. (1)] to the time-domain (TD) spectra trans-forms them into the phase-domain (PD), which further enhances the sensitivity and enables the extraction of (semi)-quantitative micro-kinetic data.

$$E_k(\phi_k^{PSD}) = \frac{2}{T}\int_0^T E(t)sin(k\omega t + \phi_k)dt \tag{2.1}$$

In equation (1), T is the length of one period, ω is the stimulation frequency, ϕ_k is the demodulation phase angle, ϕ_k^{delay} is the phase delay, k is the demodulation index (k=1 throughout this study), E(t) is the measured response in the TD and E_k the response in the PD. The transformation to the PD leads to a dependence of the vibrational signals on the phase angle ϕ (adsorption from 0°to 180°desorption from 180°to 360°) instead of the time (60s adsorption; 60s desorption). In the following PD

spectra, 36 phase-resolved spectra are shown with increments of 10°(corresponding to 3 seconds in the TD) which represent one whole period in the PD. In an ideal experiment, *i.e.* without diffusion limitation and immediate exchange of the cell volume (*i.e.* zero dead volume), the amplitude of the active species response, which corresponds to absorbance in the time-domain, would be 0 at 0°and 180°. A shift to larger phase angles can be attributed to hindered transport to the active site or, in the case of a reaction, to consecutive reaction steps. A detailed analysis of the spectra at various phase angles therefore provides valuable information on adsorption and reaction dynamics as will be demonstrated below. To perform an ATR-IR MES experiment, the catalyst needs to be deposited as a thin film (ca. 15 μm) onto an ATR crystal. The penetration depth of an ATR experi-ment depends on the refractive indices of the sample and the crystal and is also wavelength dependent.[26] A rough estimation with the refractive index of SiO_2 (1.45) yields a penetration depth of 1-2 μm at 1000 cm^{-1}. Hence, mainly the pores within the catalyst particles are probed. The conditions for the spectroscopic experiments were chosen so that diffusion effects within the ATR cell are minimized and differences in phase delays can be attributed to diffusion within the catalyst as well as consecutive reaction steps (see Ref.[22] and experimental section for more details). In order to investigate the catalytic cycle, the adsorption and reaction of citronellal was studied by switching between a solution of 20 mM citronellal in toluene and pure toluene. Figure 2.2a shows a projection of the TD of three averaged periods for the modulation over SBA-15 at 333 K. In the TD one major signal appears at 1727 cm^{-1}, which originates from the ν(C=O) vibration of liquid-phase citronellal (see Figure A.8 for IR spectra of pure substances in toluene). At 1605 cm^{-1} the aromatic C-C vibration of the toluene solvent appears with a small negative absorbance band, indicating the displacement of toluene from the solid-liquid interface by citronellal. The transformation to PD allows for a more detailed analysis of the micro-kinetics and a more sensitive and selective detection of signals as only active species appear in the PD spectra. Furthermore, the clear assign-ment of an absolute phase delay to the corresponding maximum absorbance of a vibration in the TD makes a comparison between different experiments easier and allows for a semi-quantitative

analysis. Figure 2.2c shows the PD spectra corresponding to the TD spectra from Figure 2.2a. The citronellal C=O peak appears with an ab-solute phase delay (*viz.* the maximum in PD) of 30°, which also corresponds to the minimum of the toluene band at the same angle. Furthermore, it is slightly skewed to lower wavenumbers, indicating only weak interactions with the solid catalyst. Complete citronellal desorption occurs at a phase angle of 220°, which can be seen by a maximum in the toluene peak and a minimum in the citronellal peak. The incorporation of Sn(IV) into the SBA-15 framework leads to different observations (Figure 2.2d). Next to the liquid-phase citronellal peak, a shoulder at 1712 cm^{-1} stemming from citronellal C=O groups interacting with the Sn(IV) site appears at 50°, *i.e.* 20°(or 6 seconds) delayed compared to the liquid-phase peak. At 70°, a peak at 1643 cm^{-1}, assigned to the ν(C=C) vibration of the primary double bond in the product isopulegol, indicates that the catalytic reaction is taking place. Simultaneously, a red-shifted shoulder next to the liquid-phase peak ap-pears, due to an interaction of isopulegol with either a Sn(IV) site and/or the silica framework.[193;202] For Si-Beta almost identical PD spectra were obtained as for SBA-15, but at larger phase angles (Figure 2.2e), indicating a longer time for citronellal to diffuse in the pores. When Sn(IV) is incorporated into the Beta framework, the peak at 1712 cm^{-1} becomes significantly more intense than the liquid-phase citronellal peak at 1727 cm^{-1}. The more intense peak at 1643 cm^{-1} indicates increased productivity, in agreement with the batch experiments (see Table 2.1). Note that the C=O vibration of citronellal coordinated to Sn(IV) appears at the exact same spectral position (1712 cm^{-1}) for both Sn(IV)-containing materials, *i.e.* both catalysts perturb the C=O stretch vibration of citronellal to the same extent under reaction conditions. Even though the metal content in Sn-Beta is ca. three times lower than in Sn-SBA-15, the absolute coverage of citronellal coordinated to Sn(IV) is clearly much higher in case of the zeolite. This observation suggests confinement effects as a likely reason for the increased productivity, rather than the stronger Lewis acidity of Sn-Beta (Ref.[185] and Figure. A.10 for liquid-phase d_3-acetonitrile adsorption). The confined space inside the zeolite pore of molecular dimension (6.7 Å[203]) leads to more negative adsorption enthalpies due to van der Waals interactions[204] which might additionally stabilize

the coordination of citronellal, resulting in increased coverage of the tin site.

Interestingly, the red-shifted product shoulder (ca. 1625 cm^{-1}), *i.e.* adsorbed isopulegol, is also more intense compared to Sn-SBA-15 and reaches a maximum at 80°, while the liquid-phase product peak reaches a maximum at 100°. This implies that the shoulder most likely originates from an isopulegol species inside the zeolite pore that might relax to a different conformation once it leaves the pore. Also the ν(OH) vibration of isopulegol appears as a broad signal centered at 3250 cm^{-1}, corroborating an interaction of isopulegol with the zeolite (Figure S25). Under vacuum conditions, isolated Si-OH and Sn-OH bands show a signal at 3740 and 3664 cm^{-1} respectively (see Figure A.9 and Ref.[177]). Surprisingly, no significant change in either of these bands could be observed for both of the Sn(IV)-containing catalysts upon the adsorp-tion of citronellal from the liquid phase (Figures A.14, A.15, A.24, A.25). However, it is likely that the presence of a solvent shifts these signals to lower wavenumbers, broad-ens them and weakens their intensity.[205] The adsorption of citronellal on Sn-Beta leads to two negative bands, one at 3600 cm^{-1} and a smaller one at 3700 cm^{-1}, both bands are present in the low-defect Si-Beta as well but with lower intensity (Figures A.17 and A.18). We therefore assign the band at 3700 cm^{-1} to isolated Si-OH groups interacting with citronellal in Beta zeolites. Dealuminated Beta shows a distinct negative band at 3600 cm^{-1} at the same phase delay as the appearance of citronellal, which we therefore assign to an interaction of citronellal with silanol groups (Figures A.19-A.22). For an interaction of citronellal with a Sn-OH group, we would expect a signal at lower wavenumbers than the Si-OH peaks. This was however not observed. Hence, the present study does not confirm the direct participation of a Sn-OH group in the reaction mechanism for both Sn-Beta and Sn-SBA-15. Nevertheless, as many different species (isopulegol, Si-OH, Sn-OH, water impurities) possi-bly show a signal in this spectral region, and the concentration of Sn-OH species is supposed to be rather small, the absence of evidence cannot be interpreted as the evidence for absence. Testing another Beta sample with a ten times higher tin loading resulted in similar spectra and also no indication of a distortion of Sn-OH vibrations when adsorbing citronellal (see Figure A.26). Yet, the above findings exemplify the consecutive steps needed for

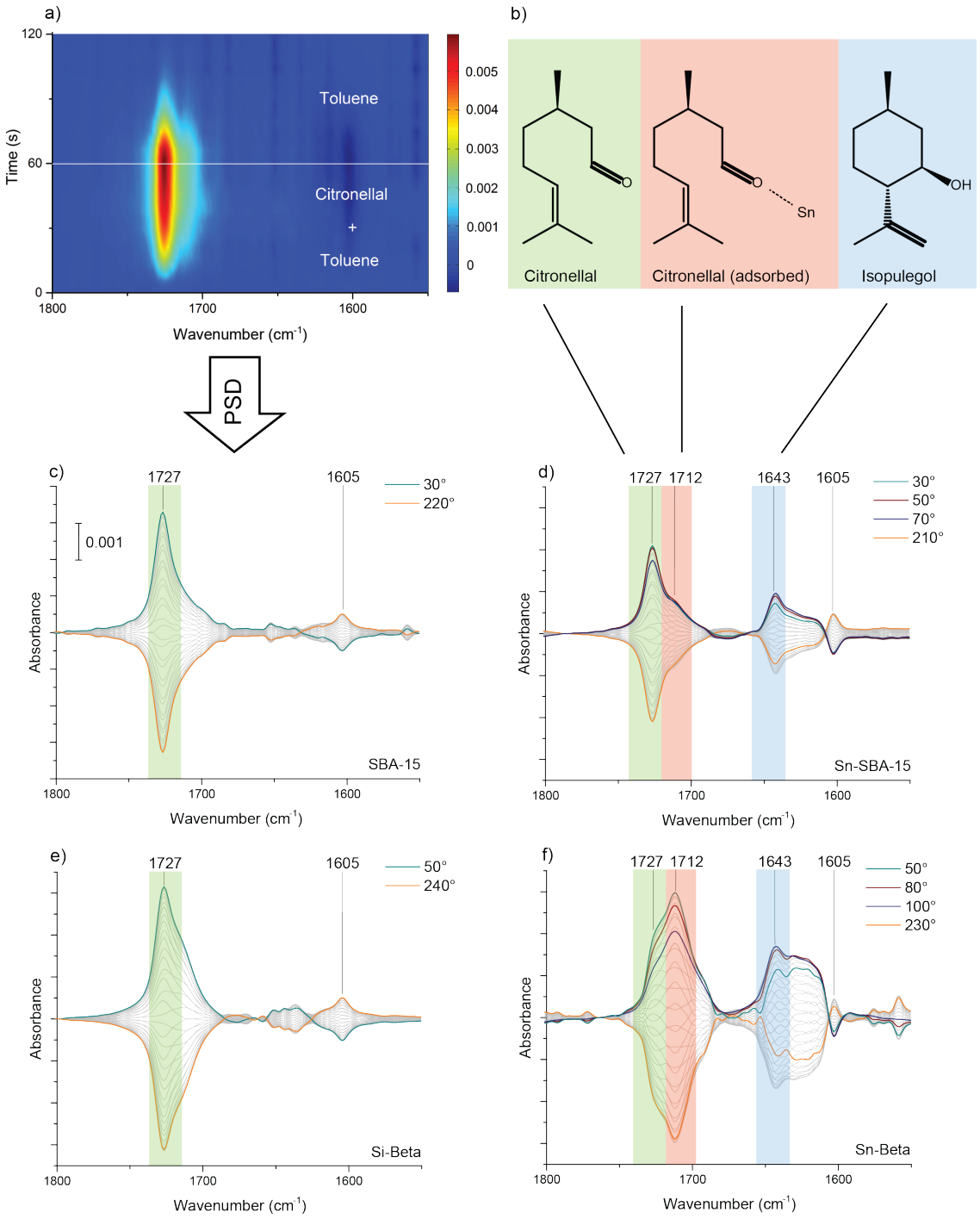

Figure 2.2: a) Time-domain spectra for the modulation of 20 mM citronellal in toluene at 333 K for SBA-15, b) Schematic representation of the most important molecular structures and their assignment, Phase-domain transformed spectra for c) SBA-15, d) Sn-SBA-15, e) Si-Beta and f) Sn-Beta.

this reaction to occur: (1) citronellal coordi-nates to the Sn(IV) site, (2) citronellal is converted to isopulegol inside the pores of Sn-Beta, (3) isopulegol interacts with either the Sn(IV) site and/or the pore walls until (4) isopulegol diffuses out of the pore (vide infra). Additionally, the overall larger phase delays found for Sn-Beta compared to Sn-SBA-15 suggest diffusion limitations caused by the smaller pores in Sn-Beta.[22] As citronellal has a small kinetic diameter and is flexible (*viz.* it can freely rotate around its C-C bonds), it can diffuse more easily inside the zeolite pore channels and find its way to a tin site. The cyclization leads to a more rigid product with a larger kinetic diameter, inducing diffusion limitations inside the micropores. However, as the Sn(IV) sites in Sn-Beta are embedded in a confined space stabilizing the coordination of citronellal, it still outperforms Sn-SBA-15.

Competitive adsorption of (-)-isopulegol and citronellal

In order to get insights into the competitive adsorption behavior of substrate and product, the concentration of (-)-isopulegol was modulated in presence of a constant citronellal concentration. In the case of SBA-15 and Si-Beta, a relatively sharp ν(C=C) vibration is visible at 1643 cm^{-1}, corresponding to liquid (-)-isopulegol (Figures A.27-A.30). For Sn-SBA-15 (Figure 2.3a), the spectra are significantly different. Other than expected, the liquid-phase citronellal peak (1727 cm^{-1}) appears. The absolute phase delay for this peak is 40°, which is 10°delayed from the C=C vibration of (-)-isopulegol, indicating a production of citronellal from (-)-isopulegol, *i.e.* the reverse reaction. However, compared to the reaction from citronellal a considerably smaller red-shifted shoulder next to the liquid-phase peak appears. In a further batch experiment (-)-isopulegol was used as substrate over Sn-SBA-15 and only little conversion was observed (see Figure A.5), suggesting that this is only a minor effect on a macroscopic scale. When (-)-isopulegol is adsorbed on Sn-Beta (Figure 2.3b), its C=C stretch vibration appears at 1643 cm^{-1} and no red-shifted shoulder can be observed. In addition, a small and broad feature at 1712 cm^{-1} is visible with an absolute phase delay of 200°. This strongly suggests the adsorption of isopulegol to the few accessible external or pore mouth Lewis acid sites which leads

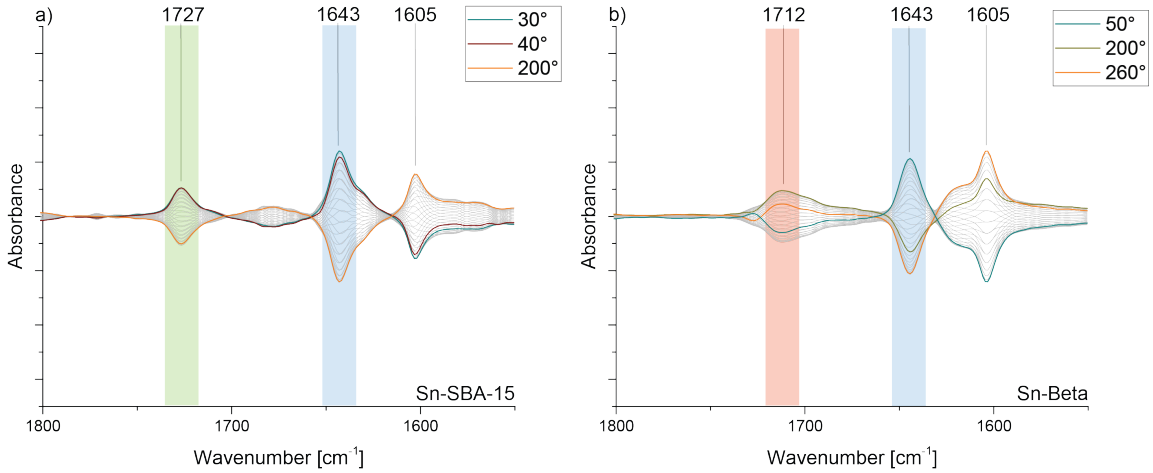

Figure 2.3: Phase-domain spectra of modulation experiments with 20 mM (-)-isopulegol in a solution of 20 mM of citronellal in toluene at 333 K for Sn-SBA-15 a) and Sn-Beta b).

to a distortion of the citronellal signal. In the TD spectra (Figure A.31), the change in intensity is hardly visible, which further confirms that this is only a minor effect and demonstrates the increased sensitivity when applying PSD. The presented data demonstrate that (-)-isopulegol does not enter the zeolite pore and thus can only compete for the active site if it is formed inside the pores. Consequently, the reverse reaction is hindered and a higher productivity is obtained. This finding is further confirmed by a batch experiment, in which 0.5 M (-)-isopulegol was added to the reaction mixture (Table S2 entries 10, 11, 22, 23), which leads to a significantly stronger decrease in activity for Sn-SBA-15 than Sn-Beta, due to this size-exclusion effect. The main by-products of the studied reaction are isopulegol ethers formed through condensation reactions.[206] As such an acid-catalyzed bimolecular reaction proceeds through a bulky transition state, it is highly unlikely to occur in the small pores of the zeolite, where most of the Lewis and Brønsted acid sites are located. Sn-SBA-15 on the other hand possesses readily accessible Sn(IV) and silanol sites and can catalyze the reverse reaction, as well as by-product formation.

Competitive adsorption of acetonitrile and citronellal

To rationalize the vast difference in catalytic performance of Sn-SBA-15 and Sn-Beta in presence of acetonitrile (Table 2.1), a competitive adsorption study was performed. As the physicochemical properties of acetonitrile (higher polarity, lower refractive index than toluene) impede sensitive ATR measurements,[26;192] we decided to assess the influence of acetonitrile by adding it to toluene in different acetonitrile/citronellal ratios. In these experiments, the concentration of citronellal was modulated in presence of a constant acetonitrile concentration. As expected from batch experiments, SBA-15 is hardly active in the presence of acetonitrile. Only a liquid-phase citronellal signal appears at 1727 cm^{-1} and a small peak around 1640 cm^{-1}, assigned to minor production of isopulegol, is visible for an acetonitrile/citronellal molar ratio of 1:1. At a ratio of 3:1, the minor isopulegol signal completely disappears (Figures A.33-A.36). No distortion of the ν(CN) region (ca. 2263 cm^{-1}) was observed for either of the two ratios. The adsorption on Si-Beta results in similar spectra, only showing a small product peak at 1643 cm^{-1} and the liquid-phase citronellal peak. However, when the acetonitrile content was increased to a 3:1 ratio with respect to citronellal, additionally a ν(CN) vibration with negative absorbance was observed, as well as an even smaller product peak. In the case of Sn-SBA-15 (Figure 2.4a), the addition of acetonitrile in a 1:1 ratio leads to the complete disappearance of the shoulder at 1712 cm^{-1} observed in pure toluene. No negative peak in the ν(CN) region can be observed which means that almost no acetonitrile is displaced from the solid-liquid interface by citronellal. A small product band at 1646 cm^{-1} reveals still minor activity. By further increasing the acetonitrile/citronellal ratio to 3:1 (Figure 2.4c) this band gets even smaller and still no perturbed ν(CN) peak is visible. Additionally, the small product peak shows a maximum at a phase angle of 100°showing an increased induction time until a steady product concentration is reached. Even though only a shoulder is observed in the liquid-phase CD_3CN adsorp-tion experiment (Figure A.10), indicating weak Lewis acidity, this competitive study implies that acetonitrile binds more strongly to the Sn(IV) sites in Sn-SBA-15 than citronellal. This effect will be further amplified

when pure acetonitrile is used as solvent, which results in poor activity (Table 2.1). For Sn-Beta, an activated C=O peak is visible at 1715 cm^{-1} for an acetonitrile/citronellal ratio of 1:1 and 3:1 (Figures 2.4b and 2.4d). This peak is shifted by 3 cm^{-1} compared to pure toluene as solvent, indicating a minor distortion of the citronellal coordination by acetonitrile. Nevertheless, inside the zeolite pores, citronellal is able to displace acetonitrile as can be seen by the negative ν(CN) band at 2263 cm^{-1}. Furthermore, the absolute phase delay of the (liquid phase) product peak at 1646 cm^{-1} is 70°, which is 30°less than in pure toluene. A 3:1 acetonitrile/citronellal ratio also leads to a faster transport and/or adsorption of citronellal to the Sn(IV) site, which is reflected in the 40°absolute phase delay of the peak at 1715 cm^{-1}, *i.e.* 10°less than in pure toluene. These findings demonstrate that the addition of acetonitrile leads to facilitated transport of citronellal and isopulegol inside the zeolite pores, possibly due to the smaller molecular size of the additive and competitive adsorption/desorption. The coordination of citronellal is also stabilized in the presence of the Lewis base acetonitrile. For the mesoporous Sn-SBA-15, however, the Sn(IV) sites are more accessible, which leads to detrimental competitive adsorption.

2.3 Discussion

On the timescale of the ATR-IR MES experiments, no significant deactivation was observed. Hence, the obtained spectroscopic data can be correlated with the reactivity of the initial phase of the batch reactions. Based on our experimental observations, the different effects influencing the cyclization of citronellal over Sn-SBA-15 and Sn-Beta are thus summarized in Scheme 2. In the case of Sn-SBA-15 in toluene, citronellal can easily diffuse to the Sn(IV) site. The citronellal coverage on Sn(IV) sites is relatively low, as solvent molecules can effectively interfere with the coordinated citronellal. Once the product is formed, it can easily diffuse away, but it can also re-coordinate to the site and undergo the reverse reaction, or form undesired by-products. The size-restricted micropore structure of the Beta zeolite increases the coverage of citronellal on Sn(IV) sites. Confinement effects, as indicated by the same spectral position of the ν(C=O) vibration but a vastly different

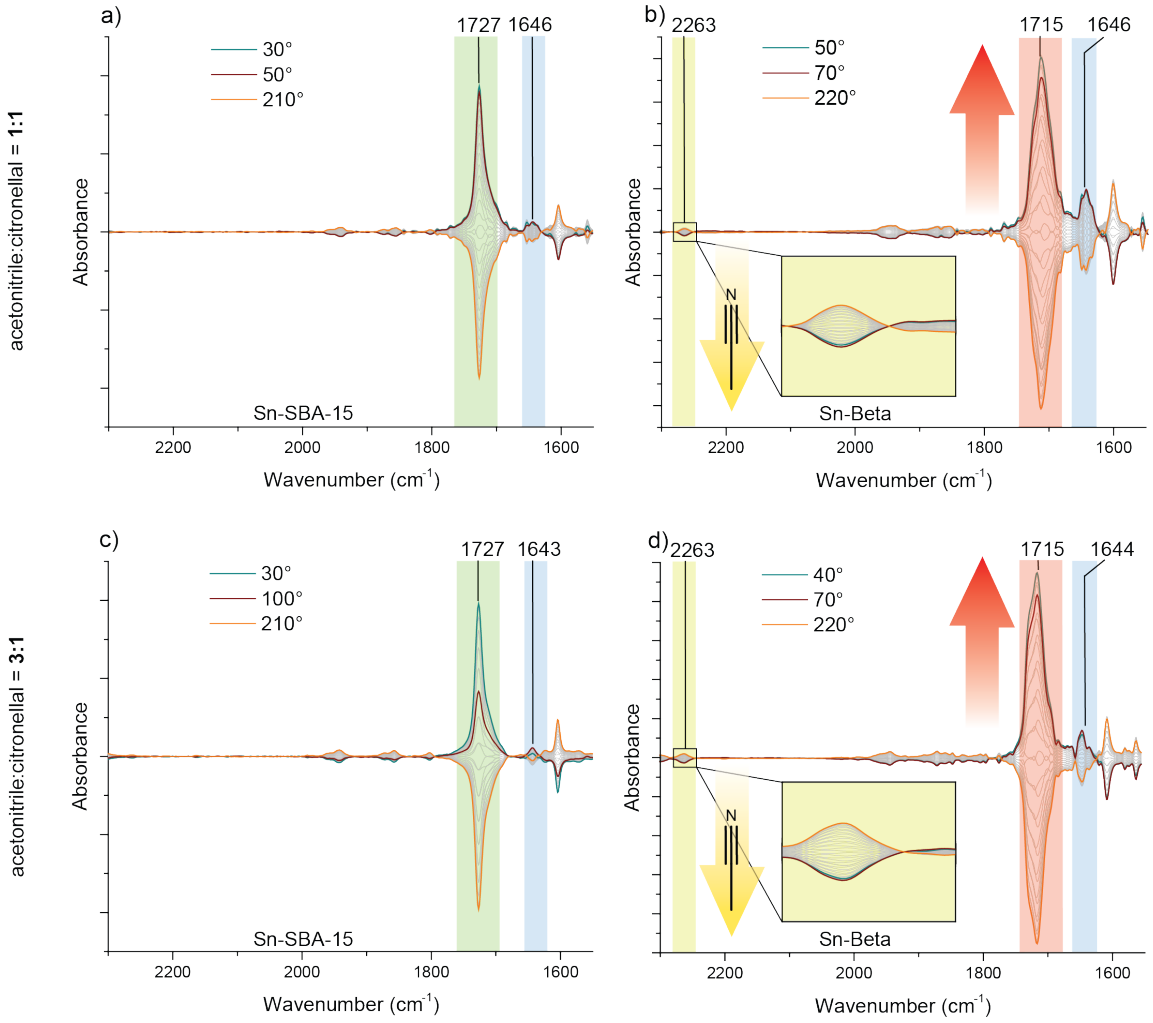

Figure 2.4: Phase-domain spectra for the modulation of 20 mM citronellal in a solution of 20 mM acetonitrile in toluene (top) and 60 mM acetonitrile in toluene (bottom) for Sn-SBA-15 a) and c) and Sn-Beta b) and d).

coverage for the two materials, most likely lead to a more stabilized coordination which increases the productivity. The micropore structure hinders the product from diffusing out of the pores, but also reduces by-product formation and the reverse reaction becomes unlikely as the product cannot re-enter the pore. When the Lewis base acetonitrile is used as solvent, the higher solvent concentration of the smaller molecule leads to a significant loss in activity. Our MES-ATR-IR study with 1:1 and 3:1 acetonitrile/citronellal ratios suggests a stronger interference of the solvent with citronellal coordinated to the Sn(IV) site as a possible explanation. On the other hand, a simultaneous coordination of citronellal and acetonitrile to the Sn(IV) site inside the micropore of Sn-Beta induces better diastereoselectivity. Similar to a bulky ligand in a homogeneous catalyst,[207;208] acetonitrile reduces the space around the active site and hence the formation of (-)-isopulegol is favored. The latter hypothesis was suggested before, but could never be observed experimentally.[190] Finally, acetonitrile leads to easier diffusion of both reactant and product in the micropores, as indicated by smaller absolute phase delays, which likely enhances the overall reactivity. The amorphous Sn-SiO_2 presents the other extreme case as the active Sn(IV) sites are present at the external surface where the solvent can easily interfere with the coordinated citronellal. Accord-ing to the liquid-phase acetonitrile adsorption (Figure A.10), Sn-SiO_2 was found to be more acidic than Sn-SBA-15, but it is still less active. Hence, a plausible explanation for the difference in activity could be the much smaller total micropore volume of Sn-SiO_2 compared to Sn-SBA-15 (Table S1), *i.e.* some of the Sn(IV) sites in Sn-SBA-15 are present in a microporous environment which might explain the higher activity. A similar effect has also been found for the conversion of tetrose sugars over Sn(IV)-containing materials, where Sn-SBA-15 showed a different temperature-dependency than the purely mesoporous Sn-MCM-41.[176] However, this is just a hypothesis and needs further experimental validation. As shown with the illustrative examples above, the Lewis acidity, even when measured under *in situ* conditions, is not a sufficient descriptor for the reactivity of stannosilicates. It is therefore highly important to gain insights into the molecular composition near the active site to understand complex heterogeneous liquid-phase catalysis. The use of MES-ATR-IR provides a

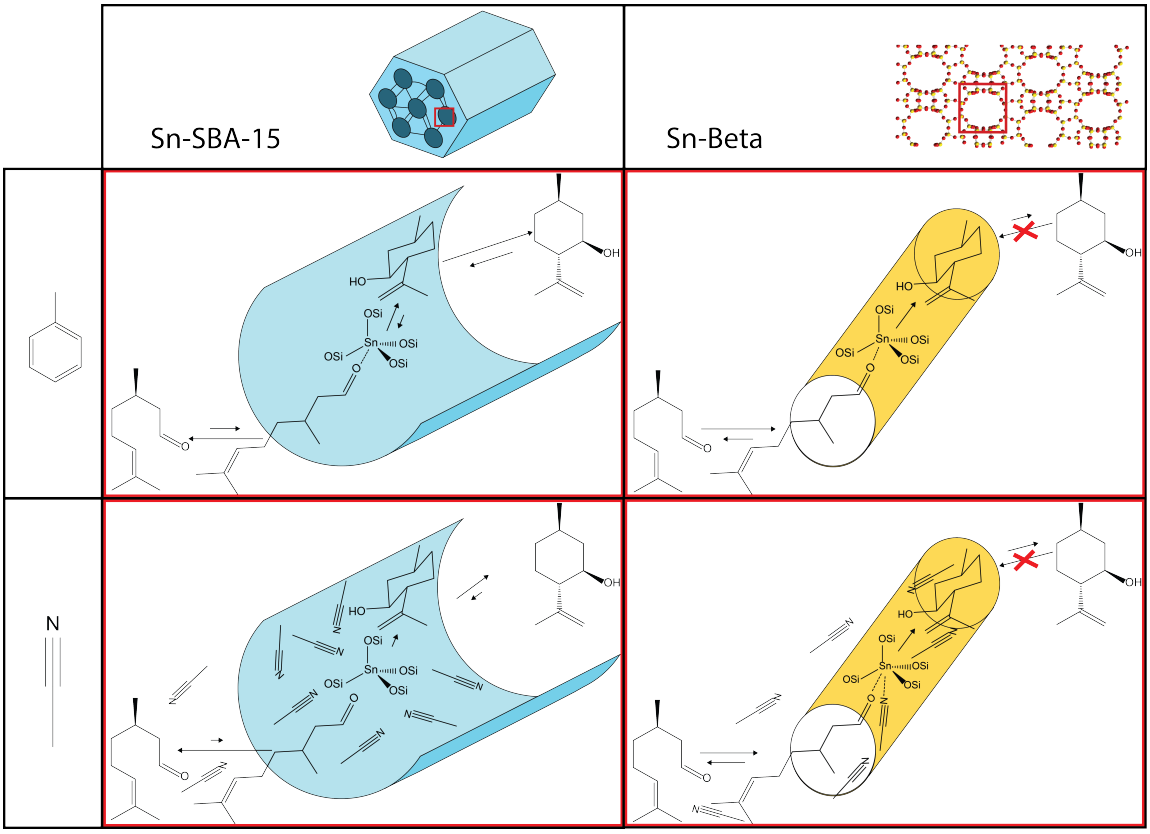

Figure 2.5: Representation of effects occurring during the cyclization of citronellal over Sn-SBA-15 and Sn-Beta in the presence of acetonitrile and toluene.

unique tool to probe dynamics at the solid-liquid interface with high sensitivity.

2.4 Conclusions

In conclusion, we studied the cyclization of citronellal as a case study to get insights into solid Lewis acid catalyzed liquid-phase reactions. A combination of batch experiments and ATR-IR-MES spectroscopic investigations revealed important details on pore size and solvent effects. The reaction mechanism over Sn-SBA-15 and Sn-Beta could be followed spectroscopically and involves the coordination of citronellal with its carbonyl group to the Sn(IV) site, followed by the cyclization step

and product desorption. The coordination is amplified in Sn-Beta because of the stronger Lewis acidity and confinement effects inside the micropore. As the product isopulegol is too big to enter the pores of the Sn-Beta zeolite, by-product formation and the reverse reaction are hindered due to size exclusion resulting in a better catalytic performance. In Sn-SBA-15 on the other hand, the Sn(IV) sites are readily accessible for substrate, product and solvent, resulting in a lower overall activity and selectivity. The addition of the Lewis base acetonitrile leads to a stronger loss in catalyst performance for Sn-SBA-15 due to competition for the Lewis acid site. This effect is not as pronounced in the microporous Sn-Beta because the local acetonitrile concentration is lower as citronellal is able to displace acetonitrile from the active site. Additionally, the simultaneous coordination of citronellal and acetonitrile enhances stereoselectivity as it beneficially reduces the space around the active site and accelerates substrate and product diffusion inside the micropores. As shown with these examples, confinement and solvent effects play an important role in understanding why certain catalytic systems are highly active. As the local molecular composition close to the active site is often not known and the reaction mechanisms are highly complex, a sensitive spectroscopic technique is crucial to obtain insights on a molecular level. ATR-IR spectroscopy in combination with MES is an ideal tool in that regard and can be applied to many other relevant heterogeneously catalyzed reactions as well.

2.5 Experimental Details

Materials synthesis

The mesoporous SBA-15 material was synthesized ac-cording to a literature procedure:[198] 3.5 g of Pluronic P123 was fully dissolved in 62.8 g of water and 2 g of HCl (37%) at 308 K. After the addition of 7.44 g tetraethylorthosilicate (TEOS), the solution was stirred for a day. Then, the mixture was hydrothermally treated in a Teflon-lined autoclave for 42 hours at 373 K. The obtained SBA-15 was washed with 5 L of water, dried in an oven overnight at 373 K and calcined in air at 823 K for 6 h.

The mesoporous Sn-SBA-15 material was synthesized using a method reported by Selvaraj *et al.*[194;195] 4 g of Pluronic P123 was stirred with 25 mL of water to yield a clear solution. Afterwards, a dilute HCl solution was prepared by mixing 12.8 g HCl (37%) with 144.8 g of water, added to the solution, and stirred for 1 h. Then, 9 g of TEOS and 3.06 g of SnCl4 were added and stirred for 24 h at 313 K. The solid products were recovered by filtration, washed several times with water and dried overnight at 373 K. Finally, the sample was calcined in air at 823 K for 6 h. Pure Si-Beta zeolite was prepared following a literature procedure.[197] To 25.5g tetraethylammonium hydroxide solution (35 wt%, SACHEM) 23g tetraethyl orthosilicate (TEOS, 99% Sigma Aldrich) was added. The reaction mixture was stirred under ambient conditions allowing ethanol and water to evaporate until the desired final composition was obtained. After adding 2.4g of hydrofluoric acid (HF, 48 wt%, Sigma Aldrich) dropwise and homogenizing the synthesis gel with a PTFE spatula, the thick paste was transferred into a 45 mL stainless steel autoclave equipped with a PTFE liner. Hydrother-mal crystallization was carried out at 140 °C and 60 rpm for 7 days. The final product was filtered, washed with water and acetone and dried at 120 °C over night. To remove the organics the sample was calcined at 853 K for 6h. The Sn-Beta zeolite was prepared through a post-synthetic method reported elsewhere.[160;161;196] Dealumination of the parent commercial Al-Beta zeolite (Zeolyst, SiO_2/Al_2O_3=300) was done by acid leaching (13 M HNO_3, 20 mL g^{-1}, 373 K, 20 h). Tin was incorporated via solid-solid ion-exchange by grinding dealuminated Beta with the appropriate amount of the tin(II) acetate precursor followed by subsequent heat treatments under N_2 and air for 3 h each at 823 K. The amorphous Sn-SiO_2 material was synthesized via a xerogel method.[193] 7 g of TEOS was diluted with 8.7 g of water. 1.9 g of a 0.1 M HCl solution was added and the resulting solution was stirred for 2 hours. Then, a solution of 0.2 g of $SnCl_4 \cdot 5\,H_2O$ in 2 g of water was prepared and added dropwise to the first solution. After another hour of stirring, a 40 wt% tetrapropylammonium hydroxide solution was added dropwise until the gel hard-ened. The resulting gel was dried at 373 K overnight and calcined in air at 853 K for 6 h.

Ex Situ Characterization

The different materials were analyzed with various techniques: Si, Al and Sn contents were determined by ICP-OES after digesting the solids in HF. The small-angle powder XRD-patterns for calcined samples were recorded under ambient conditions on a Bruker D8 advance diffractometer with Cu Kα radiation (λ=1.5406 Å). N_2-physisorption measurements were performed on a Micromeritics 3flex apparatus. The samples were degassed prior to measurement for 4 hours at 373 K. Adsorption isotherms were collected at 77 K and analyzed using BET, t-plot and DFT methods. DRUV-Vis analysis was performed with a Maya2000 Pro spectrometer (Ocean Optics) equipped with a deuterium/halogen light source (DH-200-BAL from Mikropack) using $BaSO_4$ as matrix.

Batch reactivity

Batch reactions were performed in 10 mL thick-walled glass reactors sealed with PTFE caps under vigorous stirring at 600 rpm and were heated in a temperature controlled oil bath. Typically, the reactions were performed at 333 K with 50 mg of catalyst, and 5 mL of a 0.5 M citronellal solution for 4 hours. Biphenyl was used as an internal standard. Samples were taken periodically and analyzed using an HP6890 gas chromatograph (Agilent) equipped with an HP-5 column. By-products were mainly condensation products.

ATR-IR & MES

The preparation of a catalyst layer was done by adding 10 mL of a 1:25 times diluted Collodion solution (5%, in 75:25 diethyl ether:ethanol, Fisher Scientific) to 100 mg of catalyst. The resulting suspension was stirred for 1 hour and then sonicated for 5 minutes. 1 mL of this solution was deposited onto the ZnSe crystal and put in an oven to dry at 353 K for 30 minutes to yield ca. 9 mg of deposited catalyst. The influence of the added Collodion on reactivity was tested in a batch reaction and was only minor (see Table S2). All ATR-IR measurements were performed

on a Bruker Vertex 70 spectrometer equipped with a liquid nitrogen cooled MCT detector. Typically 32 scans with a resolution of 4 cm^{-1} were co-added to give one spectrum. The switching between the two liquid reservoirs was accomplished through air-actuated valves (Parker) and modulation frequencies of 10-50 mHz. The ATR accessory was homemade and made use of a 45° ZnSe crystal. Measurements with a bare crystal showed a total exchange of the cell volume within less than 2 sec-onds under typical conditions. The liquids were drawn by a peristaltic pump (Ismatec) at flow rates of 3-25 mL/min. See Figure A.45 for a schematic of the setup. Absorbance is given in arbitrary units for all spectra in the time- and phase-domain.

3 SOLVENT EFFECTS INFLUENCING THE CYCLIZATION OF CITRONELLAL

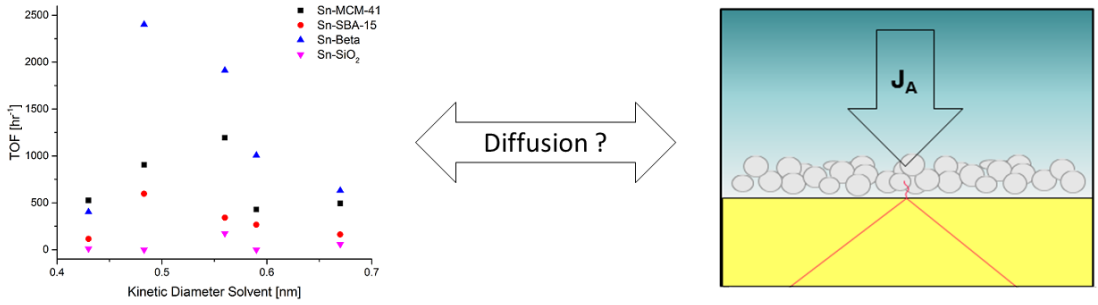

This chapter is the continuation of Chapter 2, where instead of only studying acetonitrile and toluene as a solvent, other solvents were tested as well. Significant differences in activity were found and we tried to understand why certain solvents worked better for this reaction than others by studying diffusion of citronellal solutions within various stannosilicates.

3.1 Introduction

In Chapter 2 of this thesis, we introduced the cyclization of citronellal as a unimolecular probe reaction to study the reactvity of heterogeneous Lewis acids and, in particular, stannosilicates. Interesting details about the reaction mechanism were found such as the influence of pore size and choice of solvent on this reaction. However, the solvents that were tested in Chapter 2 were limited to acetonitrile and toluene, two compounds with vastly different properties. In this chapter, other solvents have also been tested in trying to obtain a general understanding of solvent effects influencing reactions with porous heterogeneous catalysts.
Solvent effects are generally poorly understood in heterogeneous liquid-phase catalysis and most often different solvents are simply experimentally screened to reach

highest activity, selectivity or yield. Solvents can influence heterogeneously catalyzed reactions in different ways. They can affect reactant or product solubilities, polarity, the acid-base characteristics, all of which have an impact on the reactivity. In the case of porous catalysts, confinement effects can lead to selectivity and reactivity control due to diffusion, shape selectivity, or competitive adsorption.[209] In fact, one can consider molecular sieves as a "solid solvent". Decreasing the Si/Al ratio enhances the material's polarity/hydrophilicity which might influence the sorption capacity and diffusion properties for a given molecule. The polarisability of a zeolite can be changed by substituting Al for different other elements. As discussed earlier, this approach is often used to introduce softer or harder Lewis acids by substituting Al for group IV and V metals. The pore structure of a zeolite, in particular the ratio of reactant size to pore size, influences the physisorption and chemisorption properties of the zeolite. Furthermore, the added solvent will, depending on its size, also enter the pores and influence diffusion and adsorption properties of reactants and products. All of these parameters play a role when choosing an ideal catalyst-reaction-solvent system and are difficult to disentangle. We were already able to see some of these effects in Chapter 2 and will now further expand on those findings.

3.2 Results & Discussion

Materials & Batch Reactivity

In addition to the stannosilicates used in Chapter 2 of this thesis, we synthesized a mesoporous Sn-MCM-41 catalyst.[186;210;211] As can be seen in Figure 3.1, the synthesized Sn-MCM-41 catalyst has an average pore size of 38 Å and does not contain any micropores. Sn-SBA-15, on the other hand, has bigger mesopores of a size of ca. 80 Å, but also some micropores below 20 Å. Sn-Beta shows a distinct pore size at about 6 Å, as expected for the purely microporous zeolite. The pore size distribution of Sn-SiO_2 shows a broad distribution of different pores and does not possess clearly defined micropores or mesopores.

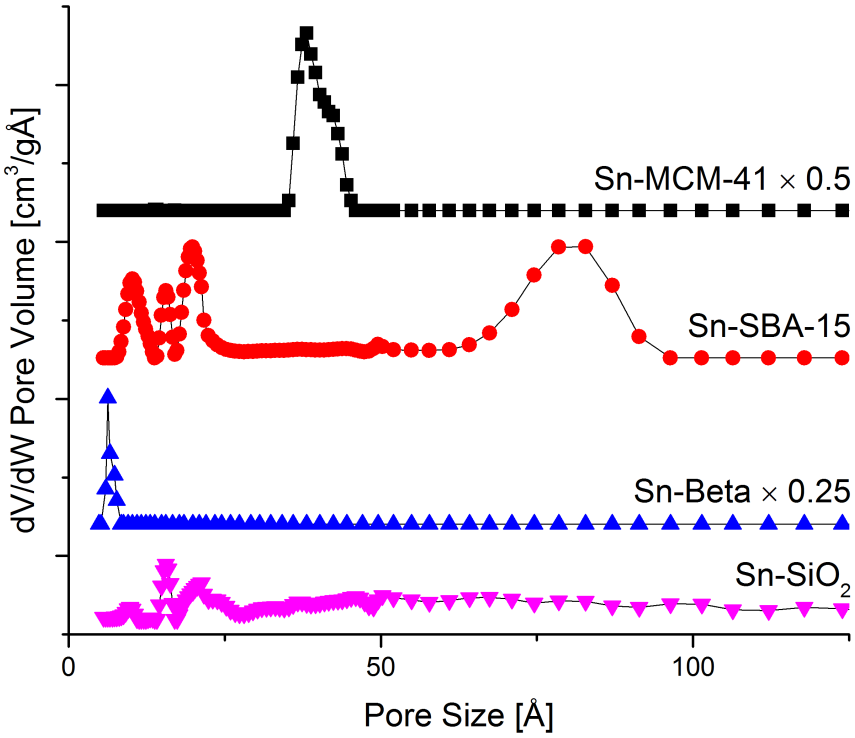

Figure 3.1: Pore size distribution of the stannosilicates calculated by a DFT method from the N_2 physisorption results.

When using these catalysts in the cyclization of citronellal, different activities were observed in toluene and acetonitrile (see Chapter 2). Additionally, these catalysts were tested with hexane, chloroform, *p*-xylene and 2,3-dimethylbutane as solvents. We chose these solvents because they do not possess any functional groups but vary significantly in size. Except for hexane, where Sn-MCM-41 is slightly more active, Sn-Beta generally shows highest activity. When plotting the turnover frequency (TOF), *i.e.* the activity normalized per Sn atom, as a function of the solvent polarity ϵ no clear trend can be observed (Figure 3.2a). When plotting the TOF as a function of the kinetic diameter of the solvent molecules, on the other hand,

it appears that a volcano-type plot is generated for all of the catalysts (Figure 3.2b). Interestingly, the maximum activity for Sn-Beta and Sn-SBA-15, both possessing significant amounts of of micropores <20 Å, was observed for chloroform (size of 4.8 Å), whereas the other two catalysts Sn-MCM-41 and Sn-SiO_2 show a maximum for 2,3-dimethylbutane (size of 5.6 Å) as solvent. In principle, molecules with a size of up to 6 Å can diffuse through all dimensions of Sn-Beta.[203] If, however, the observed differences in activity are indeed related to diffusion, our results suggest that the ideal solvent facilitating diffusion has to be slightly smaller than the pore diameter. Hence, we attempt to better understand diffusion through different stannosilicate catalyst beds with ATR-IR in this study.

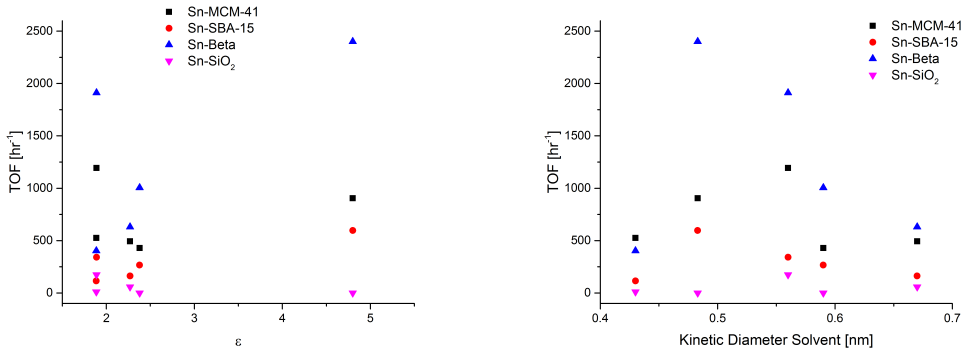

(a) As a function of the solvent's dielectric constant ϵ.

(b) As a function of the kinetic diameter of the solvent molecule.

Figure 3.2: Turnover frequencies for the different stannosilicates.

SEM characterization

As briefly described in Chapter 2, the deposition of the catalyst onto the internal reflection element (IRE) can be challenging depending on the type of catalyst, the IRE material, and solvent that are used. Usually, the more polar the solvent, the more likely the catalyst layer will be washed off the IRE when flowing a solvent over it. To circumvent this issue, we used Collodion as an adhesive material, by mixing the catalyst in a Collodion solution that is diluted in ethanol and diethyl

ether, dripping this solution onto the IRE and letting the solvent evaporate to create a catalyst layer. After the catalyst layer was prepared, we used scanning electron microscopy (SEM) to get an image of the deposited catalyst. Figure 3.3a shows a top-view of the catalyst layer. The catalyst particles are well distributed on the ZnSe crystal, but show a surprisingly broad particle size distribution ranging from a few hundred nm to ca. 5 μm. SEM micrographs of postsynthetic Sn-Beta have been reported previously and have shown particles of ca. 500 nm in size.[173] Hence, some of the bigger particles might be agglomerates of several Sn-Beta particles glued together by Collodion. When testing the reactivity of a Collodion impregnated catalyst (see Chapter 2), no significant loss in activity/selectivity was found, strongly suggesting that the observed agglomeration is not affecting the catalysis. The layer is packed densly, but there are still visible intraparticle voids that allow for diffusion through the catalyst layer. When looking at the IRE from the side, the catalyst layer is visible on top with a thickness of ca. 10 μm, followed by a thinner layer that is enriched with the adhesive. Energy-dispersive X-Ray spectroscopy (EDS) was used to determine the Zn, Se, Si, C, and O atom ratios at different positions on the sample. Figure A.46 shows such a mapping and it is obvious that even when the layer is relatively thin (less than 1 μm) almost no signals from Zn and Se could be detected (Table A.4), indicating an even distribution and a fully covered IRE.

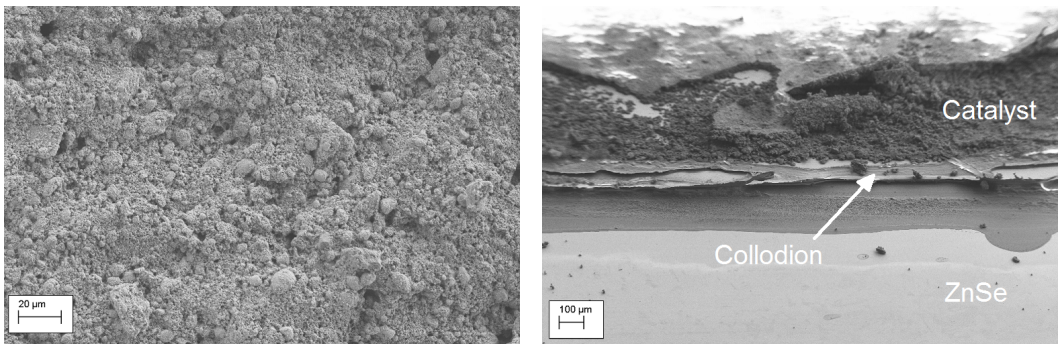

(a) Top view (b) Side view

Figure 3.3: SEM image of a ZnSe crystal coated with Sn-Beta.

This catalyst layer was used for the diffusion experiments that will be discussed

in the following section. SEM images of the spent catalyst are shown in Figures A.47 & A.48. The layer remained intact, even after several hours on stream and under flows of up to 3.7 mL/min which was used for the diffusion experiments. Unfortunately, it proved to be more difficult to obtain SEM images of the mesoporous catalysts. Even at lower acceleration voltages (2 kV), the layers got damaged and changed their morphology during image acquisition. Nevertheless, some images are shown in the appendix (see Figures A.49, A.50 and A.51).

Diffusion experiments

The prepared catalyst layers can then be used to study the diffusion of a reactant as illustrated in Figure 3.4. By quickly pulsing a high concentration of a reactant over the catalyst layer, the diffusion through the catalyst layer can be analyzed. In our case we used citronellal as diffusing molecule and monitored its most intense IR vibration at ca. 1720 cm^{-1} (C=O stretch) over time. As time progresses, citronellal will diffuse through the layer and the concentration at the interface with the IRE, where the infrared light is attenuated, will increase leading to a higher intensity at 1720 cm^{-1}.

A mathematical model can then be fitted to the time-dependent change in infrared intensity to extract diffusion coefficients. The diffusion through a layer can be described using Fick's laws.[22]

$$\frac{\partial C_A}{\partial t} = D_A \frac{\partial^2 C_A}{\partial z^2} \tag{3.1}$$

$$J_A = -D_A \frac{\partial C_A}{\partial z} \tag{3.2}$$

where D_A is the diffusion coefficient of component A, C_A is the concentration of component A, z is the distance in z direction (perpendicular to IRE surface), and J_A is the flux. The initial and boundary conditions were fixed as follows:

$$\text{I.C.} \qquad 0 \leqslant z \leqslant d; \quad t = 0,\ C_A = 0 \tag{3.3}$$

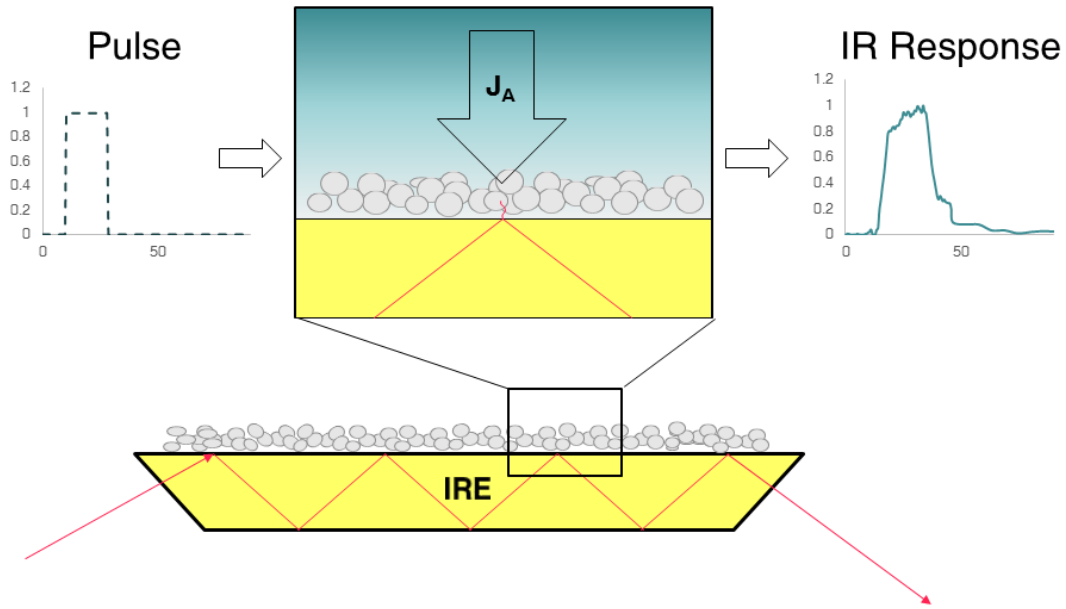

Figure 3.4: Schematic view of diffusion through a catalyst layer deposited on an IRE, where reactant A is pulsed and the corresponding IR response is monitored.

$$\text{B.C.} \qquad z = 0, J_A = 0; \quad z = d,\ C_A = SW(t) \tag{3.4}$$

To identify an appropriate diffusion layer thickness, the penetration depth for an ATR experiment was determined. The intensity of the evanescent electric field at the interface of the ATR crystal and the sample undergoes an exponential decay according to Equation 3.5

$$E(z) = E_0 exp(-\frac{z}{d_p}) \tag{3.5}$$

where E(z) is the electric field amplitude at a distance z to the crystal, and E_0 is the

electric field at the interface. The penetration depth d_p is defined as:

$$d_p = \frac{\lambda}{2\pi(n_1^2 sin^2(\theta) - n_2^2)^{0.5}} \tag{3.6}$$

where λ is the wavelength, and n_{21} is the ratio of refractive indices of the sample and of the IRE.

With refractive indices of $n_1 = 2.4$ for ZnSe and $n_2 = 1.2$ for the catalyst/solvent mixture,[26;212] an angle of incidence θ of 45°, $d_p = 2.4$ μm results. This value was taken and fixed as diffusion layer thickness in the following analysis. To fit the experimentally measured data, we varied the diffusion coefficient D_A such that the least square difference between the experiment and the fit was minimized. Hence, an experimentally determined diffusion coefficient could be obtained for the diffusion through the catalyst layer. The following table illustrates the results of these fits for three stannosilicates and the blank experiments, where the bare ZnSe crystal was used.

Table 3.1: Experimentally determined diffusion coefficients in $10^{-9} m/s^2$.

	blank	Sn-Beta	Sn-MCM-41	Sn-SBA-15
chloroform	2.02	0.70	0.25	0.21
hexane	3.10	0.56	0.21	0.17
2,3-dimethylbutane	1.65	0.69	0.25	0.17
toluene	2.56	0.65	0.26	0.24
p-xylene	2.31	0.63	0.25	0.26

The corresponding plots with the experimental and fitted data can be found in the Appendix (Figures A.52 - A.71). Interestingly, the diffusion coefficients measured on the blank crystal do not transfer to the coated ones, *i.e.* the highest diffusion coefficient in blank is the lowest in all of the catalysts. All of the diffusion coefficients get significantly lower over the catalysts compared to the blank crystal(from 2-3 down to <1).

The determined diffusion coefficients for the two mesoporous materials Sn-MCM-41 and Sn-SBA-15 are in a similar range, whereas the coefficient for Sn-Beta

is almost a factor of 3 higher. This might be counterintuitive at first, as it would be expected that the bigger pores enable easier diffusion. However, there are several things that could lead to this behavior. a) the use of Collodion might lead to stronger pore blocking in the mesoporous materials, b) citronellal might be stabilized by the smaller pore due to van der Waals interactions, as hypothesized in Chapter 2, leading to faster uptake, c) even though the same mass of catalyst was used for the different layers, the actual layer thickness might vary due to different porosity in these materials leading to different absolute values for the diffusion coefficients. Hence, it is advisable just to compare the values for the different solvents within the same catalyst layer. When then plotting the turnover frequencies for the different catalysts versus the experimentally determined diffusion coefficients (Figure 3.5, trends between diffusivity and activity can be analyzed. When comparing those two parameters, only Sn-Beta shows a clear trend, that is, the bigger the experimentally determined diffusion coefficient, the higher the activity. The two mesoporous materials do not follow a clear trend and the spread of diffusion coefficients is also not as large.

The behavior of the Sn-SBA-15 that contains micropores, but still does not follow a clear trend correlating diffusion coefficients with activity, might indicate that these micropores are not improving the catalyst and that most activity occurs on the external surface. The fact that the microporous Sn-Beta is more active with most solvents suggests that the stabilization of citronellal adsorption in the smaller zeolite micropores, as discussed in Chapter 2, might be the main reason for its superior activity. The right solvent, however, improves the transport from and to the active sites within the micropores and hence increases the turnover frequencies. To further improve the catalysts, it would be desirable to reduce the diffusion lengths in Sn-Beta. There are different possibilities to achieve this. Smaller catalyst particles, or layered zeolites could be synthesized, leading to shorter diffusion lengths and hence better utilization of the Sn sites. Alternatively, hierarchical zeolites could be synthesized that consist of a bigger mesopore network that leads to easy access to the micropores. There have already been several examples where such concepts have been successfully applied.[213–215]

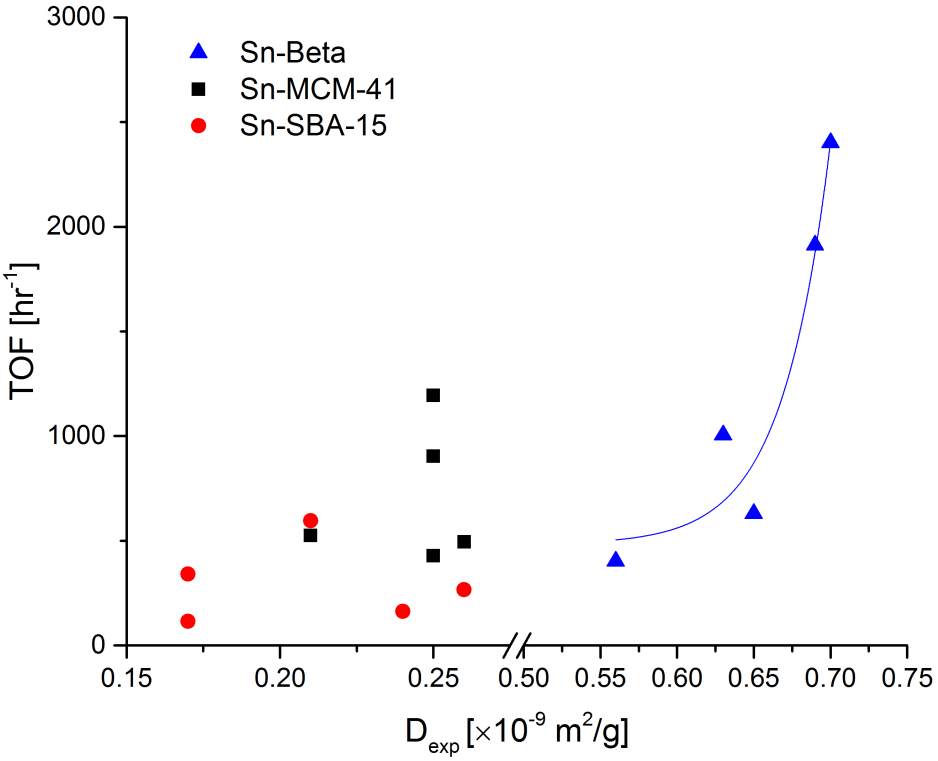

Figure 3.5: Turnover frequency as a function of the experimentally determined diffusion coefficient.

3.3 Conclusions

The cyclization of citronellal was studied using stannosilicates with different pore structures as well as different solvents. It was found that the activity does not correlate with the polarity of the solvent. Instead, a volcano-type dependence of the turnover frequency with the size of the solvent molecule was found and it was therefore hypothesized that diffusion might be responsible for such a behavior. Hence, the diffusion of citronellal through catalyst layers was investigated using ATR-IR spectroscopy. A mathematical model describing diffusion through a layer was fitted to the data and experimental diffusion coefficients were determined. The

diffusivity through the catalyst bed was lower for all tested catalysts compared to liquid-phase diffusion. However, only Sn-Beta showed a clear trend, increasing its activity when the diffusion coefficient increases. Hence, in the case of the mesoporous catalysts the reaction most likely occurs on the outer surface, unlike Sn-Beta in which citronellal is stabilized in the micropores, leading to good reactivity but also diffusion restrictions. Thus, decreasing the diffusion length in Sn-Beta will likely increase its activity in this particular reaction and chosing the right solvent (size) will further boost activity.

3.4 Experimental Details

See Chapter 2 for experimental details for the material synthesis. Additionally, a Sn-MCM-41 catalyst was synthesized following a reported procedure.[186;210] 13.0 g of hexadecyltrimethylammonium bromide (CTAB) was dissolved in 38 g of DI H_2O. A solution of 26.4 g of tetramethylammonium silicate (TMAS, 15-20 wt %) was added slowly and then stirred for 50 minutes. 0.106 g $SnCl_4$ pentahydrate was dissolved in 2.1 g H_2O and 0.345 g HCl (37 wt%) and added dropwise to the solution. This mixture was stirred for 1.5 hours at which point 12.2 g of tetraethylorthosilicate (TEOS) was added. The resulting mixture was stirred for 3 more hours, then transfered to a Teflon-lined autoclave and heated to 140 °C for 15 hours.

The pore size distribution was determined using a DFT method (Tarazona NLDFT, cylinder geometry as implemented in Microactive, Micromeritics Inc.) based on N_2-physisorption measurements on the dehydrated samples. (see Chapter 2 for further details)

The details on the characterization and batch reactivity are given in Chapter 2 as well. All reactions were performed at 60 °C and 900 rpm. Scanning electron microscopy (SEM) was performed using a LEO SUPRA 55 VP S3 field-emission scanning electron microscope operated at 2-3 kV. Energy-dispersive X-ray spectroscopy (EDS, 15 kV) was further used to analyze the composition of the deposited catalyst layers.

The diffusion experiments were performed as follows: A layer was prepared following the procedure described in Chapter 2, using ca. 8 mg of catalyst per layer. The same layer was used for all of the diffusion experiments. The order of solvents was changed and no significant differences between the runs were observed. The measurements were taken at room temperature to avoid undesired reactivity. The catalyst layer was first flushed with the pure solvent for five minutes at a flow rate of 3.7 mL/min. Then it was switched to a tank filled with 40 mM citronellal dissolved in the solvent. The IR response was monitored between 800 and 2000 cm^{-1} at a resolution of 8 cm^{-1} and averaging over 32 scans, which leads to a time resolution of 0.6 s using the RapidScan feature of the Bruker Vertex 70. The concentration was held at 40 mM for 100 seconds, then it was switched back to pure solvent for 300 seconds. This process was repeated three times and the three runs were averaged into one. A baseline correction was performed and the trace at the highest C=O stretch vibration signal (1705-1725 cm^{-1}, depending on solvent and catalyst) was extracted and normalized. This trace was then fitted to minimize the least-square error by changing the diffusion coefficient and keeping the layer thickness the same at 2.4 μm.

The diffusion coefficient of citronellal in hexane was estimated using the following approximation[216]

$$D_{12}^{0,l} = 4.4 \cdot 10^{-15} \frac{T}{\eta_2} \left(\frac{V_2}{V_1}\right)^{1/6} \left(\frac{L_2^{vap}}{L_1^{vap}}\right)^{1/2} \tag{3.7}$$

where T is the temperature, η is the dynamic viscosity, V is the molar volume of compounds 1 and 2 and L^{vap} is the heat of vaporization. For the estimation, we used the heat of vaporization of citral, as the one for citronellal could not be found.[212] The experimentally measured diffusion coefficient for the blank citronellal in hexane experiment was underestimated, likely due to an overestimated diffusion layer thickness or non-idealities in the spectra acquistion. Hence, a correction factor was used based on the estimated value using equation 3.7.

4 MECHANISTIC STUDY ON THE LEWIS-ACID CATALYZED SYNTHESIS OF 1,3-BUTADIENE OVER TA-BEA USING MODULATED *operando* DRIFTS-MS

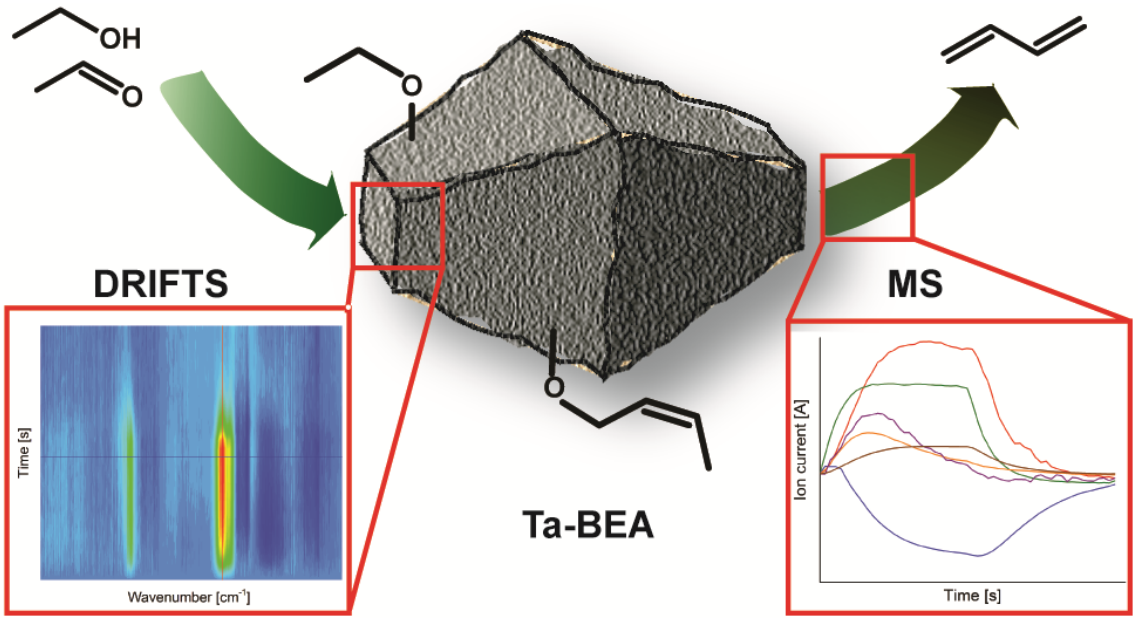

In this chapter the first application of a newly developed gas-phase DRIFTS-MS setup is shown with a mechanistic study on the formation of 1,3-butadiene from a mixture of ethanol and acetaldehyde over Ta-BEA. Due to an increasing gap between the demand and supply of butadiene, the on-purpose production process from renewable ethanol has regained the attention of the scientific and industrial community. Getting a molecular-level understanding of the reaction mechanism is hence important to improve the process. Published in ACS Catalysis.[97]

4.1 Introduction

1,3-Butadiene (BD) is a commodity chemical with a worldwide production capacity of over 14 Mt per year[217] that finds applications as a monomer in the production of synthetic rubbers,[218;219] in the synthesis of the nylon intermediate adiponitrile,[220] and in Diels-Alder reactions forming cycloalkanes and cycloalkenes.[221] Traditionally, BD is obtained as a byproduct of ethylene production from steam cracking. However, the recent shift to lighter feedstocks and changing cracking technologies has led to a decrease in the BD supply.[222;223] Especially as the demand in developing countries steadily increases, a renewed interest in alternative routes to on-purpose BD was observed in the past decade.[224;225] A promising strategy in this regard is the use of renewable bioethanol as the feedstock.[226] Accordingly, many studies have been devoted to understanding the mechanism of this reaction over different heterogeneous catalysts.[227–231] The mechanism is particularly complex because it consists of many reaction steps involving various compounds and catalyst functionalities. Despite that, a generally accepted reaction pathway has been put forward as shown in Figure 4.1.[230;232;233] The formation of diethyl ether (DEE) is shown as a specific example of an undesired sidereaction. Other possible byproducts are 1-butanol, ethylene, propylene, and trienes.[222;230;234] While avoiding byproducts is important for getting high BD yields, in this contribution we focus on the main pathways of BD formation. In general, two processes for the production of BD from ethanol (EtOH) can be differentiated: the one-step process, *i.e.* the direct transformation of EtOH to BD, catalyzed by mixed oxides with a significant basic character, and the two-step process mainly performed over Lewis acids, where acetaldehyde (AA) is cofed. Chieregato *et al.* recently studied the EtOH coupling reaction over basic MgO.[227] Based on an observed IR vibration at 1143 cm^{-1} combined with computational predictions, they concluded that BD is most likely formed from EtOH in a concerted mechanism involving a carbanion intermediate. As the intermediate acetaldol (AOL) undergoes the reverse reaction when fed over MgO,[227] and yields less BD than equivalent amounts of acetaldehyde over other catalysts,[232] it is still an ongoing debate whether the pathway in Figure 4.1 is generally valid. For the

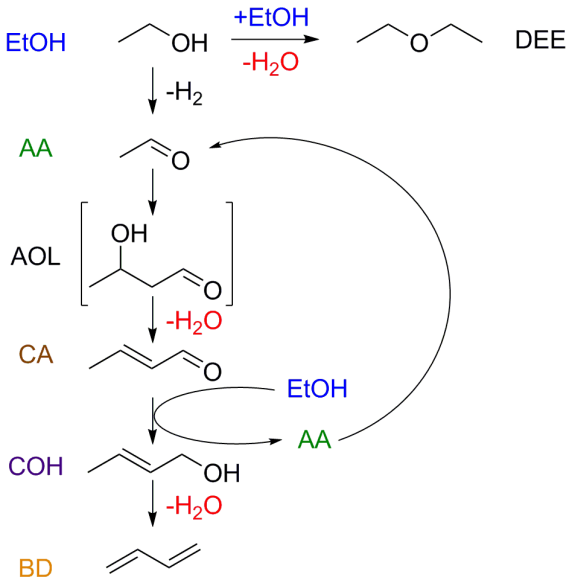

Figure 4.1: Reaction pathway for the coupling of ethanol to 1,3-butadiene. Ethanol (EtOH) is dehydrogenated to acetaldehyde (AA), which undergoes self-condensation to form the unstable intermediate acetaldol (AOL). Dehydration of AOL leads to the formation of crotonaldehyde (CA) that undergoes a Meerwein-Ponndorf-Verley (MPV) reduction with ethanol as hydrogen donor producing crotyl alcohol (COH). Crotyl alcohol can then be dehydrated to yield the desired product 1,3-butadiene (BD). Alternatively, an initial dehydration reaction between two molecules of EtOH leads to the by-product diethyl ether (DEE).

two-step process, different Lewis acid based catalysts have been reported.[230;235–239] The Lewis acidic functions on those materials, either in the form of supported metal oxides (Ta/SiO_2, Zr/SiO_2, etc.) or heteroatom substituted zeolites (Zr-BEA and Ta-BEA), are not efficient for the dehydrogenation of EtOH to AA. Therefore, AA has to be cofed, or a metal promoter has to be added[230;237;240;241] that facilitates the first step. Nevertheless, these catalysts show high activity and selectivity and the mechanism starting from AA is likely similar irrespective of the first step. Other than for the one-step process, most investigations on these materials have been limited to macrokinetic studies, and a general understanding on a molecular level is still lacking. Hence, we study the reaction mechanism of the Lewis acid catalyzed

coupling of EtOH/AA over Ta-BEA under actual reaction conditions. We developed an *operando* DRIFTS-MS setup that allows for a precise control and analysis of changes in the gas-phase composition as well as studying adsorbed intermediates. We apply a modulation approach that enables us to better understand the origin of consecutive reaction products. Finally, we propose a reaction mechanism based on our obtained data.

4.2 Results & Discussion

Materials & Characterization

The Ta-BEA zeolite was synthesized following a postsynthetic procedure established by Dzwigaj and co-workers.[163] In short, a commercial BEA zeolite was dealuminated, followed by the incorporation of tantalum (2.5 wt %). The diffuse reflectance UV-vis spectrum of the calcined material (Figure 4.2) shows a narrow peak at 222 nm, indicating the successful incorporation of isolated tantalum sites.[169] Indeed, the UV-vis spectrum of the reference bulk tantalum oxide is significantly broader and shifted, supporting the isolated nature of the Ta sites in Ta-BEA.

Furthermore, the preserved X-ray diffraction pattern (see Figure A.72) of Ta-BEA and the large surface area and micropore volume (Figure A.73, Table A.5) after tantalum incorporation affirm a successful synthesis. To assess the acidity of Ta-BEA, a self-supporting IR wafer was outgassed under vacuum (10^{-6} mbar) at 573 K for 1 h before pyridine was adsorbed at room temperature. The transmission IR spectra for Ta-BEA after desorption at different temperatures are shown in Figure 4.3a, in good agreement with reported spectra in the literature.[169]

The presence of a weak band at 1545 cm^{-1}, characteristic for (strong) Brønsted acid sites, and strong bands at 1610, 1595, 1490, and 1444 cm^{-1} indicate that mainly Lewis acid sites are present.[28;242;243] In a second experiment the substituted and bulky 2,6-di-tertbutylpyridine (dTBPy; kinetic diameter ~7 Å), that is not able to enter the small pores of the BEA zeolite (window size ~6 Å), was used as an adsorbate to probe the external surface/pore mouth. It has been shown that bands

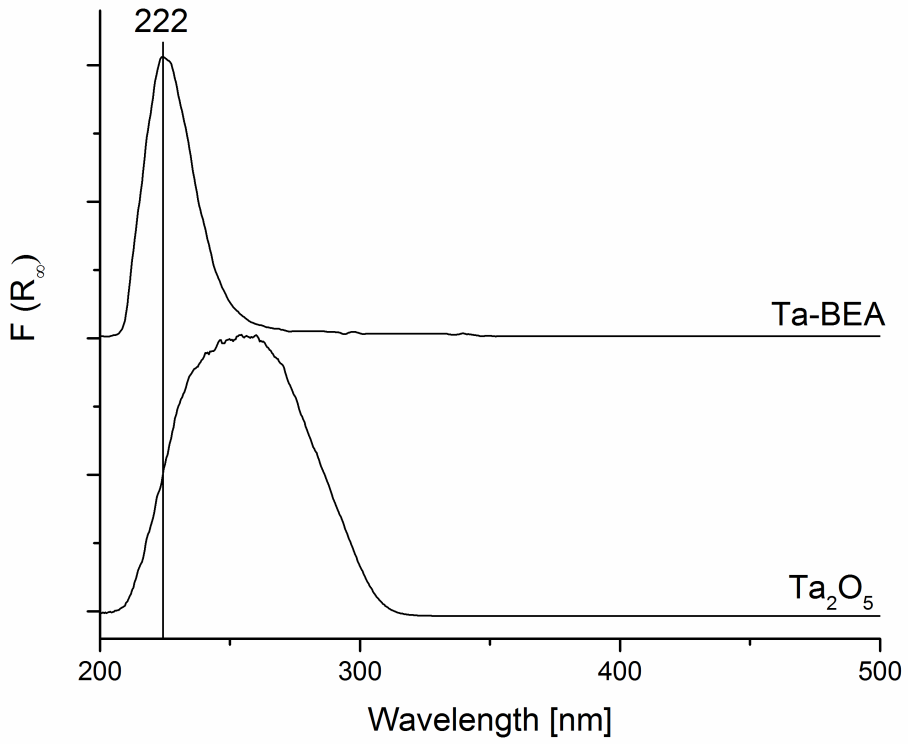

Figure 4.2: Diffuse Reflectance UV-VIS spectra of Ta-BEA and bulk tantalum oxide.

at 1615 and 1530 cm^{-1} can be associated with protonated $dTBPyH^+$, while bands at 1600-1590 and 1450 cm^{-1} originate from interactions with Lewis acid sites.[244;245] The spectrum in Figure 4.3b suggests a relatively high Brønsted acidity at the external surface. However, Lewis acid sites are also present, as indicated by the band at 1450 cm^{-1}. This feature only starts to disappear at 150 °C, suggesting that the Lewis acid sites at the external surface are relatively strong. In order to investigate the state of the catalyst under reaction conditions, we performed *in situ* EXAFS (extended X-ray absorption fine structure) experiments of the Ta L_3 edge. First, a spectrum of the catalyst was taken at ambient conditions (see Figure A.74). Then, the catalyst was heated to 300 °C under a He flow. This leads to a shift of

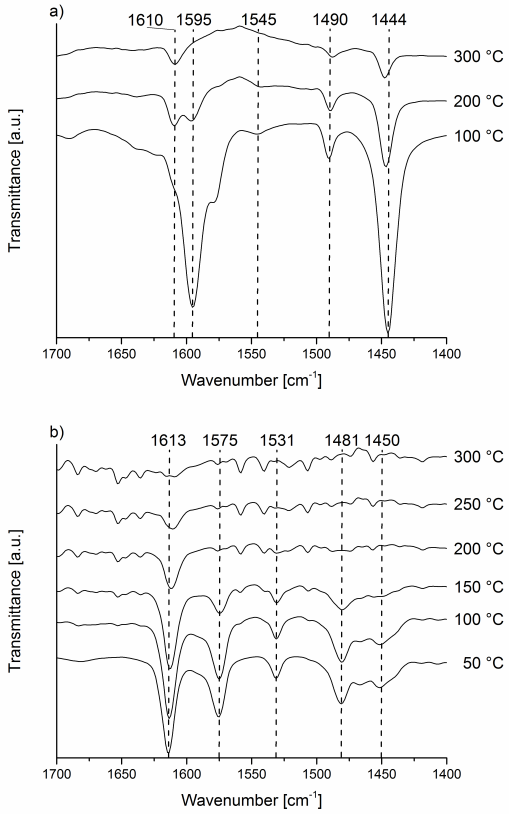

Figure 4.3: Transmission infrared spectra of Ta-BEA after outgassing and the adsorption of (a) pyridine and (b) 2,6-di-tertbutylpyridine at different temperatures.

the XANES (X-ray absorption near edge spectroscopy) edge energy from 9887 to 9886 eV and a narrower white line signal. This value is in line with reported edge energies for isolated tantalum sites on silica, and no evidence for bulk Ta_2O_5 was found in our spectra.[246] In the R-space of the Fourier transform of (E), the position of the first coordination shell shifts from 1.84 to 1.80 Å upon heating to 300 °C under He flow. The desorption of water from the tantalum site, as observed in the mass spectrometer signal, seems to shorten the Ta-O distance, suggesting hydrogen bonding of water to the tantalum site under ambient conditions. The introduction of neither EtOH nor a reaction mixture (EtOH/AA in a 3:1 molar ratio) into the He flow significantly changes the spectrum. These experiments suggest that the active

site is not substantially modified under reaction conditions (after 1 h on stream).

Operando DRIFTS-MS Modulation Experiments

To further investigate the reaction mechanism of the production of BD from a mixture of EtOH and AA over Ta-BEA, we developed an *operando* DRIFTS-MS (diffuse reflectance infrared Fourier transform spectroscopy-mass spectrometry) setup that allows for the introduction and vaporization of liquid substrates and switching between two different flows. A schematic overview of the setup is given in Figure 4.4. Helium was used as carrier gas and connected to two independent mass flow controllers. Two syringe pumps were used to introduce liquids that are evaporated in a heated spiral before reaching an electronically controlled two-position-four-way valve. Depending on the position of this valve, either flow A or B is admitted into the DRIFTS accessory. Finally, the gas-phase composition is monitored with an online mass spectrometer. By periodically switching between flow A and B, the influence of either component on the reaction can be analyzed in a transient manner. This concept of modulation excitation spectroscopy has been widely applied for liquid-phase reactions[20;64;76] and in some cases for gas-phase reactions.[110;117] After reaching a quasi-steady state (normally after 2-3 switching periods), three ratio. The simultaneous probing of adsorbed species and the gas-phase is highly important to be able to correlate the evolution of products with intermediates at the gas-solid interface. The use of syringe pumps instead of commonly used saturators[96] allows us to precisely control the gas-phase concentrations, which leads to reproducible experiments under actual reaction conditions. As this reaction involves many intermediates (Figure 4.1), it is not trivial to detangle signals originating from different compounds. In Table 4.1, we show the chosen m/z values for the most important intermediates. This choice is based on the MS fragmentation patterns of these intermediates while avoiding contributions from other compounds and still getting large enough intensities (see Table A.6 for details).[247] For instance, the most intense signal of AA at m/z = 29 also has contributions from EtOH, which is why we chose the second most intense signal at m/z = 44 instead that still showed a relative intensity

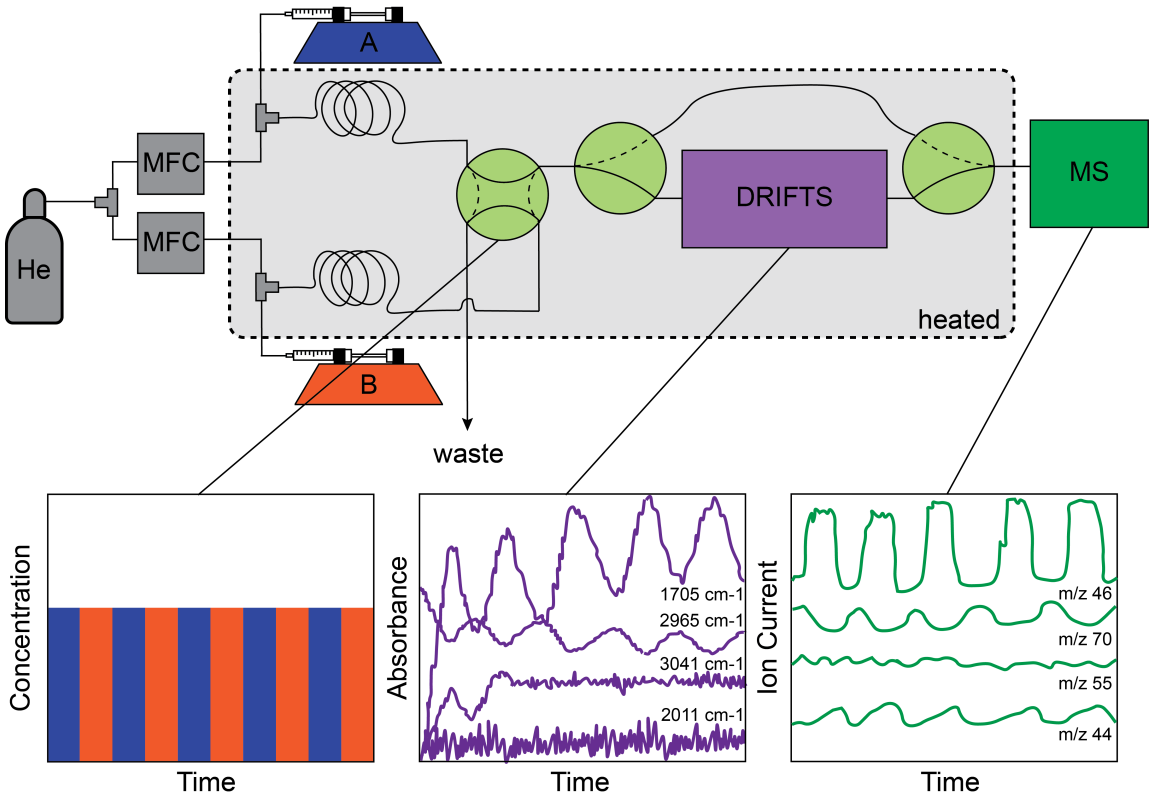

Figure 4.4: Schematic overview of the DRIFTS-MS setup. By using two syringe pumps and heated coils that enter a two-position-four-way valve, the gas-phase composition can be modulated between substrates A and B. Depending on the chosen position, either flow A or B flows through the DRIFTS accessory followed by the online mass spectrometer. In addition, two three-way-valves allow the substrates to bypass the DRIFTS accessory to ensure steady gas-phase concentrations prior to measurements.

of 80%. In addition to these m/z signals, we also recorded the signal of H_2O (m/z = 18). Furthermore, Table 4.1 lists the gasphase infrared vibrational frequencies of these compounds obtained from reference databases[248;249] and confirmed in our setup.

Table 4.1: Chosen m/z signals and some IR vibrational frequencies for the most important intermediates.

Molecule	m/z[i]	C-H stretch [cm^{-1}][ii]	C=O stretch [cm^{-1}][ii]	C=C stretch [cm^{-1}][ii]	other vibrations [cm^{-1}][ii]
EtOH	46	2988, 2970, 2900	-	-	1065
AA	44	2820, 2725, 2700	1750	-	-
BD	54	3108, 3090, 3045	-	1605, 1588	-
CA	70	2935, 2820, 2730	1722, 1710	1640	-
COH	57	3025, 2937, 2880	-	1676	1450, 1440

[i] signals were chosen from reference[247]. See Table A.6 for details.
[ii] for gas-phase infrared spectrum from reference[248] &[249] and blank measurements.

Modulation Experiments with EtOH and AA

In a first set of experiments, we studied the reaction of EtOH and AA. In all of the following experiments, we first saturated the surface with the compound that is given in the second half of the MS plot (right). For instance, in the case of Figure 4.5a, the surface is saturated with EtOH before periodically switching to the compounds on the left, in this case a 3:1 molar mixture of EtOH/AA. We chose similar reaction conditions as reported for Ta-BEA[236] for all of the following experiments. These conditions give high BD selectivity (>80%) at a significant level of conversion (>40%) over tantalum catalysts.[232;235;236;250] In Figure 4.5a and 4.5b the MS signals (gas phase) and the IR spectra (surface species) of three averaged modulation periods are shown. For both plots a background was taken at the beginning of the measurement and the differences upon switching the flow are shown. The MS signals are scaled for better visibility. The corresponding m/z values and the applied scaling factor are given in the legend. As soon as AA is admitted to the cell, BD is produced, indicated by the appearance of the m/z = 54 signal. Interestingly, the signal for CA (m/z = 70) follows the one for BD. The m/z = 57 signal for COH is weaker but also increases in the presence of AA. The signal for water that can be formed in two dehydration steps follows the same pattern as well. When just switching between pure He and an AA flow (see Figure A.75), on the other hand, CA is formed but only negligible amounts of BD are produced. The signal for COH remains essentially a flat line. This corroborates the importance of EtOH in the formation of BD from COH via transfer hydrogenation of CA. The infrared spectrum (Figure 4.5b) shows negative peaks between 2987 and 2898 cm^{-1} indicative of partial desorption and/or reaction of surface-bound EtOH and reaches a minimum at around 150 s, *i.e.* 30 s after switching from EtOH/AA to EtOH. This delay suggests that EtOH is not directly reacting with AA, but likely reacts with a consecutive product (*e.g.*, CA). Bands between 2800 and 2703 cm^{-1} evolve and are assigned to the C-H stretch vibrations of AA. In the C=O stretch region, three main bands appear. We assign the one at 1760 cm^{-1} to AA weakly bound to the catalyst. A similar signal was also observed for the adsorption of

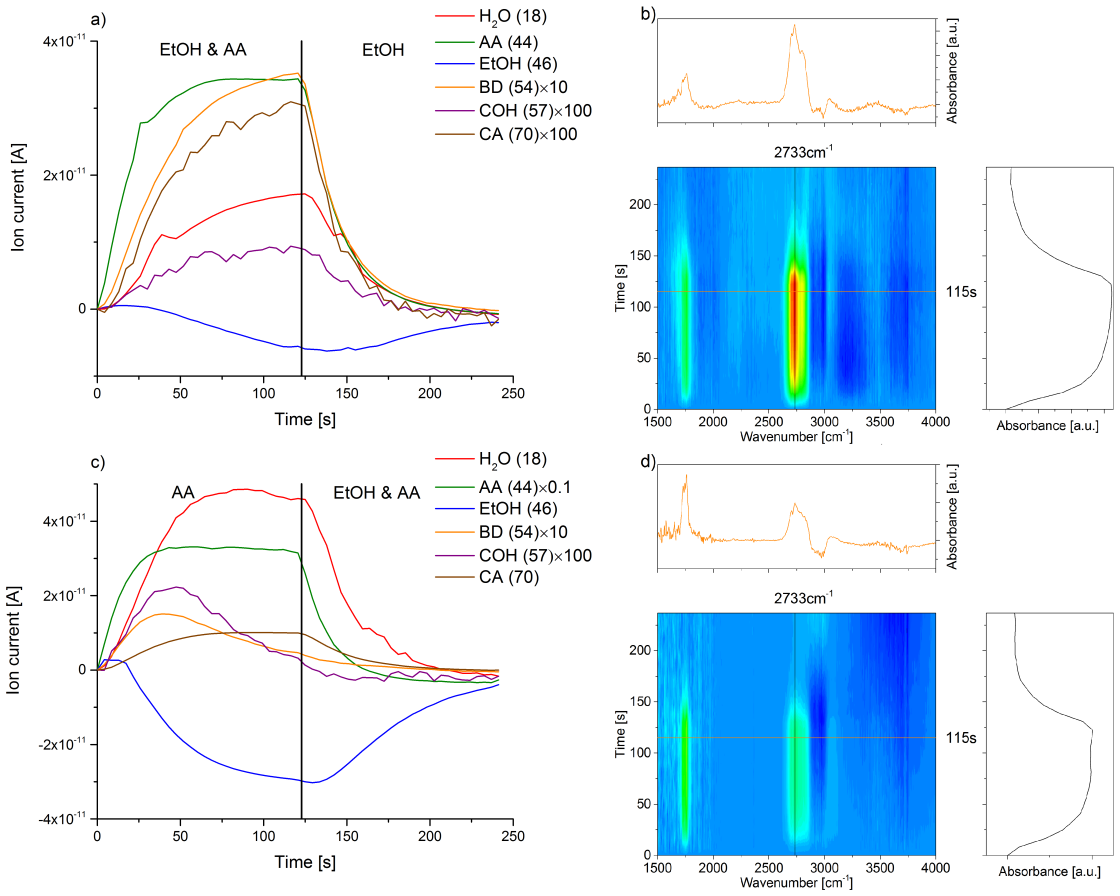

Figure 4.5: Modulation experiments between pure EtOH in He and a 3:1 mixture of EtOH/AA over Ta-BEA at 300 °C. a) shows the recorded MS signals of a modulation experiment, where the surface was first saturated with EtOH followed by periodically switching to EtOH/AA. b) shows the corresponding infrared spectra. In c) the surface was first saturated with the reaction mixture EtOH/AA followed by pure AA flow, and d) shows the corresponding infrared spectra. The switch from one flow to another was done after 120 seconds as indicated by the black line. Three periods were averaged when quasi steady-state was reached.

AA on Ta-BEA and on pure SiO_2 (Figures A.76-A.78). Additionally, a band at 1726 cm^{-1} is observed that can be assigned to an adsorbed CA species. Finally, a weak signal at 1690 cm^{-1} emerges. The origin of this peak is not completely clear at this point. The wavenumber is too high for it to be assigned to a C=C stretch vibration of

COH and too low for a C=O stretch vibration of CA. It could originate from a C=O vibration of a species that is more strongly bound to the catalyst. In the OH-region, a negative peak centered around 3740 cm^{-1} appears that is more pronounced in the first half-period, suggesting a possible interaction between the AA and OH groups of the catalyst. When performing the reverse experiment, *i.e.* switching from the EtOH/AA mixture to pure AA, the MS signals look quite different (Figure 4.5c). Both the CA and COH signals increase quickly, go through a maximum, and then reach a value close to zero. As it is relatively easy to couple AA to form CA over Ta-BEA (see Figure A.75), it is likely that switching to pure AA triggers a higher production of CA. As the desorption of CA is not occurring quickly (*vide infra*) and surface-bound EtOH is still present, as seen in the IR, the formed CA can immediately be transformed to COH that can easily be dehydrated to BD (see Figures A.79 and A.80). The BD signal decreases again, when EtOH is consumed or desorbs from the gas-solid interface. Simultaneously, the CA signal increases, as it cannot react further in the absence of EtOH. The infrared spectra (Figure 4.5d) generally look comparable to the first experiment, and consequently, similar surface species are present. In the C-H stretching region, positive signals between 2700 and 2800 cm^{-1} originating from adsorbed AA and negative bands between 2900 and 3000 cm^{-1} from EtOH can be observed. As before, a peak for CA at 1726 cm^{-1} appears. This peak does not fully disappear upon switching to EtOH and AA and shifts toward lower wavenumbers (1717 cm^{-1}). Thus, in the presence of EtOH, the produced CA seems to be coordinated more strongly to the Ta site than in the presence of pure AA. A weak band at 1687 cm^{-1} is present which likely originates from the same species as the unassigned peak at 1690 cm^{-1} in Figure 4.5b. Also for this experiment, negative peaks in the OH region (3740 cm^{-1}) can be observed. Even though the concentration of BD in the gas-phase is relatively high, no characteristic IR peaks for BD are observed in either case. This points toward fast desorption of BD from the gas-solid interface immediately after its formation, and/or dehydration of COH in the gas-phase. To summarize these first experiments, we found that AA is required in order to produce BD. However, when only AA is present, CA is produced but not converted further. EtOH is important

for the transformation of CA to BD, but does not directly react with AA. This is in line with the mechanistic hypothesis (Figure 4.1) where EtOH is reacting with CA. Furthermore, we found a strongly bound CA species that is likely a reaction intermediate. The appropriate ratio of AA/EtOH and consequently CA/EtOH seem to be crucial to achieve high BD productivity. Finally, COH and BD follow similar patterns, indicating that they originate from the same intermediate.

Modulation Experiments with EtOH and CA

To further study the role of CA, we performed experiments with CA and EtOH following the same methodology. In the experiment shown in Figure 4.6a, the catalyst was first saturated with EtOH, followed by periodically switching to a 3:1 molar mixture of EtOH/CA. Evidently, BD is only produced when CA is present in the flow. However, the signal for CA does not significantly change in intensity, indicating that most of the CA is being either adsorbed or consumed. The COH signal, on the other hand, follows a similar pattern as the one of BD. The increase of the signal for m/z = 44 assigned to AA suggests a MPV reaction that produces AA from EtOH. In the IR spectrum (Figure 4.6b) we find similar trends as in Figure 4.5b, where negative EtOH bands (2990-2900 cm^{-1}) and positive CA bands are observed (2730-2700 cm^{-1} and 1724-1700 cm^{-1}). Similar to the case of EtOH and AA, a small peak around 1688 cm^{-1} can be observed that follows the MS signal of BD. The reverse experiment (Figures 4.6c and 4.6d) again shows distinctively different features. The MS signal for BD goes through two maxima, one at roughly 60 s and one in the second half period at about 140 s. The signals for water and AA follow a similar trend. Likely, the BD productivity first increases due to the presence of EtOH that reacts with CA. Once a certain CA/ EtOH ratio is reached, the BD productivity decreases. When switching back to the pure CA flow, the CA/EtOH ratio increases again, leading to a maximum in the BD productivity, before it decreases when the CA/EtOH ratio gets too high. The infrared spectra show negative peaks in the C-H stretch region of EtOH (2900-3000 cm^{-1}), indicating a consumption of adsorbed EtOH by CA. A negative C-H stretch vibration from

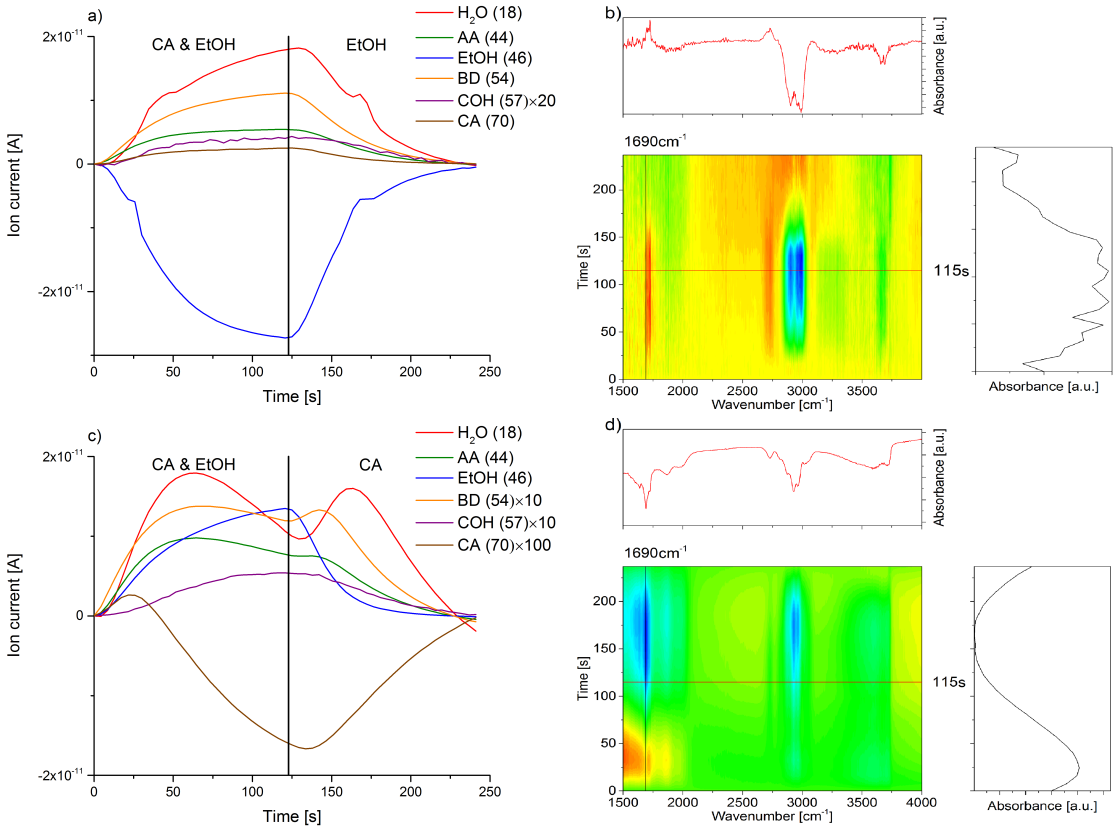

Figure 4.6: Modulation experiments between pure EtOH in He and a 3:1 mixture of EtOH/CA over Ta-BEA at 300 °C. a) shows the recorded MS signals of a modulation experiment, where the surface was first saturated with EtOH followed by periodically switching to EtOH/CA. b) shows the corresponding infrared spectra. In c) the surface was first saturated with CA followed by EtOH/CA flow, and d) shows the corresponding infrared spectra. The switch from one flow to another was done after 120 seconds as indicated by the black line. Three periods were averaged when quasi steady-state was reached.

CA at 2730 cm^{-1} corroborates this finding. In the C=O stretch region, three main bands appear. We assign those at 1722 and 1705 cm^{-1} to CA and, similar to the previous experiments, the third one at 1690 cm^{-1} to a strongly adsorbed CA species. Interestingly, only a band at ca. 1710 cm^{-1} is present when pure CA is adsorbed on Ta-BEA (Figure A.81) and none more redshifted at 1690 cm^{-1}, indicating that EtOH,

either from the gasphase or preadsorbed, is needed to form the latter species and that it could originate from a reaction intermediate.[251] Additionally, we performed a modulation experiment, where the catalyst was first saturated with EtOH, followed by periodically switching to pure CA. The MS signals (Figure A.82) reveal similar but more pronounced patterns than those in Figure 4.6. This suggests that either preadsorbed EtOH or CA can react with the other component to form BD. In the IR spectra (Figure A.83), similar features as for the reaction of the mixture (Figure 4.6) can be observed. The peak at 1690 cm^{-1} is also present in these spectra. To summarize these experiments, we found that the MPV reaction is occurring in the presence of CA and EtOH. As in the previous experiments, a strongly bound CA species was found, likely a reaction intermediate that follows a similar pattern as the MS signal of BD, suggesting its importance in the reaction mechanism.

Modulation Experiments with EtOD and CA

To get further insights into the reaction mechanism, we used monodeuterated EtOH (EtOD), where only the proton at the alcohol group was exchanged for deuterium. By additionally monitoring the MS signals of HDO (m/z = 19), D_2O (m/z = 20), EtOD (m/z = 47), and COD (m/z = 73), further details of the reaction mechanisms can be extracted. When EtOD is adsorbed on Ta-BEA (Figure A.84) only in the first two modulation periods, significantly more HDO is formed than in the following periods. The signal for D_2O, on the other hand, steadily increases. The same experiment with SiO_2 shows a different behavior, where signals for HDO and D_2O steadily increase (Figure A.85). As the hydroxyl groups in both materials are initially saturated with protons, these findings indicate fast exchange of protons/deuterons between EtOH/EtOD and Ta-BEA through direct exchange and/or the formation of an ethoxy species.[251] Note that this exchange is much faster for EtOH than, *e.g.*, for CA, due to the double bond in the α-position to the carbonyl that hampers enolate formation. Thus, these experiments should not be strongly obscured by direct H/D-exchange on the surface. After saturating the surface with EtOD, as observed with steady O-D bands in the IR spectra and steady MS signals, we performed the

same experiment as in Figure 4.6a, but with a 3:1 molar mixture of EtOD/CA. The signal for COD (m/z = 73) clearly follows the modulation (Figure 4.7a), indicating that EtOD is involved in the formation of this species.

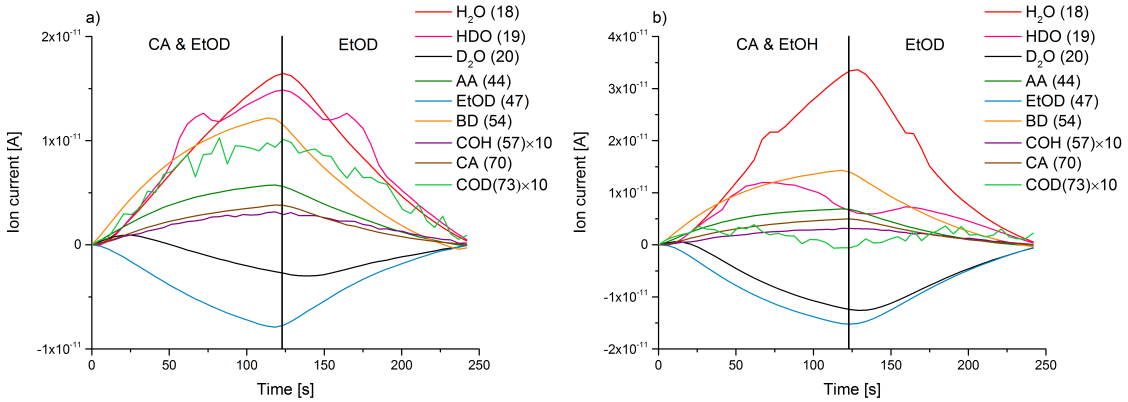

Figure 4.7: Modulation experiments between pure EtOD/EtOH in He and a 3:1 mixture of EtOD/EtOH/CA over Ta-BEA at 300 °C. a) shows the recorded MS signals of an experiment, where the surface was first saturated with EtOD followed by periodically switching to EtOD/CA. b) shows the recorded MS signals of an experiment, where the surface was first saturat-ed with EtOD followed by periodically switching to EtOH/CA. The switch from one flow to another was done after 120 seconds as indicated by the black line. Three periods were averaged when quasi steady-state was reached.

Also the signal for HDO that could be formed upon the dehydration of COD follows the same pattern. The signals for BD and AA follow the modulation as well, while D2O that could be formed upon the dehydration of EtOD to the byproduct diethyl ether,[252;253] shows a negative signal. DEE synthesis is supposedly going through an ethoxy intermediate over Lewis or Brønsted acids. Hence, the negative D_2O signal suggests the same intermediate responsible for BD production and DEE synthesis, *i.e.* that is, in the presence of CA, the ethoxy reacts with CA instead of another gas-phase EtOD molecule. When, on the other hand, first saturating the surface with EtOD and then switching to a CA/EtOH mixture (Figure 4.7b), the signal for COD is essentially a flat line and the other signals basically follow the same pattern as in Figure 4.6a. This observation suggests that the same surface

species is formed when saturating the surface with EtOD or EtOH and that the alcohol is transferring its proton/deuteron to CA to form COH/COD. Interestingly, the signal for HDO goes through two maxima. We attribute this observation to the formation of ethoxy species. When the surface is saturated with EtOD, surface Si-OH or Ta-OH are converted to Si-OD or Ta-OD, as can be seen by positive OD stretch vibrations at 2750 cm^{-1} (Figure A.89) and negative OH bands around 3750 cm^{-1}.[254] Upon switching to the other alcohol, the formation of an ethoxy produces HDO.

Proposed Mechanisms

As for any zeolitic material, the nature and distribution of active sites in Ta-BEA is highly complicated.[173;255] According to previous studies, Ta might be incorporated in different configurations into the framework.[169;256] Figure 4.8 shows three different sites that are relatively stable and could be present under reaction conditions. To simplify the discussion, we will focus on active site III, as this is the most stable one.

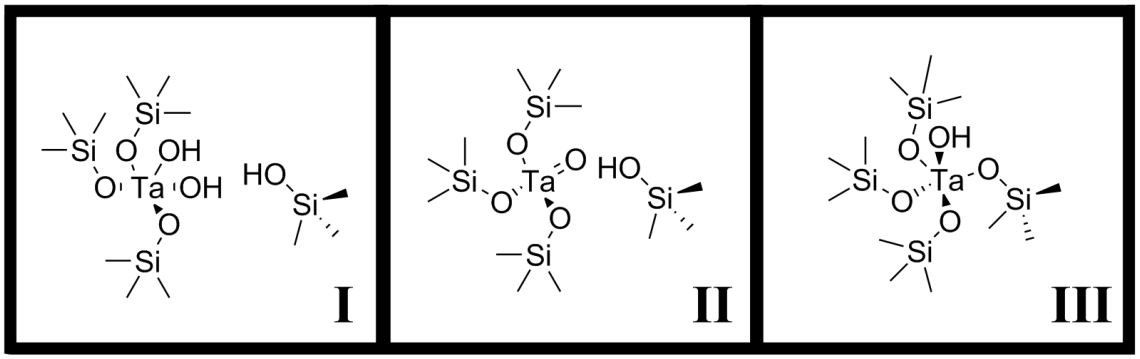

Figure 4.8: Environments of three relatively stable active sites in Ta-BEA.[169]

The first step in the reaction scheme for the two-step production of BD is the coupling of two acetaldehyde molecules. Taking active site III, a possible mechanism for this step is shown in Figure 4.9 on the left. First, two AA molecules coordinate to the Ta site ($0 \rightarrow 1$, $1 \rightarrow 2$) through hydrogen bonding. Then, the proposed

mechanism goes through an eight-membered ring transition state (2 → 3) and forms the unstable intermediate AOL that is quickly dehydrated to CA. A similar mechanism has been proposed for pure silica.[257;258] Another possibility for the coupling of AA would be the soft enolization mechanism on Lewis acid sites, as proposed for aldol couplings in the liquid phase over Sn-BEA.[259;260] As the active site in Sn-BEA is different[168] and breaking a Ta-O bond (Figure A.90) would lead to a less stable site,[169;256] it is not clear if this mechanism is valid for Ta-BEA as well. When adsorbing AA on Ta-BEA, the C=O stretch vibration of acetaldehyde does not shift significantly, which indicates only weak interactions with the catalyst. We also did not observe any significant IR signals originating from an enolate species. The coupling reaction can also occur on weakly acidic silanol groups, as reported in the literature.[261] Consistently, we observed CA formation when AA was adsorbed on SiO_2 (Figures A.77 and A.78). Furthermore, Davis *et al.* have recently shown[262] that C-H activation is not kinetically relevant over TiO_2, another widely studied catalyst for aldol coupling reactions.[263;264] Hence, we tend toward the mechanism in Figure 4.9 instead of a soft enolization mechanism. The pyridine and dTBPy adsorption experiments show more Brønsted acid sites at the external surface of the zeolite. Hence, it is likely that the coupling occurs over external/pore mouth Ta-OH groups, and/or external/pore mouth silanol groups that show enhanced acidity due to neighboring Ta atoms.[169;265;266] The IR spectra in the OH stretch region also show negative bands upon the adsorption of AA, corroborating such an interaction. Finally,the addition of EtOH (Figure 4.5a) does not significantly alter the AA signals in the C=O stretch region. Thus, it is unlikely that EtOH directly takes part in the coupling step. The second step, *i.e.* the MPV reaction between EtOH and CA, is thought to be catalyzed by tantalum.[232] It is well-known that ethoxy species can be formed on silica.[267] As we clearly show with our isotopic labeling experiments, such species also form on Ta-BEA and are involved in the formation of COH. Since Ta-OH sites are also more acidic than silanols,[169] the first step in our proposed MPV reaction mechanism is therefore the formation of an ethoxy species on a Ta site (4). Calculations showed that the Ta-OH stretch vibration in Ta-BEA is in the same region (ca. 3700-3800 cm^{-1}) as the Si-OH vibrations.[169]

Hence, a clear distinction between the two sites is not possible. However, upon the adsorption of EtOH, two negative signals at 3740 and 3745 cm^{-1} appear that could be attributed to Si-OH and Ta-OH and are indicative of their consumption. Furthermore, we observe the formation of water in the MS, corroborating the formation of structure 4. In a second step, CA coordinates to the Ta site, leading to intermediate 5. We attribute the C=O stretch vibrations at 1700-1722 cm^{-1} to this type of coordination of CA to Ta. The reaction would then go through a six-membered ring transition state, where hydrogen transfer leads to an adsorbed AA (6). AA can then desorb from the site, as observed in the MS, and potentially undergo coupling with another AA molecule itself. An incoming EtOH molecule displaces COH from the active site, closing the catalytic cycle ($7 \rightarrow 4$). Further evidence for this last step can be found in Figure A.87, where we performed a modulation experiment between pure EtOH and pure AA. Upon switching from EtOH to AA, BD production quickly goes through a maximum, as expected when surface-bound EtOH is consumed. However, upon switching back to EtOH, a change in slope of the BD signal can be observed, indicating the importance of EtOH in the desorption of COH. The final dehydration step to form BD occurs fast under reaction conditions, and no significant characteristic IR bands of BD were observed on the catalyst surface. When the surface is saturated with CA (Figures 4.6c and 4.6d) that is likely coordinated to the Lewis acidic Ta site, EtOH first has to displace CA from the site before it can undergo the reaction. Thus, only if a proper ratio of CA and EtOH is present, the catalyst performs well. Furthermore, the peak at 1690 cm^{-1} that we assigned to a strongly adsorbed CA species could be originating from a "crotoxy" (7) and is an important intermediate within the mechanism. This peak was also observed when coadsorbing methanol and CA (Figures A.91 and A.92) that also undergo MPV reaction and finally form BD, confirming this assignment. A similar mechanism has also been proposed for the MPV reaction of 2-propanol and cyclohexanone over ZrO_2.[268] It has been shown for Zr-BEA zeolites that the open sites, i.e. the partially hydrolyzed sites with one Zr-OH group, are more active in the production of BD.[269] Thus, an analogous mechanism to the one proposed in Figure 4.9 could also be valid for Zr-BEA zeolites and other Lewis acids. Taking all

the information and interpretations together, it appears that it is highly important to have precise control over the ratio of different adsorbed species in order to maximize the production of BD. A high AA concentration will lead to large amounts of CA, which will not react further. The additional water that is formed in the dehydration of AOL to CA shifts the equilibrium away from the reactive ethoxy species, reducing the contribution of the right catalytic cycle that forms BD. When, on the other hand, the EtOH concentration is too high, not enough CA will be produced, as the Ta sites will be covered with EtOH such that AA cannot react efficiently anymore. Hence, these findings explain why the BD productivity is so sensitive toward changes in the feed composition.[232;235;236] The influence of the ratio of EtOH/AA has been studied for different catalysts, and an optimal value was found to be around 3 for most of them.[235;236;250] The ratio needs to be this high to maintain a high ethoxy coverage even when water is produced in the dehydration steps and to desorb COH from the surface of the catalyst to close the catalytic cycle.

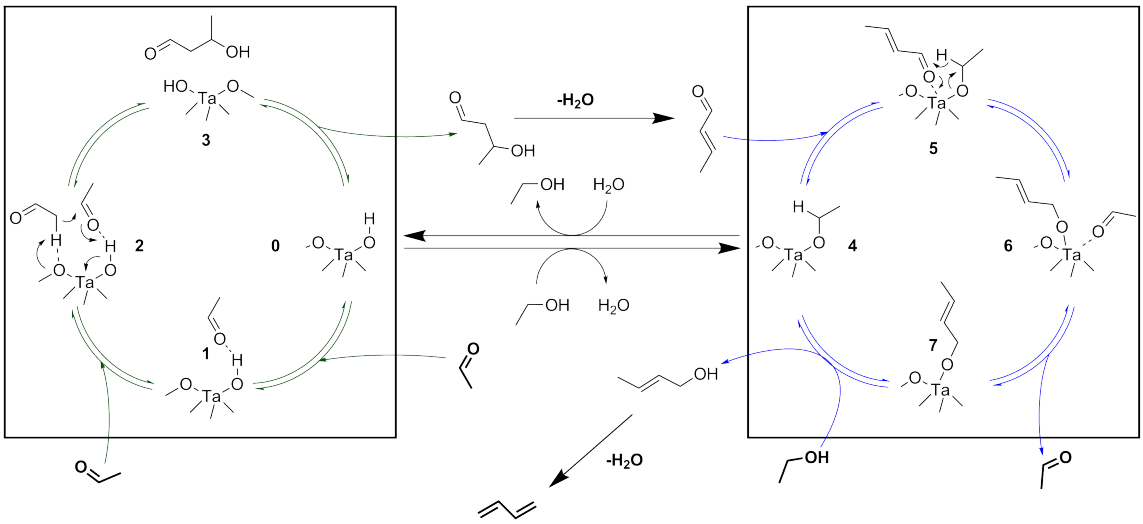

Figure 4.9: Tentative mechanism of the coupling of acetaldehyde over Ta-BEA on the left, followed by the MPV reaction between EtOH and CA on the right. The molecules represented in bold show the overall stoichiometry of the reaction: 2 AA + EtOH $\rightarrow$ BD + AA + 2 H_2O

4.3 Conclusions

In conclusion, we have studied the reaction mechanism for the coupling of EtOH/AA to form BD over Ta-BEA. According to UV-vis and *in situ* IR measurements, the catalyst consists of isolated, mostly Lewis acidic, tantalum sites. *In situ* EXAFS experiments further show that the active site does not change under reaction conditions when EtOH or a mixture of EtOH/AA is present. We developed an *operando* DRIFTS-MS setup that enables precise control and analysis of changes in the gas phase composition as well as studying adsorbed species under reaction conditions. Modulation experiments helped us analyze the different consecutive reaction steps. The generally accepted reaction pathway, *i.e.* first AA coupling to form CA, followed by an MPV reaction of CA with EtOH to form COH that undergoes dehydration to form BD, seems to be valid. For the first time, we propose molecular-level reaction mechanisms for the Ta catalyzed reaction that is in line with our new data. These findings explain why the BD productivity is sensitive toward changes in the EtOH/AA ratio. An optimal value for this ratio is around 3 in order to maintain a high ethoxy coverage and to efficiently desorb the intermediate COH from the surface of the catalyst. The gained insights might also be relevant for other recently developed zeolite catalysts such as Zr-BEA.

4.4 Experimental Details

Materials Synthesis

The Ta-BEA catalyst was prepared according to a reported postsynthetic preparation.[163] Dealumination of the parent commercial Al-Beta zeolite (Zeolyst, SiO_2/Al_2O_3 = 25) was done by acid leaching (13 M HNO_3, 20 mL g^{-1}, 373 K, 20 h). After filtering and drying at 373 K overnight, tantalum was incorporated by stirring 2 g of deAl-BEA for 3 h at 353 K in 100 mL of an isopropanol solution containing 2.2 $\cdot 10^{-3}$ mol L^{-1} tantalum ethoxide in dry isopropanol. Then the suspension was stirred for 1 h in air at 353 K until the solvent had completely evaporated. The solid

was filtered off, washed three times with water, dried in air at 353 K overnight, and finally calcined at 723 K for 3 h.

Characterization

The different materials were analyzed with various techniques: Si, Al, and Ta contents were determined by ICP-OES after digesting the solids in HF. The small-angle powder XRD-patterns for calcined samples were recorded under ambient conditions on a Bruker D8 advance diffractometer with Cu Kα radiation (λ = 1.5406 Å). N_2-physisorption measurements were performed on a Micromeritics 3flex apparatus. The samples were degassed prior to measurement for 4 h at 373 K. Adsorption isotherms were collected at 77 K and analyzed using the BET method. DRUV-vis analysis was performed with a Maya2000 Pro spectrometer (Ocean Optics) equipped with a deuterium/halogen light source (DH-200-BAL from Mikropack) using $BaSO_4$ as matrix. Intensities are given in Kubelka-Munk units and normalized. X-ray absorption near-edge spectra (XANES) and extended X-ray absorption fine structure (EXAFS) spectra were obtained at the Ta L_3-edge (9.8762 keV) using bending magnet station B at sector 20 of the Advanced Photon Source beamline (20-BMB) at Argonne National Laboratory. The beam energy and detector were calibrated to the Ta L_3-edge using pure tantalum foil. The beam energy was controlled using a Si(111) monochromator with $1.4 \cdot 10^{-4}$ eV resolution. Samples were pressed into self-supporting wafers, and the sample holder was sealed in a quartz tube fitted with Kapton windows on either end. The quartz tube was then heated in a tube furnace while flowing He at 20 mL/min. A flow rate of 5 μL/min of EtOH or a 3:1 EtOH/AA mixture was introduced into the system with a syringe pump and evaporated before contact with the sample. A mass spectrometer was attached to the outlet of the quartz tube to monitor the gas-phase composition. All spectra were collected in transmission mode. XANES and EXAFS spectra were normalized and energy calibrated with the Athena XAS analysis software. The edge energy was determined as the maximum of the first derivative of XANES spectra, plotted against energy. EXAFS spectra were plotted

in R-space using the Athena software. This first computes $\chi(E) = \frac{\mu(E)-\mu_0(E)}{\Delta\mu_0(E)}$, using values directly obtained from XANES spectra. (E) can simply be converted to χ(k) using $k = \sqrt{\frac{2m(E-E_0)}{\hbar^2}}$, where m is the mass of an electron and $\hbar$ is Planck's constant. Taking the Fourier transform converts (k) to χ(R). The real portion of this function ($|\ \chi(R)\ |$) is plotted in the SI. All IR measurements were performed on a Bruker Vertex 70 spectrometer equipped with a liquid nitrogen cooled MCT detector. Typically 64 scans with a resolution of 4 cm^{-1} were coadded to give one spectrum. The intensities for the *operando* IR spectra are given in Kubelka-Munk units. Pyridine adsorption was performed in a home-built stainless steel IR accessory. The samples were pressed into self-supporting wafers, loaded into the accessory, and outgassed at 573 K and 10^{-6} mbar for 1 h. Then, pyridine was adsorbed at room temperature for 5 min, followed by flushing with N_2 for 15 min. The sample was heated to the desired temperatures, where the temperature was held for 15 min and a spectrum was taken. The blank catalyst was subtracted and the spectra were baseline-corrected using the OPUS software package (OPUS 7.2, Bruker Optik GmbH). An overview of the Modulation Excitation setup is given in Figure 4.4. The mass flow controllers (Brooks 5850E) were operated with a control unit (Brooks, Model 5876). The liquids were introduced using syringe pumps (Fusion200, Chemyx). The flow rate for the carrier gas (He) was 25 mL/min, and the liquid flow rate was 5 µL/min. The switching between the different flows was achieved with a two-position-four-way valve (VICI GC valve), that was controlled with a two-position actuator control module (VICI). The DRIFTS accessory was purchased from Pike Technologies (DiffusIR) and equipped with an environmental chamber that can be connected to 1/8“ stainless steel tubing. All of the tubing was kept in stainless steel and heated with heating tape to 130 °C. Ca. 5 mg of catalyst was loaded in a ceramic crucible. The gas-phase composition was monitored online with a mass spectrometer (ThermoStar, Pfeiffer Vacuum). The dead volume was kept as small as possible to avoid backmixing and delays in the signals. Temporal resolution was one spectrum/MS data-point every 3-4 s. The analysis of the spectra was performed using MATLAB codes that were written in-house and plotted in Origin.

5 INFLUENCE OF METAL-DOPING ON THE LEWIS-ACID CATALYZED PRODUCTION OF BUTADIENE FROM ETHANOL STUDIED BY MODULATED OPERANDO DRIFTS-MS

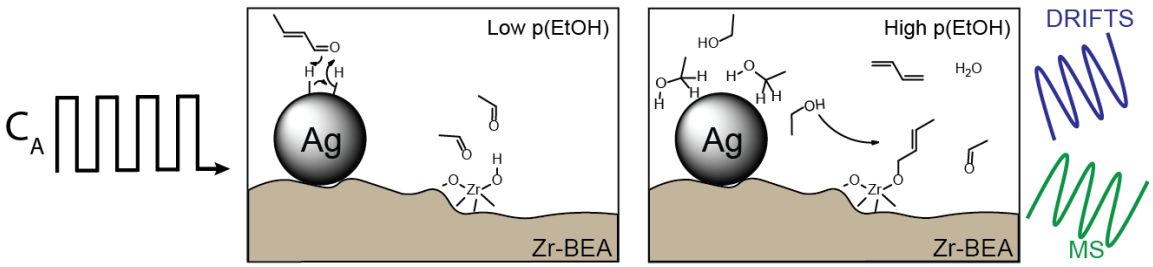

In this chapter we took a step further to understand the Lewis acid catalyzed conversion of ethanol into 1,3-butadiene. By adding a metal promoter to the Lewis acidic zeolite, the catalyst is able to dehydrogenate ethanol to acetaldehyde and hence directly converts ethanol to 1,3-butadiene. It was, however, unclear if the metal also had an influence in other reaction steps. Hence, we investigate this system with the setup developed and applied in Chapter 4. Submitted to ChemCatChem.[270]

5.1 Introduction

The desire for more sustainable manufacturing technologies - preferably from renewable resources - initiated significant research in the utilization of biomass-derived feedstocks using heterogeneous catalysis.[178;224;271;272] The coupling of ethanol (EtOH) to 1,3-butadiene (BD) - an important polymer precursor with a yearly production volume of >10 Mt - is a historically important example that is currently attracting renewed attention.[217;218;222;223] Traditionally, BD is obtained as a by-product in ethylene production *via* steam cracking. The trend towards the use of lighter feedstock (*i.e.* shale gas) for steam cracking results, however, in a lower BD production which affects its price volatility and the supply of BD.[222] Hence, a flexible drop-in process producing renewable BD would offer several advantages. EtOH

has already been recognized as a convenient feedstock to produce BD in the early 20th century, *i.e.* prior to the large-scale implementation of cracking technology. During World War II, Union Carbide and Carbon Corporation produced up to 0.3 Mt of BD from EtOH per year.[273] After World War II, naphtha cracking outcompeted this route. However, with the recent changes in cracking feedstock, as well as the increased production of biomass-derived ethanol, interest in the EtOH coupling has been sparked again and research efforts are devoted to it. In order to make the technology (again) economically attractive, we need to further improve the selectivity. Fundamental understanding of molecular level interactions of reactants and intermediates with the catalyst surface using sophisticated *operando* spectroscopic tools might help to further improve the performance and make this approach economically viable.

BD can be produced from EtOH using two different approaches that use different catalysts ranging from solid bases to solid Lewis acids.[228–230;232;233;236] In the one-step process, catalysts directly use EtOH as a feedstock, while in the two-step process, AA needs to be co-fed because Lewis acid sites are not able to dehydrogenate EtOH to AA. It is thus possible to transform a two-step catalyst into a one-step catalyst and to utilize EtOH directly, by simply adding a dehydrogenation functionality. This concept has been applied for Lewis acidic Zr-BEA and Ta-BEA zeolites that were doped with Ag and Cu,[230;237;274] but also the more traditional one-step SiO_2-MgO system has been doped with Ag, Cu, and Zn.[241;275–277] In both cases the metal addition lead to improved activity and selectivity toward BD as shown in Table 5.1 for some examples with silver.

Table 5.1: Catalyst performance for selected silver-doped catalysts in the direct conversion of EtOH.

Catalyst	Conversion [i]	BD selectivity [ii]	BD yield [iii]	reference
Ag-Zr-BEA	0.324	0.672	0.218	[237]
Ta-BEA	0.133	0.164	0.022	[274]
Ag-Ta-BEA	0.829	0.626	0.519	[274]
$MgO\text{-}SiO_2$	0.100	0.360	0.036	[275]
$Ag\text{-}MgO\text{-}SiO_2$	0.440	0.460	0.202	[275]

The reaction mechanism is particularly complex because it consists of many reaction steps that proceed over different catalyst functionalities. The generally accepted pathway is displayed in Figure 5.1.[222;233]

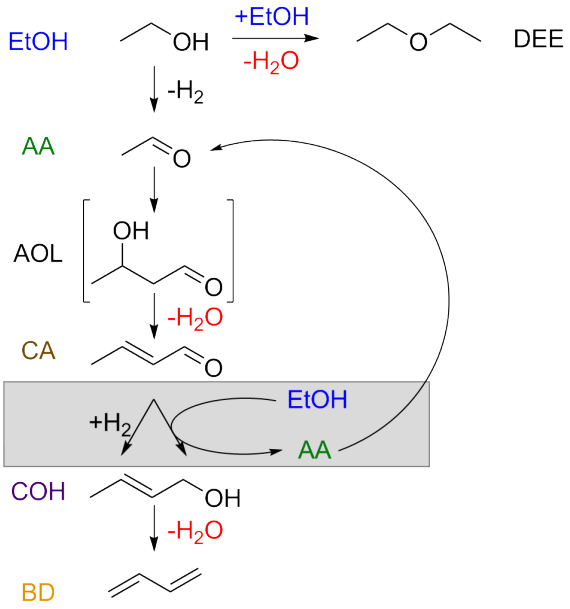

Figure 5.1: Generally accepted reaction pathway for the coupling of ethanol to 1,3-butadiene.

[i] defined as moles of EtOH consumed divided by moles of EtOH fed
[ii] defined as moles of BD produced per 2 moles of EtOH consumed
[iii] defined as conversion multiplied by selectivity

EtOH gets dehydrogenated to acetaldehyde (AA) that couples with another AA molecule to give the instable intermediate acetaldol (AOL) that is easily dehydrated to form crotonaldehyde (CA). Then, CA is transformed into crotyl alcohol (COH) either through a Meerwein-Ponndorf-Verley (MPV, right) reaction with EtOH forming AA, or through direct hydrogenation of the aldehyde (left). A final dehydration step produces BD. Alternatively, EtOH can get directly coupled with another EtOH molecule to form the by-product diethyl ether (DEE), releasing water. Other by-products such as ethylene, propylene, and trienes have also been observed.[230] While avoiding the formation of such products is important to maximize the selectivity, we focus on the major pathways in this manuscript.

We have recently studied the Lewis acidic two-step catalyst Ta-BEA and put forward a molecular level description of the reaction mechanism.[97] The mechanism over Zr-BEA, on the other hand, has not been studied in detail yet. Also, the influence of the added metal in Lewis acidic one-step catalysts, in our case Ag-Zr-BEA, on the reaction mechanism has not been rigorously studied yet. Its primary role is most likely the dehydrogenation of EtOH to AA. But the addition of Ag might also open up other reaction pathways. For instance, it could be possible to directly hydrogenate the aldehyde functional group in CA instead of performing the MPV reaction with EtOH as shown in the grey box in Figure 5.1. It has been reported that Ag-SiO_2 can be used as catalyst for the hydrogenation of acrolein with H_2, predominantly forming allyl alcohol. Furthermore, Ag deposited on other supports such as TiO_2 have been used as catalysts for CA hydrogenation with H_2, predominantly yielding crotyl alcohol over butyraldehyde.[278–280] Hence, it is possible that the direct hydrogenation of CA takes place under reaction conditions over metal-doped Lewis acid catalysts as well. The additional Ag particles might also influence the formation of by-products, such as the fully hydrogenated butanol that could be formed from COH. In the present work, we hence investigate the influence of Ag addition to a Lewis acidic Zr-BEA catalyst. First, we characterize the material thoroughly using Inductively Coupled Plasma - Optical Emission Spectroscopy (ICP-OES), N_2-physisorption, NH_3 Temperature Programmed Desorption (TPD), UV-vis spectroscopy, X-ray Photoelectron Spectroscopy (XPS), and Fourier

Transform Infrared spectroscopy (FTIR) of adsorbed pyridine. Then, we perform an *operando* Diffuse Reflectance Infrared Fourier Transform Spectroscopy - Mass Spectrometry (DRIFTS-MS) study to investigate the reaction mechanism with a setup that allows to simultaneously monitor dynamic changes on the catalyst surface as well as the product distribution in the gas phase. To do so, we use a modulation approach that simplifies our understanding of the origin of consecutive reaction products compared to steady-state studies. Finally, we propose a mechanism that rationalizes the influence of Ag addition to Zr-BEA, which is likely generally valid for metal-doped Lewis acid catalysts.

5.2 Results & Discussion

Material Synthesis and Characterization

Throughout this study we investigate three different catalysts. The Zr-BEA was prepared using a post-synthetic procedure, starting from a commercially available Al-BEA zeolite that was dealuminated and then subjected to a liquid phase impregnation with $ZrOCl_2$ in DMSO.[281] After calcination, this sample was impregnated with an appropriate amount of aqueous silver nitrate solution (incipient wetness impregnation) giving the sample denoted as Ag-Zr-BEA with loadings of 2.2 wt% Zr and 0.8 wt% Ag. For comparison, we furthermore impregnated silica with Ag, resulting in the sample denoted as Ag-SiO_2 with 1.0 wt% Ag. The key characteristics of these catalysts are summarized in Table 5.2. The BET surface area slightly decreases upon Ag incorporation, while leaving the microporous network intact. The number of acid sites determined with NH_3-TPD (Figure A.94) also decreases when Ag is added and might arise from filling up some remaining silanol nests within Zr-BEA with Ag(I), as has been previously shown by Dzwigaj *et al.*[282;283] As expected, Ag-SiO_2 possesses a low number of weakly acidic sites. FTIR of adsorbed pyridine was used to determine the ratio of Lewis to BrÃ¸nsted acid sites. The absence of a significant peak at 1545 cm^{-1} upon adsorption of pyridine that is assigned to the pyridinium ions that form over BrÃ¸nsted acid sites, indicates that

in all samples mainly Lewis acid sites are present (Lewis/Brønsted ratios >10, see Figures A.95a, A.95b, A.95c).

Table 5.2: Key characteristics of the synthesized catalysts.

Catalyst	Ag content [iv]	Zr content [wt%][i]	S_{BET} [v]	V_{micro} [vi]	S_{ext} [vii]	N_{acid} [viii]
Ag-SiO_2	1.0	-	255	0.01	233	49
Zr-BEA	-	2.1	715	0.22	250	261
Ag-Zr-BEA	0.8	2.2	686	0.22	240	180

To study the electronic state of the silver particles in these materials, we measured UV-vis spectra of our catalysts, as shown in Figure 5.2. The band centered around 220 nm in the Zr-BEA sample can be assigned to ligand-to-metal-charge-transfer of neighboring oxygen atoms to isolated Zr(IV) centers and is indicative of a successful Zr incorporation.[284] When silver is added to this sample, much stronger bands centered around 245 nm superimpose the Zr band. Signals below ca. 230 nm can be assigned to Ag(I), while bands up to ca. 320 nm are assigned to small positively charged clusters. Absorbance above 320 nm is indicative of metallic Ag(0) and plasmonic resonances.[285] Hence, mainly small clusters of slightly oxidized Ag are present in our samples. Upon reduction, the Ag(I) band gets smaller but does not completely disappear and an additional broad peak in the Ag(0) region appears, indicating non-complete reduction of Ag in the system. There are small differences in the position and shape of the Ag(0) bands, but Ag remains mainly metallic under reaction conditions irrespective of the used carrier gas (Ag-Zr-BEA sHe for catalyst spent in He for 90 minutes and Ag-Zr-BEA sH_2 for catalyst spent in H_2 for 90 minutes in Figure 5.2).

XPS was also used to study the oxidation state of Ag and Zr. The Zr 3d photoelectron spectra are given in the appendix (Figure A.96). The calcined Zr-BEA shows a signal at 184.3 eV, which is higher than previous literature spectra for

[iv] [wt%] as determined from ICP-OES
[v] BET surface area from N_2 physisorption [m^2/g]
[vi] micropore volume [cm^3/g]
[vii] external surface area [m^2/g]
[viii] from NH_3-TPD [$\mu mol/g$]

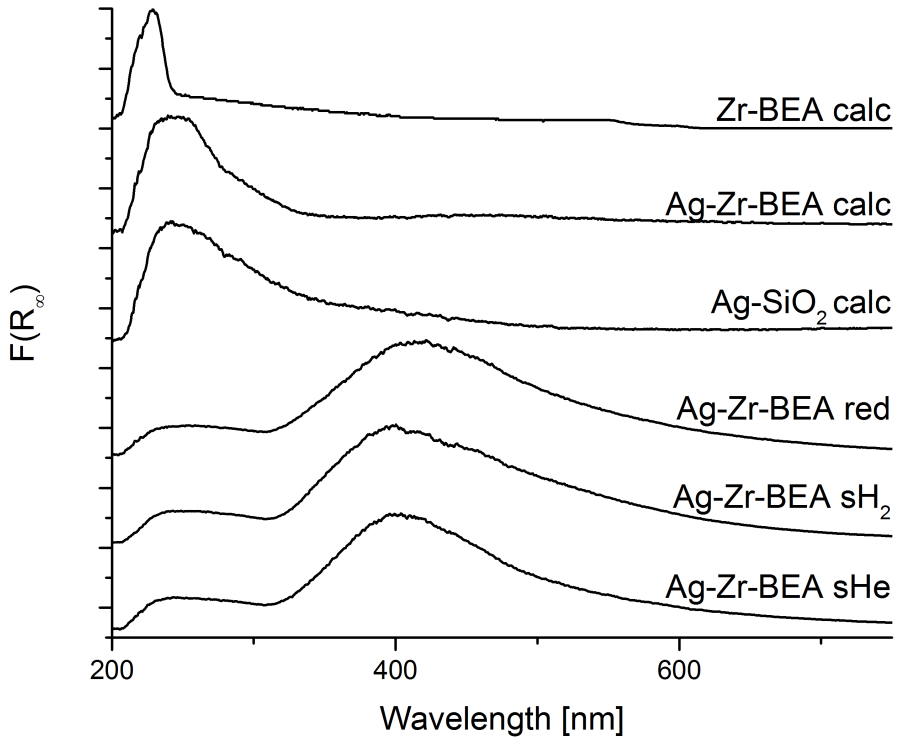

Figure 5.2: UV-vis spectra of the three synthesized catalysts measured under ambient condition. Ag-Zr-BEA was pre-treated for 30 minutes in a H_2 flow (Ag-Zr-BEA red), followed by an ethanol treatment under reaction conditions for 90 minutes (Ag-Zr-BEA sHe), and modified reaction conditions by using H_2 as carrier gas (Ag-Zr-BEA sH_2). The spectra are normalized to the biggest signal in each spectrum.

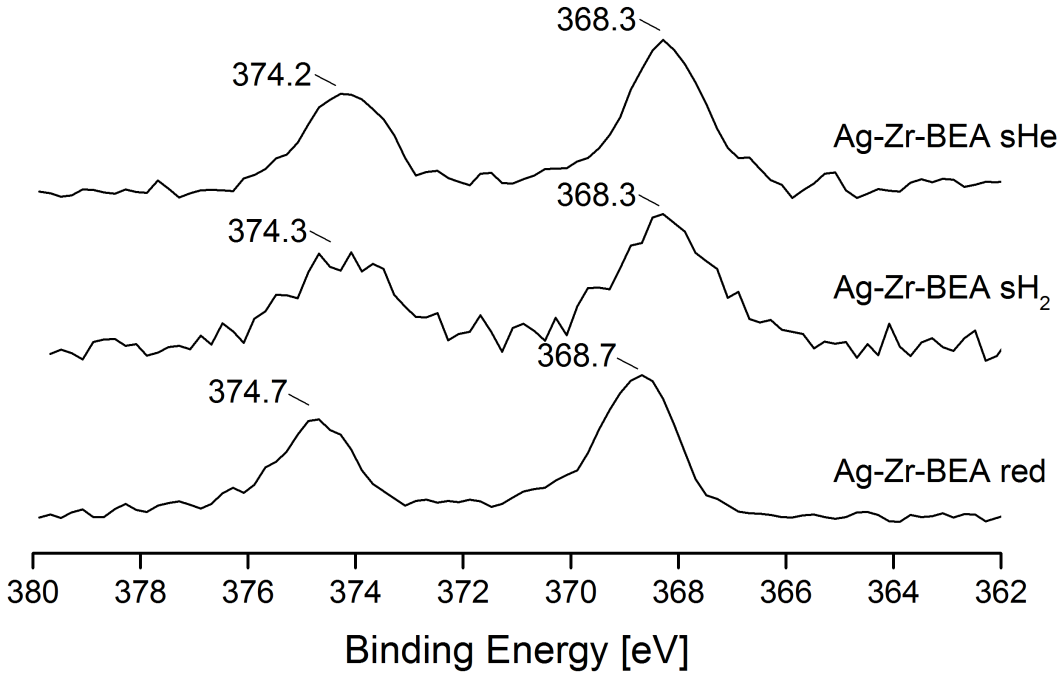

Figure 5.3: XPS spectra of the 3d photoelectron lines for Ag-Zr-BEA treated under different conditions.

hydrothermal Zr-BEA[286]. It is possible that the post-synthetic preparation method leads to slightly different Zr sites as has been observed with Sn-BEA zeolites before.[174] The addition of Ag shifts the BE downward to 184.0 eV. The spent catalysts are shifted even further to 183.8 eV indicating a slightly more reduced Zr species. This shift could be induced by the formation of ethoxy/crotoxy species on Zr-OH sites, or coke, or a change in the electronic structure of the Ag particles as will be discussed next. Upon recalcination the signal shifts back to the initial position at 184.3 eV, potentially restoring Zr-OH by burning of organic species.

In Figure 5.3 the Ag XPS spectra are shown for Ag-Zr-BEA treated under different conditions. The reduced catalyst shows $3d_{3/2}$ and $3d_{5/2}$ photoelectron lines at BEs of 368.7 and 374.7 eV, respectively. These values are shifted to higher binding energies compared to Ag-SiO_2 (see Figure A.96) or bulk Ag, which can be explained by

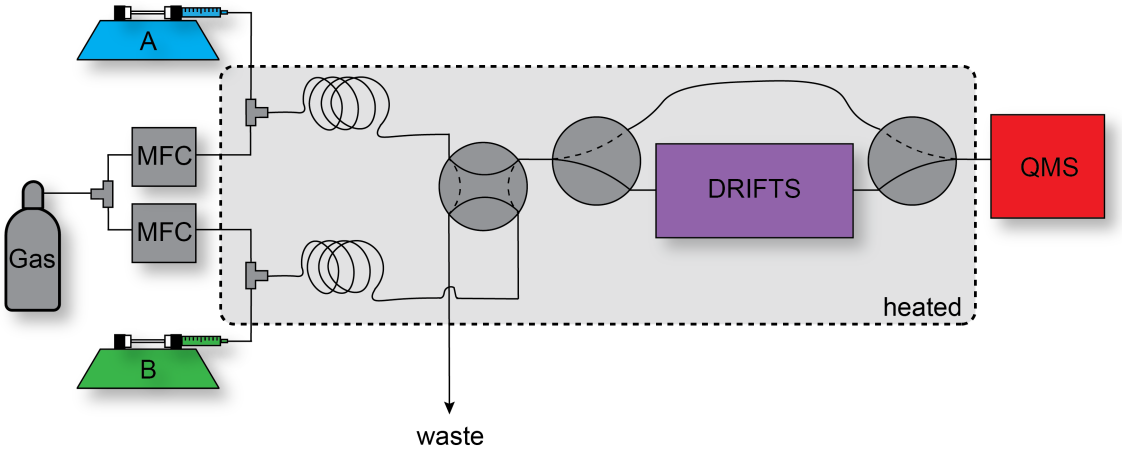

Figure 5.4: Schematic overview over the DRIFTS-MS setup. Gases are connected to two individual mass flow controllers. Two liquid pumps deliver substrates into heated spiral, where evaporation takes place and the two-position-four-way-valve selects substrate A or B to pass over the catalyst in the DRIFTS accessory. An online quadrupole mass spectrometer continuously collects spectra at the reactor outlet.

weaker core hole screening for small nanoparticles. Furthermore, the support can induce both initial and final state effects depending on the conductivity and the core hole screening by the support.[287] Generally, the silver core level BE decreases when oxidized. In our case the spent catalysts show a slightly lower BE, indicating partial oxidation of the silver particles. When the spent catalysts are calcined a second time, the BEs return to their initial positions (see Figure A.97).

Operando DRIFTS-MS Modulation Experiments

To further investigate the reaction mechanism, we used an *operando* DRIFTS-MS setup that is represented in Figure 5.4 and that we described in detail previously.[97]

In short, a two-position-four-way-valve allows for a quick change in the gas-phase composition that flows over a heated catalyst bed in the DRIFTS accessory. At the outlet of the accessory, an online mass spectrometer continuously collects spectra. The whole apparatus is heated to avoid condensation of liquid products. Two independent mass-flow controllers and syringe pumps enable evaporation of liquid

substrates and precise control over the gas-phase concentrations. By periodically switching between two different flows, the influence of certain components on the reaction mechanism can be followed in a dynamic fashion. This approach, known as modulation excitation spectroscopy (MES), has been used for heterogeneous liquid-phase and gas-phase catalysis before.[1] In a standard experiment, the catalyst is heated to reaction temperature (320 °C) under a He flow and then pre-reduced for 30 minutes under H_2. The catalyst is then subjected to the initial flow A (given in the right hand side in the following MS figures) until steady signals from the IR and the MS are achieved. Then, the modulation experiment starts, by switching to flow B for 120 seconds (left hand side in the following MS figures) and back to A for 120 seconds, while continuously acquiring IR and MS spectra. This procedure is repeated several times until a quasi-steady state is reached at which point the spectra of 3-12 of these periods are collected and averaged to improve the signal-to-noise ratio. After averaging the spectra, the first spectrum is taken as reference and the relative changes compared to the reference are shown.

Modulation Experiments with Zr-BEA

Figure 5.6 displays the results of an MES experiment for Zr-BEA. The catalyst was first saturated with EtOH, followed by periodically switching to a 3:1 mixture of EtOH/AA, a ratio that has been shown to be optimal for BD production over Ta-BEA.[236] The displayed m/z values have been chosen based on their MS fragmentation patterns while avoiding contributions from other compounds (see Table A.6 for details). As expected for a purely Lewis acidic catalyst, the addition of AA is required for a significant production of BD; using pure EtOH mainly leads to the by-products DEE and ethylene (MS signals not shown).[236] When switching back from the mixture to pure EtOH, the BD signal rapidly decreases and ultimately reaches zero. The signals for the intermediates, CA and COH follow a similar pattern as BD, indicating that they are part of the same reaction pathway. The results of this experiment, together with additional data given in the supporting information (see Figures A.98, A.99, A.100), show very similar patterns to Ta-BEA

and suggest that the general pathway of BD formation over these different Lewis acid catalysts is very similar. It has been suggested that the open site in Zr-BEA, *i.e.* a Zr(IV) ion in tetrahedral framework position, where one bond is hydrolyzed to form a Zr-OH group, is more active in the coupling of EtOH to BD.[269] Together with the similar spectroscopic patterns, it is hence likely that our proposed mechanism for Ta-BEA that is based on a Ta-OH group is valid for Zr-BEA as well. In this mechanism, an ethoxy group is formed on the open site and then gets exchanged with an incoming CA molecule to form a "crotoxy" intermediate with a distinct IR signal at 1690 cm^{-1} (Structure 3 in Figure 5.5) that gets exchanged with EtOH again to form COH.[97] This mechanism might also explain the observed shift in the Zr 3d XPS signals for the spent catalysts. As discussed earlier, the change from a Zr-OH to a Zr-ethoxy or Zr-crotoxy species might lead to such a subtle but significant shift.

In the case of Zr-BEA (Figure 5.6 b), the IR signal for the crotoxy species is observed at 1693 cm^{-1} instead of 1690 $cm^{-1}$for Ta-BEA, possibly due to differences in the acid strength of Ta and Zr. The signals originating from C=O stretch vibrations of AA and CA can be observed at higher wavenumbers (1710 cm^{-1} - 1760 cm^{-1} also see Table A.6 for an assignment of important vibrations). A stronger bond to the surface weakens the C=O band shifting the frequency down, which is why the "crotoxy" intermediate is expected to vibrate with a lower frequency than gas-phase or physisorbed CA. The positive signals between 2700 and 2850 cm^{-1} can be assigned to C-H stretch vibrations from adsorbed AA and CA. The negative signals above 2900 cm^{-1} can be assigned to C-H stretch vibrations of COH and predominantly EtOH that desorb or get consumed in the first half-period. A weak negative signal around 3745 cm^{-1} that can be assigned to Si-OH vibrations appears to be more negative in presence of AA, suggesting only a weak interaction of AA with surface Si-OH (or Zr-OH) groups.

Modulation Experiments with Ag-SiO_2

As shown in Figure 5.7, the adsorption of EtOH to Ag-SiO_2 enables the dehydrogenation of EtOH and forms AA. However, the MS signal for crotonaldehyde is

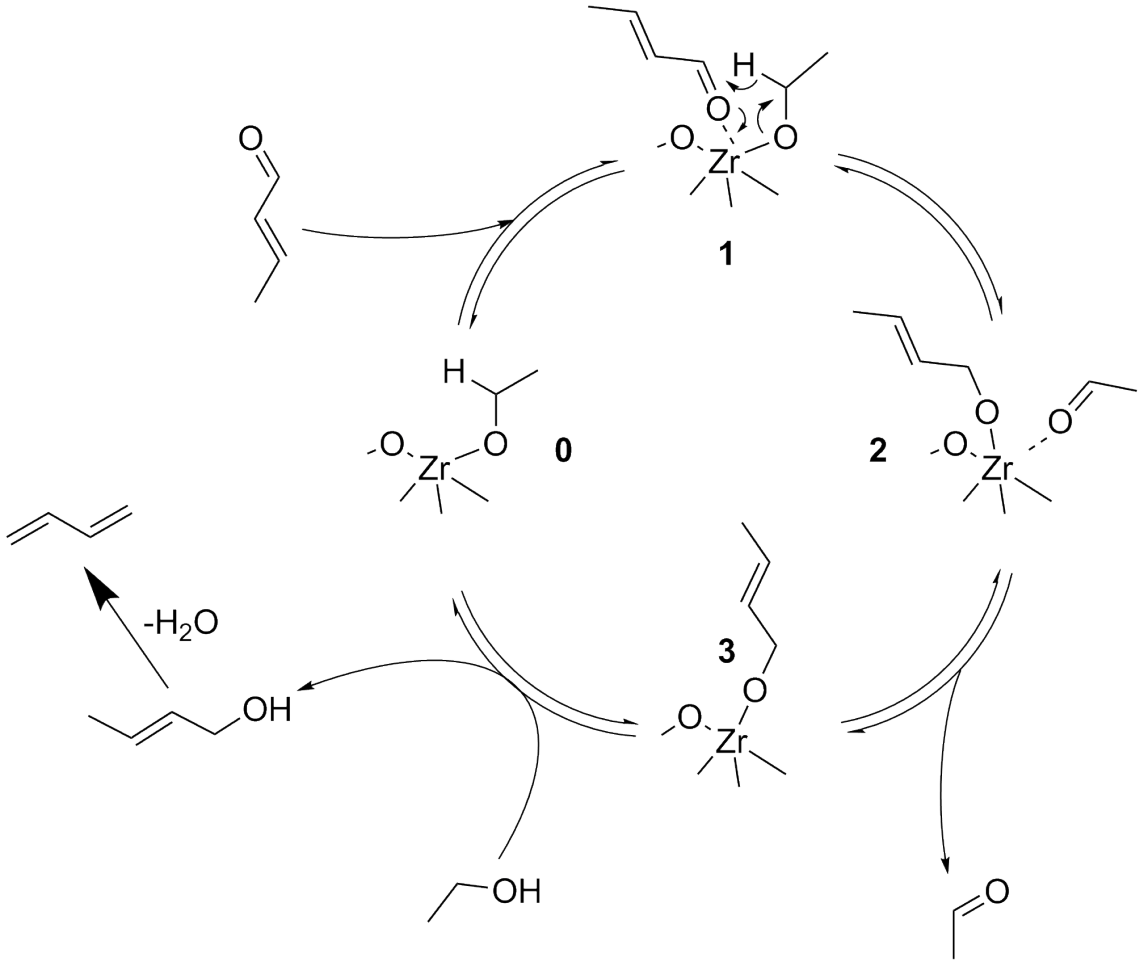

Figure 5.5: Proposed mechanism for the Meerwein-Ponndorf-Verley reaction of CA and EtOH over Lewis acid catalysts.

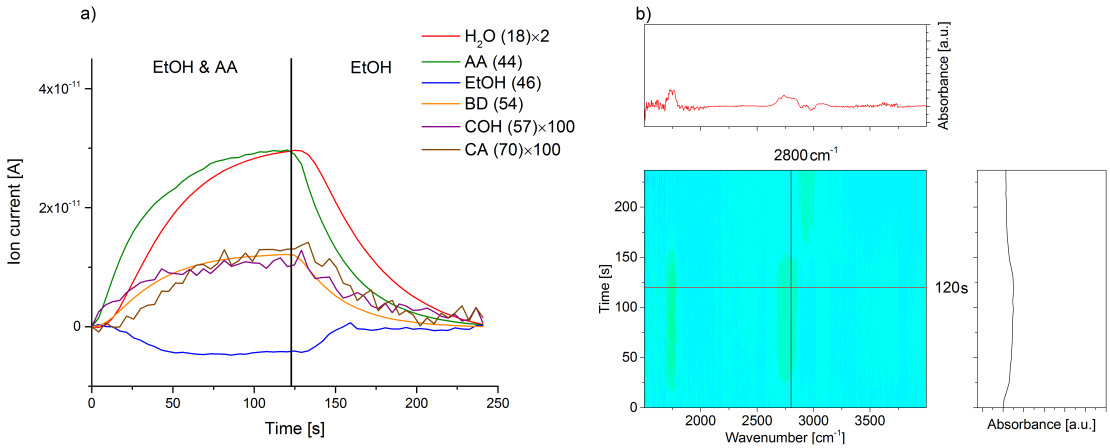

Figure 5.6: Modulation experiment between EtOH in He and a 3:1 mixture of EtOH/AA over Zr-BEA at 320 °C. The figure on the left (a) shows the recorded MS spectra of selected m/z signals and the figure on the right (b) shows the corresponding surface IR spectra. The black line corresponds to the time at which the gas streams are switched.

almost a flat line, indicating insufficient coupling activity. Also, signals from COH and BD are essentially zero, clearly showing that an acid functionality is required to go further than AA in the reaction pathway. In the IR spectra, no significant signals in the C=O stretch region could be observed, indicating fast desorption of AA after its formation. A strong negative signal at 3745 cm^{-1} is indicative of consumption of Si-OH groups, *i.e.* together with the simultaneous appearance of positive signals in the C-H stretch region at 2900-3000 cm^{-1} it can be concluded that mainly inactive physisorbed ethanol or ethoxy species are formed.[267] The emergence of a broad IR band centered around 3250 cm^{-1} can be interpreted as Si-OH groups interacting with ethanol molecules physisorbed on the surface. In an in situ transmission FTIR study on Ag-SiO_2, where the catalyst was pressed into a wafer, exposed to EtOH vapor for 30 seconds and then kept at 373 K for 5 minutes, the production of AA could be observed by the emergence of a band at 1726 cm^{-1}.[288] The absence of this signal in our spectra exemplifies the importance of performing spectroscopic studies under reaction conditions. Neither in that study nor in our spectra, could we find an indication for Ag-H species that would be expected around 1800 cm^{-1}.[289]

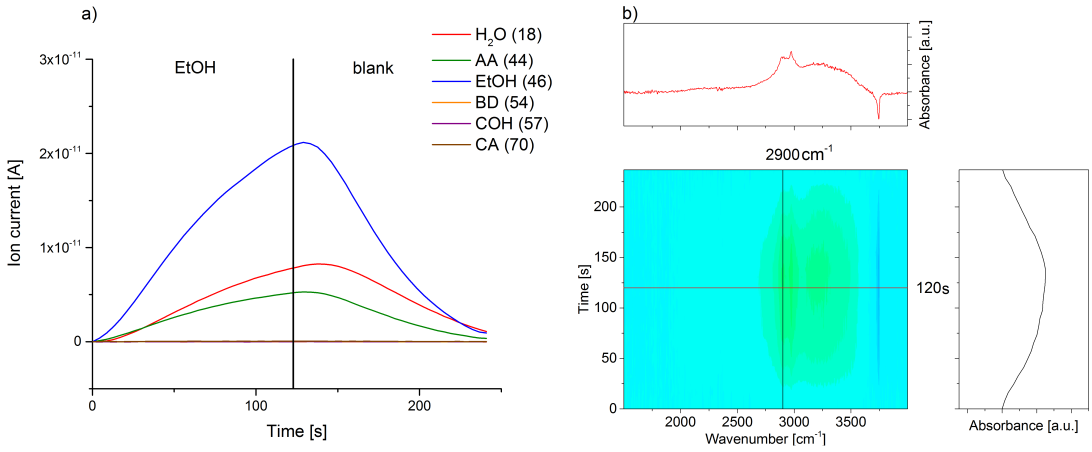

Figure 5.7: Modulation experiment between EtOH in He and pure He over Ag-SiO_2 at 320 °C. The left figure shows the recorded MS spectra of selected m/z signals and the right figure shows the corresponding surface IR spectra. The black line corresponds to the time at which the gas streams are switched.

Thus, AA and H_2 desorption are unlikely to be kinetically relevant steps.

Modulation Experiments with Ag-Zr-BEA

The previous modulation experiments showed that Zr-BEA follows a reaction mechanism similar to Ta-BEA and enables the formation of BD from a mixture of EtOH and AA. Ag-SiO_2 is able to dehydrogenate EtOH to AA, but the acid functionality is missing to go further in the reaction mechanism. When, on the other hand, Ag is incorporated in Zr-BEA (Figure 5.8), the reaction goes to completion and produces BD. Interestingly, the BD signal shows a maximum in the second half-period, indicating hindered desorption of either an intermediate or BD when the EtOH concentration is too high. As such behavior was not observed in the case of Zr-BEA where a mixture of EtOH/AA was fed, it is likely that the Ag is responsible for this. It might be that intermediates and/or BD adsorb to the Ag surface and the desorption only occurs at low EtOH pressures. The MS signals of COH and CA are relatively low and are almost constant throughout a modulation period. This is surprising as for the two-step catalysts Ta-BEA and Zr-BEA, the

MS signals for CA and COH were usually coupled, showing distinct signals and similar patterns. This result might be caused by a different rate-determining step compared to the two-step catalysts. It has been reported that for one-step catalysts such as SiO_2-MgO, the rate-determining step is the dehydrogenation of EtOH.[222;233] However, the fact that both EtOH and AA show significant signals might indicate that both the dehydrogenation and the coupling of AA are kinetically relevant steps in the reaction mechanism. The IR spectra in Figure 5.8 show similar results to the spectra of Ag-SiO_2 (Figure 5.7). Positive signals in the C-H stretch region for EtOH (2900-3000 cm^{-1}) and negative signals in the Si-OH region (3745 cm^{-1}) are visible and indicative of the formation of physisorbed ethanol or ethoxy species. However, the C-H signals are more intense compared to Ag-SiO_2 demonstrating the stronger binding of the ethoxy species on Zr-BEA. In the C=O stretch region around 1700 cm^{-1} no significant signals were observed. However, there is a small shoulder below 2900 cm^{-1} that is assigned to either CA or AA. Greenler's surface selection rule states that infrared vibrations with an oscillating dipole moment parallel to the metal surface for metal particles larger than 20 Å get suppressed.[290] Hence, it is possible that the reason for the absence of C=O stretch vibrations is the parallel adsorption mode of CA and/or AA on the Ag particles. When adsorbing AA to Ag-Zr-BEA, on the other hand, CA is formed but no COH (see Figure A.111). In the IR spectra, some C=O stretch vibrations are visible, but no signal around 1690 cm^{-1} that we assigned to the crotoxy intermediate. This further demonstrates the importance of EtOH in the formation of this intermediate, which seems to be crucial for BD production.

To study the effect of silver addition in more detail, we went a step further in the reaction pathway and investigated the conversion of CA to COH and finally BD. As mentioned in the introduction, due to the added Ag, it is possible to perform the direct hydrogenation of CA to COH. Thermodynamically, the alternative MPV reaction with EtOH and CA as reactant producing COH and AA is neutral, while the direct hydrogenation is unfavorable by about 35 kcal/mol.[222;291] Nevertheless, it is possible to use Ag as a hydrogenation catalyst for CA hydrogenation with H_2.[279] Accordingly, when CA is adsorbed to Ag-Zr-BEA under H_2 flow, COH and

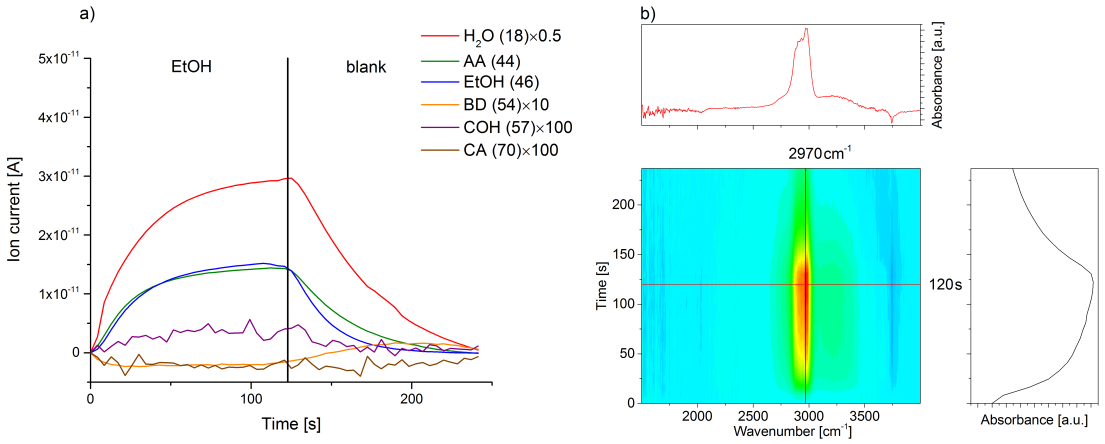

Figure 5.8: Modulation experiment between EtOH in He and pure He over Ag-Zr-BEA at 320 °C. The figure on the left (a) shows the recorded MS spectra of selected m/z signals and the figure on the right (b) shows the corresponding surface IR spectra. The black line corresponds to the time at which the gas streams are switched.

BD can be observed in the product stream (see Figure A.116). When deuterium is used as carrier gas, the Si-OH groups exchange to form Si-OD as can be seen by following the decrease at 3745 cm^{-1} and increase at ca. 2750 cm^{-1} (see Figure A.110). Upon the adsorption of CA under D_2 flow, the main products are now the singly and doubly deuterated COH and consequently the singly deuterated BD with a m/z = 55 (see Figure 5.9). However, irrespective of the carrier gas, the retro aldol condensation seems to take place as AA is formed in significant amounts as well.

To get further insight into the formation of COH, we modulated the EtOH concentration at a constant CA concentration over Ag-Zr-BEA with different carrier gases as shown in Figure 5.10. With He as carrier gas, the addition of EtOH leads to higher AA and BD formation. However, the COH concentration shows a reverse pattern, where the maximum is in the second half-period. Note that under He flow, the Ag mainly stays reduced as the XPS and UV-vis results suggested. Hence, the H_2 produced from the EtOH dehydrogenation can be used for the direct hydrogenation of CA as well.

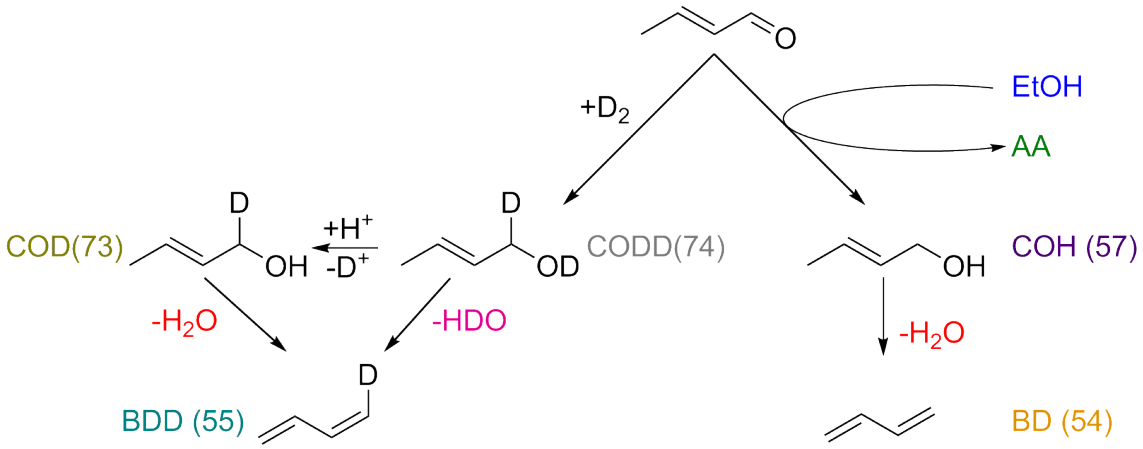

Figure 5.9: Possible reaction pathways for the formation of COH from CA. On the left, the pathway for the direct hydrogenation with deuterium is shown, while on the right the MPV reaction pathway is displayed. The numbers next to the molecule stand for their respective molecular masses.

The lower COH yield in the presence of EtOH can be explained by competitive adsorption on Ag sites. When suddenly the EtOH concentration is increased, the sites that used to produce COH through direct hydrogenation now perform EtOH dehydrogenation. On the other hand, the Zr sites are able to perform the MPV reaction and, unlike for the COH formed on the Ag particles, the (weak) acid sites required for COH dehydration are available in close proximity to where COH is formed, such that BD can readily be produced. Additionally, the MPV reaction is thermodynamically favored, leading to higher COH yield. In the IR spectra, negative signals in the C=O stretch region indicate consumption of adsorbed CA. Positive peaks in the C-H region above 2900 cm^{-1} indicate the adsorption of ethanol and formation of some ethoxy species on the catalyst surface. In the Si-OH and Zr-OH region, a negative signal can be observed, indicating consumption of these groups upon ethanol adsorption. Similar spectra have been obtained when H_2 was used as carrier gas (see Figure A.118).

In presence of deuterium as carrier gas, it is now possible to detangle the contributions of COH production from the direct hydrogenation and the MPV reaction.

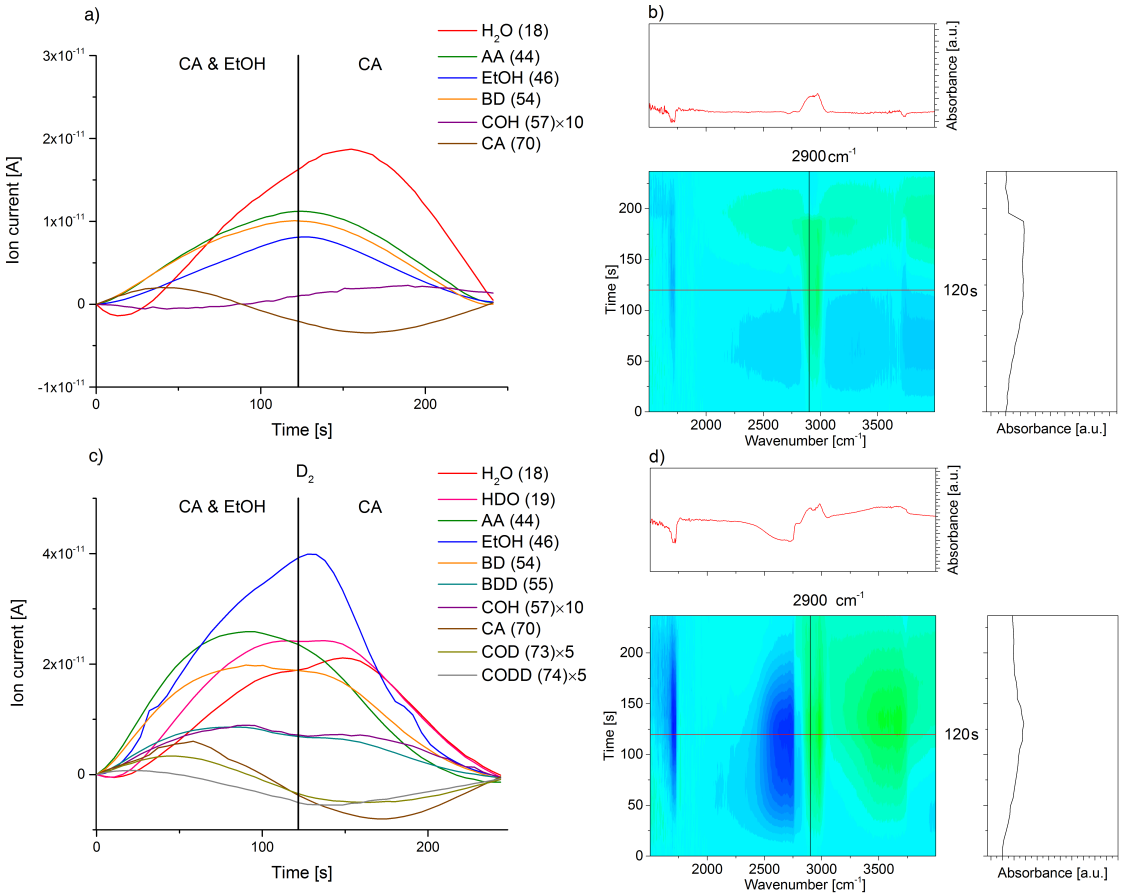

Figure 5.10: Modulation experiment between a 3:1 mixture of EtOH/CA in He and CA in He over Ag-Zr-BEA at 320 °C. The figure on the left (a) for He as carrier gas, c) for D_2 as carrier gas) shows the recorded MS spectra of selected m/z signals and the figure on the right (b) for He as carrier gas, d) for D_2 as carrier gas) shows the corresponding surface IR spectra. The black line corresponds to the time at which the gas streams are switched.

As shown in Figure 5.9, the direct hydrogenation product gives the doubly deuterated crotyl alcohol (CODD) with a signal at m/z = 74. Due to the presence of water, and easily exchangeable Si-OH and Si-OD groups, it is likely that the singly deuterated crotyl alcohol (COD) is formed as well. Both of these compounds can then be dehydrated, releasing either H_2O or HDO and a singly deuterated BD (BDD) with a signal at m/z = 55. Unfortunately, butanol also shows a signal at this m/z value, which makes a clear determination of the BDD production impossible. The non-deuterated BD signal at m/z = 54, on the other hand, clearly increases in presence of EtOH and decreases again under pure CA flow, indicating that mainly the MPV pathway is responsible for its production. The COH signal at m/z = 57 follows a similar pattern as the BD signal, suggesting the same reaction pathway for these compounds. The deuterated crotyl alcohol species at m/z= 73 and m/z = 74, on the other hand, follow a similar pattern as the gas phase CA signal, also indicating that the appearances of these compounds are linked.

In the IR spectra, consumption of CA and crotoxy species can be observed in the presence of EtOH by negative signals below 1724 cm^{-1}. A small positive peak around 1762 cm^{-1} can also be seen, indicative of the production of AA, either from EtOH dehydrogenation, from retro aldol condensation of CA, or MPV reaction of CA and EtOH. In the region below 2750 cm^{-1}, negative signals are observed that can be assigned to the consumption of Si-OD (or Zr-OD) groups upon the adsorption of EtOH. At the same time, the Si-OH region below 3745 cm^{-1} exhibits positive signals indicating some formation of Si-OH. However, these bands are broad, indicating they are likely interacting with EtOH. The positive signals in the C-H stretch region between 2900 and 3000 cm^{-1} originate from physisorbed EtOH or the formation of ethoxy species.

Mechanistic Interpretation

In Figure 5.11, we summarize the findings of this work for the coupling of EtOH to BD over the one-step catalyst Ag-Zr-BEA. When EtOH pressures are low (left side of the figure), Ag particles are available for the hydrogenation of CA to COH (A).

Consequently, COH desorbs from the metal surface and diffuses to an available acid site (B), where the dehydration to BD and H_2O takes place. In the meantime, EtOH can adsorb to a silver particle (C) where the dehydrogenation takes place and AA is released. Hydrogen atoms either desorb in the form of H_2 (as also observed in the MS spectra), or remain on the surface until another CA molecule comes in and can be hydrogenated. As the EtOH pressure is low, Zr-OH sites are also available for coupling of two AA molecules to form CA (D, see reference[97] for details on the Ta-BEA mechanism). When, on the other hand, the EtOH pressure is high (as it usually is under reaction conditions), Ag particles are mostly covered with EtOH and perform the dehydrogenation of EtOH to AA, leaving fewer sites for the direct hydrogenation of CA (A). AA then easily desorbs, couples over the acid site and produces CA (B). At this point there are two reaction paths for CA to take: either it gets directly hydrogenated over Ag, or it undergoes MPV reaction over the Zr site (C). At high EtOH pressure, not only the EtOH coverage on Ag is high, but also ethoxy species are likely present on the Zr group. We proposed this to be an intermediate in the MPV mechanism over Ta-BEA, meaning that having a high ethoxy coverage likely leads to better productivity in Zr-BEA as well. As the thermodynamics are more favorable for the MPV reaction, most of the CA will react over the Zr site, releasing COH and AA. In a final step, BD and H_2O are produced from COH.

Contrary to other previously used one-step catalysts such as MgO or mixed SiO_2-MgO catalysts, in metal-doped Lewis acid catalysts the dehydrogenation functionality and the coupling and dehydration functionalities are occurring on different active sites, which brings along certain advantages concerning catalyst design. Cavani *et al.* have studied the ethanol coupling over basic MgO and proposed a new reaction mechanism, where BD is formed from via an adsorbed carbanion intermediate that reacts with another adsorbed acetaldehyde molecule instead of an MPV process.[227] They also showed that the reaction of COH over MgO does not yield BD with high selectivities. This suggests that the addition of a weak acid functionality such as SiO_2 gives the catalyst enough acidity to perform this last reaction step.[292] However, in these acid-base systems, changing one parameter

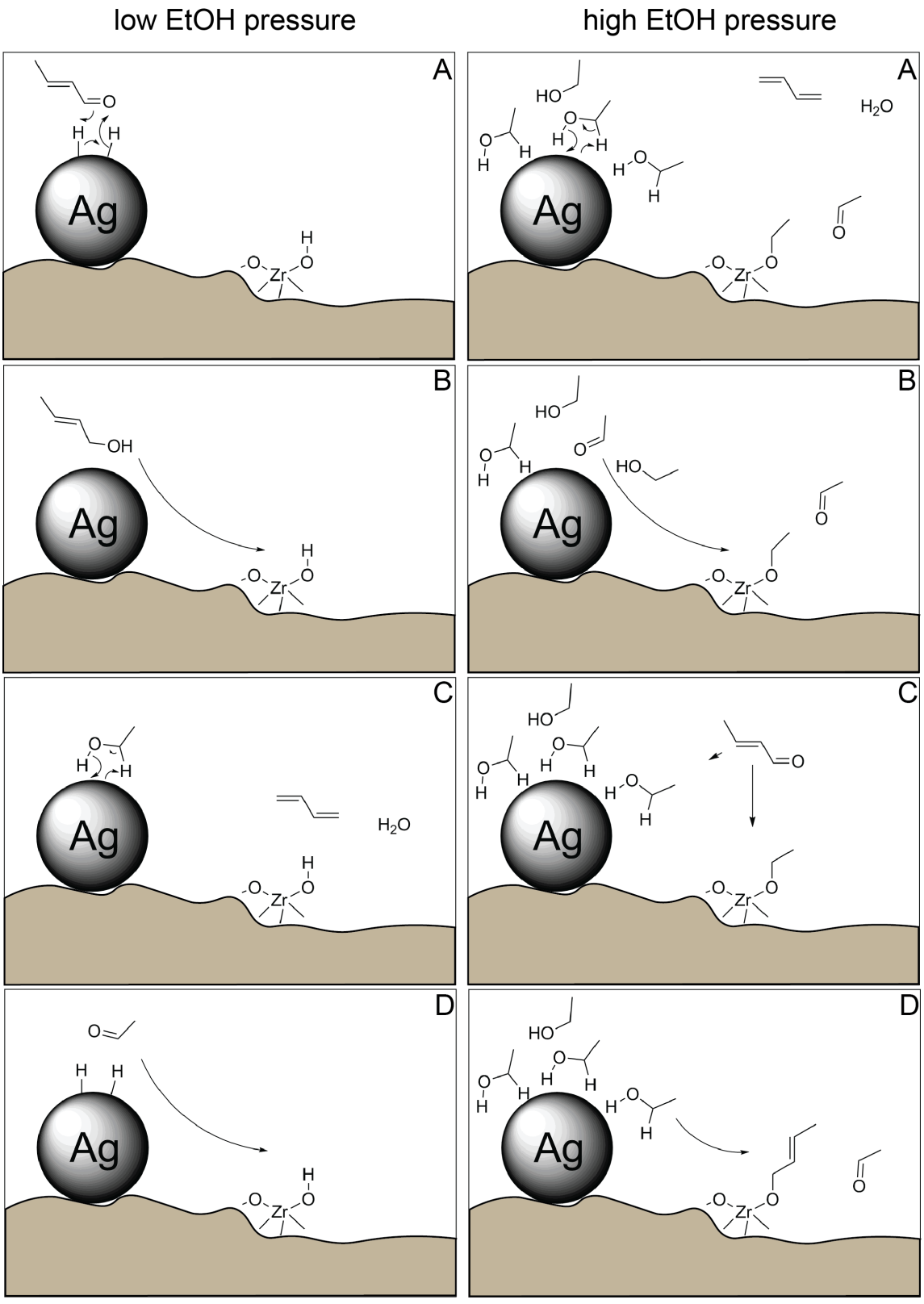

Figure 5.11: Tentative reaction scheme for the coupling of EtOH to BD over the one-step catalyst Ag-Zr-BEA. On the left side, the mechanism for low EtOH pressures is shown, while on the right side the case of high EtOH pressures is presented.

such as the SiO_2 loading might also influence the amount of basic sites and their strength, making rational catalyst design highly challenging. Furthermore, the preparation method also influences the type and amount of sites present in the final catalysts.[226;240;293] For metal-doped Lewis acid catalysts, on the other hand, the addition of Ag, for instance, does not add or remove significant amounts of acidity/basicity to the system and is mainly responsible for dehydrogenation activity. Hence, if the EtOH conversion is too low, adding more Ag to the catalyst might be a solution to boost activity, whereas if more coupling and dehydration activity is needed, the Zr loading should be increased. Interestingly, for Ta-BEA it was found that doping with Cu leads to higher BD productivity than doping with Ag or Zn.[274] Hence, a targeted catalyst design might be possible by tuning the acidity of the catalyst and adding different loadings and types of metals for dehydrogenation.

5.3 Conclusions

In this study, we present new insights into the mechanisms of EtOH coupling over a silver-doped Zr-BEA catalyst. A thorough catalyst characterization was performed where it was found that Ag forms small nanoparticles that stay mostly reduced under reaction conditions. The Zr(IV) sites are isolated and highly Lewis acidic. A modulated *operando* DRIFTS-MS study revealed that the reaction mechanism for the two-step process over Zr-BEA proceeds similarly to one proposed earlier for Ta-BEA,[97] explaining why the open site in Zr-BEA is more active in this reaction. The addition of Ag enables the dehydrogenation of EtOH to AA. Lewis acidity is required for the coupling and dehydration steps. When combined in one catalyst (Ag-Zr-BEA), it is possible to form the crucial intermediate COH in two ways. Either CA gets directly hydrogenated over Ag, or it forms COH through an exchange with EtOH in an MPV mechanism over the Lewis acid site. At high EtOH pressures, which are present under actual reaction conditions, the latter is more likely to take place and is mainly responsible for the production of BD. Finally, the use of metal doped Lewis acids as one-step catalysts has the advantage of easier catalyst design, as the dehydrogenation and coupling events take place on different active sites

within the catalyst.

5.4 Experimental Details

Material Synthesis

The Zr-BEA zeolite was synthesized following a post-synthetic procedure published elsewhere.[281] The parent zeolite (Zeolyst, $SiO_2/Al_2O_3 = 25$) was dealuminated by acid leaching (13 M HNO_3, 20 mL g^{-1}, 373 K, 20 h) leading to SiO_2/Al_2O_3 ratios of >1500. The dealuminated zeolite was filtered off, dried in an oven at 373 K overnight, followed by drying under vacuum at 423 K for 8 h. 3 g of the sample was then added to a solution of 24 g of $ZrOCl_2 \cdot 8H_2O$ in 170 g of DMSO. This suspension was then heated to 403 K and held at this temperature for 12 h. After that, it was added to 1 L of deionized water, filtered off, rinsed with water and dried at 373 K overnight. The catalyst was calcined under an air flow with a ramp of 3 K min^{-1} to 473 K, where the temperature was held for 6 h, followed by another ramp of 3 K min^{-1} to 823 K, where the temperature was held for 6 h.

The SiO_2 was from Evonik (Aerosil 300) and was used as received. The silver was added in an incipient wetness impregnation from an aqueous $AgNO_3$ solution, followed by a calcination in air at 823 K for 6 h. The Ag-containing catalysts were activated by reduction under a hydrogen flow for 30 minutes before the DRIFTS experiments.

Characterization

ICP-OES was used to determine the Ag and Zr content in the samples after digesting the solids in HF. N_2-physisorption measurements were performed on a Micromeritics 3flex apparatus. The samples were degassed prior to measurement for 4 h at 373 K. Adsorption isotherms were collected at 77 K and analyzed using the BET method. DRUV-vis analysis was performed with a Maya2000 Pro spectrometer (Ocean Optics) equipped with a deuterium/halogen light source

(DH-200-BAL from Mikropack) using $BaSO_4$ as matrix. Intensities are given in Kubelka-Munk units. NH_3-TPD was performed on a Micromeritics Autochem II instrument equipped with a TCD detector. Ca. 100 mg of sample were placed in the reactor tube and dehydrated prior to adsorption (550 °C, 3 °C min^{-1}, held for 180 min, 40 mL min^{-1} He). In the case of the metal-doped materials, the catalysts were further reduced for 30 minutes in 5% H_2 in Ar flow at 320 °C. NH_3 was consequently adsorbed at 100 °C by flowing 10% NH_3 in Ar at 40 mL min^{-1}. Desorption was performed under He flow (40 mL min^{-1}) and a heating ramp of 5 °C min^{-1}.

The surface oxidation states of the catalysts used in this study were characterized by XPS using a K-alpha XPS (Thermo Scientific) instrument with a micro-focused monochromatic Al Kα X-ray source. Prior to analysis, some of the catalysts were heated to 320 °C at a rate of 5 °C min^{-1} and then reduced under H_2 for 30 minutes, sealed and stored in an oxygen-free environment, where they could be loaded in an air-tight sample holder (Thermo Scientific) for transport to the spectrometer. Samples were analyzed at 10^{-7} mbar pressure and room temperature. Spectra in the C1s, O1s, Si2p, Ag3d, and Zr3d regions were collected over multiple scans; the number of scans for each element (C = 10, O = 10, Si = 10, Ag = 25, Zr = 25), as well as the dwell time for each element (C = 50 ms, O = 50 ms, Si = 50 ms, Ag = 150 ms, Zr = 150 ms), was adjusted to obtain an acceptable signal/noise ratio. The pass energy was held at 50 eV, and the energy step size was held at 0.2 eV for each region. Each region was plotted using the Avantage (Thermo Scientific) software package.

All IR measurements were performed on a Bruker Vertex 70 spectrometer equipped with a liquid nitrogen cooled MCT detector. The DRIFTS-MS-MES setup is described in more detail elsewhere[97]. Typically 64 scans with a resolution of 4 cm^{-1} were coadded to give one spectrum. The intensities for the operando IR spectra are given in Kubelka-Munk units. The flow rate for the carrier gas (He or H_2) was 25 mL/min, and the liquid flow rate was 5 μL/min. Temporal resolution was one spectrum/MS data-point every 3-4 s.

Pyridine adsorption was performed in a home-built stainless steel IR accessory. The samples were pressed into self-supporting wagers, loaded into the accessory and outgassed at 573 K and 10^{-6} mbar for 1 h. Then, pyridine was adsorbed at 298

K for 5 minutes, followed by flushing N_2 to remove physisorbed pyridine for 15 minutes. The sample was then heated to the desired temperature at a rate of 10 °C min^{-1} and held at the desired temperature for 15 minutes before a spectrum was taken. The blank catalyst was subtracted and baseline correction was applied using the OPUS software package (OPUS 7.2, Bruker Optik GmbH). The analysis of the spectra was performed using MATLAB codes that were written in-house and Origin was used to generate the plots.

6 CONCLUSIONS & OUTLOOK

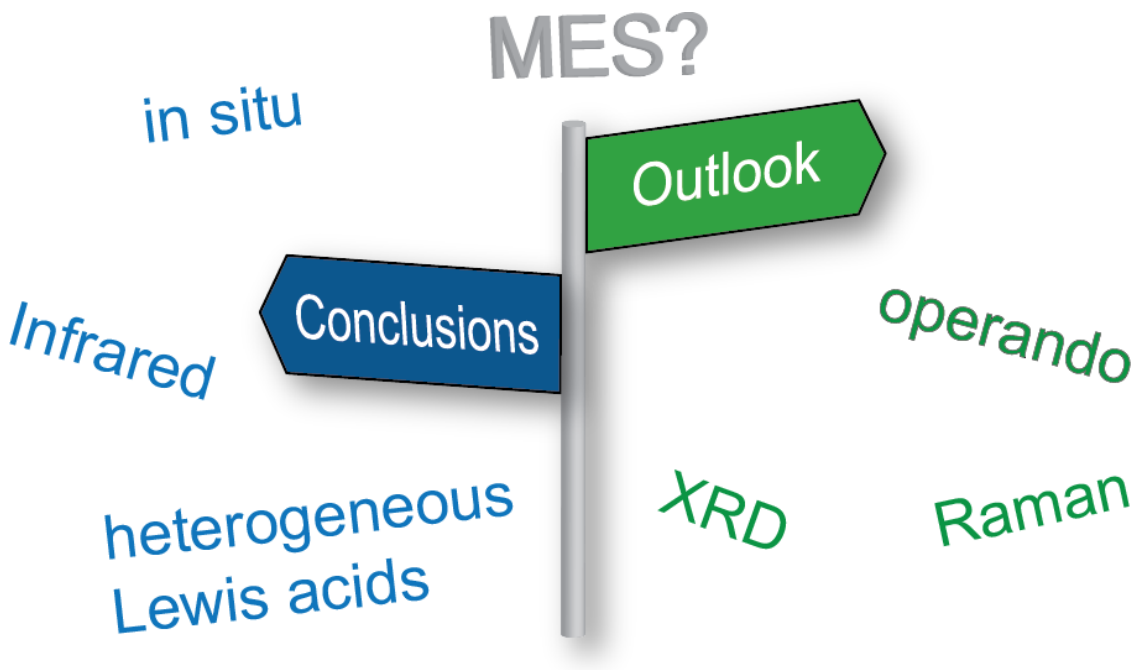

This chapter gives conclusions of this work and suggests future directions of MES. Parts of this chapter were published in the form of a review article in Industrial & Engineering Chemistry Research.[1]

6.1 Conclusions

The aim of this thesis was to apply modulation excitation spectroscopy on heterogenous Lewis acid catalysts. These experiments, conducted both in the liquid phase and in the gas phase, lead to unprecedented molecular level insights.

In chapter 2, we explored the cyclization of citronellal over Sn-Beta and Sn-SBA-15 as a first case study in the liquid phase. The reaction mechanism is identical over both catalysts and involves the coordination of citronellal with its carbonyl group to the Sn(IV) site, followed by the cyclization step and product desorption.

The citronellal coordination is amplified in the micropores of Sn-Beta because of the stronger Lewis acidity and confinement effects, leading to greater activity and selectivity despite diffusion limitations. The addition of the Lewis base acetonitrile leads to a significant loss in catalyst performance for Sn-SBA-15 due to competition for the Lewis acid site, whereas this effect was much less pronounced for Sn-Beta because citronellal is able to displace acetonitrile from the active site within the micropore. Furthermore, the analysis of phase-domain spectra revealed that substrate and product diffusion is enhanced when adding acetonitrile. In chapter 3, we further investigated the influence of different solvents on this reaction. A distinct dependence of the activity with the size of the solvent molecules was found, suggesting that diffusion effects might influence the performance of these catalysts. To investigate this hypothesis, the diffusion of citronellal through catalyst layers was studied using ATR-IR spectroscopy and experimental diffusion coefficients were determined. Interestingly, only Sn-Beta showed a clear trend, increasing its activity when the diffusion coefficient increases. Hence, in the case of the mesoporous catalysts the reaction most likely occurs on the external surface. In Sn-Beta, on the other hand, which citronellal is stabilized in the micropores, leading to good reactivity but also diffusion restrictions. The appropriate solvent will weaken these diffusion limitations and significantly boost catalytic performance while maintaining a high selectivity. Both of these chapters reveal the importance of diffusion in reactions involving porous heterogeneous Lewis acids and ATR-IR-MES proves to be a valuable tool to study such effects under relevant reaction conditions.

In chapter 4, we then moved from liquid phase to gas phase reactions by studying the Lewis acid catalyzed coupling of ethanol to 1,3-butadiene, a sustainable alternative to produce this important commodity chemical. We developed an *operando* DRIFTS-MS setup that enables precise control and analysis of changes in the gas phase composition as well as studying adsorbed species under reaction conditions. Modulation experiments helped us analyze the different consecutive reaction steps of this multi-step reaction. The generally accepted reaction pathway involving an MPV reaction of crotonaldehyde with ethanol forming crotyl alco-

hol occurs over the Lewis acidic Ta-BEA catalyst. For the first time, we propose molecular-level reaction mechanisms for this reaction based on surface intermediates observed in our MES data. These findings explain why the 1,3-butadiene productivity is remarkably sensitive toward changes in the ethanol to acetaldehyde ratio. An optimal value for this ratio is around 3 in order to maintain a high ethoxy coverage and to efficiently desorb the intermediate crotyl alcohol from the surface of the catalyst. In chapter 5, we study the influence of metal-doping on the one-step production of 1,3-butadiene from ethanol catalyzed by Ag-Zr-BEA. Using the same setup as in chapter 4, our experiments revealed that the reaction mechanism for the two-step process over Zr-BEA proceeds similarly to the one over Ta-BEA explaining why the open site in Zr-BEA is more active in this reaction. The addition of Ag enables the dehydrogenation of ethanol to acetaldehyde, while the Lewis acidity is required for the coupling and dehydration steps. The advantage of the Ag-Zr-BEA catalyst is that it is possible to form the crucial intermediate crotyl alcohol in two ways. Either crotonaldehyde is directly hydrogenated over Ag, or it forms crotyl alcohol through the MPV mechanism as in the purely Lewis acidic Ta-BEA and Zr-BEA. At high ethanol pressures, which represent actual reaction conditions, the MPV mechanism is more likely to take place and is mainly responsible for the production of 1,3-butadiene. Hence, the use of bifunctional metal doped Lewis acids, in contrast to other state-of-the-art catalysts, allows for precise catalyst design, as the dehydrogenation and coupling events take place on different active sites within the catalyst. Both of these studies exemplify the use of modulated infrared spectroscopy for the investigation of heterogeneously catalyzed gas phase reactions. Obtaining such molecular level insights into heterogeneously catalyzed reaction mechanisms are essential for improving catalytic processes that might ultimately lead to more sustainable chemical manufacturing.

6.2 Future Directions/Outlook

Even though the number of studies using modulation excitation spectroscopy has been growing recently, especially in heterogeneous catalysis, it is still not a widely

used technique. It would certainly be unreasonable to apply MES on every reaction combined with every spectroscopic technique. However, when choosing the appropriate technique and experimental parameters for a given catalytic system, high-quality phase-resolved spectra can be obtained. The following conditions are important: (i) the studied reactions are reversible or pseudo-reversible (ii) the time resolution of the chosen spectroscopic technique matches the kinetics of the reaction (iii) no significant catalyst deactivation occurs over the period of one experiment, and (iv) mass transport limitations are avoided in order to get kinetically relevant information. However, when applied properly, MES can lead to information that might be overlooked with standard steady-state experiments and can lead to selective measurements with a high signal-to-noise ratio. One reason why it might not be used on a more regular basis may be the mathematical framework that must be implemented in order to perform the data analysis. Researchers from the Paul Scherrer Institute published their Matlab codes on their website, together with a tutorial on MES,[294] which should make it easier for other researchers to implement MES in their laboratories, including use with other spectroscopic techniques.

An important recent development, especially in heterogeneous catalysis, is the combination of several characterization techniques into one cell, as also briefly mentioned in the introduction.[295;296] This approach allows for a simultaneous measurement of different catalyst properties. There have been some examples, where X-ray absorption spectroscopy (XAS) has been successfully combined with diffuse reflectance infrared spectroscopy (DRIFTS), Raman spectroscopy, or ultraviolet-visible spectroscopy (UV-vis).[136;297–299] In order to have a fast exchange of the gas or liquid phase, a low dead volume is required to obtain kinetically relevant information, especially using MES. This has been attempted by miniaturizing the reactors (*e.g.*, using capillary reactors). However, geometrical constraints, especially for infrared cells, makes it challenging to combine all desired spectroscopic techniques into one cell. Hence, another approach could be to design a cell with a small dead volume that can be measured consequently instead of simultaneously with the different techniques, provided the catalyst does not deactivate over the time course of these measurements. It is also important to move toward more "*operando*" MES,

meaning that the used cells should allow one to attain (heat and mass transport) conditions applied in the actual reactors, as well as simultaneously monitoring activity to be able to get reliable and transferable information.[300] First steps into that direction have been made by routinely monitoring the gas-phase composition at the outlet of the reactor cells using online mass spectrometry, as also shown in this thesis. Reducing the dead volumes and optimizing the flow patterns can further lead to truly differential reactors that yield reliable kinetics.

For liquid-phase reactions that are still often performed under batch conditions, an attempt was made to use attenuated total reflection infrared spectroscopy (ATR-IR) with a recycle reactor to simulate batch conditions.[301] This approach further enables monitoring of the bulk liquid-phase composition, which can then be subtracted from the solid-liquid spectra, yielding true surface spectra. This reactor setup was already tested for MES applications and showed promising results, especially for reactions where additives are required such as asymmetric hydrogenations over cinchonidine-modified noble metals. Well-designed experiments will allow the extraction of kinetic information, which might not be accessible from conventional time-resolved spectra. In most of the described applications in the introduction as well as in the main text, the discussion of the phase-domain data remains on a qualitative or semi-quantitative level. Admittedly, this also is related to inherent limitations of the applied techniques. DRIFTS, for instance, is relatively difficult to quantify because of the scattering nature of the reflected light. The same is true for ATR-IR, where slight changes of the refractive index of the sample lead to drastic changes in the penetration depth of the evanescent wave. Nevertheless, it would be desirable to be able to back-transform the highly smoothened phase-domain spectra into the time-domain to get quantitative kinetic information. As briefly mentioned above, other data analysis concepts such as two-dimensional (2D) correlation spectroscopy,[131;302] principal component analysis (PCA) or multivariate curve resolution (MCR) could be applied to analyze MES data.[126;303] MCR allows for the extraction of information from large and complex time-resolved (modulated) datasets. It is a highly automated algorithm that allows one to efficiently process spectra and is a blind-source method, which might lead to easier access to highly

sensitive spectra in contrast to PSD.

In terms of applications, pressure modulation is a stimulation that has not been explored with MES so far.[304] A change in pressure can affect heterogeneous reactions in at least two ways.[305] For porous catalysts, pressure modulation can significantly increase transport within the pores or at the catalyst surface, especially for gas-solid and gas-liquid-solid reactions. Second, probably a rarer case, is that reactions that involve adjacent active sites or that are inhibited by a strongly adsorbing reactant or product may be sensitive to pressure changes. In some examples, pressure modulation did, indeed, lead to higher overall reaction rates. Such effects could be studied with MES, provided a setup periodically changing the pressure could be incorporated into an existing spectroscopic accessory.

As we've shown in this thesis, applying MES on porous catalysts is possible and allows for the extraction of information that is not obtainable with conventional steady-state measurements. Generally, we believe that the number of applications of MES will keep increasing, especially for the discussed fairly new techniques (XRD, imaging) as well as other spectroscopic techniques. As shown with the examples in the introduction and in this thesis, MES with PSD proves to be a versatile tool to obtain spectra with high signal-to-noise ratio, the possibility to distinguish between spectator, and active species, as well as an analysis of the dynamics of different species.

A.1 Annexes Chapter 2

Table A.1: Key characteristics of the synthesized catalysts.

Catalyst	Sn content [wt%][i]	S_{BET} [m^2/g] [ii]	V_{micro} [cm^3/g] [iii]	S_{ext} [m^2/g] [iv]
SBA-15	0	1010	0.06	902
Sn-SBA-15	2.9	1033	0.16	658
Sn-SiO_2	3.6	573	0.03	552
Si-Beta	0	517	0.18	40
Sn-Beta	1.1	637	0.20	151

[i] determined by ICP-OES, Na content was <1 ppm in all samples
[ii] BET surface area
[iii] Micropore volume determined with t-plot method
[iv] external surface area determined with t-plot method

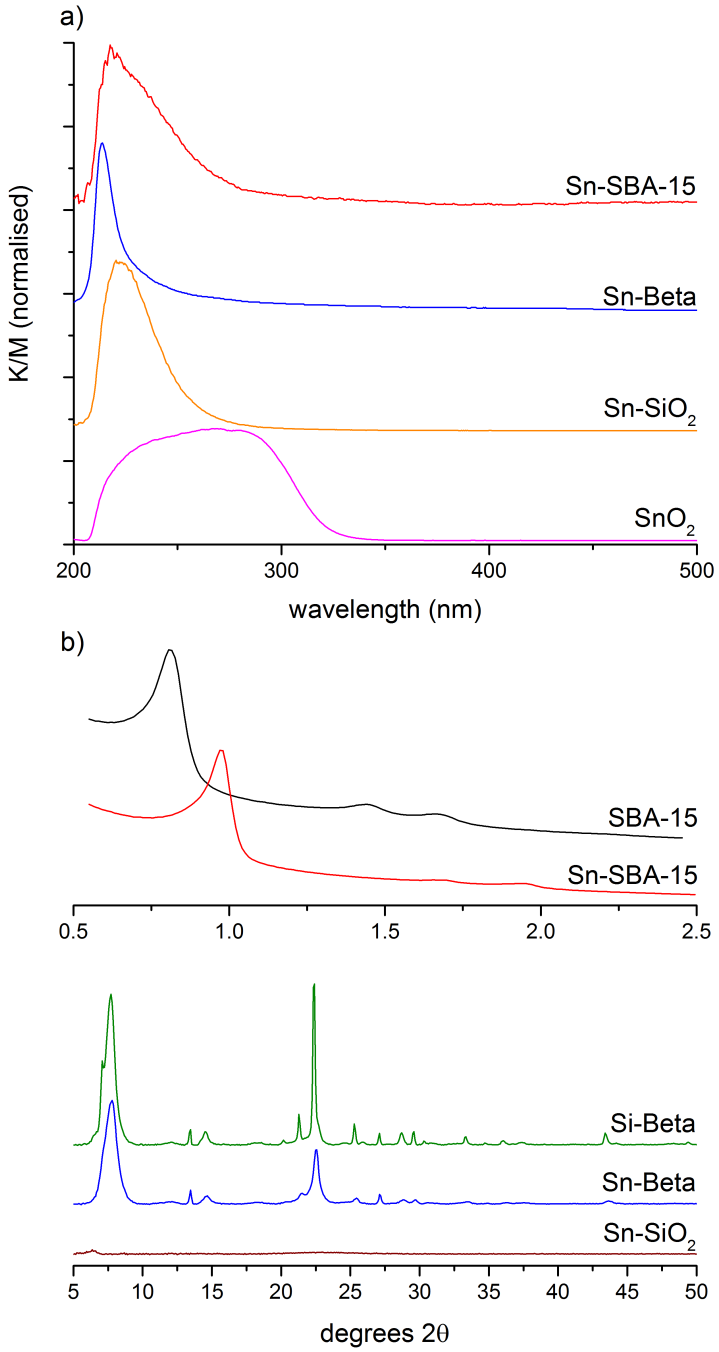

Figure A.1: a) DRUV-Vis spectra of the synthesized Sn-containing materials and of a reference SnO_2 sample and b) XRD patterns of the materials.

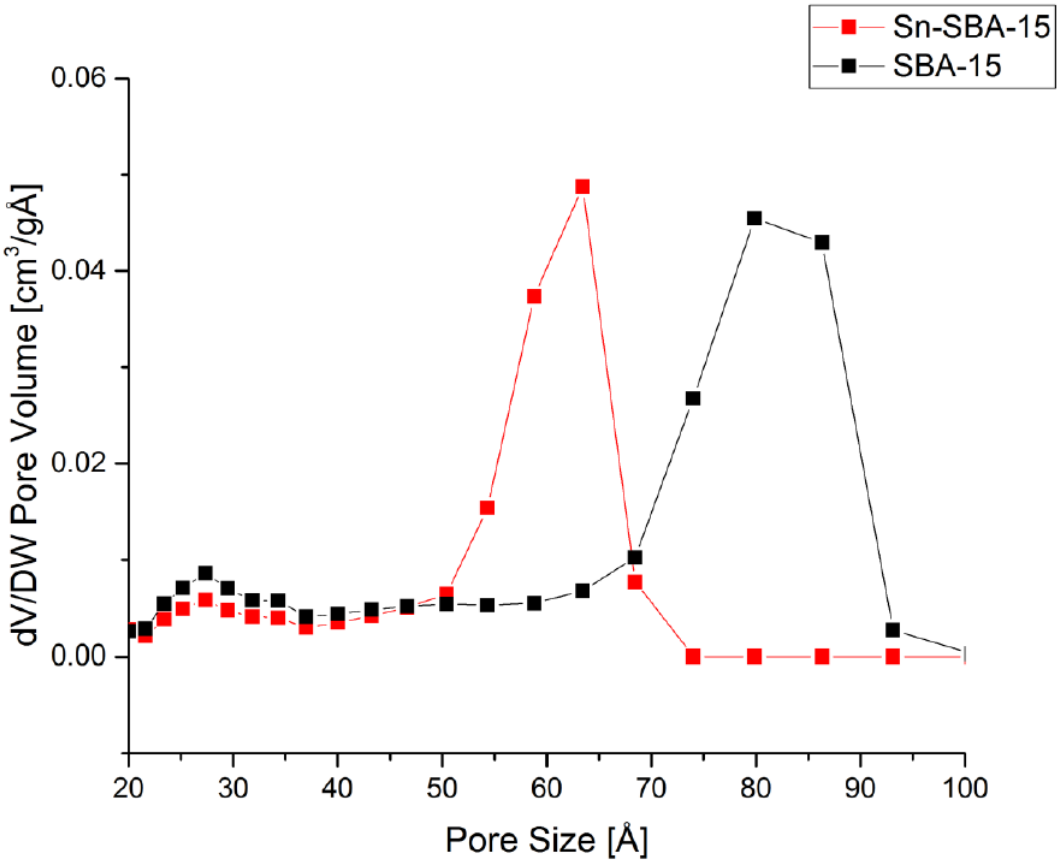

Figure A.2: Pore Size Distribution of the mesoporous materials calculated by a DFT method with N_2-physisorption data.

Table A.2: Batch reactivity data for the cyclization of citronellal over different catalysts.

Entry	Catalyst [v]	Solvent	Conv. [%] [vi]	TOF [h^{-1}] [vii]	Sel. [%] [viii]	$Sel._{dia}$ [%][ix]
1	-	Toluene	4	-	50	67
2	SBA-15	Toluene	27	-	67	66
3	Sn-SBA-15	Toluene	89	115	92	64
4	Sn-SiO_2	Toluene	60	42	90	65
5	Si-Beta	Toluene	9	-	40	70
6	deAl-Beta	Toluene	24	-	75	77
7	Sn-Beta	Toluene	66	185	89	70
8	HT-Sn-Beta	Toluene	61	194	97	81
9	C-Sn-SBA-15[x]	Toluene	84	105	91	63
10	Sn-SBA-15	Tol. + Isopul.[xi]	55	31	83	86
11	Sn-Beta	Tol. + Isopul.[xi]	38	73	92	95
12	-	Acetonitrile	-	-	-	-
13	SBA-15	Acetonitrile	-	-	-	-
14	Sn-SBA-15	Acetonitrile	15	12	50	65
15	Sn-SiO_2	Acetonitrile	7	6	0	0
16	Si-Beta	Acetonitrile	-	-	-	-
17	Sn-Beta	Acetonitrile	63	127	88	77
19	-	2-BuOH	12	-	50	69
20	Sn-SBA-15	2-BuOH	68	78	60	65
21	Sn-Beta	2-BuOH	90	268	84	76
22	Sn-SBA-15	2-BuOH + Isopul.[xi]	48	18	60	82
23	Sn-Beta	2-BuOH + Isopul.[xi]	87	170	89	93

[v]Reaction conditions: 50 mg of catalyst, 5 mL of 0.5 M citronellal solution in solvent at 333 K, reaction time 4 hr.

[vi]Conversion = (moles of citronellal initial - moles of citronellal after 4 hr)/moles of citronellal initial

[vii]Turnover frequency (TOF) = moles of citronellal converted/moles of Sn after 1 hr

[viii]Selectivity is defined as the moles of all produced isomers of isopulegol divided by the moles of converted citronellal

[ix]Diastereoselectivity is defined as the moles of produced (-)-isopulgeol divided by the moles of all isomers of isopulegol produced.

[x]Collodion was added to the catalyst in the same ratio as for the ATR-IR experiments (see experimental section)

[xi]0.5 M isopulegol was added to the solution

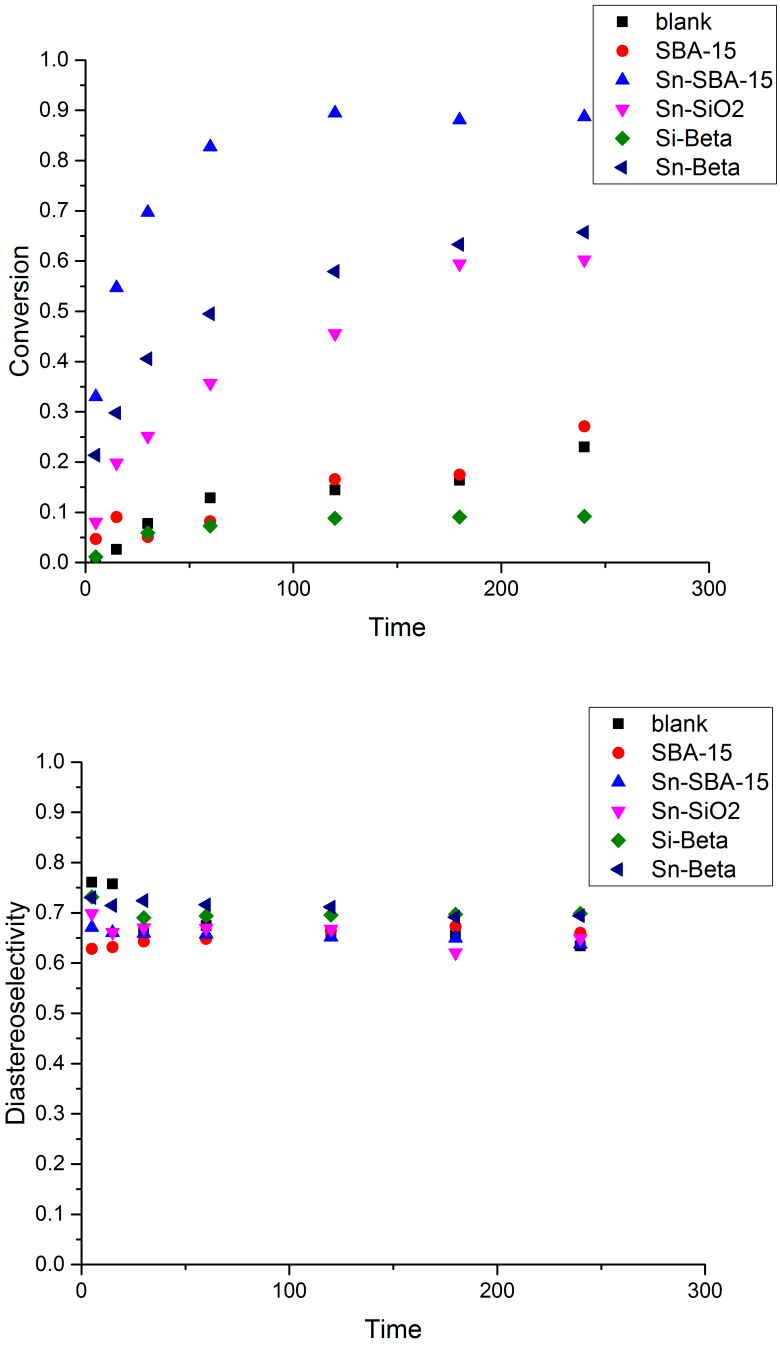

Figure A.3: Conversion versus time (top) and Diastereoselectivity versus time (bottom) for the reaction of citronellal in toluene with different catalysts. The same conditions as in Table A.2 were used.

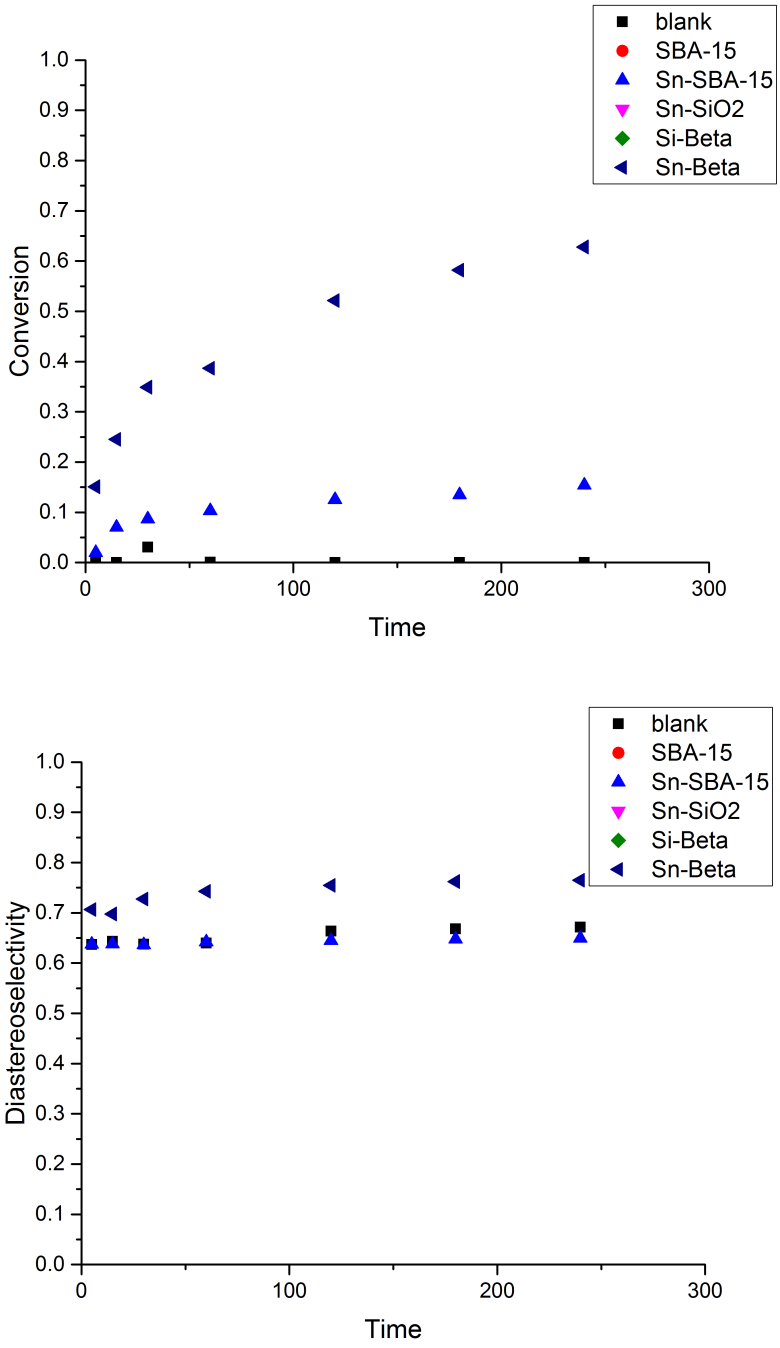

Figure A.4: Conversion versus time (top) and Diastereoselectivity versus time (bottom) for the reaction of citronellal in acetonitrile with different catalysts. The same conditions as in Table A.2 were used.

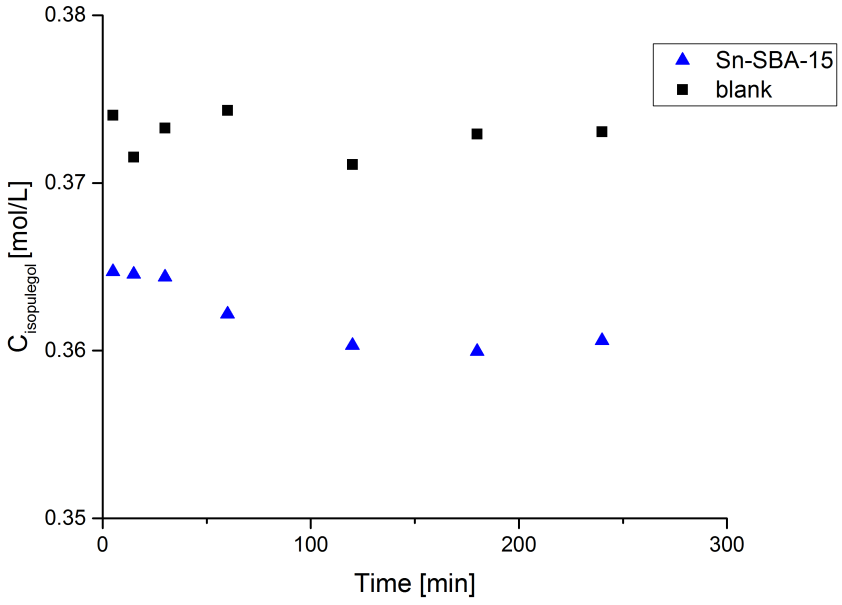

Figure A.5: Concentration profile of the reaction of 0.37 M isopulegol in toluene at 333 K without catalyst and with 50 mg Sn-SBA-15. The citronellal concentration was too low to be analyzed.

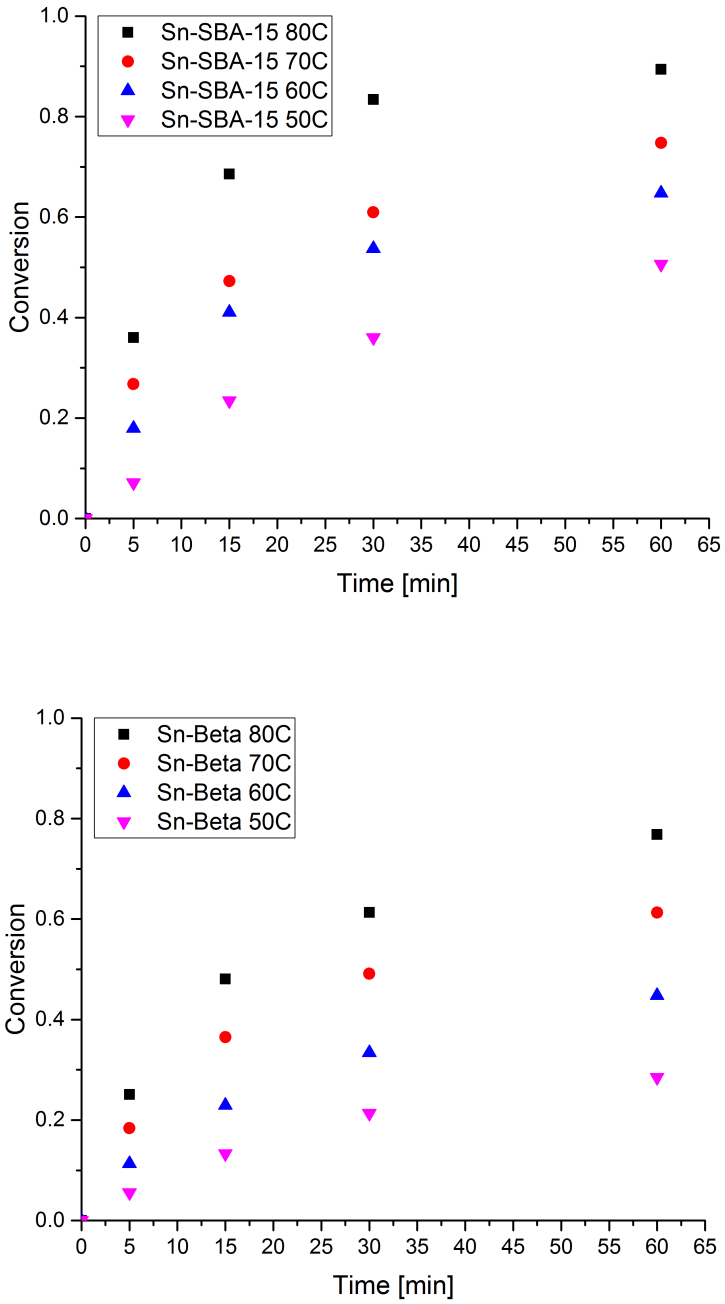

Figure A.6: Concentration profiles of the reaction of 0.3 M citronellal in toluene at different temperatures top with Sn-SBA-15 and bottom with Sn-Beta.

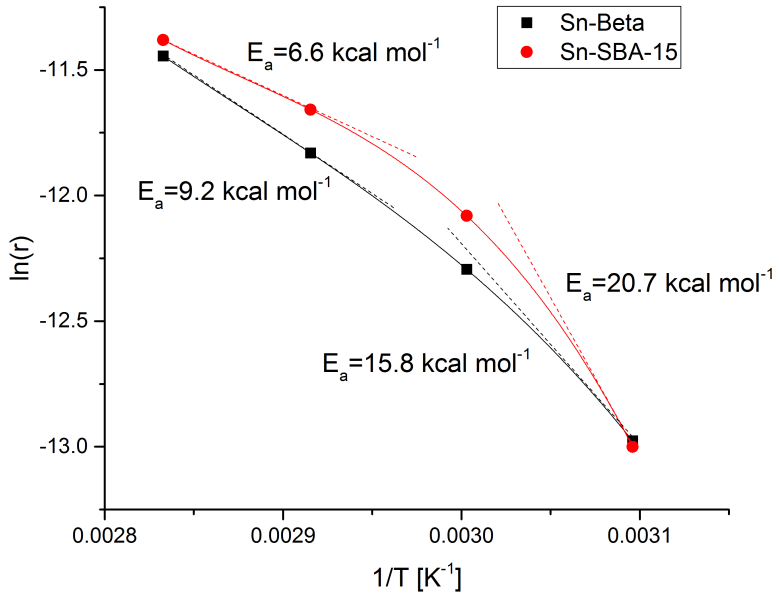

Figure A.7: Arrhenius plots for Sn-Beta and Sn-SBA-15 between 50 and 80 °C. The curved line indicates mass transport limitations.

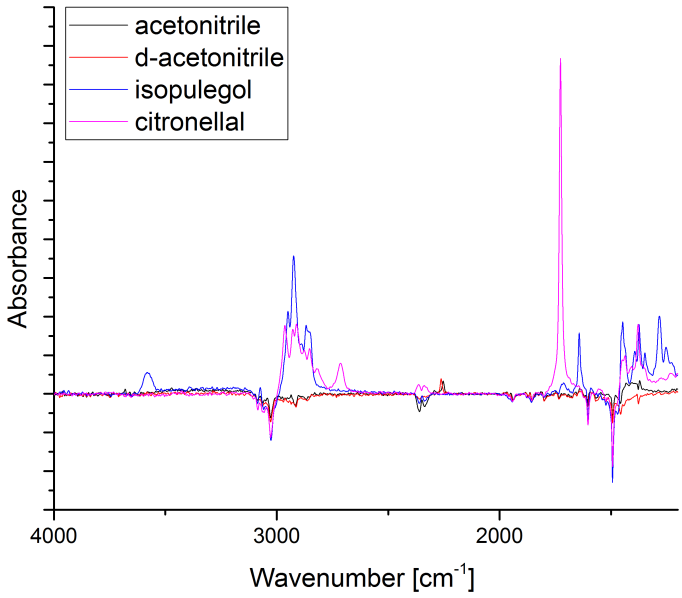

Figure A.8: IR spectra of 20 mM solution in toluene (acetonitrile, d-acetonitrile. Isopulegol and citronellal). Negative signals originate from toluene.

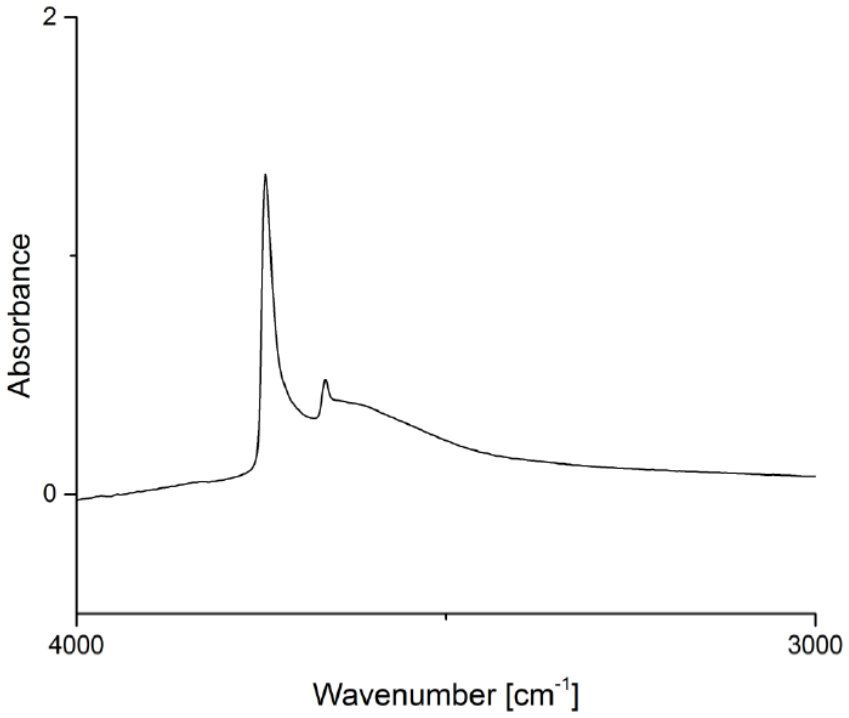

Figure A.9: Transmission Infrared spectrum of dehydrated 10 wt% Sn-Beta.

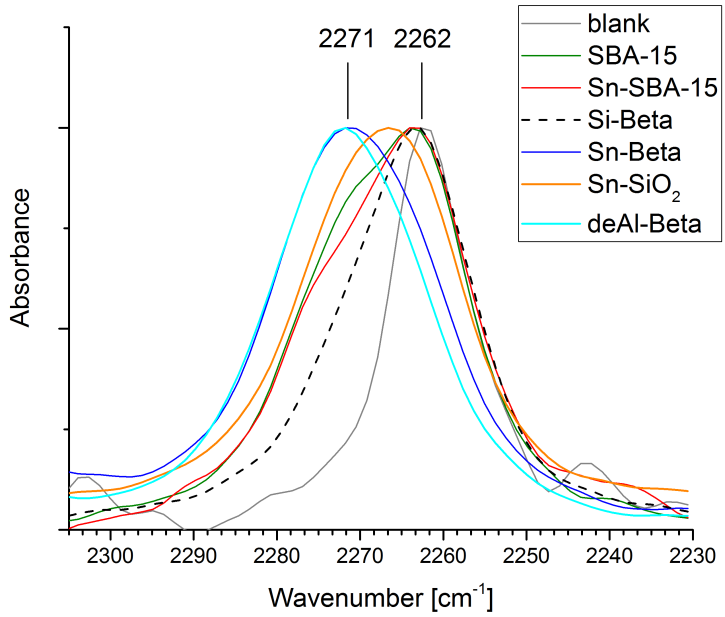

Figure A.10: Normalized IR spectra of 20 mM d_3-acetonitrile in toluene adsorbed on different catalysts.

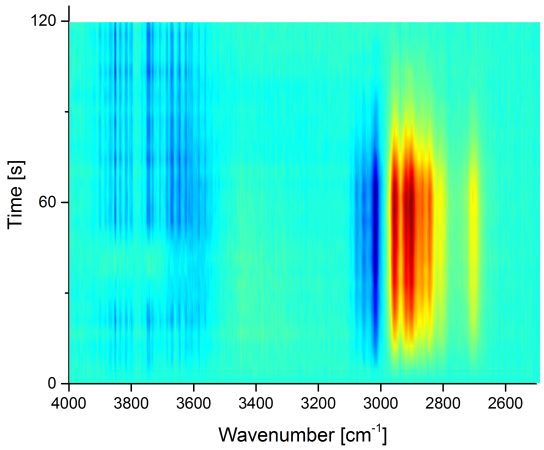

Figure A.11: Time-domain spectra for the modulation of 20 mM citronellal in toluene at 333 K for SBA-15.

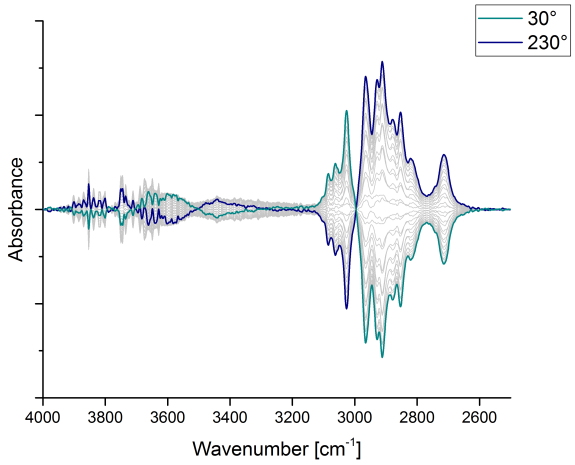

Figure A.12: Phase-domain spectra for the modulation of 20 mM citronellal in toluene at 333 K for SBA-15.

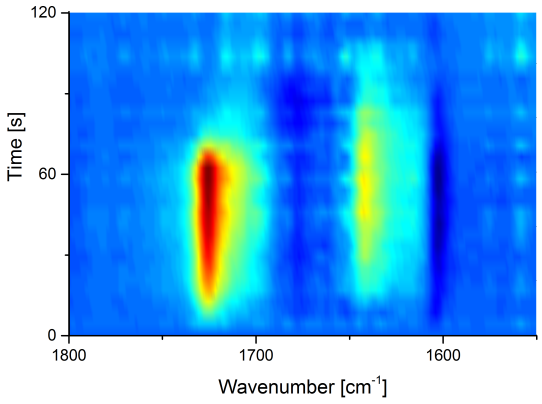

Figure A.13: Time-domain spectra for the modulation of 20 mM citronellal in toluene at 333 K for Sn-SBA-15.

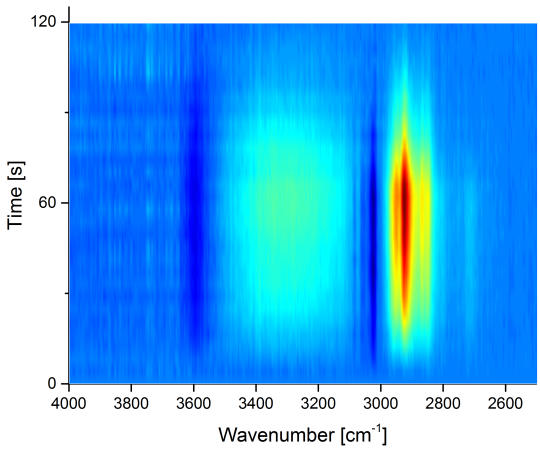

Figure A.14: Time-domain spectra for the modulation of 20 mM citronellal in toluene at 333 K for Sn-SBA-15.

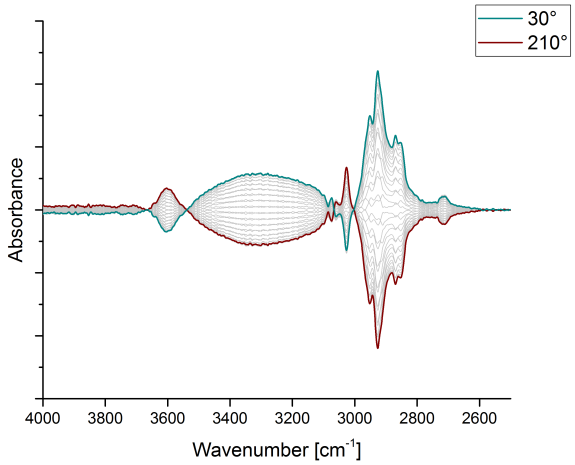

Figure A.15: Phase-domain spectra for the modulation of 20 mM citronellal in toluene at 333 K for Sn-SBA-15.

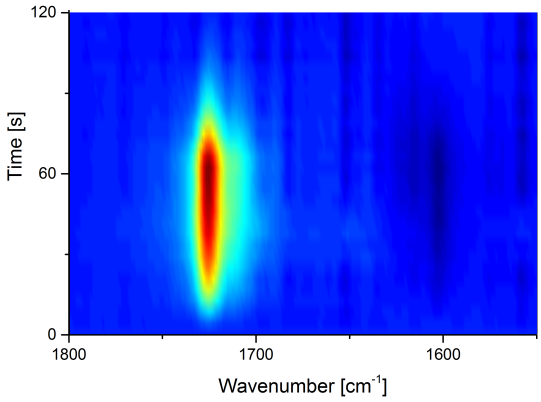

Figure A.16: Time-domain spectra for the modulation of 20 mM citronellal in toluene at 333 K for Si-Beta.

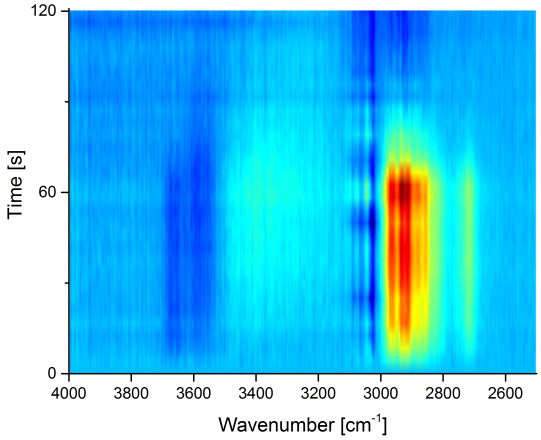

Figure A.17: Time-domain spectra for the modulation of 20 mM citronellal in toluene at 333 K for Si-Beta.

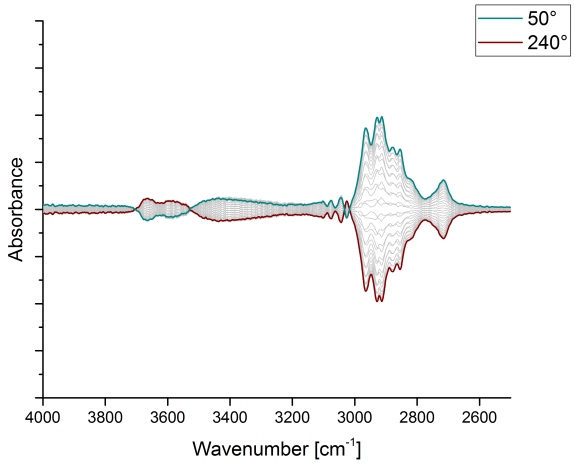

Figure A.18: Phase-domain spectra for the modulation of 20 mM citronellal in toluene at 333 K for Si-Beta.

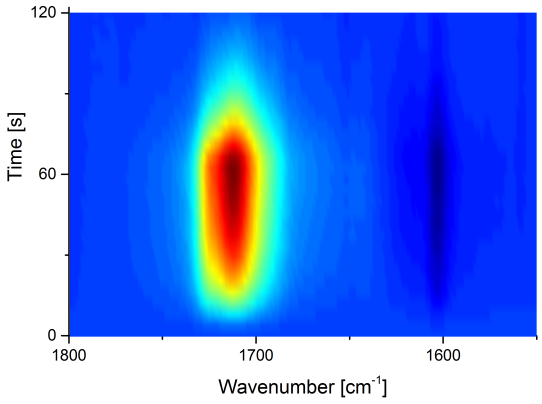

Figure A.19: Time-domain spectra for the modulation of 20 mM citronellal in toluene at 333 K for deAl-Beta.

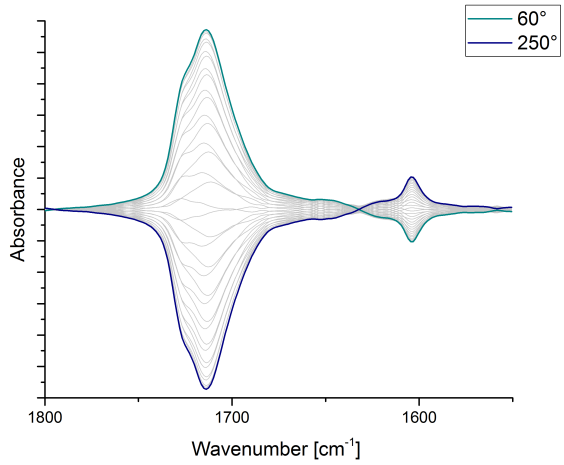

Figure A.20: Phase-domain spectra for the modulation of 20 mM citronellal in toluene at 333 K for deAl-Beta.

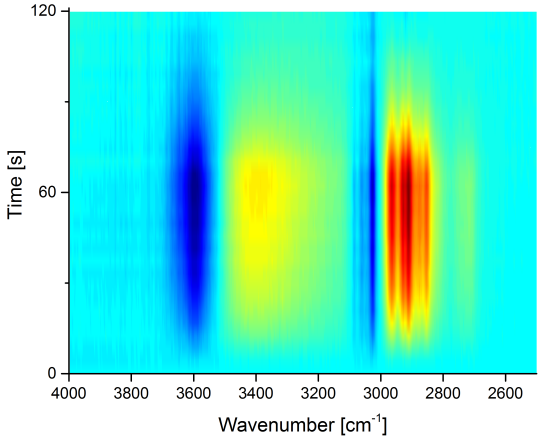

Figure A.21: Time-domain spectra for the modulation of 20 mM citronellal in toluene at 333 K for deAl-Beta.

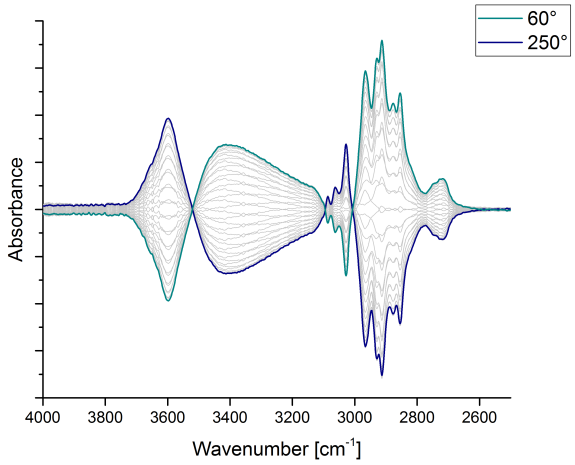

Figure A.22: Phase-domain spectra for the modulation of 20 mM citronellal in toluene at 333 K for deAl-Beta.

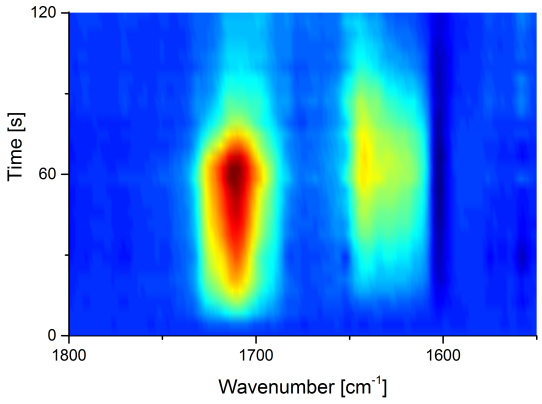

Figure A.23: Time-domain spectra for the modulation of 20 mM citronellal in toluene at 333 K for Sn-Beta.

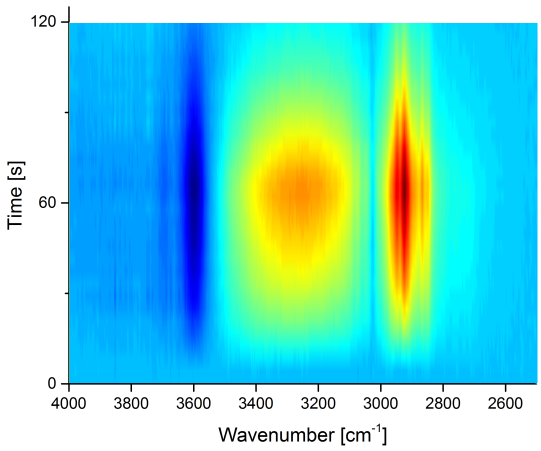

Figure A.24: Time-domain spectra for the modulation of 20 mM citronellal in toluene at 333 K for Sn-Beta.

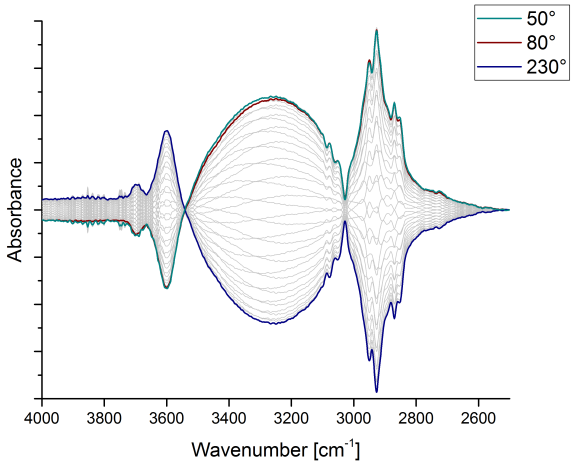

Figure A.25: Phase-domain spectra for the modulation of 20 mM citronellal in toluene at 333 K for Sn-Beta.

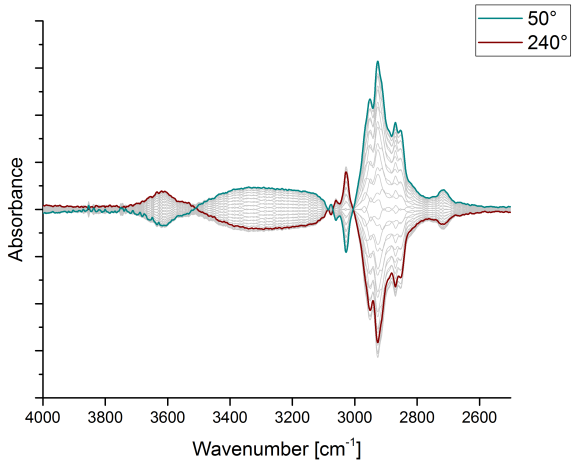

Figure A.26: Phase-domain spectra for the modulation of 20 mM citronellal in toluene at 333 K for 10wt% Sn-Beta.

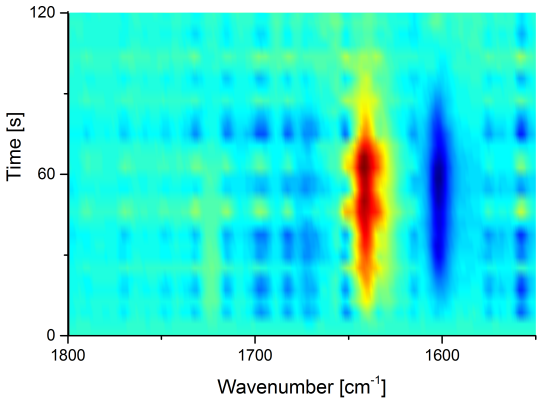

Figure A.27: Time-domain spectra of modulation experiments with 20 mM (-)-isopulegol in a solution of 20 mM citronellal in toluene at 333 K for SBA-15.

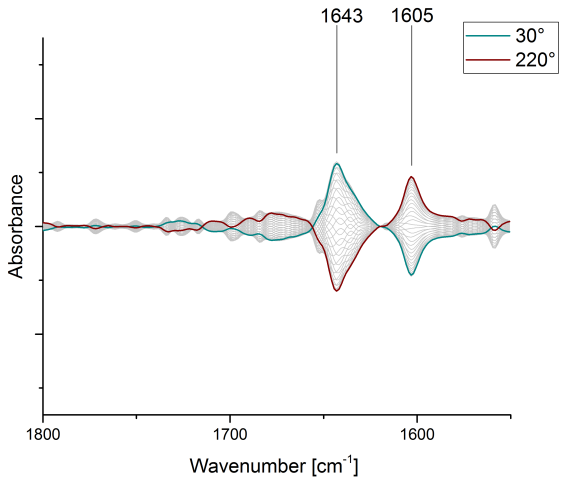

Figure A.28: Phase-domain spectra of modulation experiments with 20 mM (-)-isopulegol in a solution of 20 mM citronellal in toluene at 333 K for SBA-15.

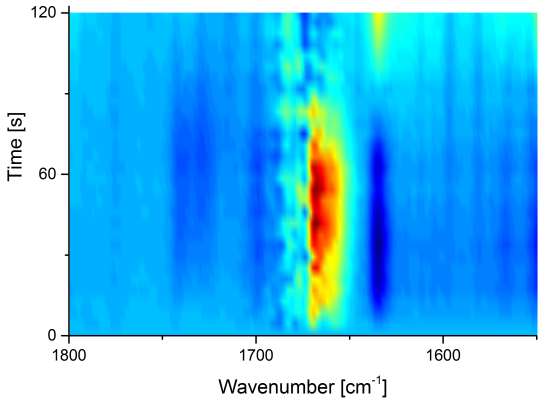

Figure A.29: Time-domain spectra of modulation experiments with 20 mM (-)-isopulegol in a solution of 20 mM citronellal in toluene at 333 K for Si-Beta.

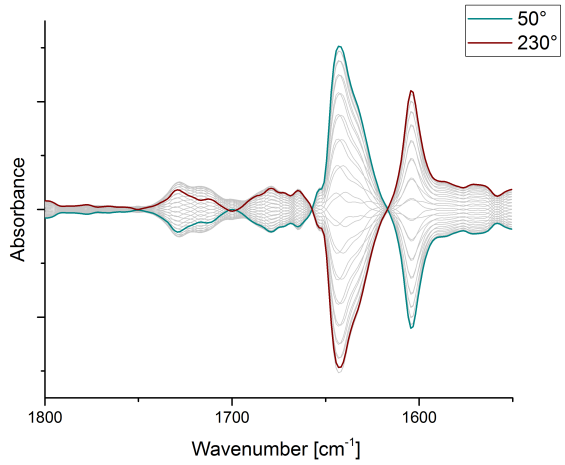

Figure A.30: Phase-domain spectra of modulation experiments with 20 mM (-)-isopulegol in a solution of 20 mM citronellal in toluene at 333 K for Si-Beta.

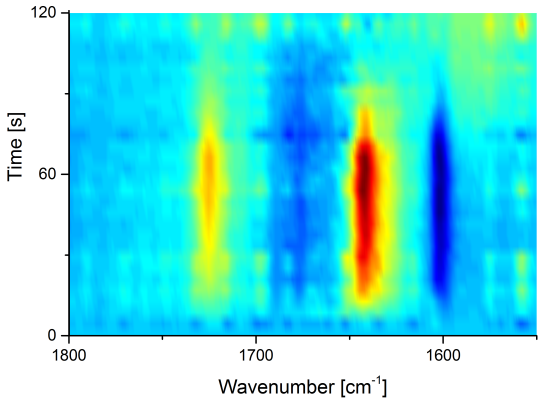

Figure A.31: Time-domain spectra of modulation experiments with 20 mM (-)-isopulegol in a solution of 20 mM citronellal in toluene at 333 K for Sn-SBA-15.

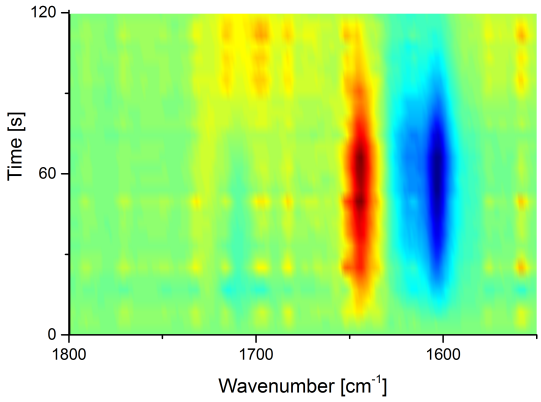

Figure A.32: Time-domain spectra of modulation experiments with 20 mM (-)-isopulegol in a solution of 20 mM citronellal in toluene at 333 K for Sn-Beta.

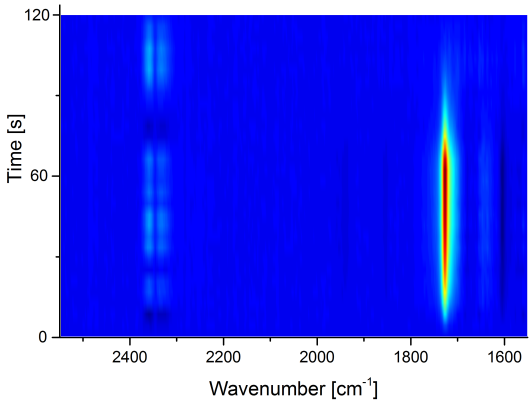

Figure A.33: Time-domain spectra of modulation experiments with 20 mM citronellal in a solution of 20 mM acetonitrile in toluene at 333 K for SBA-15.

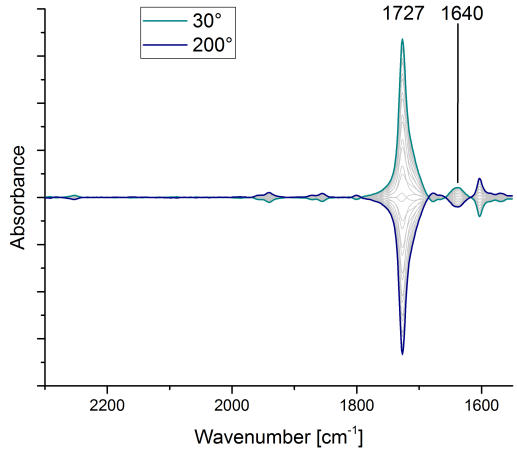

Figure A.34: Phase-domain spectra of modulation experiments with 20 mM citronellal in a solution of 20 mM acetonitrile in toluene at 333 K for SBA-15.

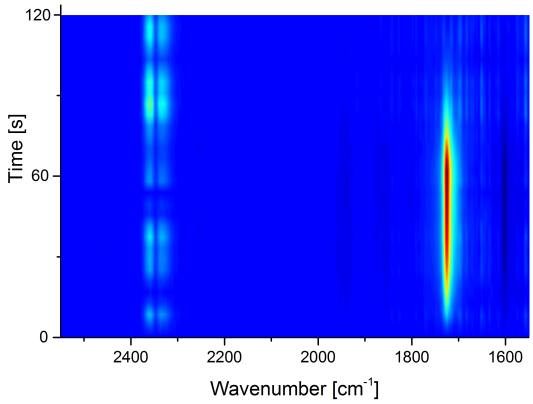

Figure A.35: Time-domain spectra of modulation experiments with 20 mM citronellal in a solution of 60 mM acetonitrile in toluene at 333 K for SBA-15.

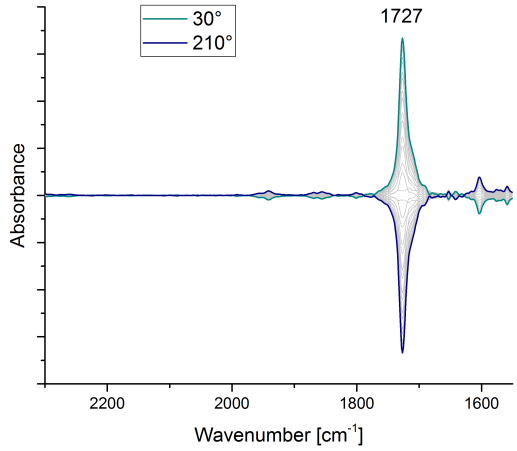

Figure A.36: Phase-domain spectra of modulation experiments with 20 mM citronellal in a solution of 60 mM acetonitrile in toluene at 333 K for SBA-15.

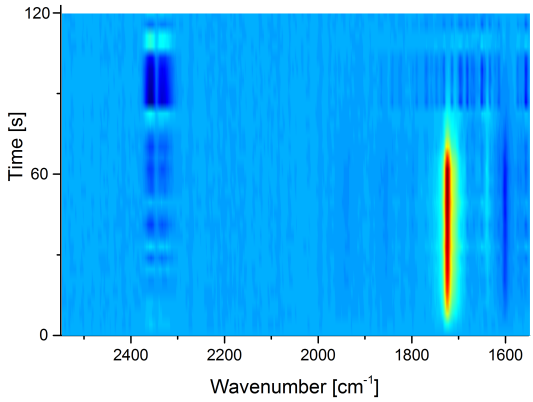

Figure A.37: Time-domain spectra of modulation experiments with 20 mM citronellal in a solution of 20 mM acetonitrile in toluene at 333 K for Sn-SBA-15.

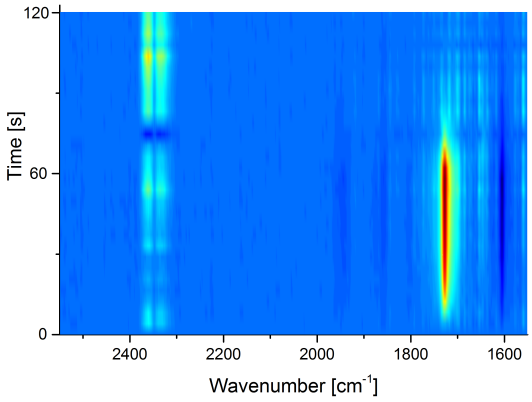

Figure A.38: Time-domain spectra of modulation experiments with 20 mM citronellal in a solution of 60 mM acetonitrile in toluene at 333 K for Sn-SBA-15.

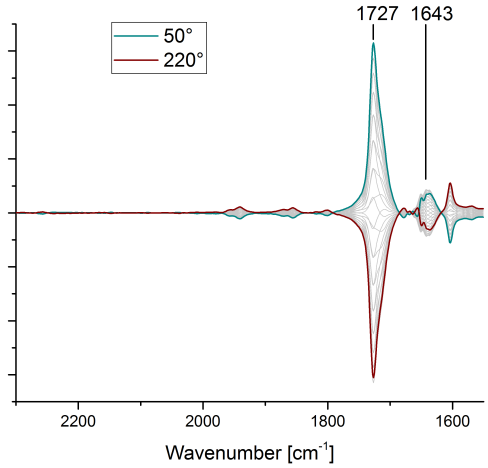

Figure A.39: Phase-domain spectra of modulation experiments with 20 mM citronellal in a solution of 20 mM acetonitrile in toluene at 333 K for Si-Beta.

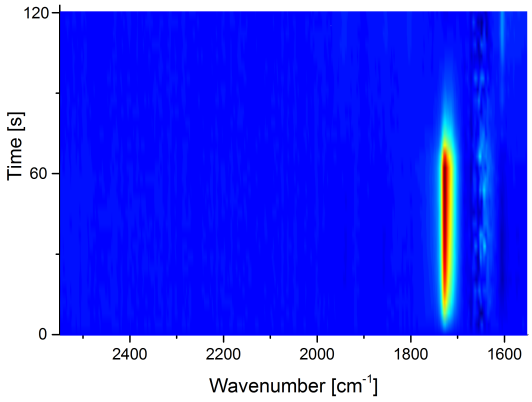

Figure A.40: Time-domain spectra of modulation experiments with 20 mM citronellal in a solution of 20 mM acetonitrile in toluene at 333 K for Si-Beta.

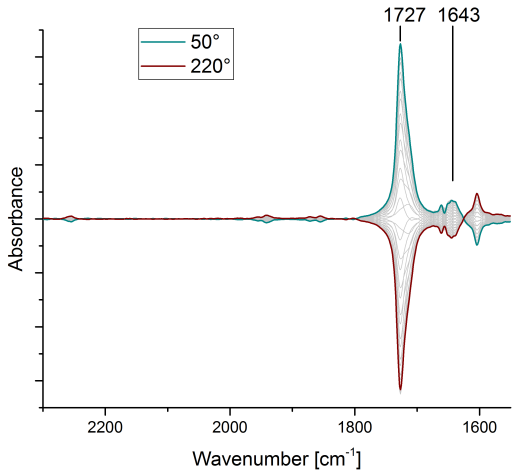

Figure A.41: Phase-domain spectra of modulation experiments with 20 mM citronellal in a solution of 60 mM acetonitrile in toluene at 333 K for Si-Beta.

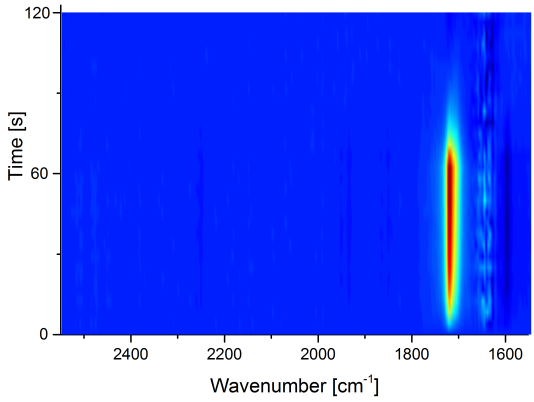

Figure A.42: Time-domain spectra of modulation experiments with 20 mM citronellal in a solution of 60 mM acetonitrile in toluene at 333 K for Si-Beta.

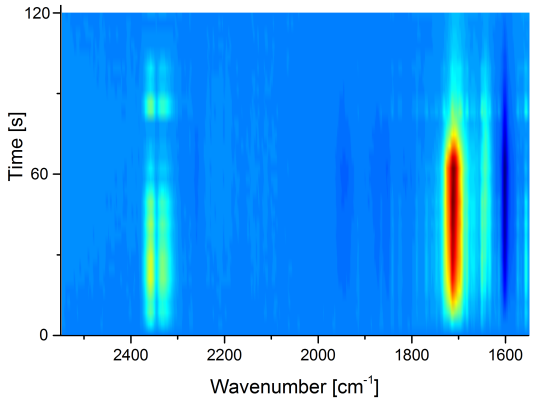

Figure A.43: Time-domain spectra of modulation experiments with 20 mM citronellal in a solution of 20 mM acetonitrile in toluene at 333 K for Sn-Beta.

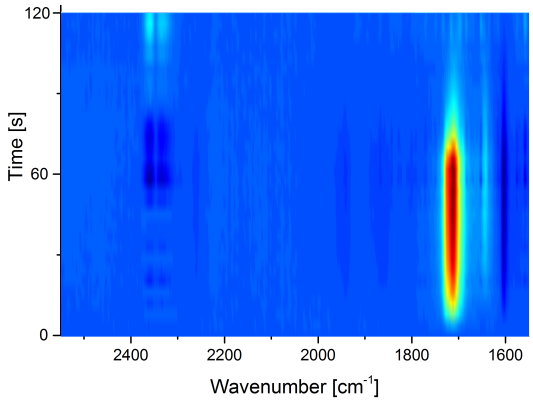

Figure A.44: Time-domain spectra of modulation experiments with 20 mM citronellal in a solution of 60 mM acetonitrile in toluene at 333 K for Sn-Beta.

Estimation of rate of diffusion for Sn-Beta

In this part, we try to estimate the rate of diffusion in Sn-Beta using the obtained spectroscopic data. The amount of catalyst deposited on the ATR crystal was usually 9 mg +- 1 mg. This would yield a layer thickness of 10 μm. Of this, only ca. 1 μm is probed by ATR, which is equal to 10% of the whole catalyst. Considering the micropore volume of Sn-Beta of 0.2 mL/g, this would mean, we are probing $2{\cdot}10^{-4}$ mL of solution. The solution contains 0.02 M citronellal, converting to total moles, this would mean, we are probing $4{\cdot}10^{-9}$ mol citronellal. In Figure 2.2 in the manuscript, it is shown, that 50°are required in the PD to reach a steady citronellal concentration in Sn-Beta. Converting this to the time-domain leaves us with a diffusion time of 15 seconds. Putting everything together:

$r_{diff} = \frac{4{\cdot}10^{-9}mol}{15s \cdot mg} = 2.6 \cdot 10^{-7} mols^{-1}g^{-1}$

The measured rate in the batch experiments was $r_{apparent} = 4.0{\cdot}10^{-7} mols^{-1}g^{-1}$ Which is in the same order of magnitude and indicates mass transfer to be crucial under these conditions.

Setup and further explanations

Explanation of a standard MES experiment: First of all, the crystal, coated with a catalyst layer, is inserted in the ATR accessory. In the simplest experiment, there are two tanks, one filled with pure toluene (c_{low} in Fig S45) and one filled with a molecule dissolved in toluene (c_{high} in Fig S45). The catalyst is then carefully flushed with pure toluene at a low flow rate and consequently the rate is slowly increased to 5 mL/min. Once a steady IR signal is achieved, a background measurement is taken and the actual MES experiment is started by switching to the second tank (c_{high}). Over a period of 60 seconds 30 spectra are recorded and stored, then the valves are automatically switched to the other tank and another 30 spectra are taken within 60 seconds. This procedure is usually repeated 6 times. Then the obtained spectra are analyzed and demodulated with an external MATLAB code. The spectra are visually inspected and three periods are chosen after the quasi-steady state is reached. These periods are then averaged and demodulated to yield

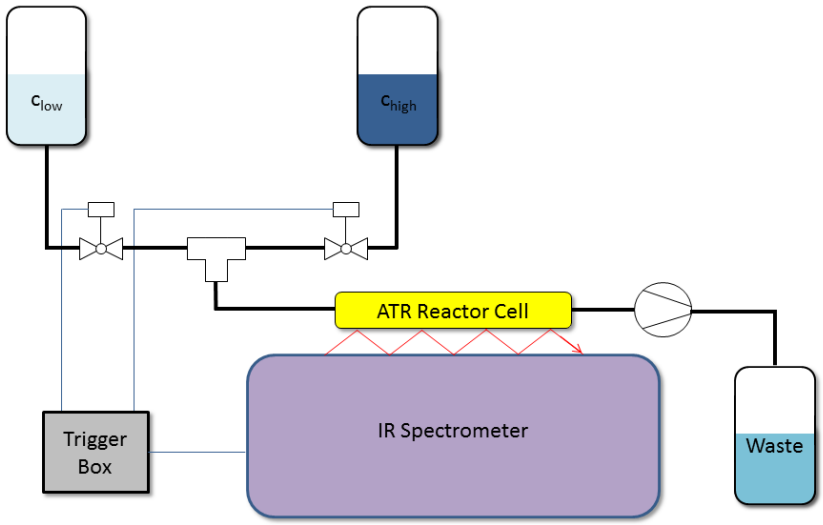

Figure A.45: Schematic representation of the setup.

phase-domain spectra. In principle, the resolution of the phase-domain spectra can be chosen arbitrarily, as they follow a sinusoidal function after the transformation. But as the time-domain spectra have a certain temporal resolution, it is advised not to increase the resolution above this limit. Considering the appropriate modulation frequency, it differs with every catalytic system, as differences in diffusion, adsorption and reaction rates influence the outcome of such a measurement. Typically some initial tests at a lower and a higher modulation frequency are performed to find an optimal value. In the given example, the modulation frequency would be 1/120 s=8 mHz. For further information on the technique, the reader is referred to the references mentioned in Chapter 2.

A.2 Annexes Chapter 3

Table A.3: Key characteristics of the synthesized catalysts.

Catalyst	Sn content [wt%][xii]	S_{BET} [m^2/g] [xiii]	V_{micro} [cm^3/g] [xiv]	S_{ext} [m^2/g] [xv]
Sn-MCM-41	1.1	781	0	781

[xii] determined by ICP-OES, Na content was <1 ppm in all samples
[xiii] BET surface area
[xiv] Micropore volume determined with t-plot method
[xv] external surface area determined with t-plot method

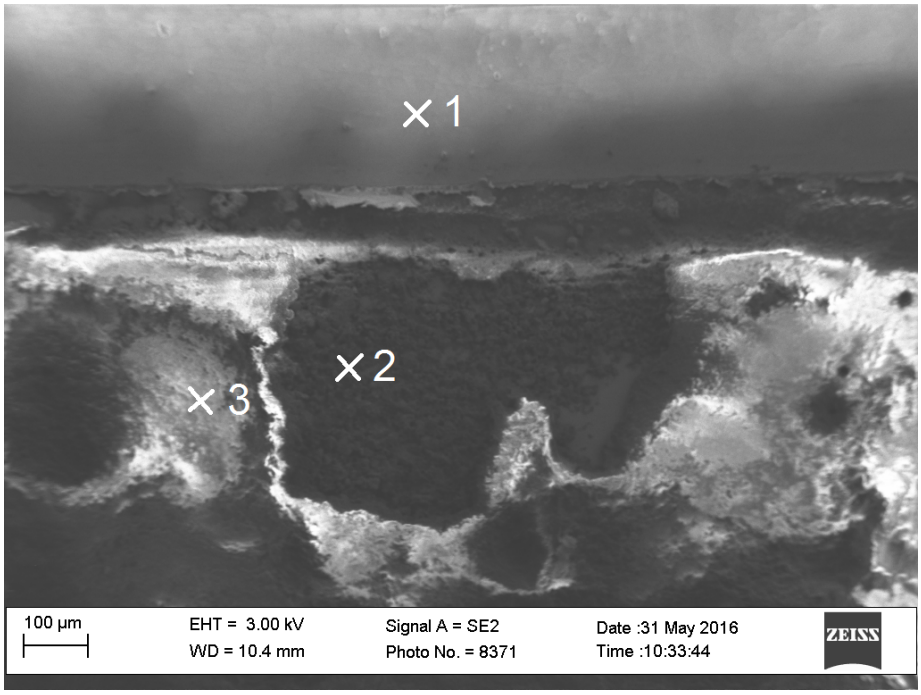

Figure A.46: SEM micrograph of Sn-Beta deposited on ZnSe. Numbers correspond to EDS positions that were analyzed in the following table.

Table A.4: EDS analysis of SEM micrograph in Figure A.46 in atom %.

	C	N	O	Si	Zn	Se
1	33.05	-	2.89	0.77	28.71	34.58
2	14.37	-	57.66	21.63	1.92	4.42
3	21.31	6.30	60.63	11.74	0.02	-

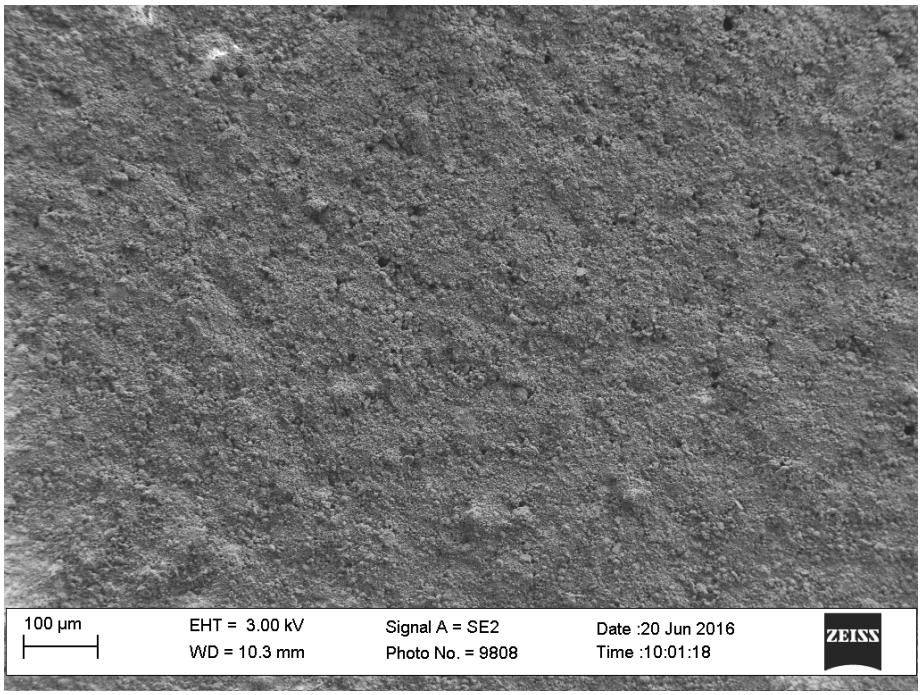

Figure A.47: SEM micrograph of Sn-Beta deposited on ZnSe after being on stream for 8 hours.

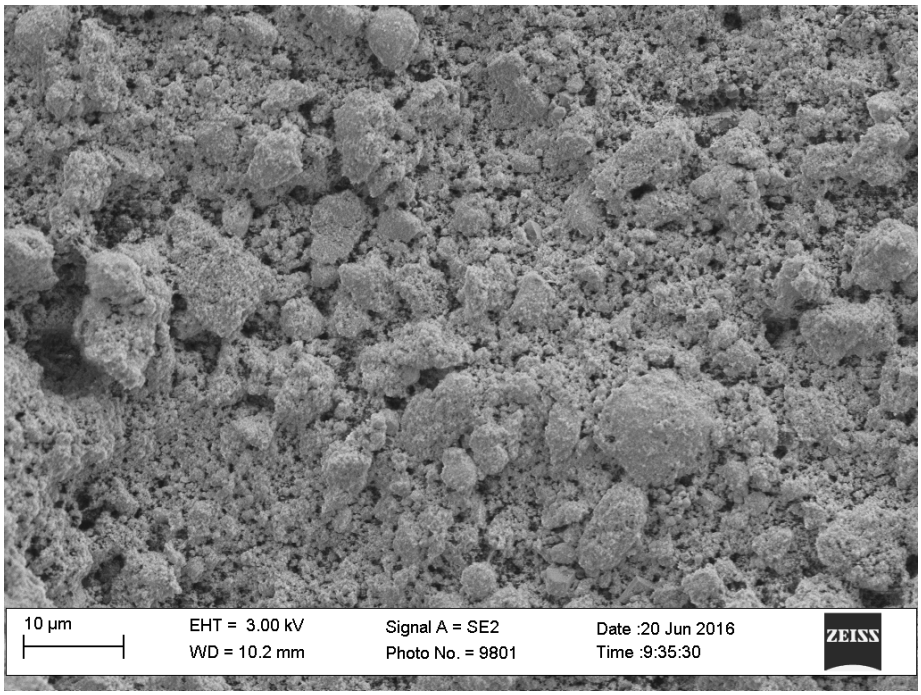

Figure A.48: SEM micrograph of Sn-Beta deposited on ZnSe after being on stream for 8 hours.

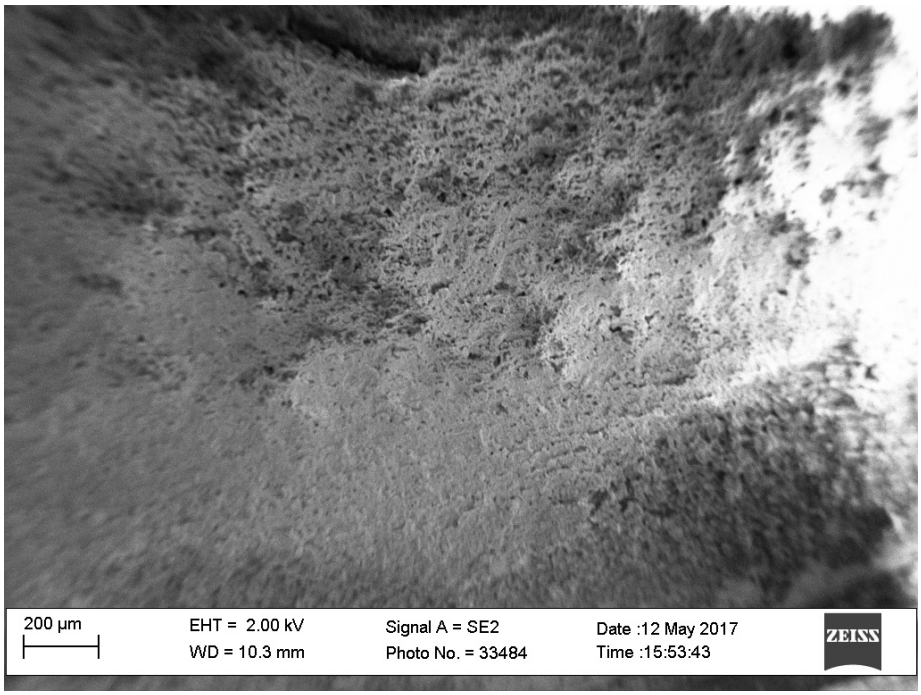

Figure A.49: SEM micrograph of Sn-MCM-41 deposited on ZnSe.

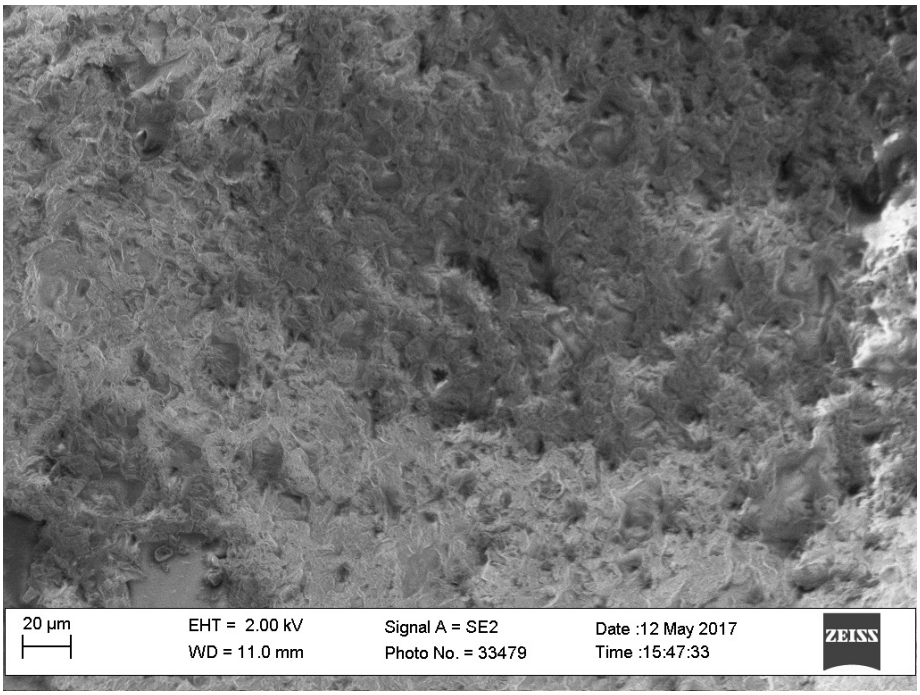

Figure A.50: SEM micrograph of Sn-MCM-41 deposited on ZnSe.

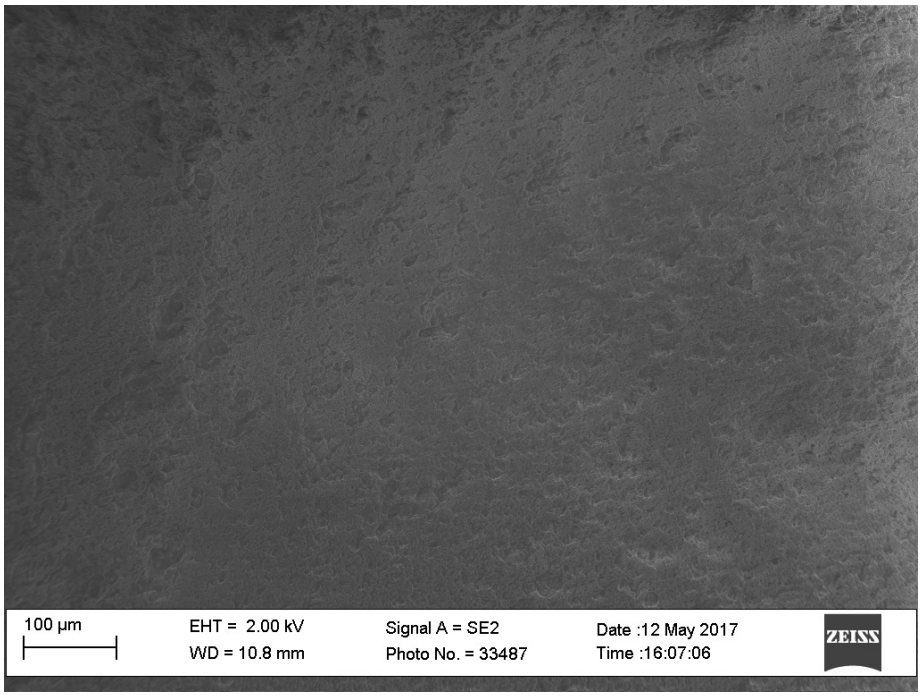

Figure A.51: SEM micrograph of Sn-SBA-15 deposited on ZnSe.

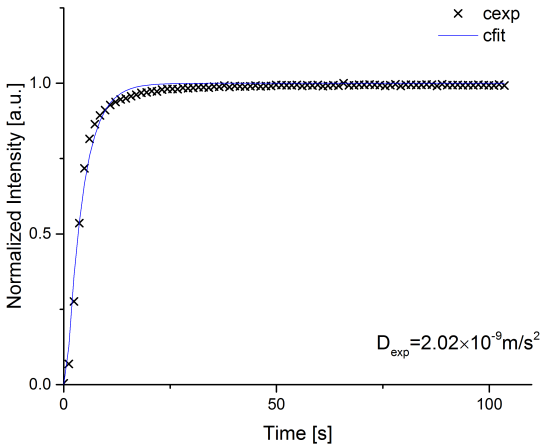

Figure A.52: 40 mM citronellal in chloroform over bare ZnSe crystal step increase, measured IR response and the corresponding fit.

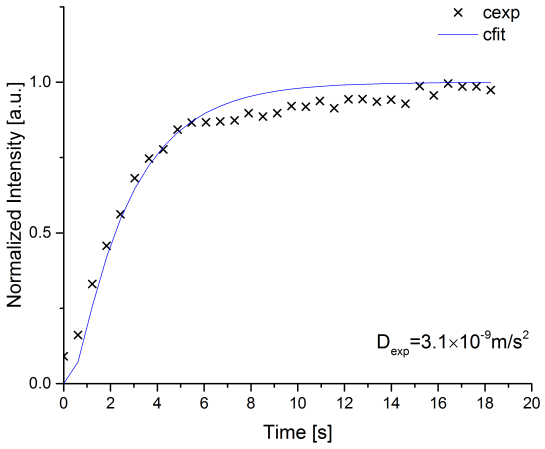

Figure A.53: 40 mM citronellal in hexane over bare ZnSe crystal step increase, measured IR response and the corresponding fit.

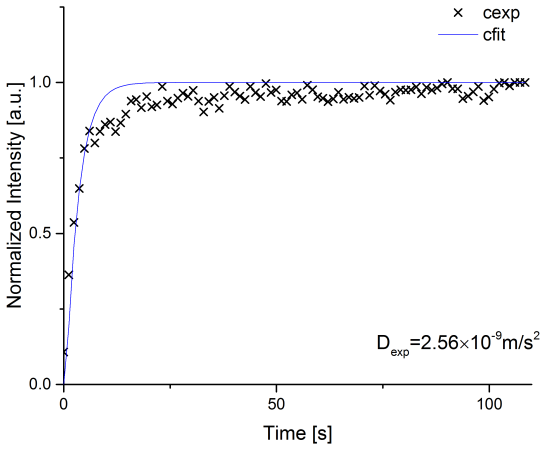

Figure A.54: 40 mM citronellal in toluene over bare ZnSe crystal step increase, measured IR response and the corresponding fit.

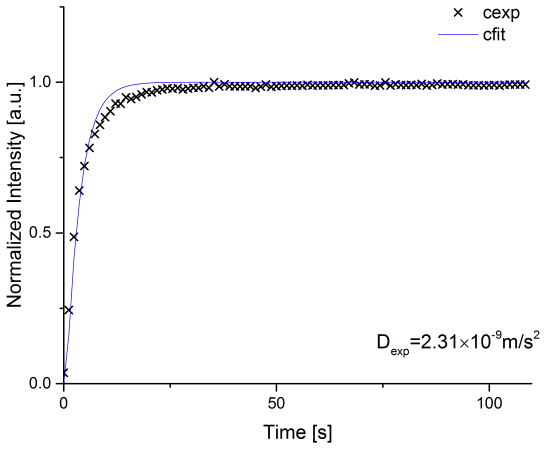

Figure A.55: 40 mM citronellal in 2,3-dimethylbutane over bare ZnSe crystal step increase, measured IR response and the corresponding fit.

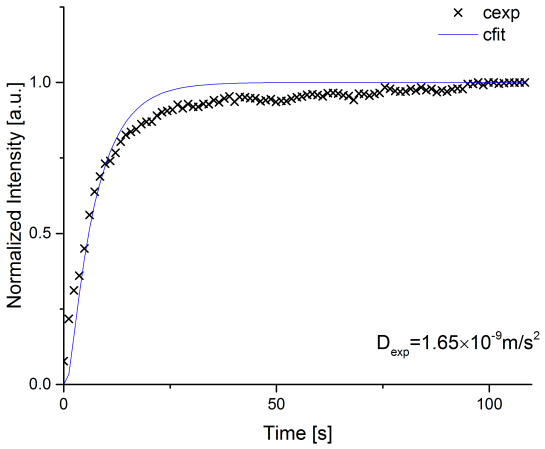

Figure A.56: 40 mM citronellal in p-xylene over bare ZnSe crystal step increase, measured IR response and the corresponding fit.

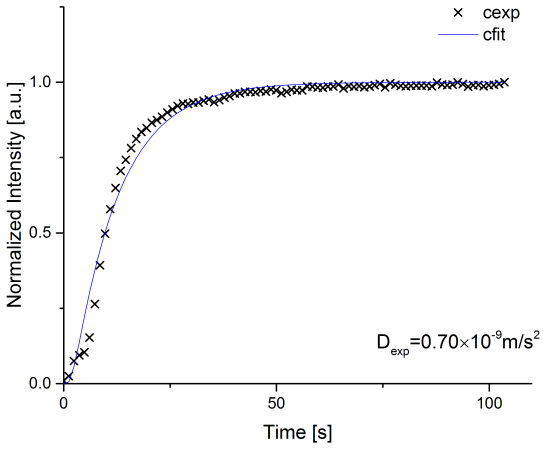

Figure A.57: 40 mM citronellal in chloroform over Sn-Beta step increase, measured IR response and the corresponding fit.

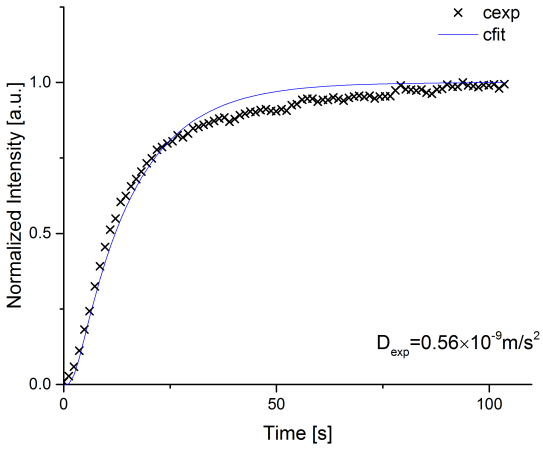

Figure A.58: 40 mM citronellal in hexane over Sn-Beta step increase, measured IR response and the corresponding fit.

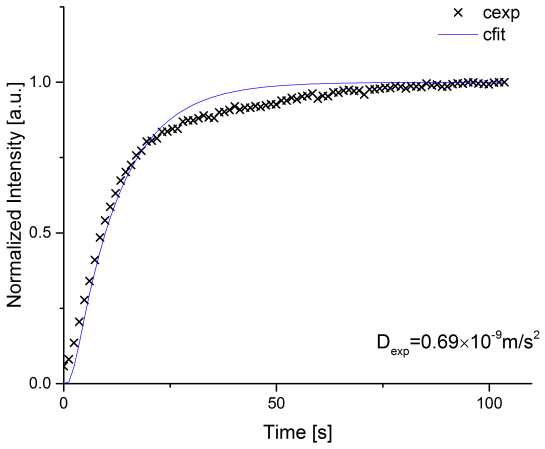

Figure A.59: 40 mM citronellal in 2,3-dimethylbutane over Sn-Beta step increase, measured IR response and the corresponding fit.

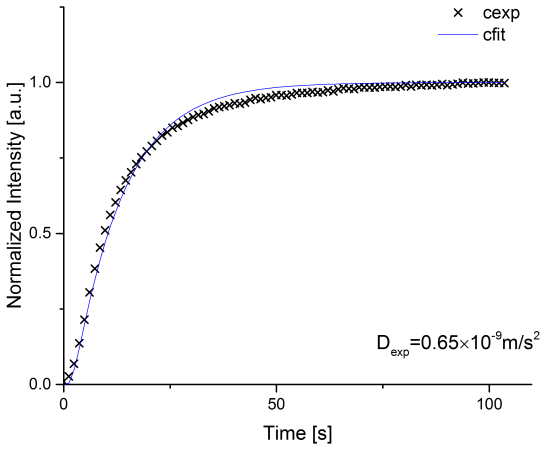

Figure A.60: 40 mM citronellal in p-xylene over Sn-Beta step increase, measured IR response and the corresponding fit.

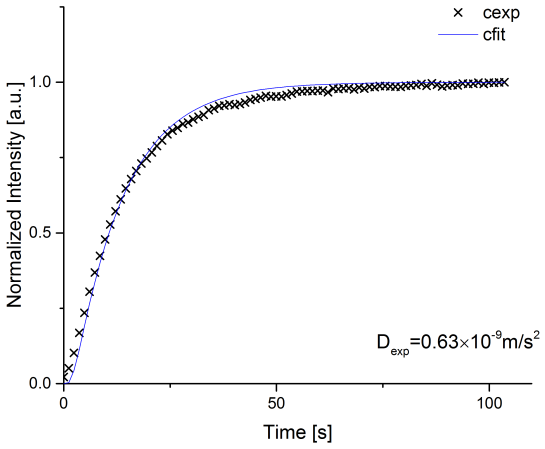

Figure A.61: 40 mM citronellal in toluene over Sn-Beta step increase, measured IR response and the corresponding fit.

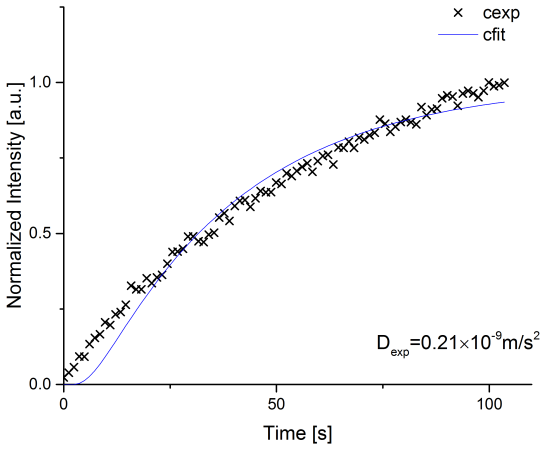

Figure A.62: 40 mM citronellal in chloroform over Sn-SBA-15 step increase, measured IR response and the corresponding fit.

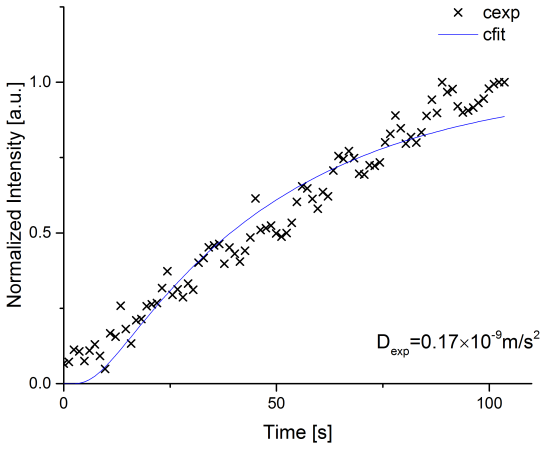

Figure A.63: 40 mM citronellal in hexane over Sn-SBA-15 step increase, measured IR response and the corresponding fit.

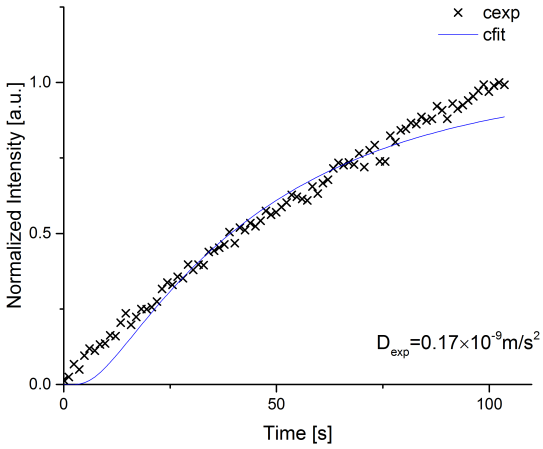

Figure A.64: 40 mM citronellal in 2,3-dimethylbutane over Sn-SBA-15 step increase, measured IR response and the corresponding fit.

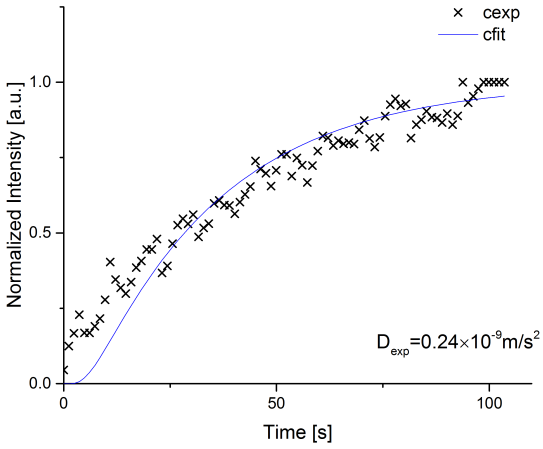

Figure A.65: 40 mM citronellal in p-xylene over Sn-SBA-15 step increase, measured IR response and the corresponding fit.

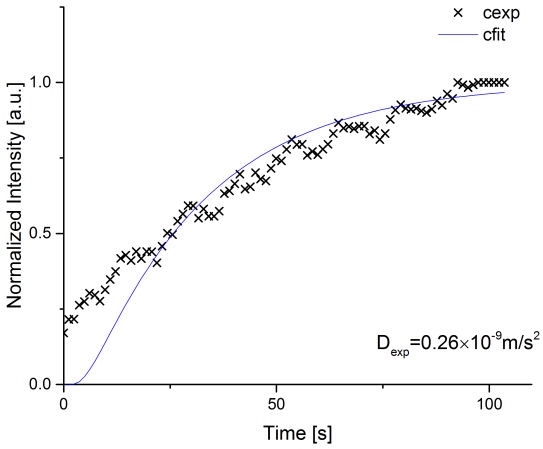

Figure A.66: 40 mM citronellal in toluene over Sn-SBA-15 step increase, measured IR response and the corresponding fit.

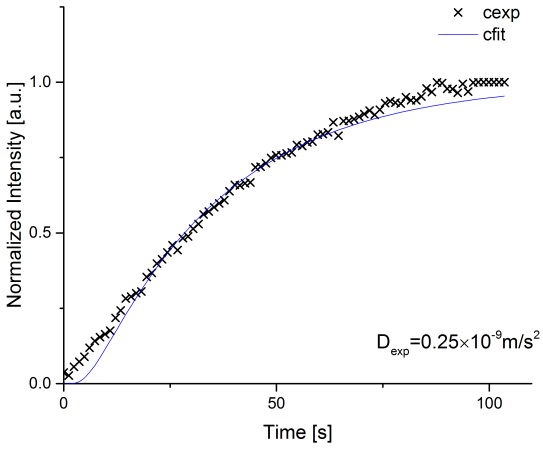

Figure A.67: 40 mM citronellal in chloroform over Sn-MCM-41 step increase, measured IR response and the corresponding fit.

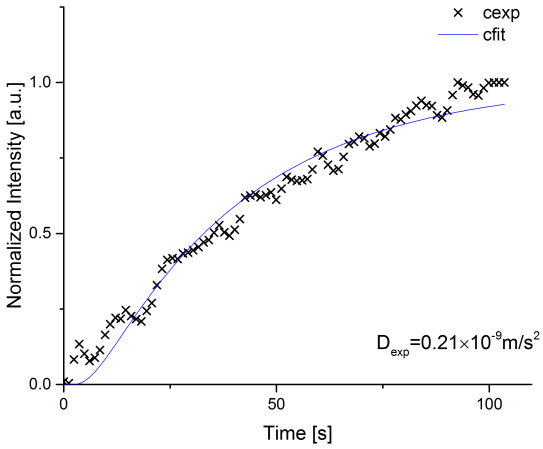

Figure A.68: 40 mM citronellal in hexane over Sn-MCM-41 step increase, measured IR response and the corresponding fit.

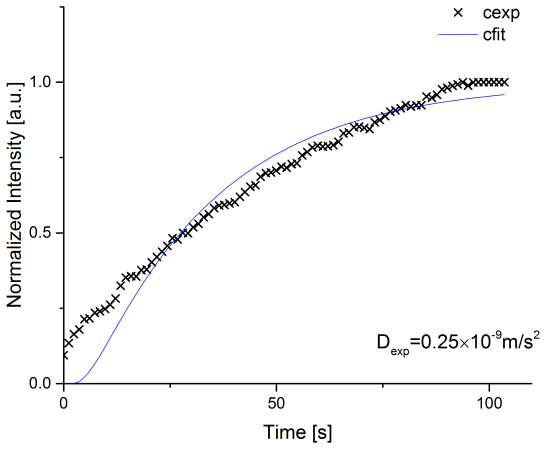

Figure A.69: 40 mM citronellal in 2,3-dimethylbutane over Sn-MCM-41 step increase, measured IR response and the corresponding fit.

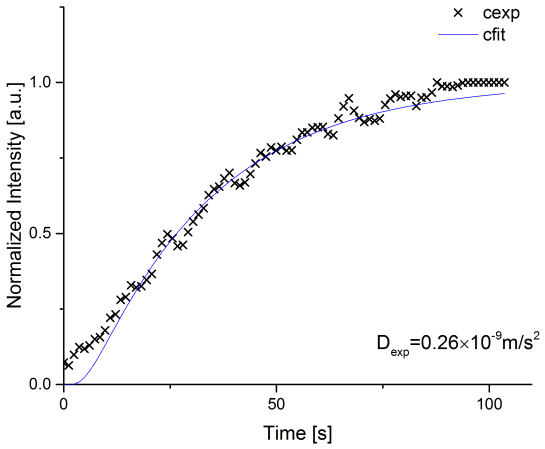

Figure A.70: 40 mM citronellal in p-xylene over Sn-MCM-41 step increase, measured IR response and the corresponding fit.

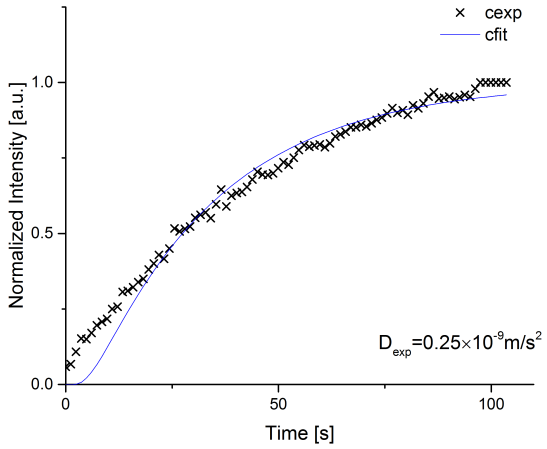

Figure A.71: 40 mM citronellal in toluene over Sn-MCM-41 step increase, measured IR response and the corresponding fit.

A.3 Annexes Chapter 4

Characterization

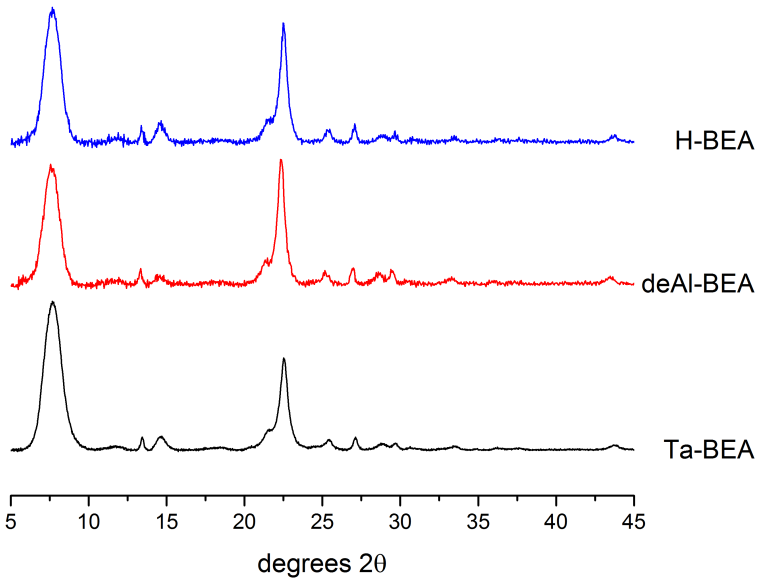

Figure A.72: X-Ray Diffraction patterns of H-BEA, deAl-BEA and Ta-BEA.

Table A.5: Key characteristics of the synthesized catalysts.

Catalyst	Ta content [wt%] [xvi]	SiO_2/Al_2O_3 [xii]	S_{BET} $[m^2/g]$ [xvii]	V_{micro} $[cm^3/g]$ [xviii]	S_{ext} [xix]
H-BEA	-	25	605	0.17	243
Ta-BEA	2.5	>1500	588	0.19	234

[xvi] determined by ICP-OES
[xvii] BET surface area
[xviii] Micropore volume determined with t-plot method
[xix] external surface area determined with t-plot method

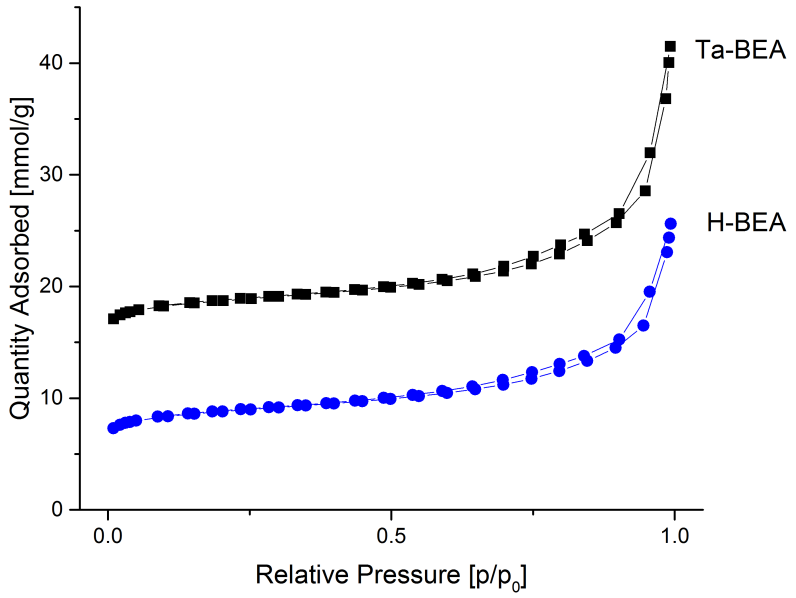

Figure A.73: N_2 adsorption and desorption isotherms of Ta-BEA and H-BEA. The values for Ta-BEA are offset by 10 mmol/g for better visibility.

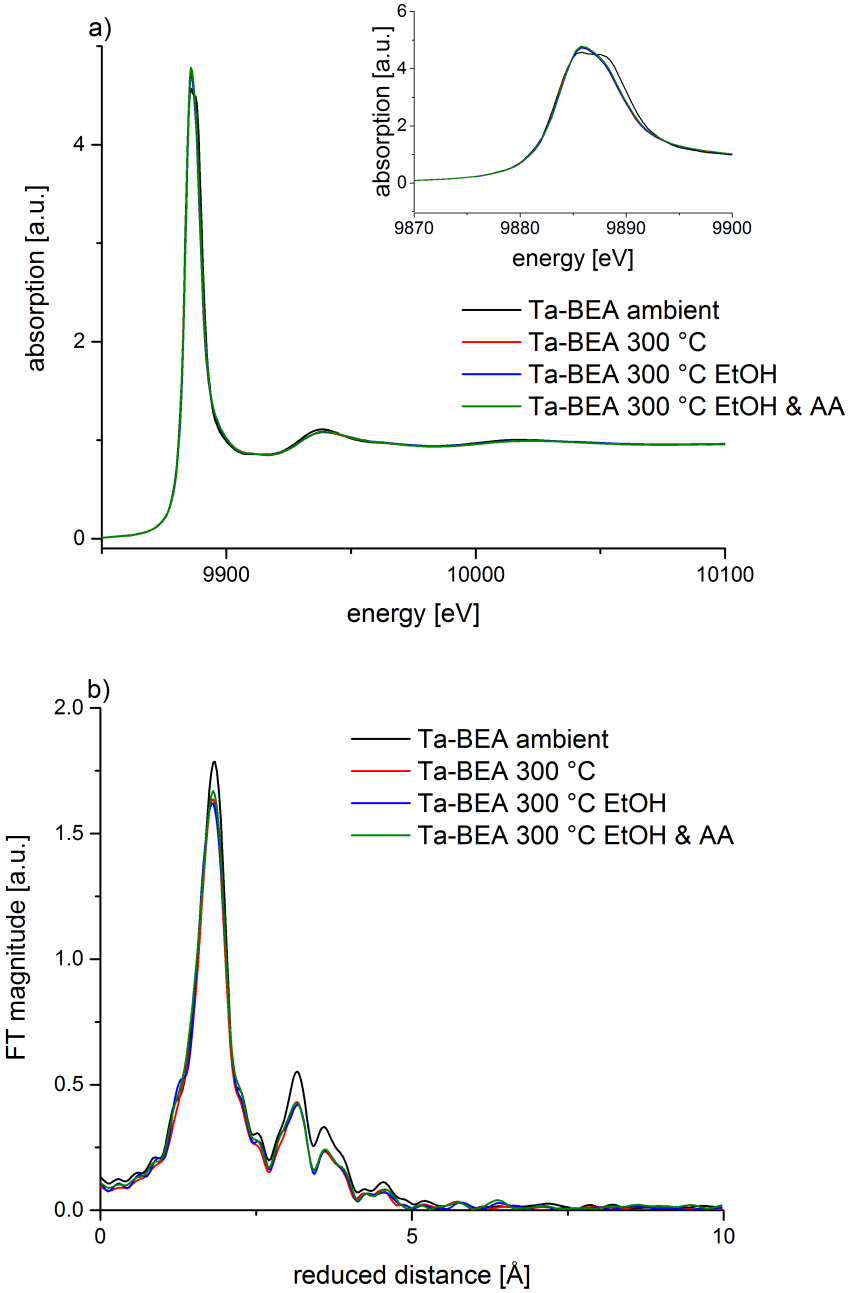

Figure A.74: *In situ* EXAFS spectra a) and Fourier Transform b) of the Ta L_3 edge in Ta-BEA under different conditions after 1 hour on stream.

Table A.6: Fragmentation patterns of the different measured compounds, based on reference[247] in the manuscript and our own measurements. Only signals with an intensity of 0.1 relative to the most intense signal are shown, with signal intensity decreasing from left to right. The chosen signals are shown in bold.

Molecule	m/z most abundant				→					least abundant
He/H_2	2									
H_2O	**18**	17								
HDO	**19**	18								
D_2O	**20**	19								
Ethylene	28	27	26							
O_2	32									
Propylene	41	39	42	27	40	38				
AA	29	**44**	43	15						
BD	39	**54**	53	27	28	50	51			
Butene	41	56	28	27						
CA	41	39	**70**	69	38	27				
COH	**57**	29	39	43	27	31	72			
Butanol	56	31	41	43	27	42	29	55	39	28
DEE	31	59	45	74	29	27				
AOL	45	42	29	43	44	41	27	39	70	
EtOH	31	45	29	27	**46**					

Modulation Experiments

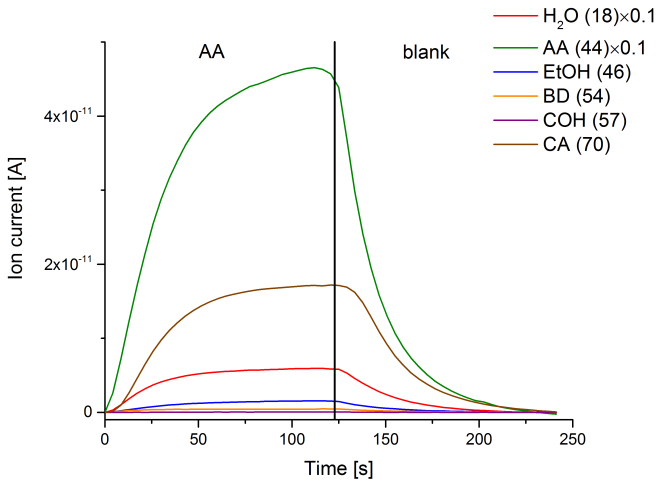

Figure A.75: Modulation experiments between AA in He and pure He over Ta-BEA at 300 °C. The recorded MS signals of a modulation experiment, where the surface was first dehydrated with He followed by periodically switching to AA are shown. The switch from one flow to another was done after 120 seconds as indicated by the black line. Three periods were averaged when quasi steady-state was reached.

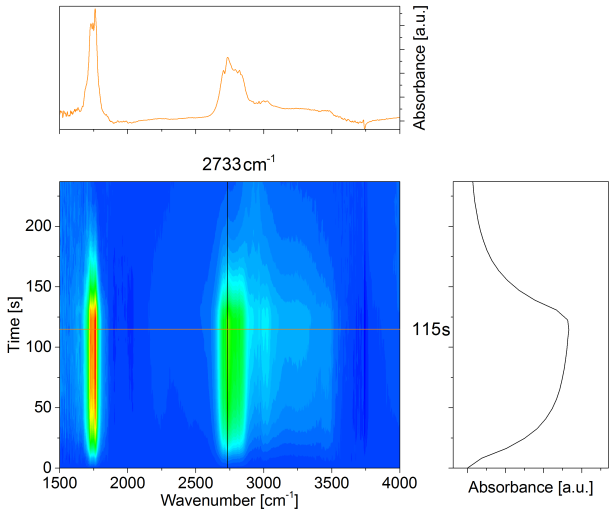

Figure A.76: Infrared spectra corresponding to the experiment in Figure A.75, where AA was adsorbed on Ta-BEA at 300 °C.

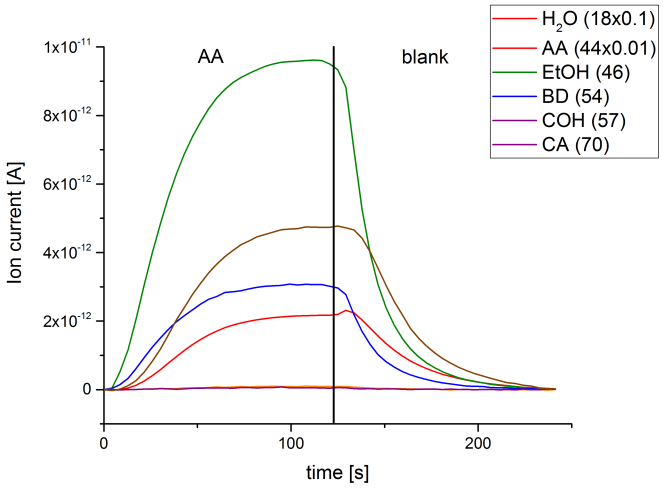

Figure A.77: Modulation experiments between AA in He and pure He over SiO_2 at 300 °C. The recorded MS signals of a modulation experiment, where the surface was first dehydrated with He followed by periodically switching to AA are shown. The switch from one flow to another was done after 120 seconds as indicated by the black line. Three periods were averaged when quasi steady-state was reached.

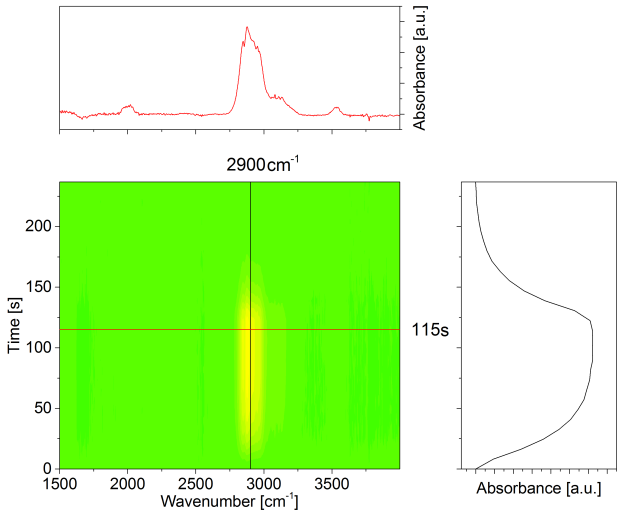

Figure A.78: Infrared spectra corresponding to the experiment in Figure A.77, where AA was adsorbed on SiO_2 at 300 °C.

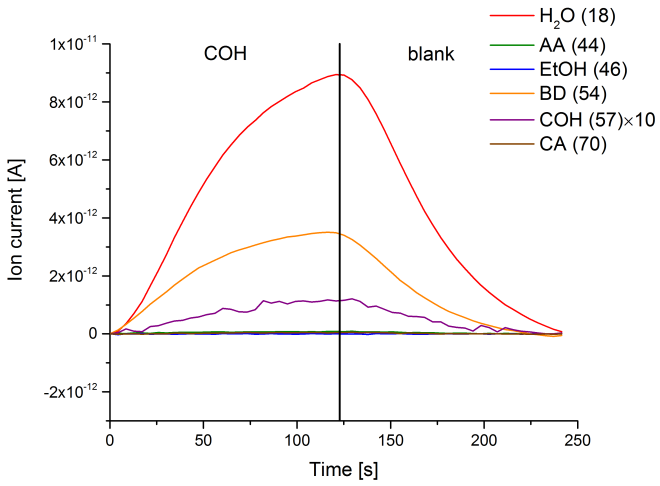

Figure A.79: Modulation experiments between COH in He and pure He over Ta-BEA at 300 °C. The recorded MS signals of a modulation experiment, where the surface was first dehydrated with He followed by periodically switching to COH are shown. The switch from one flow to another was done after 120 seconds as indicated by the black line. Three periods were averaged when quasi steady-state was reached.

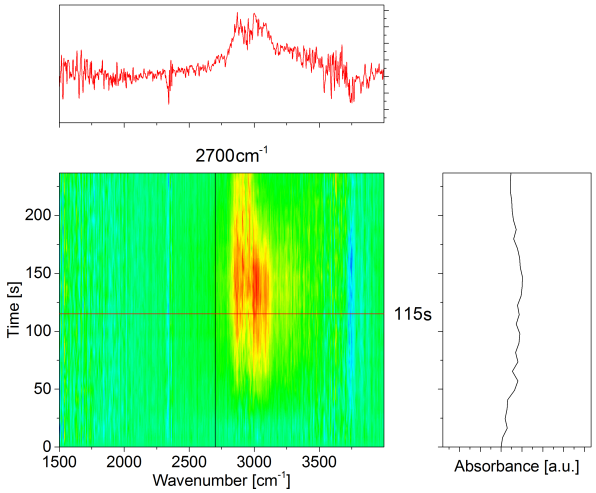

Figure A.80: Infrared spectra corresponding to the experiment in Figure A.79, where COH and He were modulated over Ta-BEA at 300 °C.

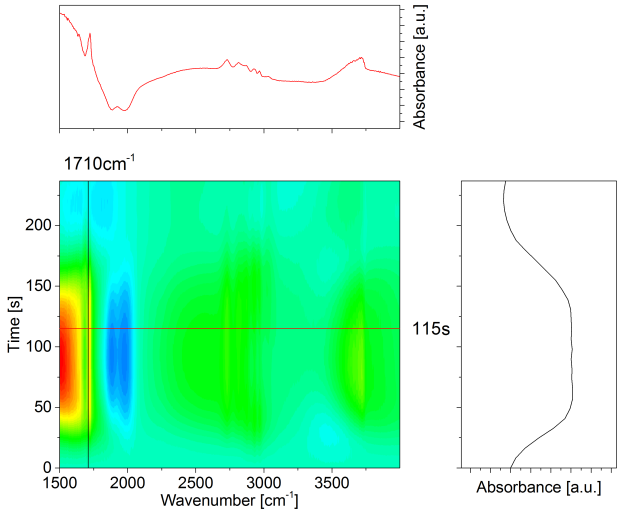

Figure A.81: Modulation experiments between CA in He and pure He over Ta-BEA at 300 °C. The IR spectra of a modulation experiment, where the surface was first dehydrated with He followed by periodically switching to AA are shown.

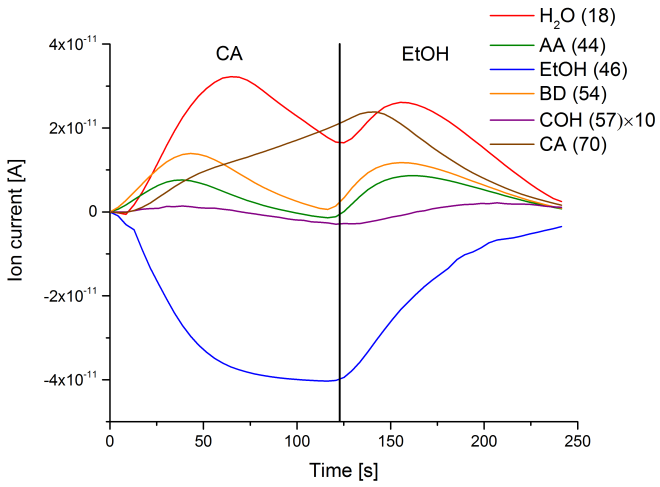

Figure A.82: Modulation experiment between EtOH in He and pure CA in He over Ta-BEA at 300 °C. The recorded MS signals of a modulation experiment, where the surface was first saturated with EtOH followed by periodically switching to CA are shown. The switch from one flow to another was done after 120 seconds as indicated by the black line. Three periods were averaged when quasi steady-state was reached.

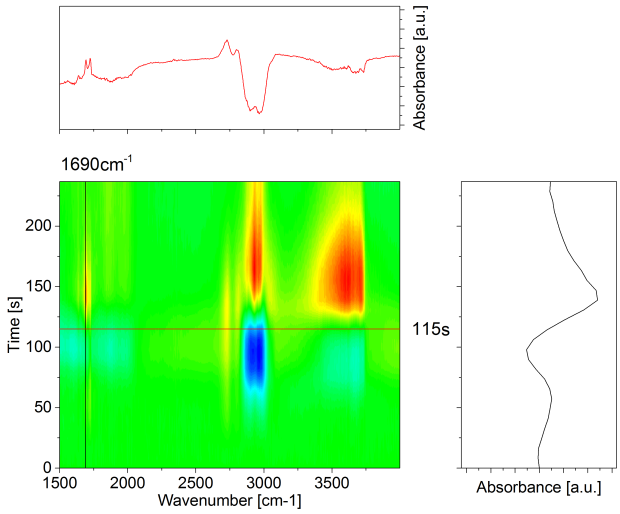

Figure A.83: Infrared spectra corresponding to the experiment in Figure A.82, where EtOH and CA were modulated over Ta-BEA at 300 °C.

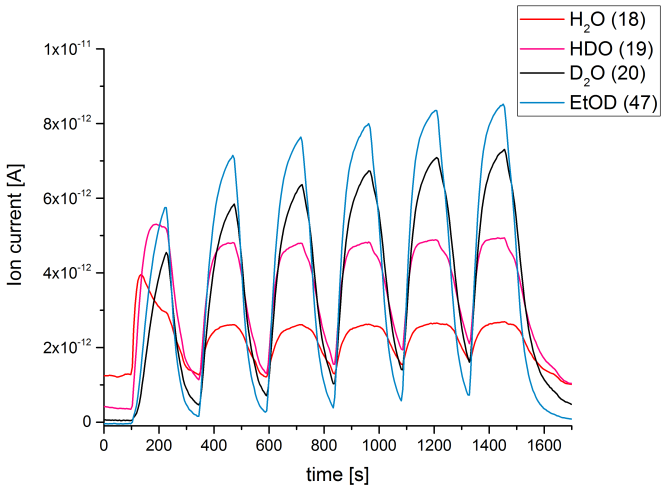

Figure A.84: MS signals of a modulated adsorption of EtOD on Ta-BEA at 300 °C. Six modulation periods are shown.

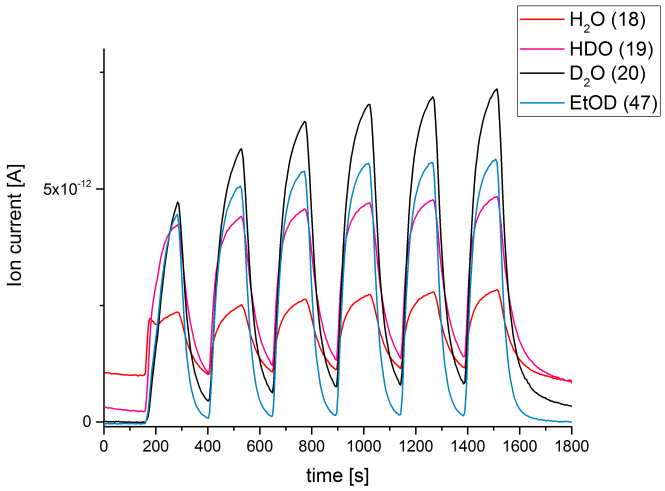

Figure A.85: MS signals of a modulated adsorption of EtOD on SiO_2 at 300 °C. Six modulation periods are shown.

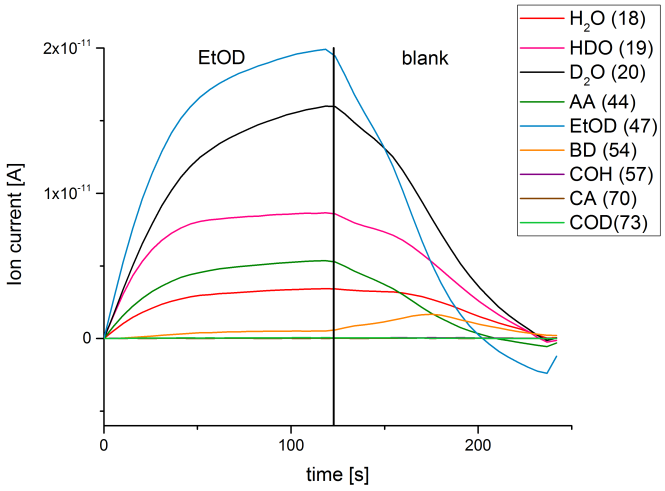

Figure A.86: Modulation experiment between EtOD in He and pure He over Ta-BEA at 300 °C. The recorded MS signals of a modulation experiment, where the surface was first dehydrated with He followed by periodically switching to EtOD are shown. The last three periods of Figure A.84 were averaged to give this figure. The switch from one flow to another was done after 120 seconds as indicated by the black line. Three periods were averaged when quasi steady-state was reached.

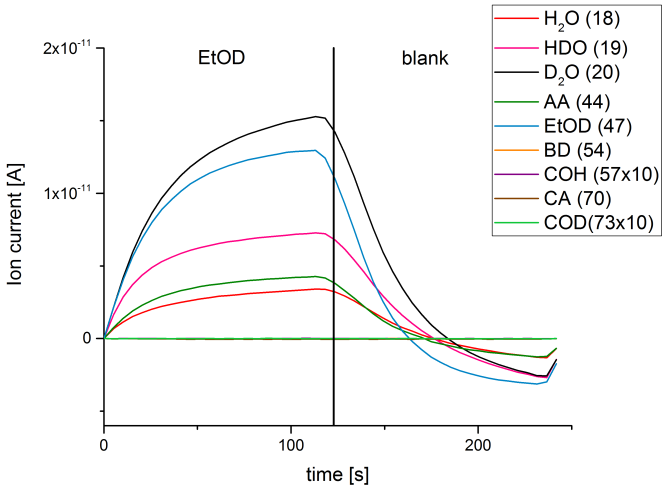

Figure A.87: Modulation experiment between EtOD in He and pure He over SiO_2 at 300 °C. The recorded MS signals of a modulation experiment, where the surface was first dehydrated with He followed by periodically switching to EtOD are shown. The last three periods of Figure A.85 were averaged to give this figure. The switch from one flow to another was done after 120 seconds as indicated by the black line. Three periods were averaged when quasi steady-state was reached.

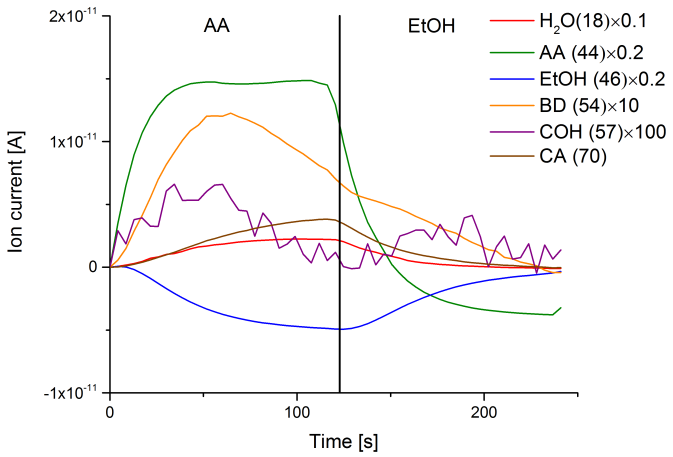

Figure A.88: Modulation experiment between EtOH in He and AA in He over Ta-BEA at 300 °C. The recorded MS signals of a modulation experiment, where the surface was first saturated with EtOH followed by periodically switching to AA are shown. The switch from one flow to another was done after 120 seconds as indicated by the black line. Three periods were averaged when quasi steady-state was reached.

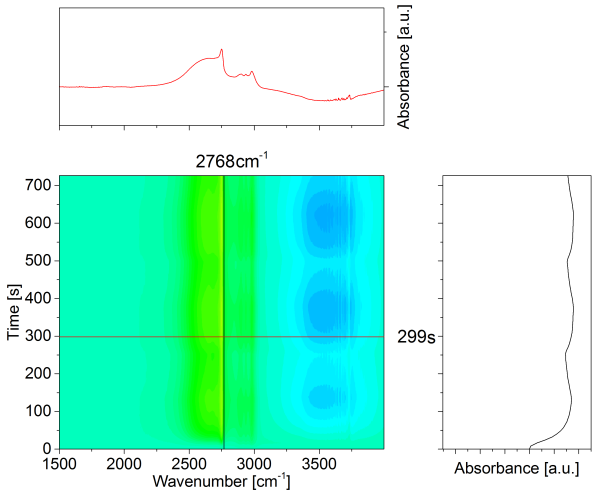

Figure A.89: Infrared spectra corresponding to the experiment in Figures A.84 & A.85, where EtOD and pure He were modulated over Ta-BEA at 300 °C. The first three periods are shown.

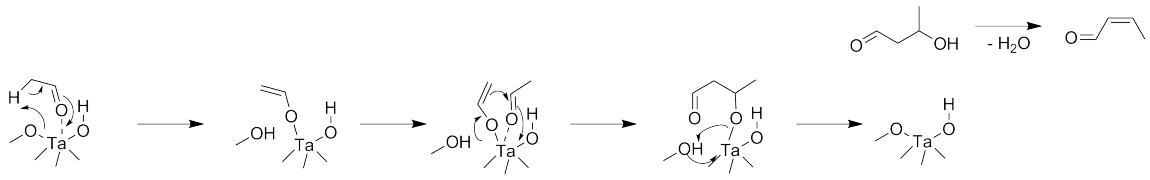

Figure A.90: Soft enolization mechanism for the AA coupling over Ta-BEA inspired by references[258] and[259].

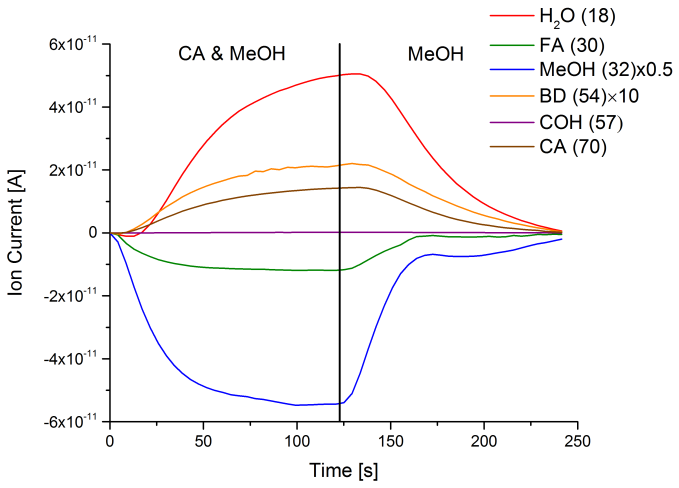

Figure A.91: Modulation experiment between MeOH/CA in He and MeOH in He over Ta-BEA at 300 °C. The recorded MS signals of a modulation experiment, where the surface was first saturated with MeOH followed by periodically switching to MeOH/CA are shown. The switch from one flow to another was done after 120 seconds as indicated by the black line. Three periods were averaged when quasi steady-state was reached.

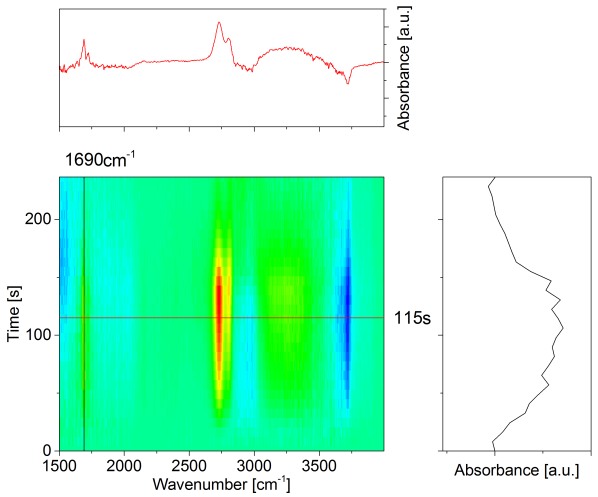

Figure A.92: Infrared spectra corresponding to the experiment in Figure A.91, where MeOH/CA and MeOH were modulated over Ta-BEA at 300 °C.

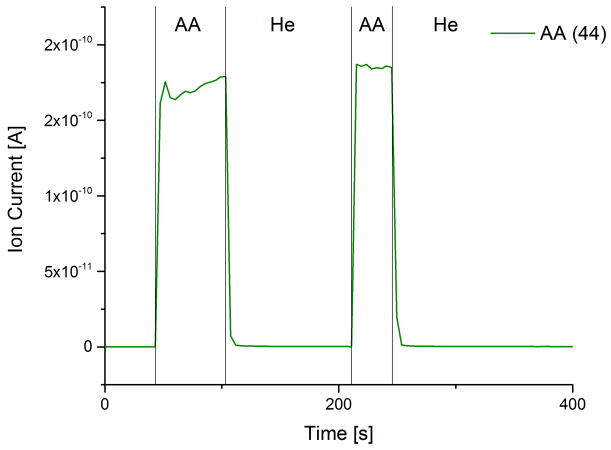

Figure A.93: MS response of switching from pure He to AA flow when going through the bypass. A fast response can be observed indicating only a small dead volume.

A.4 Annexes Chapter 5

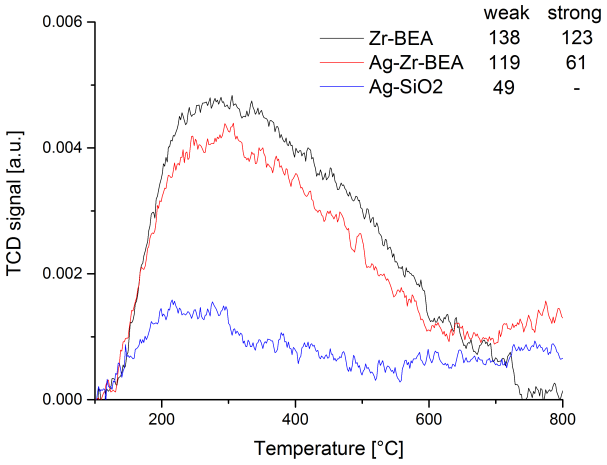

Figure A.94: NH_3-TPD profiles of the different catalysts. The numbers under weak and strong correspond to weak and strong acid sites determined after deconvolution of the signals in µmol/g.

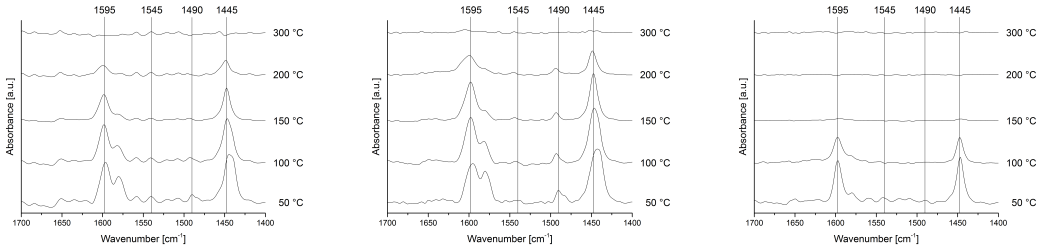

(a) Zr-BEA (b) Ag-Zr-BEA (c) Ag-SiO_2

Figure A.95: FTIR spectra of different catalysts after adsorption of pyridine at different temperatures.

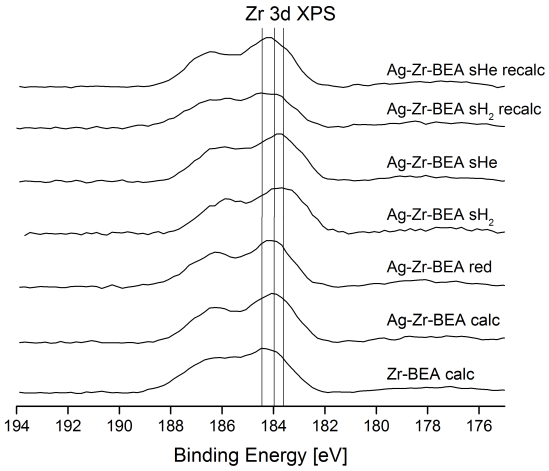

Figure A.96: X-ray photoelectron spectra of the Zr 3d line for the different catalysts.

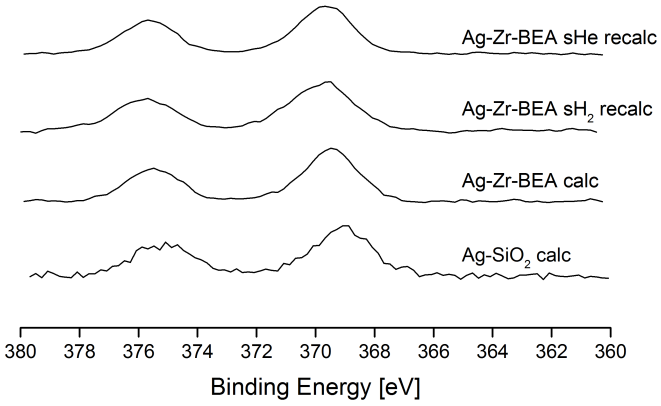

Figure A.97: X-ray photoelectron spectra of the Ag 3d line for the different catalysts.

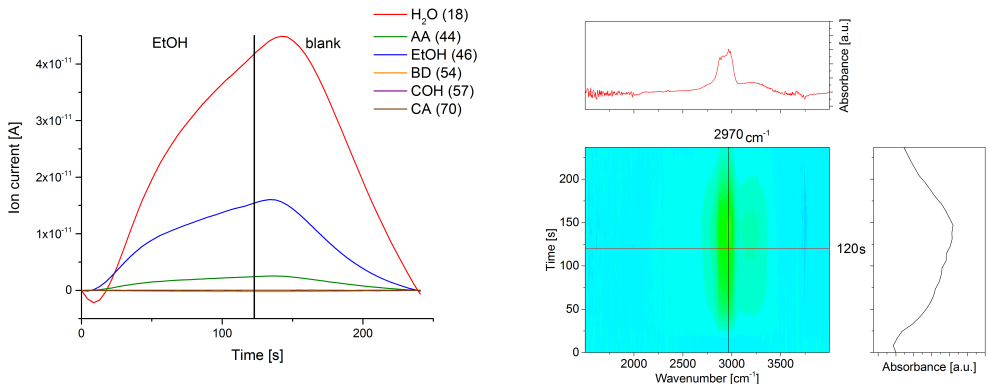

(a) MS spectra (b) IR spectra

Figure A.98: Modulation experiment between EtOH and pure He over Zr-BEA.

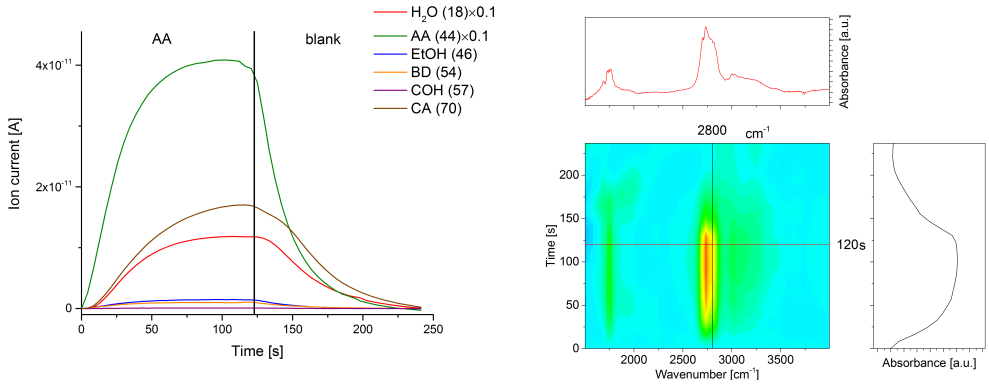

(a) MS spectra (b) IR spectra

Figure A.99: Modulation experiment between AA and pure He over Zr-BEA.

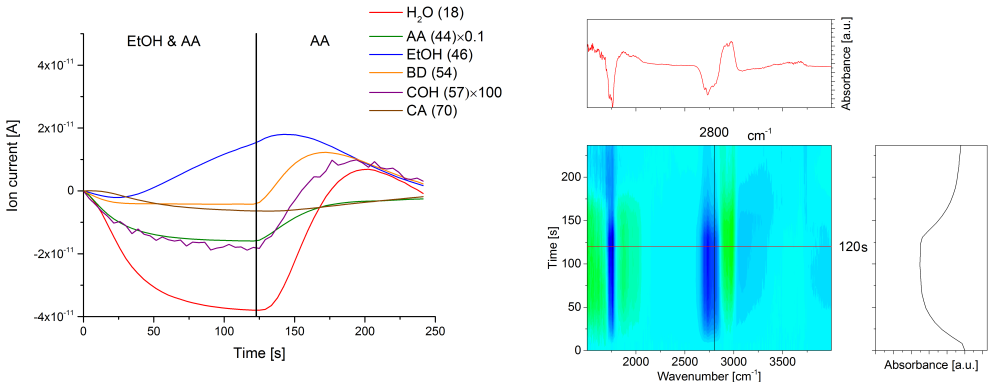

(a) MS spectra (b) IR spectra

Figure A.100: Modulation experiment between a 3:1 mixture of EtOH & AA and AA over Zr-BEA.

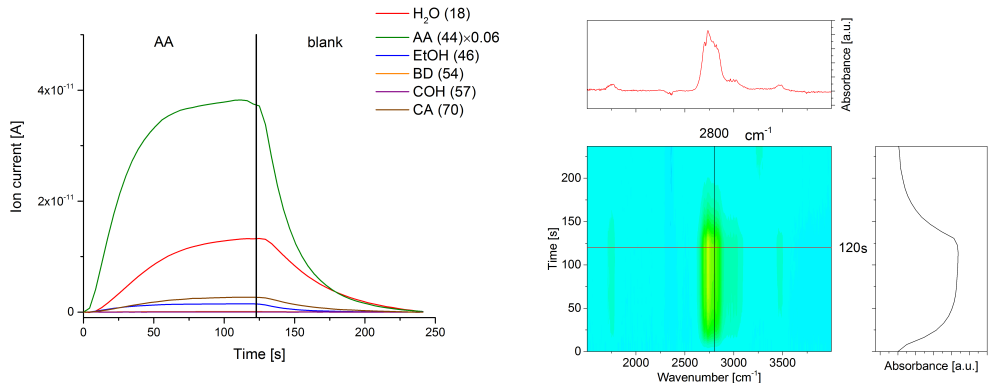

(a) MS spectra (b) IR spectra

Figure A.101: Modulation experiment between AA and pure He over Ag-SiO_2.

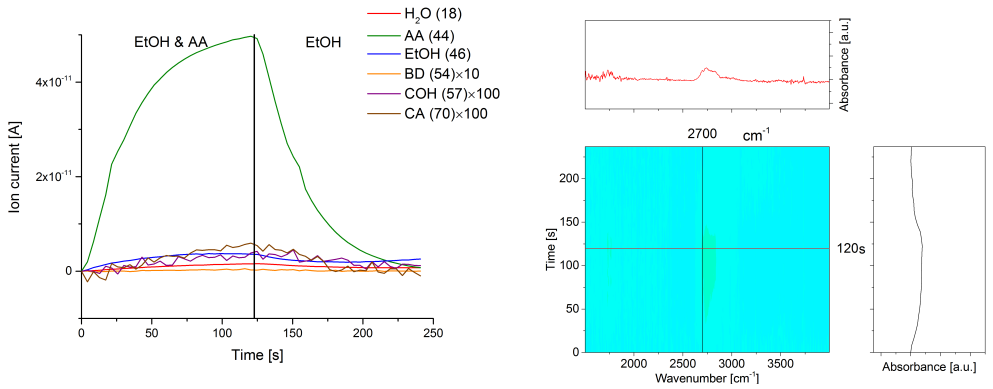

(a) MS spectra (b) IR spectra

Figure A.102: Modulation experiment between a 3:1 mixture of EtOH & AA and EtOH over Ag-SiO_2.

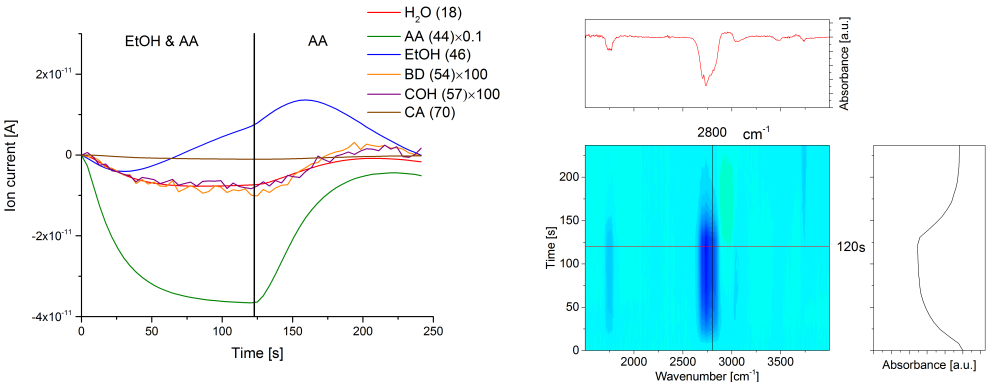

(a) MS spectra (b) IR spectra

Figure A.103: Modulation experiment between a 3:1 mixture of EtOH & AA and AA over Ag-SiO_2.

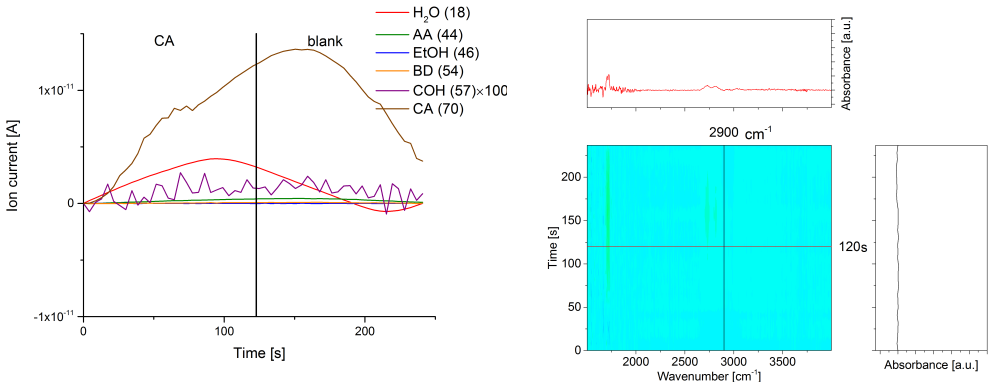

(a) MS spectra (b) IR spectra

Figure A.104: Modulation experiment between CA and pure He over Ag-SiO_2.

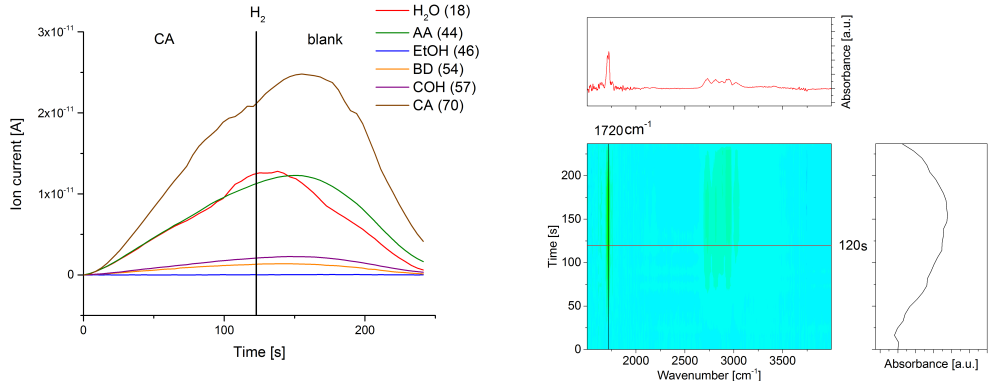

(a) MS spectra (b) IR spectra

Figure A.105: Modulation experiment between CA and pure He over Ag-SiO_2 under H_2 flow.

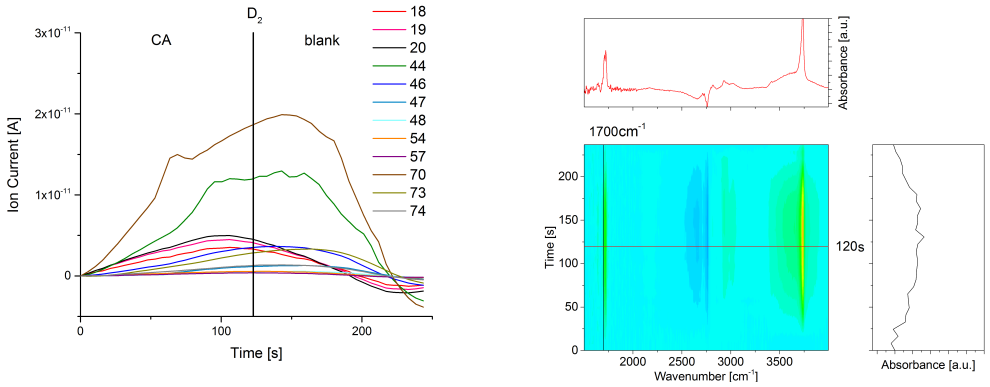

(a) MS spectra (b) IR spectra

Figure A.106: Modulation experiment between CA and pure He over Ag-SiO_2 under D_2 flow.

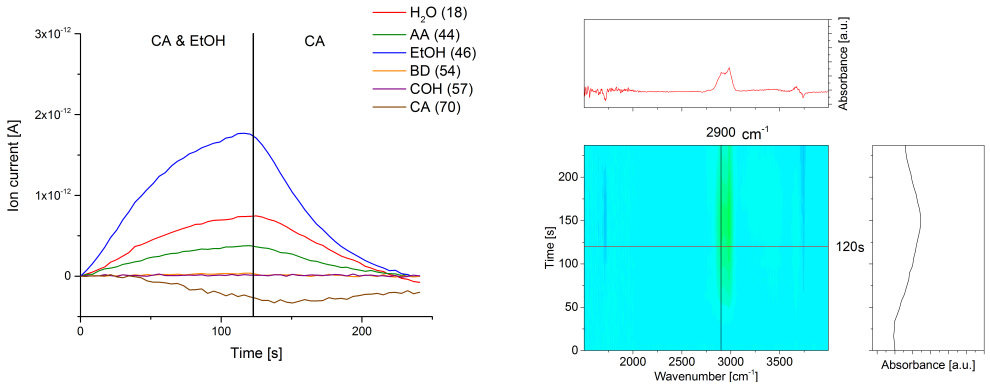

(a) MS spectra (b) IR spectra

Figure A.107: Modulation experiment between a 3:1 mixture of EtOH & CA and CA over Ag-SiO_2.

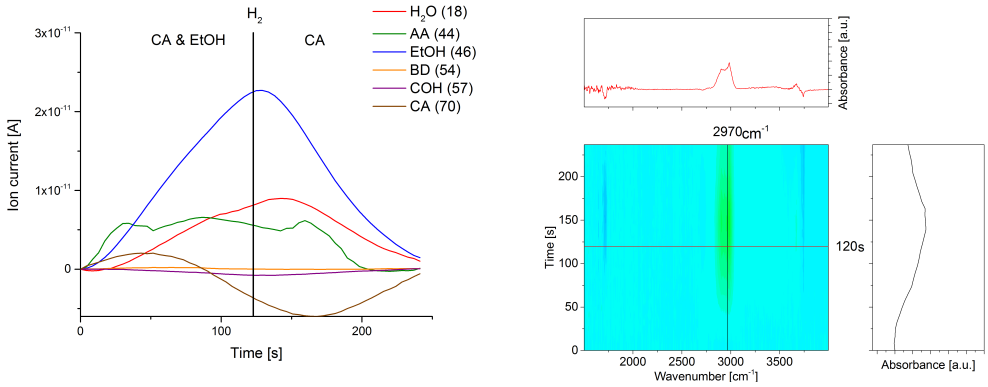

(a) MS spectra (b) IR spectra

Figure A.108: Modulation experiment between a 3:1 mixture of EtOH & CA and CA over Ag-SiO_2 under H_2 flow.

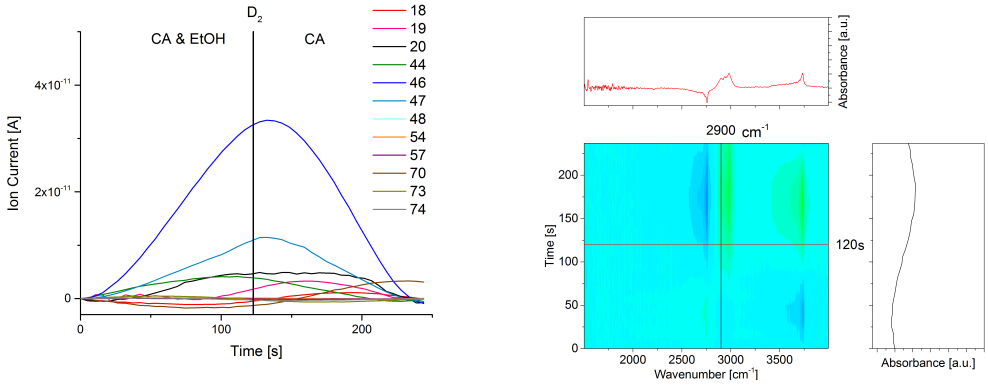

(a) MS spectra (b) IR spectra

Figure A.109: Modulation experiment between a 3:1 mixture of EtOH & CA and CA over Ag-SiO_2 under D_2 flow.

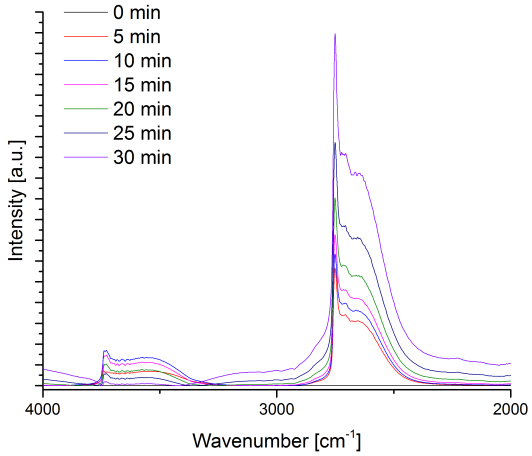

Figure A.110: IR spectra of the reduction of Ag-Zr-BEA under D_2 flow prior to modulation experiments.

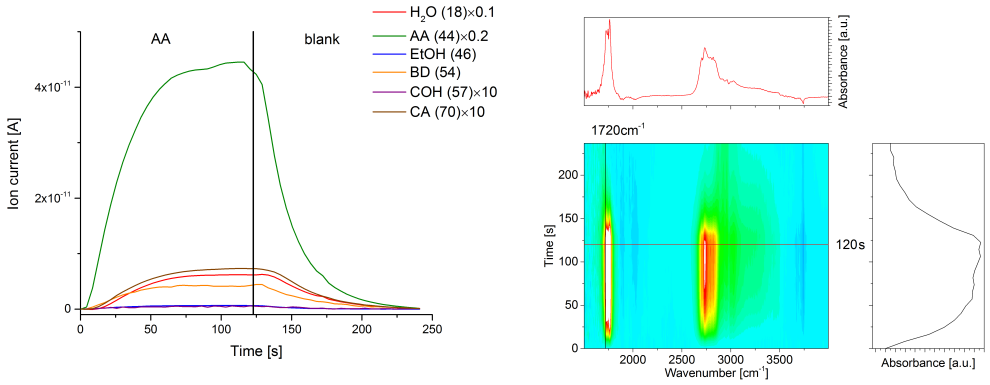

(a) MS spectra (b) IR spectra

Figure A.111: Modulation experiment between AA and pure He over Ag-Zr-BEA.

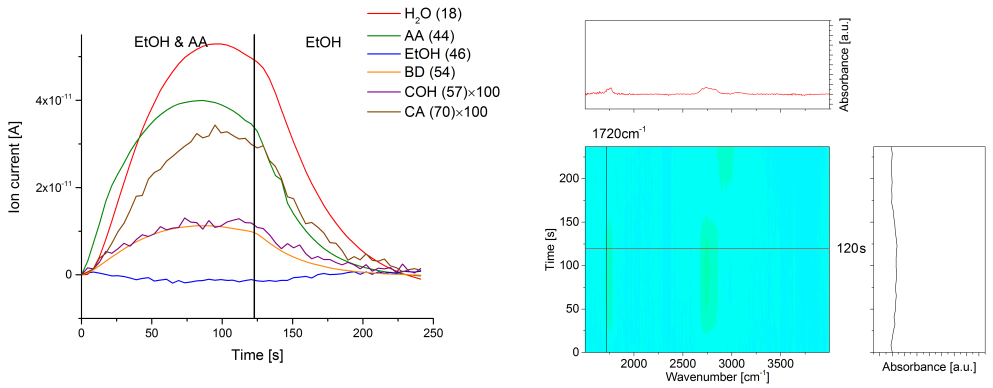

(a) MS spectra (b) IR spectra

Figure A.112: Modulation experiment between a 3:1 mixture of EtOH & AA and EtOH over Ag-Zr-BEA.

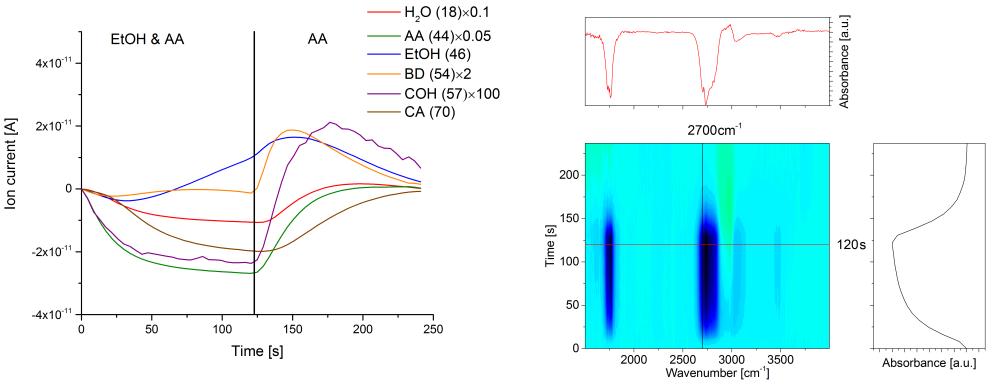

(a) MS spectra (b) IR spectra

Figure A.113: Modulation experiment between a 3:1 mixture of EtOH & AA and AA over Ag-Zr-BEA.

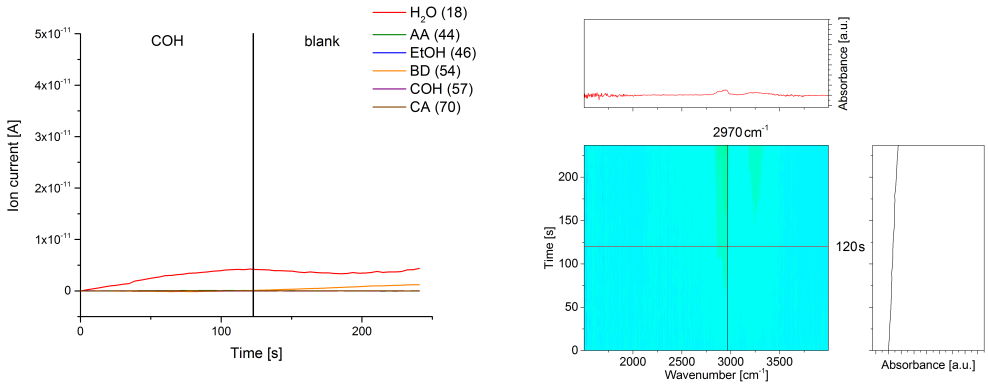

(a) MS spectra (b) IR spectra

Figure A.114: Modulation experiment between COH and pure He over Ag-Zr-BEA.

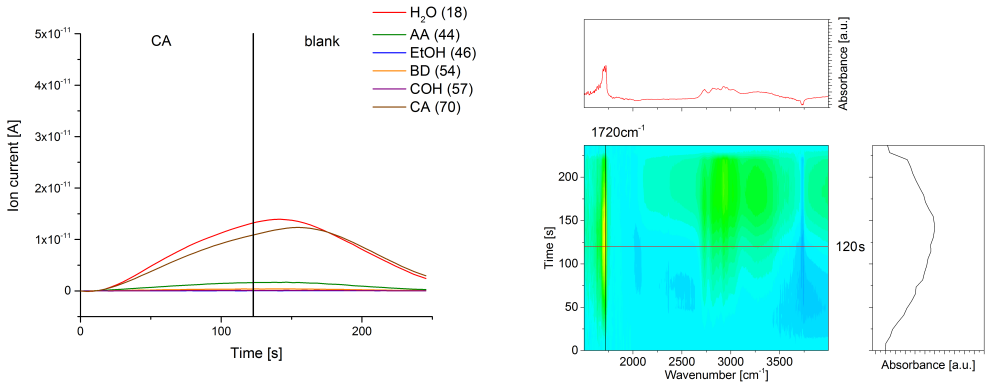

(a) MS spectra (b) IR spectra

Figure A.115: Modulation experiment between CA and pure He over Ag-Zr-BEA.

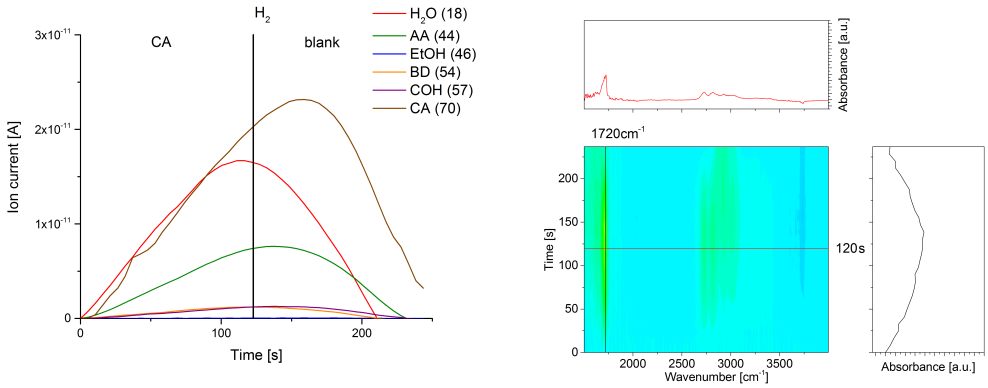

(a) MS spectra (b) IR spectra

Figure A.116: Modulation experiment between CA and pure He over Ag-Zr-BEA under H_2 flow.

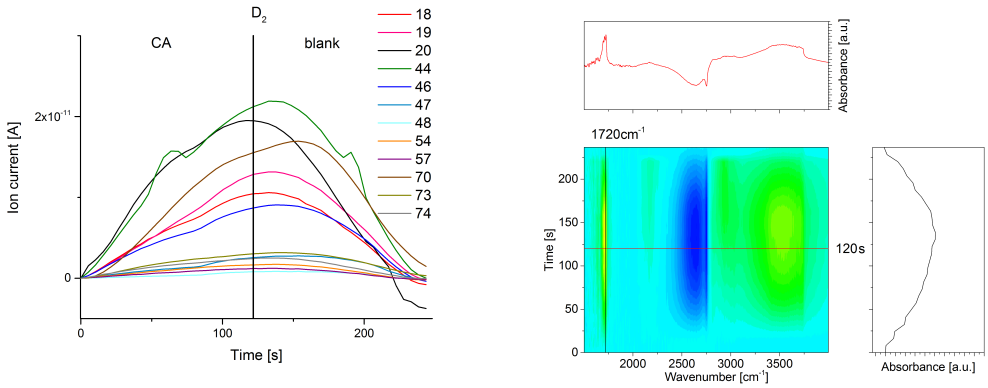

(a) MS spectra (b) IR spectra

Figure A.117: Modulation experiment between CA and pure He over Ag-Zr-BEA under D_2 flow.

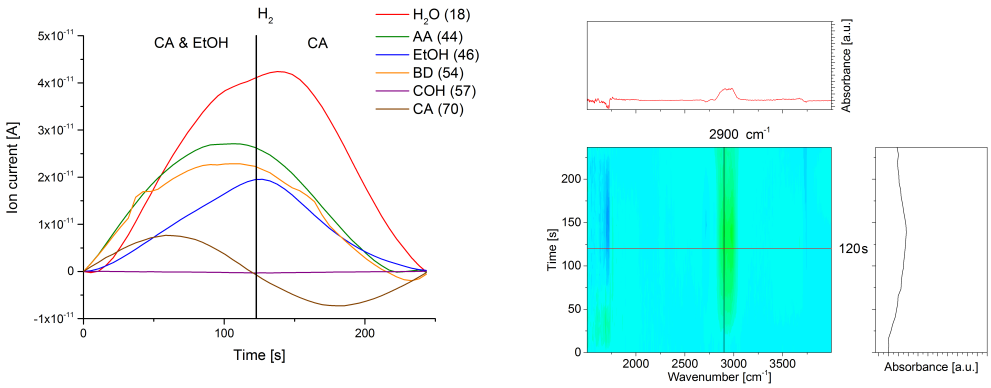

(a) MS spectra (b) IR spectra

Figure A.118: Modulation experiment between a 3:1 mixture of EtOH & CA and CA over Ag-Zr-BEA under H_2 flow.

Doctoral Publications

Monitoring the Thermal Treatment of a Heterogeneous Catalyst Using DRIFTS, Mueller, P.; Conrad, S.; Hermans, I. Spectroscopy, The Application Notebook, September 2014.

Insights into the Complexity of Heterogeneous Liquid-phase Catalysis: Case Study on the Cyclization of Citronellal, Mueller, P.; Wolf, P.; Hermans, I. ACS Catalysis, 2016, 6, 2760-2769. (Chapter 2)

Mechanistic Study on the Lewis-acid Catalyzed Synthesis of 1,3-Butadiene over Ta-BEA Using Modulated Operando DRIFTS-MS, Mueller, P.; Burt, S. P.; Love, A. M.; McDermott, W. P.; Wolf, P.; Hermans, I. ACS Catalysis, 2016, 6, 6823-6832. (Chapter 4)

Influence of Hydrophilicity on the Snβ -Catalyzed Baeyer-Villiger Oxidation of Cyclohexanone with Aqueous Hydrogen Peroxide, Conrad, S.; Wolf, P.; Mueller, P.; Orsted, H.; Hermans, I. ChemCatChem, 2017, 9, 175-182.

Selective oxidative dehydrogenation of propane to propene using boron nitride catalysts, Grant, J. T.; Carrero, C. A.; Goeltl, F.; Venegas, J.; Mueller, P.; Burt, S. P.; Specht, S. E.; McDermott, W. P.; Chieregato, A.; Hermans, I. Science, 2016, 354, 1570-1573.

Applications of Modulation Excitation Spectroscopy in Heterogeneous Catalysis, Mueller, P.; Hermans, I. Industrial & Engineering Chemistry Research, 2017, 56, 1123-1136. (Chapter 1 & 6)

Influence of Metal-Doping on the Lewis-Acid Catalyzed Production of Butadi-

ene from Ethanol Studied by Modulated Operando DRIFTS-MS, Mueller, P.; Wang, S. C.; Burt, S. P.; Hermans, I. *submitted*. (Chapter 5)

Developing a Descriptor-Based Approach for CO and NO Adsorption Strength to Transition Metal Sites in Zeolites, Goeltl, F.; Mueller, P.; Uchupalanun, P.; Sautet, P.; Hermans, I. *submitted*

The Influence of Water and Structural Defects on Optical Spectroscopy of Cu Sites in Zeolites, Goeltl, F.; Conrad, S.; Wolf, P.; Mueller, P.; Wheeler, J.; Hamers, R. J.; Hummer, K.; Kresse, G.; Hermans, I. *to be submitted*

Supported two- and three-dimensional vanadium oxide species on the surface of Beta-SiC Carrero, C. A.; Burt, S. P.; Huang, F.; Venegas, J. M.; Love, A. M.; Mueller, P.; Zhu, H.; Grant, J. T.; Mathison, R.; Hanrahan, M.; Rossini, A.; Ball, M.; Dumesic, J.; Hermans, I. *submitted*

Pre-Doctoral Publications

Simultaneous probing of bulk liquid phase and catalytic gas-liquid-solid interface under working conditions using attenuated total reflection infrared spectroscopy, Meemken, F.; Mueller, P.; Hungerbuhler, K.; Baiker, A. Rev. Sci. Instr. 85(8), 084101.

Presentations

Poster Presentations:

Understanding Heterogeneous Lewis Acid Catalysis using ATR-IR Modulation Excitation Spectroscopy, Mueller, P.; Wolf, P.; Hermans, I. Catalysis Club of Chicago, May 17, 2016, Naperville, IL

Oral Presentations:

Understanding Heterogeneous Lewis Acid Catalysis using ATR-IR Modulation Excitation Spectroscopy, Mueller, P.; Wolf, P.; Hermans, I. 252nd American Chemical Society National Meeting, August 23, 2016, Philadelphia, PA

Enhanced Two-Dimensional Dispersion of Group V Metal Oxides on Silica, Grant, J. T.; Carrero, C. A.; Love, A. M.; Verel, R.; Mueller, P.; Hermans, I. 252nd American Chemical Society National Meeting, August 25, 2016, Philadelphia, PA

Modulation Excitation Spectroscopy Applied on Heterogeneous Lewis-Acid Catalysis, Mueller, P. Catalysis Supergroup Meeting, University of Wisconsin - Madison, September 23, 2016, Madison, WI

C CURRICULUM VITAE

Name	Philipp Müller
Date of birth	April 23rd, 1989
Place of birth	Zug, Switzerland
Nationality	Swiss

Education

2014 - 2017	PhD Chemistry (Materials), University of Wisconsin - Madison, USA
2012 - 2013	MSc Chemical and Biological Engineering, ETH Zürich, Switzerland. Master Thesis under the supervision of Prof. Konrad Hungerbühler and Fabian Meemken.
2009 - 2012	BSc Chemical Engineering, ETH Zürich, Switzerland

REFERENCES

[1] P. Müller and I. Hermans. Applications of Modulation Excitation Spectroscopy in Heterogeneous Catalysis. *Industrial & Engineering Chemistry Research*, 56(5):1123–1136, 2017.

[2] D. Baurecht and U. P. Fringeli. Quantitative modulated excitation Fourier transform infrared spectroscopy. *Review of Scientific Instruments*, 72(10):3782–3792, 2001.

[3] A. Kubacka, A. Iglesias-Juez, A. Martinez-Arias, M. Di Michiel, M. A. Newton, and M. Fernandez-Garcia. Surface and Bulk Approach to Time-resolved Characterization of Heterogeneous Catalysts. *ChemCatChem*, 4(6):725–737, 2012.

[4] S. Shulda and R. M. Richards. Modulation Excitation Spectroscopy with Phase Sensitive Detection for Surface Analysis. In V.I. Parvulescu and E. Kemnitz, editors, *New Materials for Catalytic Applications*, pages 121–132. Elsevier Science, 2016.

[5] W. Uhmann, A. Becker, C. Taran, and F. Siebert. Time-Resolved FT-IR Absorption Spectroscopy Using a Step-Scan Interferometer. *Applied Spectroscopy*, 45 (3):390–397, 1991.

[6] B. Süss, F. Ringleb, and J. Heberle. New ultrarapid-scanning interferometer for FT-IR spectroscopy with microsecond time-resolution. *Review of Scientific Instruments*, 87(6):063113, 2016.

[7] R. M. Hexter. Excitation-Modulation Spectroscopy: A Technique for Obtaining Vibrational Spectra of Excited Electronic States. *Journal of the Optical Society of America*, 53(6):703–709, 1963.

[8] U. P. Fringeli and H. H. Günthard. Modulated Excitation Infrared Spectrophotometer. *Applied Optics*, 10(4):819–824, Apr 1971.

[9] M. Forster, U. P. Fringeli, and H. H. Günthard. Kinetics of Photochemical Systems with Modulated Optical Excitation. *Helvetica Chimica Acta*, 56(1): 389–407, 1973.

[10] H. Paul. Second order rate constants and cidep enhancements of transient radicals in solution by modulcation ESR spectroscopy. *Chemical Physics*, 15 (1):115 – 129, 1976.

[11] M. Forster, K. Loth, M. Andrist, U.P. Fringeli, and Hs.H. Günthard. Kinetic study of the photooxidation of pyrocatechol by modulated electronic excitation IR and ESR spectroscopy (MEIR and MESR). *Chemocal Physics*, 17(1):59 – 80, 1976.

[12] W. Lenth, C. Ortiz, and G.C. Bjorklund. Frequency modulation excitation spectroscopy. *Optics Communications*, 41(5):369 – 373, 1982.

[13] M. Müller, R. Buchet, and U. P. Fringeli. 2D-FTIR ATR Spectroscopy of Thermo-Induced Periodic Secondary Structural Changes of Poly-(l)-lysine: A Cross-Correlation Analysis of Phase-Resolved Temperature Modulation Spectra. *Journal of Physical Chemistry*, 100(25):10810–10825, 1996.

[14] Y. He, G. Wang, J. Cox, and L. Geng. Two-Dimensional Fluorescence Correlation Spectroscopy with Modulated Excitation. *Analytical Chemistry*, 73(10): 2302–2309, 2001.

[15] G. Persson, P. Thyberg, and J. Widengren. Modulated Fluorescence Correlation Spectroscopy with Complete Time Range Information . *Biophysical Journal*, 94(3):977 – 985, 2008.

[16] E.E. Ortelli, J. Wambach, and A. Wokaun. Use of periodic variations of reactant concentrations in time resolved DRIFT studies of heterogeneously catalysed reactions . *Applied Catalysis A*, 192(1):137 – 152, 2000.

[17] E.E. Ortelli and A. Wokaun. Use of periodic variations of reactant concentrations in time resolved FTIR studies of heterogeneously catalysed reactions . *Vibrational Spectroscopy*, 19(2):451 – 459, 1999.

[18] J. Kritzenberger and A. Wokaun. Time resolved FTIR study of the catalytic CO oxidation under periodic variation of the reactant concentration. *Journal of Molecular Catalysis A: Chemical*, 118(2):235 – 245, 1997.

[19] M. Cavers, J.M. Davidson, I.R. Harkness, L.V.C. Rees, and G.S. McDougall. Spectroscopic Identification of the Active Site for CO Oxidation on Rh/Al_2O_3 by Concentration Modulation in situ DRIFTS. *Journal of Catalysis*, 188(2):426 – 430, 1999.

[20] A. Urakawa, T. Bürgi, and A. Baiker. Sensitivity enhancement and dynamic behavior analysis by modulation excitation spectroscopy: Principle and application in heterogeneous catalysis. *Chemical Engineering Science*, 63(20): 4902–4909, 2008.

[21] M. M. Chen, N. Maeda, A. Baiker, and J. Huang. Molecular Insight into Pt-Catalyzed Chemoselective Hydrogenation of an Aromatic Ketone by In Situ Modulation-Excitation IR Spectroscopy. *ACS Catalysis*, 2(9):2007–2013, 2012.

[22] A. Urakawa, R. Wirz, T. Bürgi, and A. Baiker. ATR-IR flow-through cell for concentration modulation excitation spectroscopy: Diffusion experiments and simulations. *Journal of Physical Chemistry B*, 107(47):13061–13068, 2003.

[23] A. Urakawa, T. Bürgi, and A. Baiker. Kinetic analysis using square-wave stimulation in modulation excitation spectroscopy: Mixing property of a flow-through PM-IRRAS cell. *Chemical Physics*, 324(2-3):653–658, 2006.

[24] T. Bürgi. In situ spectroscopy of catalytic solid-liquid interfaces and chiral surfaces. *Chimia*, 57(10):623–627, 2003.

[25] T. Bürgi and A. Baiker. Attenuated total reflection infrared spectroscopy of solid catalysts functioning in the presence of liquid-phase reactants. In B. C. Gates and H. Knözinger, editors, *Advances in Catalysis, Vol 50*, volume 50 of *Advances in Catalysis*, pages 227–283. 2006.

[26] J.-M. Andanson and A. Baiker. Exploring catalytic solid/liquid interfaces by in situ attenuated total reflection infrared spectroscopy. *Chemical Society Reviews*, 39(12):4571–4584, 2010.

[27] D. A. Woods and C. D. Bain. Total internal reflection spectroscopy for studying soft matter. *Soft Matter*, 10(8):1071–1096, 2014.

[28] F. Zaera. New advances in the use of infrared absorption spectroscopy for the characterization of heterogeneous catalytic reactions. *Chemical Society Reviews*, 43(22):7624–7663, 2014.

[29] A. Aguirre, P. A. Kler, C. L.A. Berli, and S. E. Collins. Design and operational limits of an ATR-FTIR spectroscopic microreactor for investigating reactions at liquid-solid interface . *Chemical Engineering Journal*, 243:197 – 206, 2014.

[30] A. Aguirre, C. L.A. Berli, and S. E. Collins. ATR-FTIR spectrokinetic analysis of the CO adsorption and oxidation at water/platinum interface . *Catalysis Today*, 283:127 – 133, 2016.

[31] D. Baurecht, I. Porth, and U. P. Fringeli. A new method of phase sensitive detection in modulation spectroscopy applied to temperature induced folding and unfolding of RNase A. *Vibrational Spectroscopy*, 30(1):85–92, 2002.

[32] M. Schwarzott, H. Engelhardt, T. Kluhspies, D. Baurecht, D. Naumann, and U. P. Fringeli. In situ FTIR ATR spectroscopy of the preparation of an oriented monomolecular film of porin Omp32 on an internal reflecting element by dialysis. *Langmuir*, 19(18):7451–7459, 2003.

[33] M. Schwarzott, P. Lasch, D. Baurecht, D. Naumann, and U. P. Fringeli. Electric field-induced changes in lipids investigated by modulated excitation FTIR spectroscopy. *Biophysical Journal*, 86(1):285–295, 2004.

[34] D. Baurecht, G. Reiter, N. Hassler, M. Schwarzott, and U. P. Fringeli. Application of special FTIR ATR techniques for quantitative structural analysis of thin surface layers. *Chimia*, 59(5):226–235, 2005.

[35] C. Nowak, C. Luening, D. Schach, D. Baurecht, W. Knoll, and R. L. C. Naumann. Electron Transfer Kinetics of Cytochrome C in the Submillisecond Time Regime Using Time-Resolved Surface-Enhanced Infrared Absorption Spectroscopy. *Journal of Physical Chemistry C*, 113(6):2256–2262, 2009.

[36] C. Nowak, D. Schach, M. Grosseruschkamp, W. Knoll, and R. L. C. Naumann. Cytochrome C as a benchmark system for a two-layer gold surface with improved surface-enhancement for spectro-electrochemistry. *Spectroscopy*, 24(1-2):173–176, 2010.

[37] A. Schwaighofer, S. Ferguson-Miller, R. L. C. Naumann, W. Knoll, and C. Nowak. Phase-Sensitive Detection in Modulation Excitation Spectroscopy Applied to Potential Induced Electron Transfer in Cytochrome c Oxidase. *Applied Spectroscopy*, 68(1):5–13, 2014.

[38] T. Bürgi. *Attenuated total reflection infrared (ATR-IR) spectroscopy, modulation excitation spectroscopy (MES), and vibrational circular dichroism (VCD)*. Biointerface Characterization by Advanced IR Spectroscopy. 2011.

[39] R. Wirz, T. Bürgi, and A. Baiker. Probing enantiospecific interactions at chiral solid-liquid interfaces by absolute configuration modulation infrared spectroscopy. *Langmuir*, 19(3):785–792, 2003.

[40] R. Wirz, T. Bürgi, W. Lindner, and A. Baiker. Absolute configuration modulation attenuated total reflection IR spectroscopy: An in situ method for probing chiral recognition in liquid chromatography. *Analytical Chemistry*, 76(18):5319–5330, 2004.

[41] R. Wirz, D. Ferri, and A. Baiker. Enantioselective interactions at the solid-liquid interface of an HPLC column under working conditions. *Analytical Chemistry*, 80(10):3572–3583, 2008.

[42] M. Bieri and T. Bürgi. Adsorption kinetics, orientation, and self-assembling of N-acetyl-L-cysteine on gold: A combined ATR-IR, PM-IRRAS, and QCM study. *Journal of Physical Chemistry B*, 109(47):22476–22485, 2005.

[43] M. Bieri and T. Bürgi. D-penicillamine adsorption on gold: An in situ ATR-IR spectroscopic and QCM study. *Langmuir*, 22(20):8379–8386, 2006.

[44] M. Bieri and T. Bürgi. Enantiodiscrimination between an N-acetyl-L-cysteine SAM and proline: An in situ spectroscopic and computational study. *ChemPhysChem*, 7(2):514–523, 2006.

[45] M. Bieri and T. Bürgi. Probing enantiospecific interactions between proline and an L-glutathione self-assembled monolayer by modulation excitation ATR-IR spectroscopy. *Journal of Physical Chemistry B*, 109(20):10243–10250, 2005.

[46] M. Bieri and T. Bürgi. L-Glutathione chemisorption on gold and acid/base induced structural changes: A PM-IRRAS and time-resolved in situ ATR-IR spectroscopic study. *Langmuir*, 21(4):1354–1363, 2005.

[47] M. Bieri, C. Gautier, and T. Bürgi. Probing chiral interfaces by infrared spectroscopic methods. *Physical Chemistry Chemical Physics*, 9(6):671–685, 2007.

[48] C. Gautier, M. Bieri, I. Dolamic, S. Angeloni, J. Boudon, and T. Bürgi. Probing chiral nanoparticles and surfaces by infrared spectroscopy. *Chimia*, 60(11): A777–A782, 2006.

[49] T. Bürgi. Shining Light at Working Interfaces and Chiral Nanoparticles. *Chimia*, 65(3):157–167, 2011.

[50] S. Reimann, A. Urakawa, and A. Baiker. BINAP Adsorption on Palladium: A Combined Infrared Spectroscopy and Theoretical Study. *Journal of Physical Chemistry C*, 114(41):17836–17844, 2010.

[51] N. Hassler, D. Baurecht, G. Reiter, and U. P. Fringeli. In Situ FTIR ATR Spectroscopic Study of the Interaction of Immobilized Human Serum Albumin with Cholate in Aqueous Environment. *Journal of Physical Chemistry C*, 115 (4):1064–1072, 2011.

[52] A. Gisler, T. Bürgi, and A. Baiker. Epoxidation on titania-silica aerogel catalysts studied by attenuated total reflection Fourier transform infrared and modulation spectroscopy. *Physical Chemistry Chemical Physics*, 5(16):3539–3548, 2003.

[53] A. Gisler, T. Bürgi, and A. Baiker. Epoxidation of cyclic allylic alcohols on titania-silica aerogels studied by attenuated total reflection infrared and modulation spectroscopy. *Journal of Catalysis*, 222(2):461–469, 2004.

[54] P. Haider, J. D. Grunwaldt, and A. Baiker. Gold supported on Mg, Al and Cu containing mixed oxides: Relation between surface properties and behavior in catalytic aerobic oxidation of 1-phenylethanol. *Catalysis Today*, 141(3-4): 349–354, 2009.

[55] P. Haider, A. Urakawa, E. Schmidt, and A. Baiker. Selective blocking of active sites on supported gold catalysts by adsorbed thiols and its effect on the catalytic behavior: A combined experimental and theoretical study. *Journal of Molecular Catalysis A: Chemical*, 305(1-2):161–169, 2009.

[56] C. Mondelli, D. Ferri, and A. Baiker. Ruthenium at work in Ru-hydroxyapatite during the aerobic oxidation of benzyl alcohol: An in situ ATR-IR spectroscopy study. *Journal of Catalysis*, 258(1):170–176, 2008.

[57] P. Haider and A. Baiker. Gold supported on Cu-Mg-Al-mixed oxides: Strong enhancement of activity in aerobic alcohol oxidation by concerted effect of copper and magnesium. *Journal of Catalysis*, 248(2):175–187, 2007.

[58] T. Bürgi and M. Bieri. Time-resolved in situ ATR Spectroscopy of 2-propanol oxidation over Pd/Al2O3: Evidence for 2-propoxide intermediate. *Journal of Physical Chemistry B*, 108(35), 2004.

[59] S. Lavoie, M.-A. Laliberte, I. Temprano, and P. H. McBreen. A Generalized Two-Point H-Bonding Model for Catalytic Stereoselective Hydrogenation of Activated Ketones on Chirally Modified Platinum. *Journal of the American Chemical Society*, 128(23):7588–7593, 2006.

[60] A. Baiker. Crucial aspects in the design of chirally modified noble metal catalysts for asymmetric hydrogenation of activated ketones. *Chemical Society Reviews*, 44:7449–7464, 2015.

[61] T. Bürgi and A. Baiker. In situ infrared spectroscopy of catalytic solid-liquid interfaces using phase-sensitive detection: Enantioselective hydrogenation of a pyrone over Pd/TiO_2. *Journal of Physical Chemistry B*, 106(41):10649–10658, 2002.

[62] N. Bonalumi, T. Bürgi, and A. Baiker. Interaction between ketopantolactone and chirally modified Pt investigated by attenuated total reflection IR concentration modulation spectroscopy. *Journal of the American Chemical Society*, 125(44):13342–13343, 2003.

[63] N. Maeda, K. Hungerbühler, and A. Baiker. Asymmetric Hydrogenation on Chirally Modified Pt: Origin of Hydrogen in the N-H-O Interaction between Cinchonidine and Ketone. *Journal of the American Chemical Society*, 133(49): 19567–19569, 2011.

[64] F. Meemken, N. Maeda, K. Hungerbühler, and A. Baiker. Platinum-Catalyzed Asymmetric Hydrogenation: Spectroscopic Evidence for an O-H-O Hydrogen-Bond Interaction between Substrate and Modifier. *Angewandte Chemie - International Edition*, 51(33):8212–8216, 2012.

[65] D. M. Meier, A. Urakawa, N. Turra, H. Ruegger, and A. Baiker. Hydrogen-bonding interactions in cinchonidine-2-methyl-2-hexenoic acid complexes: A

combined spectroscopic and theoretical study. *Journal of Physical Chemistry A*, 112(27):6150–6158, 2008.

[66] M. M. Chen, N. Maeda, A. Baiker, and J. Huang. In-situ Modulation Excitation IR study on the dominant product of Pt-catalyzed aromatic ketone hydrogenation. In K. Kida, editor, *Advanced Materials and Engineering Materials II*, volume 683 of *Advanced Materials Research*, pages 271–274. Trans Tech Publications Ltd, Stafa-Zurich, 2013.

[67] N. Maeda, S. Sano, T. Mallat, K. Hungerbühler, and A. Baiker. Heterogeneous Asymmetric Hydrogenation of Activated Ketones: Mechanistic Insight into the Role of Alcohol Products by in Situ Modulation-Excitation IR Spectroscopy. *Journal of Physical Chemistry C*, 116(6):4182–4188, 2012.

[68] F. Meemken, N. Maeda, K. Hungerbühler, and A. Baiker. Heterogeneous Asymmetric Hydrogenation of Prochiral Alkenoic Acid: Origin of Rate and Enantioselectivity Enhancement by Amine Addition. *ACS Catalysis*, 2(3): 464–467, 2012.

[69] F. Meemken, A. Baiker, S. Schenker, and K. Hungerbühler. Chiral Modification of Platinum by Co-Adsorbed Cinchonidine and Trifluoroacetic Acid: Origin of Enhanced Stereocontrol in the Hydrogenation of Trifluoroacetophenone. *Chemistry - A European Journal*, 20(5):1298–1309, 2014.

[70] F. Meemken, K. Hungerbühler, and A. Baiker. Monitoring Surface Processes During Heterogeneous Asymmetric Hydrogenation of Ketones on a Chirally Modified Platinum Catalyst by Operando Spectroscopy. *Angewandte Chemie - International Edition*, 53(33):8640–8644, 2014.

[71] L. Rodriguez-Garcia, K. Hungerbühler, A. Baiker, and F. Meemken. Enantioselection on Heterogeneous Noble Metal Catalyst: Proline-Induced Asymmetry in the Hydrogenation of Isophorone on Pd Catalyst. *Journal of the American Chemical Society*, 137(37):12121–12130, 2015.

[72] I. Dolamic and T. Bürgi. Photocatalysis of dicarboxylic acids over TiO_2: An in situ ATR-IR study. *Journal of Catalysis*, 248(2):268–276, 2007.

[73] I. Dolamic and T. Bürgi. In Situ ATR-IR Study on the Photocatalytic Decomposition of Amino Acids over Au/TiO_2 and TiO_2. *Journal of Physical Chemistry C*, 115(5):2228–2234, 2011.

[74] R. Wirz, D. Ferri, and A. Baiker. ATR-IR spectroscopy of pendant NH_2 groups on silica involved in the Knoevenagel condensation. *Langmuir*, 22(8):3698–3706, 2006.

[75] A. Aguirre, A. L. Bonivardi, S. R. Matkovic, L. E. Briand, and S. E. Collins. ATR-FTIR Study of the Decomposition of Acetic Anhydride on Fosfotungstic Wells-Dawson Heteropoly Acid Using Concentration-Modulation Excitation Spectroscopy. *Topics in Catalysis*, 54(1-4):229–235, 2011.

[76] P. Müller, P. Wolf, and I. Hermans. Insights into the Complexity of Heterogeneous Liquid-Phase Catalysis: Case Study on the Cyclization of Citronellal. *ACS Catalysis*, 6(5):2760–2769, 2016.

[77] A. Urakawa, T. Bürgi, H. P. Schläpfer, and A. Baiker. Simultaneous in situ monitoring of surface and gas species and surface properties by modulation excitation polarization-modulation infrared reflection-absorption spectroscopy: CO oxidation over Pt film. *Journal of Chemical Physics*, 124(5):054717, 2006.

[78] A. Urakawa, T. Bürgi, and A. Baiker. Modulation excitation PM-IRRAS: A new possibility for simultaneous monitoring of surface and gas species and surface properties. *Chimia*, 60(4):231–233, 2006.

[79] D. M. Meier, A. Urakawa, and A. Baiker. Polarization-modulation infrared reflection-absorption spectroscopy affording time-resolved simultaneous detection of surface and liquid phase species at catalytic solid-liquid interfaces. *Analyst*, 134:1779–1780, 2009.

[80] D. M. Meier, A. Urakawa, R. Mäder, and A. Baiker. Design and performance of a flow-through polarization-modulation infrared reflection-absorption spectroscopy cell for time-resolved simultaneous surface and liquid phase detection under concentration and temperature perturbations. *Review of Scientific Instruments*, 80(9):094101, 2009.

[81] D. M. Meier, A. Urakawa, and A. Baiker. Adsorption behavior of salicylic, benzoic, and 2-methyl-2-hexenoic acid on alumina: an in situ modulation excitation PM-IRRAS study. *Physical Chemistry Chemical Physics*, 11(43):10132–10139, 2009.

[82] J. J. Venter and M. A. Vannice. Modifications of a Diffuse Reflectance Cell to Allow the Characterization of Carbon-Supported Metals by DRIFTS. *Applied Spectroscopy*, 42(6):1096–1103, 1988.

[83] M.R. Prairie, J.G. Highfield, and A. Renken. Diffuse-reflectance FTIR spectroscopy for kinetic and mechanistic studies of CO_2 hydrogenation in a continuous recycle reactor. *Chemical Engineering Science*, 46(1):113 – 121, 1991.

[84] F. C. Meunier. Pitfalls and benefits of in situ and operando diffuse reflectance FT-IR spectroscopy (DRIFTS) applied to catalytic reactions. *Reaction Chemistry & Engineering*, 1:134–141, 2016.

[85] R. G. Pavelko, J.-K. Choi, A. Urakawa, M. Yuasa, T. Kida, and K. Shimanoe. H_2O/D_2O Exchange on SnO_2 Materials in the Presence of CO: Operando Spectroscopic and Electric Resistance Measurements. *Journal of Physical Chemistry C*, 118(5):2554–2563, 2014.

[86] R. Kydd, D. Ferri, P. Hug, J. Scott, W. Y. Teoh, and R. Amal. Temperature-induced evolution of reaction sites and mechanisms during preferential oxidation of CO. *Journal of Catalysis*, 277(1):64–71, 2011.

[87] N. Maeda, F. Meemken, K. Hungerbuhler, and A. Baiker. Spectroscopic Detection of Active Species on Catalytic Surfaces: Steady-State versus Transient Method. *Chimia*, 66(9):664–667, 2012.

[88] E. del Rio, S. E. Collins, A. Aguirre, X. W. Chen, J. J. Delgado, J. J. Calvino, and S. Bernal. Reversible deactivation of a $Au/Ce_{0.62}Zr_{0.38}O_2$ catalyst in CO oxidation: A systematic study of CO_2-triggered carbonate inhibition. *Journal of Catalysis*, 316:210–218, 2014.

[89] A. Aguirre, C. E. Barrios, A. Aguilar-Tapia, R. Zanella, M. A. Baltanas, and S. E. Collins. In-Situ DRIFT Study of Au-Ir/Ceria Catalysts: Activity and Stability for CO Oxidation. *Topics in Catalysis*, 59(2-4):347–356, 2016.

[90] C. George, A. Genovese, A. Casu, M. Prato, M. Povia, L. Manna, and T. Montanari. CO Oxidation on Colloidal $Au_{0.80}Pd_{0.20}$-Fe_xO_y Dumbbell Nanocrystals. *Nano Letters*, 13(2):752–757, 2013.

[91] A. Haghofer, D. Ferri, K. Fottinger, and G. Rupprechter. Who Is Doing the Job? Unraveling the Role of Ga_2O_3 in Methanol Steam Reforming on Pd_2Ga/Ga_2O_3. *ACS Catalysis*, 2(11):2305–2315, 2012.

[92] J. Zarfl, D. Ferri, T. J. Schildhauer, J. Wambach, and A. Wokaun. DRIFTS study of a commercial Ni/gamma-Al_2O_3 CO methanation catalyst. *Applied Catalysis A*, 495:104–114, 2015.

[93] N. Maeda, F. Meemken, and A. Baiker. Insight into the Mechanism of the Preferential Oxidation of Carbon Monoxide by Using Isotope-Modulated Excitation IR Spectroscopy. *ChemCatChem*, 5(8):2199–2202, 2013.

[94] A. Aguirre and S. E. Collins. Selective detection of reaction intermediates using concentration-modulation excitation DRIFT spectroscopy. *Catalysis Today*, 205:34–40, 2013.

[95] J. Vecchietti, A. Bonivardi, W. Xu, D. Stacchiola, J. J. Delgado, M. Calatayud, and S. E. Collins. Understanding the Role of Oxygen Vacancies in the Water Gas Shift Reaction on Ceria-Supported Platinum Catalysts. *ACS Catalysis*, 4 (6):2088–2096, 2014.

[96] N. Maeda, F. Meemken, K. Hungerbühler, and A. Baiker. Selectivity-Controlling Factors in Catalytic Methanol Amination Studied by Isotopically Modulated Excitation IR Spectroscopy. *ACS Catalysis*, 3(2):219–223, 2013.

[97] P. Müller, S. P. Burt, A. M. Love, W. P. McDermott, P. Wolf, and I. Hermans. Mechanistic Study on the Lewis Acid Catalyzed Synthesis of 1,3-Butadiene over Ta-BEA Using Modulated Operando DRIFTS-MS. *ACS Catalysis*, 6(10): 6823–6832, 2016.

[98] E. Becker, P.-A. Carlsson, H. Gronbeck, and M. Skoglundh. Methane oxidation over alumina supported platinum investigated by time-resolved in situ XANES spectroscopy . *Journal of Catalysis*, 252(1):11 – 17, 2007.

[99] J. Stötzel, D. Lutzenkirchen-Hecht, R. Frahm, B. Kimmerle, A. Baiker, M. Nachtegaal, M. J. Beier, and J. D. Grunwaldt. Reduction and re-oxidation of Cu/Al_2O_3 catalysts investigated with quick-scanning XANES and EXAFS. In A. DiCicco and A. Filipponi, editors, *14th International Conference on X-Ray Absorption Fine Structure*, volume 190 of *Journal of Physics Conference Series*. 2009.

[100] E. Becker, P.-A. Carlsson, L. Kylhammar, M. A. Newton, and M. Skoglundh. In Situ Spectroscopic Investigation of Low-Temperature Oxidation of Methane over Alumina-Supported Platinum during Periodic Operation. *Journal of Physical Chemistry C*, 115(4):944–951, 2011.

[101] J. Stötzel, D. Lutzenkirchen-Hecht, R. Frahm, B. Kimmerle, A. Baiker, M. Nachtegaal, M. J. Beier, and J. D. Grunwaldt. Investigation of the ignition behaviour of the noble metal catalyzed catalytic partial oxidation of methane. In A. DiCicco and A. Filipponi, editors, *14th International Conference on X-Ray Absorption Fine Structure*, volume 190 of *Journal of Physics Conference Series*. 2009.

[102] J. Stötzel, D. Lutzenkirchen-Hecht, J. D. Grunwaldt, and R. Frahm. T-REX: new software for advanced QEXAFS data analysis. *Journal of Synchrotron Radiation*, 19:920–929, 2012.

[103] M. A. Newton and A. J. Dent. Energy-Dispersive EXAFS: Principles and Application in Heterogeneous Catalysis. *In-Situ Characterization of Heterogeneous Catalysts*, pages 75–119, 2013.

[104] M. Nachtegaal, O. Müller, C. König, and R. Frahm. QEXAFS: Techniques and Scientific Applications for Time-Resolved XAS. In *X-Ray Absorption and X-Ray Emission Spectroscopy*, pages 155–183. John Wiley & Sons, Ltd, 2016.

[105] D. Ferri, M. S. Kumar, R. Wirz, A. Eyssler, O. Korsak, P. Hug, A. Weidenkaff, and M. A. Newton. First steps in combining modulation excitation spectroscopy with synchronous dispersive EXAFS/DRIFTS/mass spectrometry for in situ time resolved study of heterogeneous catalysts. *Physical Chemistry Chemical Physics*, 12(21):5634–5646, 2010.

[106] D. Ferri, M. A. Newton, and M. Nachtegaal. Modulation Excitation X-Ray Absorption Spectroscopy to Probe Surface Species on Heterogeneous Catalysts. *Topics in Catalysis*, 54(16-18):1070–1078, 2011.

[107] D. Ferri, M. A. Newton, M. Di Michiel, S. Yoon, G. L. Chiarello, V. Marchionni, S. K. Matam, M. H. Aguirre, A. Weidenkaff, F. Wen, and J. Gieshoff. Synchrotron high energy X-ray methods coupled to phase sensitive analysis to characterize aging of solid catalysts with enhanced sensitivity. *Physical Chemistry Chemical Physics*, 15(22):8629–8639, 2013.

[108] J. Stötzel, D. Lutzenkirchen-Hecht, R. Frahm, and J. D. Grunwaldt. Improving the sensitivity of QEXAFS using modulation excitation spectroscopy. In Z. Y. Wu, editor, *15th International Conference on X-Ray Absorption Fine Structure*, volume 430 of *Journal of Physics Conference Series*. 2013.

[109] C. F. J. König, J. A. van Bokhoven, T. J. Schildhauer, and M. Nachtegaal. Quantitative Analysis of Modulated Excitation X-ray Absorption Spectra:

Enhanced Precision of EXAFS Fitting. *Journal of Physical Chemistry C*, 116(37): 19857–19866, 2012.

[110] G. L. Chiarello and D. Ferri. Modulated excitation extended X-ray absorption fine structure spectroscopy. *Physical Chemistry Chemical Physics*, 17(16):10579–10591, 2015.

[111] A. Eyssler, E. Kleymenov, A. Kupferschmid, M. Nachtegaal, M. S. Kumar, P. Hug, A. Weidenkaff, and D. Ferri. Improvement of Catalytic Activity of $LaFe_{0.95}Pd_{0.05}O_3$ for Methane Oxidation under Transient Conditions. *Journal of Physical Chemistry C*, 115(4):1231–1239, 2011.

[112] A.M. Efstathiou and X.E. Verykios. Transient methods in heterogeneous catalysis: Experimental features and application to study mechanistic aspects of the CH_4/O_2 (OCM), NH_3/O_2 and NO/He reactions. *Applied Catalysis A: General*, 151(1):109 – 166, 1997.

[113] P. Silveston, R. R. Hudgins, and A. Renken. Periodic operation of catalytic reactors-introduction and overview. *Catalysis Today*, 25(2):91 – 112, 1995.

[114] R. Burch. The Investigation of Mechanisms in Environmental Catalysis Using Time-Resolved Methods. *Topics in Catalysis*, 24(1):97–102, 2003.

[115] S. Fouladvand, M. Skoglundh, and P.-A. Carlsson. Unsteady-state operation of supported platinum catalysts for high conversion of methane. *Chemical Engineering Journal*, 292:321 – 325, 2016.

[116] C. F. J. König, T. J. Schildhauer, and M. Nachtegaal. Methane synthesis and sulfur removal over a Ru catalyst probed in situ with high sensitivity X-ray absorption spectroscopy. *Journal of Catalysis*, 305:92–100, 2013.

[117] J. Nilsson, P.-A. Carlsson, S. Fouladvand, N. M. Martin, J. Gustafson, M. A. Newton, E. Lundgren, H. Grönbeck, and M. Skoglundh. Chemistry of Supported Palladium Nanoparticles during Methane Oxidation. *ACS Catalysis*, 5 (4):2481–2489, 2015.

[118] C. Lamberti and J. A. van Bokhoven. X-Ray Absorption and Emission Spectroscopy for Catalysis. In *X-Ray Absorption and X-Ray Emission Spectroscopy*, pages 351–383. John Wiley & Sons, Ltd, 2016.

[119] V. Marchionni, J. Szlachetko, M. Nachtegaal, A. Kambolis, O. Krocher, and D. Ferri. An operando emission spectroscopy study of Pt/Al_2O_3 and $Pt/CeO_2/Al_2O_3$. *Physical Chemistry Chemical Physics*, 18:29268–29277, 2016.

[120] R. Kopelent, J. A. van Bokhoven, J. Szlachetko, J. Edebeli, C. Paun, M. Nachtegaal, and O. V. Safonova. Catalytically Active and Spectator Ce^{3+} in Ceria-Supported Metal Catalysts. *Angewandte Chemie - International Edition*, 54(30): 8728–8731, 2015.

[121] M. A. Newton, M. Di Michiel, D. Ferri, M. Fernandez-Garcia, A. M. Beale, S. D. M. Jacques, P. J. Chupas, and K. W. Chapman. Catalytic Adventures in Space and Time Using High Energy X-rays. *Catalysis Surveys from Asia*, 18(4): 134–148, 2014.

[122] L. Palin, E. Conterosito, R. Caliandro, E. Boccaleri, G. Croce, S. Kumar, W. van Beek, and M. Milanesio. Rational design of the solid-state synthesis of materials based on poly-aromatic molecular complexes. *CrystEngComm*, 18: 5930–5939, 2016.

[123] R. Caliandro, T. Sibillano, B. D. Belviso, R. Scarfiello, J. C. Hanson, E. Dooryhee, M. Manca, P. D. Cozzoli, and C. Giannini. Static and Dynamical Structural Investigations of Metal-Oxide Nanocrystals by Powder X-ray Diffraction: Colloidal Tungsten Oxide as a Case Study. *ChemPhysChem*, 17(5):699–709, 2016.

[124] D. Chernyshov, W. van Beek, H. Emerich, M. Milanesio, A. Urakawa, D. Viterbo, L. Palin, and R. Caliandro. Kinematic diffraction on a structure with periodically varying scattering function. *Acta Crystallographica Section A: Foundations*, 67(4):327–335, 2011.

[125] R. Caliandro, D. Chernyshov, H. Emerich, M. Milanesio, L. Palin, A. Urakawa, W. van Beek, and D. Viterbo. Patterson selectivity by modulation-enhanced diffraction. *Journal of Applied Crystallography*, 45:458–470, 2012.

[126] R. Caliandro, P. Guccione, G. Nico, G. Tutuncu, and J. C. Hanson. Tailored multivariate analysis for modulated enhanced diffraction. *Journal of Applied Crystallography*, 48(6):1679–1691, 2015.

[127] D. Chernyshov, V. Dyadkin, W. van Beek, and A. Urakawa. Frequency analysis for modulation-enhanced powder diffraction. *Acta Crystallographica Section A: Foundations*, 72(4):500–506, 2016.

[128] W. van Beek, H. Emerich, A. Urakawa, L. Palin, M. Milanesio, R. Caliandro, D. Viterbo, and D. Chernyshov. Untangling diffraction intensity: modulation enhanced diffraction on ZrO_2 powder. *Journal of Applied Crystallography*, 45: 738–747, 2012.

[129] D. Ferri, M. A. Newton, M. Di Michiel, G. L. Chiarello, S. Yoon, Y. Lu, and J. Andrieux. Revealing the Dynamic Structure of Complex Solid Catalysts Using Modulated Excitation X-ray Diffraction. *Angewandte Chemie - International Edition*, 53(34):8890–8894, 2014.

[130] L. Palin, R. Caliandro, D. Viterbo, and M. Milanesio. Chemical selectivity in structure determination by the time dependent analysis of in situ XRPD data: a clear view of Xe thermal behavior inside a MFI zeolite. *Physical Chemistry Chemical Physics*, 17:17480–17493, 2015.

[131] A. Urakawa, W. Van Beek, M. Monrabal-Capilla, J. R. Galan-Mascaros, L. Palin, and M. Milanesio. Combined, Modulation Enhanced X-ray Powder Diffraction and Raman Spectroscopic Study of Structural Transitions in the Spin Crossover Material $Fe(Htrz)_2(trz)$ (BF_4). *Journal of Physical Chemistry C*, 115 (4):1323–1329, 2011.

[132] W. van Beek, A. Urakawa, and M. Milanesio. XRD-Raman and Modulation Excitation Spectroscopy. *In-Situ Characterization of Heterogeneous Catalysts*, pages 411–439, 2013.

[133] J. Wang, R. A. Ando, and P. H. C. Camargo. Controlling the Selectivity of the Surface Plasmon Resonance Mediated Oxidation of p-Aminothiophenol on Au Nanoparticles by Charge Transfer from UV-excited TiO_2. *Angewandte Chemie - International Edition*, 54(23):6909–6912, 2015.

[134] Y. Lu, S. Keav, V. Marchionni, G. L. Chiarello, A. Pappacena, M. Di Michiel, M. A. Newton, A. Weidenkaff, and D. Ferri. Ageing induced improvement of methane oxidation activity of $Pd/YFeO_3$. *Catalysis Science & Technology*, 4(9): 2919–2931, 2014.

[135] O. Martin, C. Mondelli, A. Cervellino, D. Ferri, D. Curulla-Ferre, and J. Perez-Ramirez. Operando Synchrotron X-ray Powder Diffraction and Modulated-Excitation Infrared Spectroscopy Elucidate the CO_2 Promotion on a Commercial Methanol Synthesis Catalyst. *Angewandte Chemie - International Edition*, 55(37):11031–11036, 2016.

[136] G. L. Chiarello, M. Nachtegaal, V. Marchionni, L. Quaroni, and D. Ferri. Adding diffuse reflectance infrared Fourier transform spectroscopy capability to extended X-ray-absorption fine structure in a new cell to study solid catalysts in combination with a modulation approach. *Review of Scientific Instruments*, 85(7):074102, 2014.

[137] V. Marchionni, M. A. Newton, A. Kambolis, S. K. Matam, A. Weidenkaff, and D. Ferri. A modulated excitation ED-EXAFS/DRIFTS study of hydrothermal ageing of Rh/Al_2O_3. *Catalysis Today*, 229:80–87, 2014.

[138] A. Marberger, D. Ferri, M. Elsener, and O. Kröcher. The Significance of Lewis Acid Sites for the Selective Catalytic Reduction of Nitric Oxide on Vanadium-Based Catalysts. *Angewandte Chemie - International Edition*, 55(39): 11989–11994, 2016.

[139] M. Emond, T. Le Saux, S. Maurin, J. B. Baudin, R. Plasson, and L. Jullien. 2-Hydroxyazobenzenes to Tailor pH Pulses and Oscillations with Light. *Chemistry - A European Journal*, 16(29):8822–8831, 2010.

[140] K. Zrelli, T. Barilero, E. Cavatore, H. Berthoumieux, T. Le Saux, V. Croquette, A. Lemarchand, C. Gosse, and L. Jullien. Temperature Modulation and Quadrature Detection for Selective Titration of Two-State Exchanging Reactants. *Analytical Chemistry*, 83(7):2476–2484, 2011.

[141] A. Lemarchand, H. Berthoumieux, L. Jullien, and C. Gosse. Chemical Mechanism Identification from Frequency Response to Small Temperature Modulation. *Journal of Physical Chemistry A*, 116(33):8455–8463, 2012.

[142] F. Closa, C. Gosse, L. Jullien, and A. Lemarchand. Identification of two-step chemical mechanisms and determination of thermokinetic parameters using frequency responses to small temperature oscillations. *Journal of Chemical Physics*, 138(24):244109, 2013.

[143] F. Closa, C. Gosse, L. Jullien, and A. Lemarchand. Identification of two-step chemical mechanisms using small temperature oscillations and a single tagged species. *Journal of Chemical Physics*, 142(17):174108, 2015.

[144] J. Querard, A. Gautier, T. Le Saux, and L. Jullien. Expanding discriminative dimensions for analysis and imaging. *Chemical Science*, 6(5):2968–2978, 2015.

[145] J. Querard, T.-Z. Markus, M.-A. Plamont, C. Gauron, P. Wang, A. Espagne, M. Volovitch, S. Vriz, V. Croquette, A. Gautier, T. LeSaux, and L. Jullien. Photoswitching Kinetics and Phase-Sensitive Detection Add Discriminative Dimensions for Selective Fluorescence Imaging. *Angewandte Chemie - International Edition*, 54(9):2633–2637, 2015.

[146] J. Querard, T. Le Saux, A. Gautier, D. Alcor, V. Croquette, A. Lemarchand, C. Gosse, and L. Jullien. Kinetics of Reactive Modules Adds Discriminative Dimensions for Selective Cell Imaging. *ChemPhysChem*, 17(10):1396–1413, 2016.

[147] G. Busca. Acid Catalysts in Industrial Hydrocarbon Chemistry. *Chemical Reviews*, 107(11):5366–5410, 2007.

[148] K. Tanabe and W. H. Hölderich. Industrial application of solid acid-base catalysts . *Applied Catalysis A: General*, 181(2):399 – 434, 1999.

[149] B. Yilmaz and U. Müller. Catalytic Applications of Zeolites in Chemical Industry. *Topics in Catalysis*, 52(6):888–895, 2009.

[150] A. Corma and H. Garcia. Lewis acids: From conventional homogeneous to green homogeneous and heterogeneous catalysis. *Chemical Reviews*, 103(11): 4307–4365, 2003.

[151] R. A. Sheldon, I. W. C. E. Arends, and U. Hanefeld. Introduction: Green Chemistry and Catalysis. In *Green Chemistry and Catalysis*, pages 1–47. Wiley-VCH Verlag GmbH, 2007.

[152] R. A. Sheldon, I. W. C. E. Arends, and U. Hanefeld. Solid Acids and Bases as Catalysts. In *Green Chemistry and Catalysis*, pages 49–90. Wiley-VCH Verlag GmbH & Co. KGaA, 2007.

[153] R. A. Sheldon and H. van Bekkum. Introduction. In *Fine Chemicals through Heterogeneous Catalysis*, pages 1–11. Wiley-VCH Verlag GmbH, 2007.

[154] M. E. Davis. Zeolites and molecular sieves: not just ordinary catalysts. *Industrial & Engineering Chemistry Research*, 30(8):1675–1683, 1991.

[155] H. Y. Luo, J. D. Lewis, and Y. Roman-Leshkov. Lewis Acid Zeolites for Biomass Conversion: Perspectives and Challenges on Reactivity, Synthesis, and Stability. *Annual Review of Chemical and Biomolecular Engineering*, 7(1): 663–692, 2016.

[156] C. Neri, B. Anfossi, A. Esposito, and F. Buonomo. Process for the epoxidation of olefinic compounds, 1984. EP Pat. App. EP19,830,201,040.

[157] S. Van de Vyver and Y. Roman-Leshkov. Metalloenzyme-Like Zeolites as Lewis Acid Catalysts for C-C Bond Formation. *Angewandte Chemie - International Edition*, 54:12554–12561, 2015.

[158] P. Y. Dapsens, C. Mondelli, and J. Perez-Ramirez. Design of Lewis-acid centres in zeolitic matrices for the conversion of renewables. *Chemical Society Reviews*, 44:7025–7043, 2015.

[159] M. Moliner. State of the art of lewis acid-containing zeolites: lessons from fine chemistry to new biomass transformation processes. *Dalton Transactions*, 43:4197–4208, 2014.

[160] C. Hammond, S. Conrad, and I. Hermans. Simple and Scalable Preparation of Highly Active Lewis Acidic Sn-Beta. *Angewandte Chemie International Edition*, 51(47):11736–11739, 2012.

[161] P. Wolf, C. Hammond, S. Conrad, and I. Hermans. Post-synthetic preparation of Sn-, Ti- and Zr-beta: a facile route to water tolerant, highly active Lewis acidic zeolites. *Dalton Transactions*, 43(11):4514–4519, 2014.

[162] Y. Wang, J. D. Lewis, and Y. Roman-Leshkov. Synthesis of Itaconic Acid Ester Analogues via Self-Aldol Condensation of Ethyl Pyruvate Catalyzed by Hafnium BEA Zeolites. *ACS Catalysis*, 6(5):2739–2744, 2016.

[163] S. Dzwigaj, Y. Millot, and M. Che. Ta(V)-Single Site BEA Zeolite by Two-Step Postsynthesis Method: Preparation and Characterization. *Catalysis Letters*, 135(3-4):169–174, 2010.

[164] A. Corma, F. X. Llabres i Xamena, C. Prestipino, M. Renz, and S. Valencia. Water Resistant, Catalytically Active Nb and Ta Isolated Lewis Acid Sites, Homogeneously Distributed by Direct Synthesis in a Beta Zeolite. *The Journal of Physical Chemistry C*, 113(26):11306–11315, 2009.

[165] S. Dzwigaj and M. Che. Oxidation State of Vanadium Introduced in Dealuminated Beta Zeolite by Impregnation with V(IV)OSO_4 Solution:âŁ‰ Influence

of Preparation Parameters. *The Journal of Physical Chemistry B*, 109(47):22167–22174, 2005.

[166] R. Baran, F. Averseng, Y. Millot, T. Onfroy, S. Casale, and S. Dzwigaj. Incorporation of Mo into the Vacant T-Atom Sites of the Framework of BEA Zeolite as Mononuclear Mo Evidenced by XRD and FTIR, NMR, EPR, and DR UV-Vis Spectroscopies. *The Journal of Physical Chemistry C*, 118(8):4143–4150, 2014.

[167] T. R. Josephson, G. R. Jenness, D. G. Vlachos, and S. Caratzoulas. Distribution of open sites in sn-beta zeolite. *Microporous and Mesoporous Materials*, 245:45 – 50, 2017.

[168] P. Wolf, M. Valla, A. J. Rossini, A. Comas-Vives, F. Nunez-Zarur, B. Malaman, A. Lesage, L. Emsley, C. Coperet, and I. Hermans. NMR Signatures of the Active Sites in Sn-Beta Zeolite. *Angewandte Chemie - International Edition*, 53 (38):10179–10183, 2014.

[169] F. Tielens, T. Shishido, and S. Dzwigaj. What Do Tantalum Framework Sites Look Like in Zeolites? A Combined Theoretical and Experimental Investigation. *Journal of Physical Chemistry C*, 114(21):9923–9930, 2010.

[170] M. Boronat, P. Concepcion, A. Corma, M. Renz, and S. Valencia. Determination of the catalytically active oxidation Lewis acid sites in Sn-beta zeolites, and their optimisation by the combination of theoretical and experimental studies. *Journal of Catalysis*, 234(1):111–118, 2005.

[171] R. Bermejo-Deval, R. S. Assary, E. Nikolla, M. Moliner, Y. Roman-Leshkov, S.-J. Hwang, A. Palsdottir, D. Silverman, R. F. Lobo, L. A. Curtiss, and M. E. Davis. Metalloenzyme-like catalyzed isomerizations of sugars by Lewis acid zeolites. *Proceedings of the National Academy of Sciences*, 109(25):9727–9732, 2012.

[172] R. Bermejo-Deval, M. Orazov, R. Gounder, S.-J. Hwang, and M. E. Davis. Active Sites in Sn-Beta for Glucose Isomerization to Fructose and Epimerization to Mannose. *ACS Catalysis*, 4(7):2288–2297, 2014.

[173] P. Wolf, M. Valla, F. Nunez-Zarur, A. Comas-Vives, A. J. Rossini, C. Firth, H. Kallas, A. Lesage, L. Emsley, C. Coperet, and I. Hermans. Correlating Synthetic Methods, Morphology, Atomic-Level Structure, and Catalytic Activity of Sn-Beta Catalysts. *ACS Catalysis*, pages 4047–4063, 2016.

[174] P. Wolf, W.-C. Liao, T.-C. Ong, M. Valla, J. W. Harris, R. Gounder, W. N. P. van der Graaff, E. A. Pidko, E. J. M. Hensen, P. Ferrini, J. Dijkmans, B. Sels, I. Hermans, and C. Coperet. Identifying Sn Site Heterogeneities Prevalent Among Sn-Beta Zeolites. *Helvetica Chimica Acta*, 99(12):916–927, 2016.

[175] P. B. Weisz, V. J. Frilette, R. W. Maatman, and E. B. Mower. Catalysis by crystalline aluminosilicates II. Molecular-shape selective reactions. *Journal of Catalysis*, 1(4):307–312, 1962.

[176] R. De Clercq, M. Dusselier, C. Christiaens, J. Dijkmans, R. I. Iacobescu, Y. Pontikes, and B. F. Sels. Confinement Effects in Lewis Acid-Catalyzed Sugar Conversion: Steering Toward Functional Polyester Building Blocks. *ACS Catalysis*, 5(10):5803–5811, 2015.

[177] S. Conrad, R. Verel, C. Hammond, P. Wolf, F. Göltl, and I. Hermans. Silica-Grafted SnIV Catalysts in Hydrogen-Transfer Reactions. *ChemCatChem*, 7(20): 3270–3278, 2015.

[178] C. H. Zhou, X. Xia, C. X. Lin, D. S. Tong, and J. Beltramini. Catalytic conversion of lignocellulosic biomass to fine chemicals and fuels. *Chemical Society Reviews*, 40(11):5588–5617, 2011.

[179] A. Corma, M. E. Domine, and S. Valencia. Water-resistant solid Lewis acid catalysts: Meerwein-Ponndorf-Verley and Oppenauer reactions catalyzed by tin-beta zeolite. *Journal of Catalysis*, 215(2):294–304, 2003.

[180] G. S. Qi, R. T. Yang, and R. Chang. MnO_x-CeO_2 mixed oxides prepared by co-precipitation for selective catalytic reduction of NO with NH3 at low temperatures. *Applied Catalysis B*, 51(2):93–106, 2004.

[181] M. S. Holm, S. Saravanamurugan, and E. Taarning. Conversion of Sugars to Lactic Acid Derivatives Using Heterogeneous Zeotype Catalysts. *Science*, 328 (5978):602–605, 2010.

[182] Y. Roman-Leshkov, M. Moliner, J. A. Labinger, and M. E. Davis. Mechanism of Glucose Isomerization Using a Solid Lewis Acid Catalyst in Water. *Angewandte Chemie International Edition*, 49(47):8954–8957, 2010.

[183] W. R. Gunther, V. K. Michaelis, M. A. Caporini, R. G. Griffin, and Y. Roman-Leshkov. Dynamic Nuclear Polarization NMR Enables the Analysis of Sn-Beta Zeolite Prepared with Natural Abundance ^{119}Sn Precursors. *Journal of the American Chemical Society*, 136(17):6219–6222, 2014.

[184] M. Boronat, P. Concepcion, A. Corma, M. T. Navarro, M. Renz, and S. Valencia. Reactivity in the confined spaces of zeolites: the interplay between spectroscopy and theory to develop structure-activity relationships for catalysis. *Physical Chemistry Chemical Physics*, 11(16):2876–2884, 2009.

[185] C. M. Lew, N. Rajabbeigi, and M. Tsapatsis. Tin-containing zeolite for the isomerization of cellulosic sugars. *Microporous and Mesoporous Materials*, 153: 55–58, 2012.

[186] C. M. Osmundsen, M. S. Holm, S. Dahl, and E. Taarning. Tin-containing silicates: structure-activity relations. *Proceedings of the Royal Society A*, 468 (2143):2000–2016, 2012.

[187] Y.-M. Chung and H.-K. Rhee. Solvent effects in the liquid phase Beckmann rearrangement of 4-hydroxyacetophenone oxime over H-Beta catalyst. *Journal of Molecular Catalysis A: Chemical*, 159(2):389–396, 2000.

[188] S. G. Wettstein, D. M. Alonso, Y. Chong, and J. A. Dumesic. Production of levulinic acid and gamma-valerolactone (GVL) from cellulose using GVL as a solvent in biphasic systems. *Energy & Environmental Science*, 5(8):8199–8203, 2012.

[189] M. Farnesi Camellone and D. Marx. On the Impact of Solvation on a Au/TiO_2 Nanocatalyst in Contact with Water. *The Journal of Physical Chemistry Letters*, 4(3):514–518, 2013.

[190] M. Boronat, A. Corma, and M. Renz. Chapter 38 Catalysis by Lewis Acids: Basic Principles for Highly Stereoselective Heterogeneously Catalyzed Cyclization Reactions. In *Turning Points in Solid-State, Materials and Surface Science: A Book in Celebration of the Life and Work of Sir John Meurig Thomas*, pages 639–650. The Royal Society of Chemistry, 2008.

[191] R. Eccles. Menthol and Related Cooling Compounds. *Journal of Pharmacy and Pharmacology*, 46(8):618–630, 1994.

[192] B. L. Mojet, S. D. Ebbesen, and L. Lefferts. Light at the interface: the potential of attenuated total reflection infrared spectroscopy for understanding heterogeneous catalysis in water. *Chemical Society Reviews*, 39(12):4643–4655, 2010.

[193] Joshua J. Pacheco and Mark E. Davis. Synthesis of terephthalic acid via Diels-Alder reactions with ethylene and oxidized variants of 5-hydroxymethylfurfural. *Proceedings of the National Academy of Sciences*, 111 (23):8363–8367, 2014.

[194] M. Selvaraj and Y. Choe. Well ordered two-dimensional SnSBA-15 catalysts synthesized with high levels of tetrahedral tin for highly efficient and clean synthesis of Nopol. *Applied Catalysis A: General*, 373(1-2):186–191, 2010.

[195] M. Selvaraj and S. Kawi. Effect of tin precursors and crystallization temperatures on the synthesis of SBA-15 with high levels of tetrahedral tin. *Journal of Materials Chemistry*, 17(34):3610–3621, 2007.

[196] A.N. Parvulescu, U. Müller, J.H. Teles, N. Vautravers, G. Uhl, I. Hermans, P. Wolf, and C. Hammond. A tin-containing zeolitic material having a bea framework structure, 2015. WO Pat. App. WO2015067654 A1.

[197] M. A. Camblor, A. Corma, and S. Valencia. Spontaneous nucleation and growth of pure silica zeolite-beta free of connectivity defects. *Chemical Communications*, (20):2365–2366, 1996.

[198] M. Choi, W. Heo, F. Kleitz, and R. Ryoo. Facile synthesis of high quality mesoporous SBA-15 with enhanced control of the porous network connectivity and wall thickness. *Chemical Communications*, (12):1340–1341, 2003.

[199] M. L. Clarke and M. B. France. The carbonyl ene reaction. *Tetrahedron*, 64(38): 9003–9031, 2008.

[200] A. Corma and M. Renz. Sn-Beta zeolite as diastereoselective water-resistant heterogeneous Lewis-acid catalyst for carbon-carbon bond formation in the intramolecular carbonyl-ene reaction. *Chemical Communications*, (5):550–551, 2004.

[201] J. Dijkmans, M. Dusselier, W. Janssens, M. Trekels, A. Vantomme, E. Breynaert, C. Kirschhock, and B. F. Sels. An Inner-/Outer-Sphere Stabilized Sn Active Site in Beta-Zeolite: Spectroscopic Evidence and Kinetic Consequences. *ACS Catalysis*, 6(1):31–46, 2016.

[202] J. Clayden, N. Greeves, and S. Warren. *Organic Chemistry*. OUP Oxford, 2012.

[203] L.B. Baerlocher, Ch.; McCusker. Database of Zeolite Structures, 2015. URL `http://www.iza-structure.org/databases/`.

[204] R. Gounder and E. Iglesia. The catalytic diversity of zeolites: confinement and solvation effects within voids of molecular dimensions. *Chemical Communications*, 49(34):3491–3509, 2013.

[205] A. Allerhand and P. von R. Schleyer. Solvent Effects in Infrared Spectroscopic Studies of Hydrogen Bonding. *Journal of the American Chemical Society*, 85(4): 371–380, 1963.

[206] M. Fuentes, J. Magraner, C. De Las Pozas, R. Roque-Malherbe, and A. Pariente, J. P.and Corma. Cyclization of Citronellal to Isopulegol by Zeolite Catalysis. *Applied Catalysis*, 47(2):367–374, 1989.

[207] Y. Hori, T. Iwata, and Y. Okeda. Process for producing isopulegol, 2002. US Pat. App. US20020133046 A1.

[208] L. Liu, M. Leutzsch, Y. Zheng, M. W. Alachraf, W. Thiel, and B. List. Confined Acid-Catalyzed Asymmetric Carbonyl-Ene Cyclization. *Journal of the American Chemical Society*, 137(41):13268–13271, 2015.

[209] L. Gilbert and C. Mercier. Solvent effects in heterogeneous catalysis : Application to the synthesis of fine chemicals. In M. Guisnet, J. Barbier, J. Barrault, C. Bouchoule, D. Duprez, G. Perot, and C. Montassier, editors, *Heterogeneous Catalysis and Fine Chemicals III: Proceedings of the 3rd International Symposium*, volume 78 of *Studies in Surface Science and Catalysis*, pages 51 – 66. Elsevier, 1993.

[210] L. Li, C. Stroobants, K. Lin, P. A. Jacobs, B. F. Sels, and P. P. Pescarmona. Selective conversion of trioses to lactates over Lewis acid heterogeneous catalysts. *Green Chemistry*, 13:1175–1181, 2011.

[211] A. Sayari, P. Liu, M. Kruk, and M. Jaroniec. Characterization of Large-Pore MCM-41 Molecular Sieves Obtained via Hydrothermal Restructuring. *Chemistry of Materials*, 9(11):2499–2506, 1997.

[212] W. M. Haynes. *CRC Handbook of Chemistry and Physics, 97th Edition*. CRC Press/Taylor & Francis, 2017.

[213] J. Jin, X. Ye, Y. Li, Y. Wang, L. Li, J. Gu, W. Zhao, and J. Shi. Synthesis of mesoporous Beta and Sn-Beta zeolites and their catalytic performances. *Dalton Transactions*, 43:8196–8204, 2014.

[214] A. Al-Nayili, K. Yakabi, and C. Hammond. Hierarchically porous BEA stannosilicates as unique catalysts for bulky ketone conversion and continuous operation. *Journal of Materials Chemistry A*, 4:1373–1382, 2016.

[215] X. Yang, J. Bian, J. Huang, W. Xin, T. Lu, C. Chen, Y. Su, L. Zhou, F. Wang, and J. Xu. Fluoride-free and low concentration template synthesis of hierarchical Sn-Beta zeolites: efficient catalysts for conversion of glucose to alkyl lactate. *Green Chemistry*, 19:692–701, 2017.

[216] M. A. Vannice. *Kinetics of Catalytic Reactions*. Springer US, 2005.

[217] P. Sriram, B. Hyde, and K. Smith. Butadiene. In *Chemical Economics Handbook*. IHS Chemical, Houston, 2016.

[218] J. Grub and E. Löser. Butadiene. In *Ullmann's Encyclopedia of Industrial Chemistry*. Wiley-VCH Verlag GmbH & Co. KGaA, 2000.

[219] D. Threadingham, W. Obrecht, W. Wieder, G. Wachholz, and R. Engehausen. Rubber, 3. Synthetic Rubbers, Introduction and Overview. In *Ullmann's Encyclopedia of Industrial Chemistry*. Wiley-VCH Verlag GmbH & Co. KGaA, 2000.

[220] M. Rapoport. Hydrocyanation of butadiene, 1987. US Pat. App. US4714773.

[221] I. Tkatchenko. Catalytic reactions involving butadiene. *Journal of Organometallic Chemistry*, 124(3):c39–c42, 1977.

[222] E. V. Makshina, M. Dusselier, W. Janssens, J. Degreve, P. A. Jacobs, and B. F. Sels. Review of old chemistry and new catalytic advances in the on-purpose synthesis of butadiene. *Chemical Society Reviews*, 43:7917–7953, 2014.

[223] K. Weissermel and H.-J. Arpe. 1,3-Diolefins. In *Industrial Organic Chemistry*, pages 107–126. Wiley-VCH Verlag GmbH, 2008.

[224] D. Cespi, F. Passarini, I. Vassura, and F. Cavani. Butadiene from biomass, a life cycle perspective to address sustainability in the chemical industry. *Green Chemistry*, 18(6):1625–1638, 2016.

[225] NexantThinkingTM. Bio-Butadiene PERP 2013S9, Process Evaluation/Research Planning program. Report, 2013.

[226] C. Angelici, B. M. Weckhuysen, and P. C. A. Bruijnincx. Chemocatalytic Conversion of Ethanol into Butadiene and Other Bulk Chemicals. *ChemSusChem*, 6(9):1595–1614, 2013.

[227] A. Chieregato, J. V. Ochoa, C. Bandinelli, G. Fornasari, F. Cavani, and M. Mella. On the Chemistry of Ethanol on Basic Oxides: Revising Mechanisms and Intermediates in the Lebedev and Guerbet reactions. *ChemSusChem*, 8(2): 377–388, 2015.

[228] J. V. Ochoa, C. Bandinelli, O. Vozniuk, A. Chieregato, A. Malmusi, C. Recchi, and F. Cavani. An analysis of the chemical, physical and reactivity features of MgO-SiO_2 catalysts for butadiene synthesis with the Lebedev process. *Green Chemistry*, 18(6):1653–1663, 2016.

[229] M. X. Gao, Z. Z. Liu, M. H. Zhang, and L. Tong. Study on the Mechanism of Butadiene Formation from Ethanol. *Catalysis Letters*, 144(12):2071–2079, 2014.

[230] V. L. Sushkevich, I. I. Ivanova, V. V. Ordomsky, and E. Taarning. Design of a metal-promoted oxide catalyst for the selective synthesis of butadiene from ethanol. *ChemSusChem*, 7(9):2527–36, 2014.

[231] R. A. L. Baylon, J. Sun, and Y. Wang. Conversion of ethanol to 1,3-butadiene over Na doped $Zn_xZr_yO_z$ mixed metal oxides. *Catalysis Today*, 259, Part 2: 446–452, 2016.

[232] H. E. Jones, E. E. Stahly, and B. B. Corson. Butadiene from Ethanol. Reaction Mechanism. *Journal of the American Chemical Society*, 71(5):1822–1828, 1949.

[233] H. Niiyama, E. Echigoya, and S. Morii. Butadiene Formation from Ethanol over Silica-Magnesia Catalysts. *Bulletin of the Chemical Society of Japan*, 45(3): 655–659, 1972.

[234] J. I. Di Cosimo, V. K. Diez, M. Xu, E. Iglesia, and C. R. ApesteguÄ±ia. Structure and Surface and Catalytic Properties of Mg-Al Basic Oxides. *Journal of Catalysis*, 178(2):499–510, 1998.

[235] H. J. Chae, T. W. Kim, Y. K. Moon, H. K. Kim, K. E. Jeong, C. U. Kim, and S. Y. Jeong. Butadiene production from bioethanol and acetaldehyde over tantalum oxide-supported ordered mesoporous silica catalysts. *Applied Catalysis B*, 150:596–604, 2014.

[236] P. I. Kyriienko, O. V. Larina, S. O. Soloviev, S. M. Orlyk, and S. Dzwigaj. High selectivity of TaSiBEA zeolite catalysts in 1,3-butadiene production from ethanol and acetaldehyde mixture. *Catalysis Communications*, 77:123–126, 2016.

[237] V. L. Sushkevich, II Ivanova, and E. Taarning. Ethanol conversion into butadiene over Zr-containing molecular sieves doped with silver. *Green Chemistry*, 17(4):2552–2559, 2015.

[238] T.-W. Kim, J.-W. Kim, S.-Y. Kim, H.-J. Chae, J.-R. Kim, S.-Y. Jeong, and C.-U. Kim. Butadiene production from bioethanol and acetaldehyde over tantalum oxide-supported spherical silica catalysts for circulating fluidized bed. *Chemical Engineering Journal*, 278:217–223, 2015.

[239] H.J. Chae, S.Y. Jeong, T.W. Kim, K.E. Jeong, and C.U. Kim. Regular mesoporous silica-based catalyst for preparing 1,3-butadiene from ethanol, and method for preparing 1,3-butadiene using same, 2014. WO Pat. App. WO2014061917A1.

[240] E. V. Makshina, W. Janssens, B. F. Sels, and P. A. Jacobs. Catalytic study of the conversion of ethanol into 1,3-butadiene. *Catalysis Today*, 198(1):338–344, 2012.

[241] C. Angelici, M. E. Z. Velthoen, B. M. Weckhuysen, and P. C. A. Bruijnincx. Effect of Preparation Method and CuO Promotion in the Conversion of Ethanol into 1,3-Butadiene over SiO_2-MgO Catalysts. *ChemSusChem*, 7(9):2505–2515, 2014.

[242] G. Busca, G. Centi, F. Trifiro, and V. Lorenzelli. Surface acidity of vanadyl pyrophosphate, active phase in n-butane selective oxidation. *The Journal of Physical Chemistry*, 90(7):1337–1344, 1986.

[243] F. Babou, G. Coudurier, and J. C. Vedrine. Acidic Properties of Sulfated Zirconia: An Infrared Spectroscopic Study. *Journal of Catalysis*, 152(2):341–349, 1995.

[244] A. Corma, V. Fornes, L. Forni, F. Marquez, J. Martinez-Triguero, and D. Moscotti. 2,6-Di-Tert-Butyl-Pyridine as a Probe Molecule to Measure External Acidity of Zeolites. *Journal of Catalysis*, 179(2):451–458, 1998.

[245] K. Gora-Marek, K. Tarach, and M. Choi. 2,6-Di-tert-butylpyridine Sorption Approach to Quantify the External Acidity in Hierarchical Zeolites. *The Journal of Physical Chemistry C*, 118(23):12266–12274, 2014.

[246] T. Ushikubo and K. Wada. Preparation, characterization, and catalytic activities of silica-supported tantalum oxide for the vapor phase decomposition of methyl tert-butyl ether. *Applied Catalysis A*, 124(1):19–31, 1995.

[247] S.E. Stein NIST Mass Spec Data Center. *Mass Spectra*. National Institute of Standards and Technology, Gaithersburg MD, 20899, http://webbook.nist.gov, (retrieved May 3, 2016).

[248] Inc. Coblentz Society. *Evaluated Infrared Reference Spectra*. National Institute of Standards and Technology, Gaithersburg MD, 20899, http://webbook.nist.gov, (retrieved May 3, 2016).

[249] Spectral Database for Organic Compounds (SDBS). Infrared Spectra, May 3, 2016 . URL `http://riodb01.ibase.aist.go.jp/sdbs/`.

[250] B. B. Corson, E. E. Stahly, H. E. Jones, and H. D. Bishop. Butadiene from Ethyl Alcohol. *Industrial & Engineering Chemistry*, 41(5):1012–1017, 1949.

[251] C.-C. Chang and M.-C. Shu. The Chemical Origin of Defects on Silicon Dioxide Exposed to Ethanol. *The Journal of Physical Chemistry B*, 107(29): 7076–7087, 2003.

[252] Thanh Khoa Phung, Alberto Lagazzo, Miguel Angel Rivero Crespo, Vicente Sanchez Escribano, and Guido Busca. A study of commercial transition aluminas and of their catalytic activity in the dehydration of ethanol. *Journal of Catalysis*, 311:102–113, 2014.

[253] T. K. Phung, L. Proietti Hernandez, A. Lagazzo, and G. Busca. Dehydration of ethanol over zeolites, silica alumina and alumina: Lewis acidity, Bronsted acidity and confinement effects. *Applied Catalysis A*, 493:77–89, 2015.

[254] J.-P. Gallas, J.-M. Goupil, A. Vimont, J.-C. Lavalley, B. Gil, J.-P. Gilson, and O. Miserque. Quantification of Water and Silanol Species on Various Silicas by Coupling IR Spectroscopy and in-Situ Thermogravimetry. *Langmuir*, 25 (10):5825–5834, 2009.

[255] C. Paolucci, A. A. Parekh, I. Khurana, J. R. Di Iorio, H. Li, J. D. Albarracin Caballero, A. J. Shih, T. Anggara, W. N. Delgass, J. T. Miller, F. H. Ribeiro, R. Gounder, and W. F. Schneider. Catalysis in a Cage: Condition-Dependent Speciation and Dynamics of Exchanged Cu Cations in SSZ-13 Zeolites. *Journal of the American Chemical Society*, 138(18):6028–6048, 2016.

[256] A. Wojtaszek, M. Ziolek, S. Dzwigaj, and F. Tielens. Comparison of competition between T = O and T-OH groups in vanadium, niobium, tantalum BEA zeolite and SOD based zeolites. *Chemical Physics Letters*, 514(1-3):70–73, 2011.

[257] V. V. Ordomsky, V. L. Sushkevich, and II Ivanova. Study of acetaldehyde condensation chemistry over magnesia and zirconia supported on silica. *Journal of Molecular Catalysis A: Chemical*, 333(1-2):85–93, 2010.

[258] M. Singh, N. Zhou, D. K. Paul, and K. J. Klabunde. IR spectral evidence of aldol condensation: Acetaldehyde adsorption over TiO_2 surface. *Journal of Catalysis*, 260(2):371–379, 2008.

[259] J. D. Lewis, S. vandeVyver, and Y. Roman-Leshkov. Acid-Base Pairs in Lewis Acidic Zeolites Promote Direct Aldol Reactions by Soft Enolization. *Angewandte Chemie - International Edition*, 54(34):9835–9838, 2015.

[260] S. Van de Vyver, C. Odermatt, K. Romero, T. Prasomsri, and Y. Roman-Leshkov. Solid Lewis Acids Catalyze the Carbon-Carbon Coupling between Carbohydrates and Formaldehyde. *ACS Catalysis*, 5(2):972–977, 2015.

[261] R. P. Young and N. Sheppard. Infrared spectroscopic studies of adsorption and catalysis: Acetone and acetaldehyde on silica and silica-supported nickel. *Journal of Catalysis*, 7(3):223–233, 1967.

[262] Z. D. Young, S. Hanspal, and R. J. Davis. Aldol Condensation of Acetaldehyde over Titania, Hydroxyapatite, and Magnesia. *ACS Catalysis*, 6(5):3193–3202, 2016.

[263] J. E. Rekoske and M. A. Barteau. Competition between acetaldehyde and crotonaldehyde during adsorption and reaction on anatase and rutile titanium dioxide. *Langmuir*, 15(6):2061–2070, 1999.

[264] J. E. Rekoske and M. A. Barteau. Kinetics, Selectivity, and Deactivation in the Aldol Condensation of Acetaldehyde on Anatase Titanium Dioxide. *Industrial & Engineering Chemistry Research*, 50(1):41–51, 2011.

[265] Z. Dang, B. G. Anderson, Y. Amenomiya, and B. A. Morrow. Silica-Supported Zirconia. 1. Characterization by Infrared Spectroscopy, Temperature-Programmed Desorption, and X-ray Diffraction. *The Journal of Physical Chemistry*, 99(39):14437–14443, 1995.

[266] S. Radhakrishnan, P.-J. Goossens, P. C. M. M. Magusin, S.P. Sree, C. Detavernier, E. Breynaert, C. Martineau, F. Taulelle, and J. A. Martens. In Situ

Solid-State 13C NMR Observation of Pore Mouth Catalysis in Etherification of beta-Citronellene with Ethanol on Zeolite Beta. *Journal of the American Chemical Society*, 138(8):2802–2808, 2016.

[267] M. A. Natal-Santiago and J. A. Dumesic. Microcalorimetric, FTIR, and DFT studies of the adsorption of methanol, ethanol, and 2,2,2-trifluoroethanol on silica. *Journal of Catalysis*, 175(2):252–268, 1998.

[268] T. Komanoya, K. Nakajima, M. Kitano, and M. Hara. Synergistic Catalysis by Lewis Acid and Base Sites on ZrO2 for Meerwein-Ponndorf-Verley Reduction. *The Journal of Physical Chemistry C*, 119(47):26540–26546, 2015.

[269] V. L. Sushkevich, D. Palagin, and II Ivanova. With Open Arms: Open Sites of ZrBEA Zeolite Facilitate Selective Synthesis of Butadiene from Ethanol. *ACS Catalysis*, 5(8):4833–4836, 2015.

[270] P. Müller, S.-C. Wang, S. P. Burt, and I. Hermans. Influence of Metal-Doping on the Lewis-Acid Catalyzed Production of Butadiene from Ethanol Studied by Modulated Operando DRIFTS-MS. *Submitted to ChemCatChem*, 2017.

[271] J.N. Chheda, G.W. Huber, and J.A. Dumesic. Liquid-Phase Catalytic Processing of Biomass-Derived Oxygenated Hydrocarbons to Fuels and Chemicals. *Angewandte Chemie - International Edition*, 46(38):7164–7183, 2007.

[272] M. Ni, D. Y.C. Leung, and M. K.H. Leung. A review on reforming bio-ethanol for hydrogen production. *International Journal of Hydrogen Energy*, 32(15):3238 – 3247, 2007.

[273] University of Michigan. *The Michigan Technic*, page 33. Number 63-64. University of Michigan, College of Engineering, 1944.

[274] P. I. Kyriienko, O. V. Larina, S. O. Soloviev, S. M. Orlyk, C. Calers, and S. Dzwigaj. Ethanol Conversion into 1,3-Butadiene by the Lebedev Method over MTaSiBEA Zeolites (M = Ag, Cu, Zn). *ACS Sustainable Chemistry & Engineering*, 5(3):2075–2083, 2017.

[275] W. Janssens, E. V. Makshina, P. Vanelderen, F. DeâŁ…Clippel, K. Houthoofd, S. Kerkhofs, J. A. Martens, P. A. Jacobs, and B. F. Sels. Ternary Ag/MgO-SiO_2 Catalysts for the Conversion of Ethanol into Butadiene. *ChemSusChem*, 8(6): 994–1008, 2015.

[276] Y. Hayashi, S. Akiyama, A. Miyaji, Y. Sekiguchi, Y. Sakamoto, A. Shiga, T.-R. Koyama, K. Motokura, and T. Baba. Experimental and computational studies of the roles of MgO and Zn in talc for the selective formation of 1,3-butadiene in the conversion of ethanol. *Physical Chemistry Chemical Physics*, 18:25191–25209, 2016.

[277] S. DaRos, M. D. Jones, D. Mattia, J. C. Pinto, M. Schwaab, F. B. Noronha, S. A. Kondrat, T. C. Clarke, and S. H. Taylor. Ethanol to 1,3-Butadiene Conversion by using ZrZn-Containing MgO/SiO_2 Systems Prepared by Co-precipitation and Effect of Catalyst Acidity Modification. *ChemCatChem*, 8(14):2376–2386, 2016.

[278] M. Lucas and P. Claus. Hydrogenations over Silver: A Highly Active and Chemoselective Ag-In/SiO_2 Catalyst for the One-Step Synthesis of Allyl Alcohol from Acrolein. *Chemical Engineering & Technology*, 28(8):867–870, 2005.

[279] P. Claus and H. Hofmeister. Electron Microscopy and Catalytic Study of Silver Catalysts:âŁ‰ Structure Sensitivity of the Hydrogenation of Crotonaldehyde. *The Journal of Physical Chemistry B*, 103(14):2766–2775, 1999.

[280] M. Bron, D. Teschner, A. Knop-Gericke, F. C. Jentoft, J. Krohnert, J. Hohmeyer, C. Volckmar, B. Steinhauer, R. Schlögl, and P. Claus. Silver as acrolein hydrogenation catalyst: intricate effects of catalyst nature and reactant partial pressures. *Physical Chemistry Chemical Physics*, 9:3559–3569, 2007.

[281] V. L. Sushkevich and I. I. Ivanova. Ag-Promoted ZrBEA Zeolites Obtained by Post-Synthetic Modification for Conversion of Ethanol to Butadiene. *ChemSusChem*, 9(16):2216–2225, 2016.

[282] N. Popovych, P. Kyriienko, S. Soloviev, R. Baran, Y. Millot, and S. Dzwigaj. Identification of the silver state in the framework of Ag-containing zeolite by XRD, FTIR, photoluminescence, 109Ag NMR, EPR, DR UV-vis, TEM and XPS investigations. *Physical Chemistry Chemical Physics*, 18:29458–29465, 2016.

[283] S. Dzwigaj, Y. Millot, J.-M. Krafft, N. Popovych, and P. Kyriienko. Incorporation of Silver Atoms into the Vacant T-Atom Sites of the Framework of SiBEA Zeolite as Mononuclear Ag(I) Evidenced by XRD, FTIR, NMR, DR UV-vis, XPS, and TPR. *The Journal of Physical Chemistry C*, 117(24):12552–12559, 2013.

[284] B. Tang, W. Dai, X. Sun, G. Wu, N. Guan, M. Hunger, and L. Li. Mesoporous Zr-Beta zeolites prepared by a post-synthetic strategy as a robust Lewis acibigd catalyst for the ring-opening aminolysis of epoxides. *Green Chemistry*, 17:1744–1755, 2015.

[285] J. Lu, J. J. Bravo-Suarez, A. Takahashi, M. Haruta, and S. T. Oyama. In situ UV-vis studies of the effect of particle size on the epoxidation of ethylene and propylene on supported silver catalysts with molecular oxygen . *Journal of Catalysis*, 232(1):85 – 95, 2005.

[286] V. L. Sushkevich, I. I. Ivanova, S. Tolborg, and E. Taarning. Meerwein-Ponndorf-Verley-Oppenauer reaction of crotonaldehyde with ethanol over Zr-containing catalysts . *Journal of Catalysis*, 316:121 – 129, 2014.

[287] B.-H. Mao, R. Chang, L. Shi, Q.-Q. Zhuo, S. Rani, X.-S. Liu, E. C. Tyo, S. Vajda, S.-D. Wang, and Z. Liu. A near ambient pressure XPS study of subnanometer silver clusters on Al_2O_3 and TiO_2 ultrathin film supports. *Physical Chemistry Chemical Physics*, 16:26645–26652, 2014.

[288] V. L. Sushkevich, I. I. Ivanova, and E. Taarning. Mechanistic Study of Ethanol Dehydrogenation over Silica-Supported Silver. *ChemCatChem*, 5(8):2367–2373, 2013.

[289] J. O. M.A. Lins and M. A. C. Nascimento. A density functional study of some silver cluster hydrides . *Chemical Physics Letters*, 391(1-3):9 – 15, 2004.

[290] R. G. Greenler, D.R. Snider, D. Witt, and R.S. Sorbello. The metal-surface selection rule for infrared spectra of molecules adsorbed on small metal particles. *Surface Science*, 118(3):415 – 428, 1982.

[291] Value estimated from the geometry optimized DFT energies of CA, COH and H_2 using the B3LYP functional and the 6-31G(d) basis set in Gaussian.

[292] C. Angelici, M. E. Z. Velthoen, B. M. Weckhuysen, and P. C. A. Bruijnincx. Influence of acid-base properties on the Lebedev ethanol-to-butadiene process catalyzed by SiO_2-MgO materials. *Catalysis Science & Technology*, 5:2869–2879, 2015.

[293] Sang-Ho Chung, Carlo Angelici, Stijn O.M. Hinterding, Markus Weingarth, Marc Baldus, Klaartje Houben, Bert M. Weckhuysen, and Pieter C.A. Bruijnincx. Role of Magnesium Silicates in Wet-Kneaded SilicaâŁ"Magnesia Catalysts for the Lebedev Ethanol-to-Butadiene Process. *ACS Catalysis*, 6(6): 4034–4045, 2016.

[294] Paul Scherrer Institute, Modulation Excitation Spectroscopy, 2013. URL `https://www.psi.ch/sls/superxas/modulation-excitation-xas`. accessed 12/1/2016.

[295] M. A. Newton and M. Fernandez-Garcia. Combining Infrared Spectroscopy with X-ray Techniques for Interrogating Heterogeneous Catalysts. *In-Situ Characterization of Heterogeneous Catalysts*, pages 369–409, 2013.

[296] N. E. Tsakoumis, A. P. E. York, D. Chen, and M. Ronning. Catalyst characterisation techniques and reaction cells operating at realistic conditions; towards acquisition of kinetically relevant information. *Catalysis Science & Technology*, 5(11):4859–4883, 2015.

[297] M. A. Newton, M. Di Michiel, A. Kubacka, and M. Fernandez-Garcia. Combining Time-Resolved Hard X-ray Diffraction and Diffuse Reflectance Infrared Spectroscopy To Illuminate CO Dissociation and Transient Carbon Storage by

Supported Pd Nanoparticles during CO/NO Cycling. *Journal of the American Chemical Society*, 132(13):4540–4541, 2010.

[298] D. Bounechada, S. Fouladvand, L. Kylhammar, T. Pingel, E. Olsson, M. Skoglundh, J. Gustafson, M. Di Michiel, M. A. Newton, and P.-A. Carlsson. Mechanisms behind sulfur promoted oxidation of methane. *Physical Chemistry Chemical Physics*, 15:8648–8661, 2013.

[299] S. J. Tinnemans, J. G. Mesu, K. Kervinen, T. Visser, T. A. Nijhuis, A. M. Beale, D. E. Keller, A. M.J. van der Eerden, and B. M. Weckhuysen. Combining operando techniques in one spectroscopic-reaction cell: New opportunities for elucidating the active site and related reaction mechanism in catalysis . *Catalysis Today*, 113(1-2):3 – 15, 2006.

[300] A. Urakawa. Trends and advances in Operando methodology . *Current Opinion in Chemical Engineering*, 12:31 – 36, 2016.

[301] F. Meemken, P. Müller, K. Hungerbühler, and A. Baiker. Simultaneous probing of bulk liquid phase and catalytic gas-liquid-solid interface under working conditions using attenuated total reflection infrared spectroscopy. *Review of Scientific Instruments*, 85(8):084101, 2014.

[302] I. Noda. Advances in two-dimensional correlation spectroscopy. *Vibrational Spectroscopy*, 36(2):143–165, 2004.

[303] A. Voronov, A. Urakawa, W. van Beek, N. E. Tsakoumis, H. Emerich, and M. Ronning. Multivariate curve resolution applied to in situ X-ray absorption spectroscopy data: An efficient tool for data processing and analysis . *Analytica Chimica Acta*, 840:20 – 27, 2014.

[304] J. D. Grunwaldt and A. Baiker. In situ spectroscopic investigation of heterogeneous catalysts and reaction media at high pressure. *Physical Chemistry Chemical Physics*, 7(20):3526–3539, 2005.

[305] P. L. Silveston and R. R. Hudgins. Chapter 15 - Pressure Modulation. In P.L. Silveston and R.R. Hudgins, editors, *Periodic Operation of Chemical Reactors*, pages 415 – 434. Butterworth-Heinemann, Oxford, 2013.